D.I. Iudin, E.V. Koposov

FRACTALS

as simple as complex

Dmitry IUDIN
Eugeny KOPOSOV

FRACTALS:

as simple
as complex

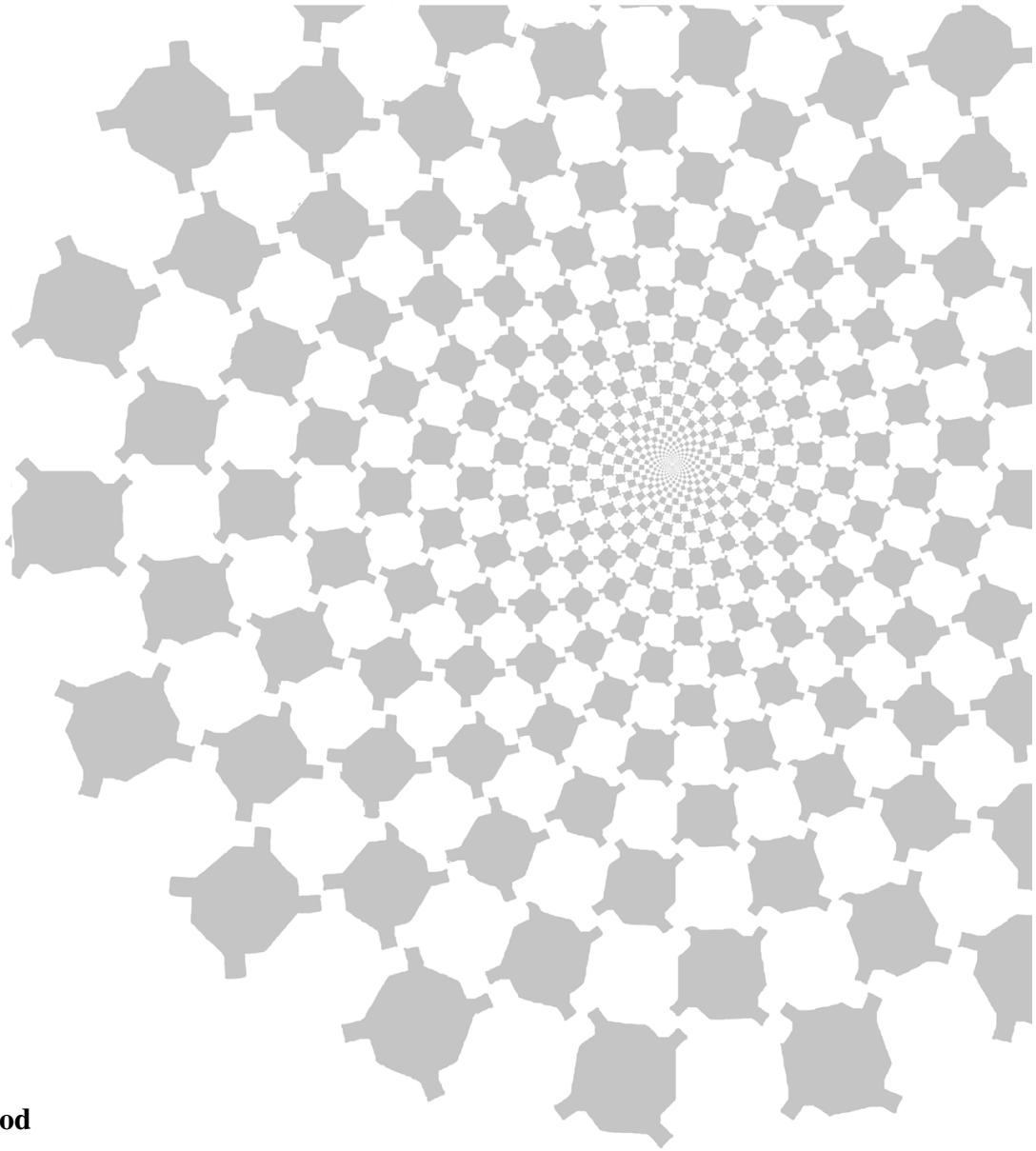

Nizhny Novgorod
2013

This book is an introduction to the world of scaling. Following the principle from simple to complex the authors start with the fundamentals of the fractal geometry. In Chapter 1 definitions of basic concepts and simple examples of regular as well as stochastic fractals are given. Then in Chapter 2 the reader gets acquainted with fractal structures occurring at geometric phase transitions. Application of the fractal geometry and percolation theory in the description of complex systems forms the content of Chapter 3. In addition, the interested reader may find examples of programme codes of fractal and percolation models realized in the MATLAB system on the cellular automation networks.

The book is addressed to a wide range of scientists, postgraduates and students who want to learn about the fundamentals of the fractal geometry, percolation theory and methods of their application to describe various phenomena of the world around us.

Published by NNGASU

Contents

Preface **3**

1 FRACTAL GEOMETRY **5**
1.1 Fractals and scaling 7
1.2 Regular fractals 9
1.3 Iterated function systems 15
1.4 Stochastic fractals 17
1.5 Methods of fractal dimension calculation 20
1.6 Chemical fractal dimension 25
1.7 Multifractals and multifractal formalism 26
1.8 Fractal geometry and physics 37

2 PERCOLATION THEORY **39**
2.1 Percolation on regular lattices 40
2.2 Percolation as a critical phenomenon 45
2.3 Structure of the percolating cluster 49
2.4 Exact solution in a one-dimensional case 54
2.5 Percolation on the Kayley tree 59
2.6 Percolation level 64
2.7 Problem of discs 69
2.8 Gradient percolation 72
2.9 Directed percolation 74

3 APPLICATION **77**
3.1 Fractal time series 78
3.2 Fractal surfaces 81
3.3 Rank distributions 91
3.4 Percolation in disperse systems 97
3.5 Fractal networks and labyrinths 104
3.6 Percolation in active media 112
3.7 Self-organizing drainage systems 122
3.8 Percolation differentiation 126
3.9 Vector percolation and neuron networks 144
3.10 Baton transition of information 148

Appendix. PROGRAMME CODES **155**
A. Iterated function systems 156
B. One-dimensional chain 157

C. Gradient percolation 158
D. Brownian landscapes 161
E. The forest fire model 164

List of figures **169**

References **173**

Index **182**

Preface

There is a wide range of natural systems which morphology and behaviour demonstrate self-similarity or so-called scaling invariance at the change of spatio-temporal ranges - one of the fundamental types of symmetries of the physical world, which play a shape-generating role in the Universe [1, 2, 17]. Tree growth and river drainage systems, vegetation cover and forest fires, structure of clouds and lightning discharges, fluid percolation through soils and seismicity, population evolution and financial crisis dynamics - all these are examples of the active demonstration of self-similarity. In other words this phenomenon is also called "scaling". Scaling can be spatial, temporal or spatio-temporal. A classic example of the spatial scaling is the ocean coast-line. Looking at the coast-line images of different scales (e.g. 1:1000000 and 1:10000) we cannot say for sure which image corresponds to what scale because both images look statistically the same. It means that a coast-line is self-similar being a scale-invariant object or in other words it is an object that has no distinctive length. The invariance with regard to the length conversion of time intervals reveals in various information flows such as financial reports, environmental monitoring data, etc. The spatio-temporal scaling is the most common demonstration of the self-similarity attributed to complex social, technogenic, geophysical and cosmic processes and systems. The history of social upheavals and technogenous disasters [17],spike neuron activity [4], forest fires [5], magnetosphere plasma dynamics [6–8] and seismic activity [39], solar outbursts and gamma activity of star-clusters [10] are the examples of it.

There are two complementary aspects of the scaling. On the one hand, the self-similarity is typical to active multi-component hierarchical systems that demonstrate a complex behaviour and need a wide range of spatio-temporal scales to realize their self-similarity. On the other hand, a mathematical form of scaling is a simple power function $f(x) = x^a$ where the exponent a is the only number characterizing a difficult iteration procedure of fractal structure formation, that is a road from small to large and from simple to complex.

The system scaling is characterized by strong correlations decaying by a power law, which are typical to critical phenomena. Physically, a power character of the correlation relationships means a simple and at the same time fundamental fact - such a system HAS NO DISTINCTIVE spatial, temporal or spatio-temporal SCALE.

Self-similarity is an essential attribute of the systems with catastrophic behaviour such as seismic activity and forest fires, wars and epidemics, sinkholes and landslides. That is why the study of scaling properties of the behaviour of complex geophysical, environmental, po-

litical, economic and other systems is important for prediction of consequences and risk assessment even if the impact on these systems is negligible.

This book is an **introduction** into the world of scaling. Following the principle "*from simple to complex*" we will start with the fundamentals of the fractal geometry in Chapter 1, where definitions of the basic concepts and simple examples of both regular and stochastic fractals will be given. Then in Chapter 2 the reader will get acquainted with fractal structures occurring at geometric phase transitions that are studied by the percolation theory appeared in 1957 [57]. The fractal boom in the 80s of the last century marked the second berth of this theory [12, 17, 29, 29]. Application of the fractal geometry and percolation theory in the description of complex systems forms the content of Chapter 3. In addition, the interested reader may find examples of programme codes of fractal and percolation models realized in the MATLAB system on the cellular automation networks.

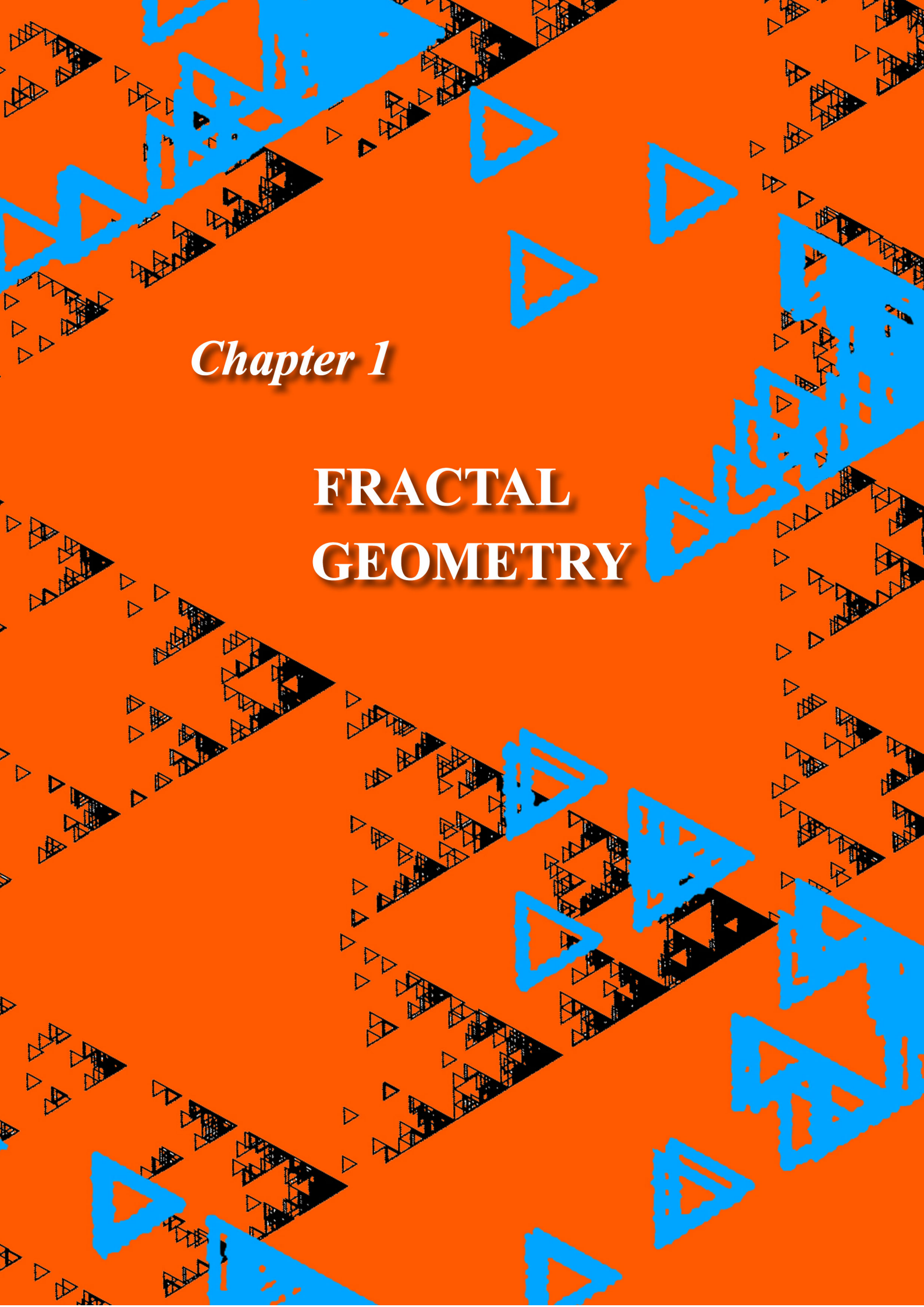

Chapter 1

FRACTAL GEOMETRY

The idea of fractal appeared rather late, already in the era of computers, due to the missionary efforts of Benoît Mandelbrot. His enlightening activities against the background of computer technologies made people hold their breath in front of the charm of fractal structures. The beauty of fractals is caused by their extraordinary practicability. Nature uses fractal structures to solve a wide spectrum of tasks: from mass distribution in space to resources accumulation and distribution in biological and geophysical objects. Initially giving an image of a strange attractor, the fractal geometry itself has become an attractive companion for researchers in different fields of knowledge. Anyhow, one should keep in mind that the triumphal demonstration of the fractal geometry that we witness now would not have been possible without a whole series of genius discoveries made by the contemporary mathematicians. It is not possible to speak about fractals without mentioning the Cantor set, Sierpiński gasket and carpet, examples of Weierstrass and van der Waerden of the non-differentiated continuous function. From the point of view of classical analysis, the self-similar objects introduced in the mathematics in the XIX century possessed pathological properties, and their inventors were considered social outcasts.

Mathematically, the self-similarity is expressed by power lows. If we multiply x by a constant in the homogeneous power function $f(x) = cx^a$ where c and a are constant values, then the function $f(x)$ will still be proportional to x^a, though with a different coefficient of proportionality. Therefore, the power lows with integral or fractional exponents are the self-similarity generators. The fact that the homogeneous power lows do not have any natural inner scale sets conditions for the scale invariance phenomenon to be widely-spread in a real world: from the Nile floods and gambler ruins in the financial markets to the distribution of galaxies in the Universe.

In other words, if scale is changed the power lows reproduce themselves, but this proposition holds strictly only for mathematic models. Real objects are never exactly scale invariant, in particular due to the so called "*end effect*" related to the natural spatio-temporal limits of physical and social phenomena.

Benoît Mandelbrot

Wacław Sierpiński

Karl Theodor Wilhelm Weierstrass

Scale-invariant systems are usually described by a nonintegral – fractal dimension. The concept of the nonintegral dimension as well as the basic features of fractal objects were studied in the XIX century by Georg Cantor, Giuseppe Peano, David Hilbert and at the beginning of the XX century by Helge von Koch, Wacław Sierpiński, Gaston Julia and Felix Hausdorff. Premises of the fractal geometry are found in the works of Carl Friedrich Gauß(1777-1855) dedicated to the arithmetics of mean geometric numbers, in the engravings by Albrecht Dürer (1471-1528) and even in the Italian mosaic of the XII century. Fractal structures are studied by the fractal geometry. This is a young but rapidly developing field of the modern mathematics. For the first time its fundamental and natural-science application was described in the works of Benoît Mandelbrot [12, 15–18].

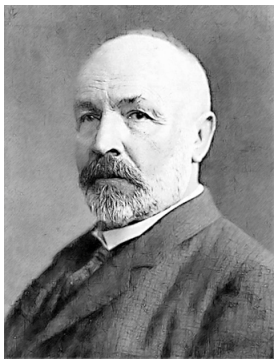

Georg Cantor

Felix Hausdorff

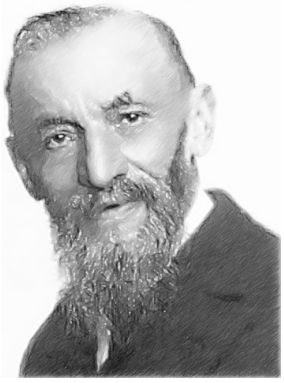

Giuseppe Peano

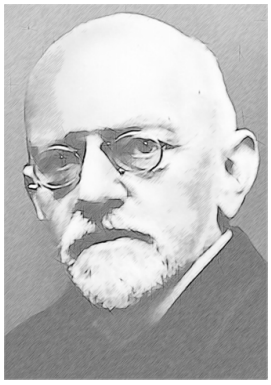

David Hilbert

1.1 Fractals and scaling

In spite of its wide use the notion "fractal" has not been clearly and precisely defined yet. The simplest and shortest definition of fractals is as follows: a fractal is a structure consisting of the parts that in someway are similar to the integer. However, such a definition does not cover the whole variety of objects related to fractals. Mandelbrot defined a fractal (in Latin fractus means "fractional") as "a set, the Hausdorff-Besikovitch dimension of which is strictly larger than its topological dimension" [12]. This definition is strict enough from a mathematical point of view, which, however, is its basic drawback, for it requires to define dimensions (topological and Hausdorff) as well. Moreover, it excludes many classes of fractal objects found in different fields of the natural science. Mandelbrot made also a more general and less formal definition: "To my idea all figures I analysed and called the fractals had the feature to be irregular but self-similar" [12]. Hence, the self-similarity becomes a key aspect of the fractal definition. It may be stated that a fractal object is statistically uniform in a wide range of scale. Theoretically, (mathematical fractal), such a self-similarity makes a fractal object invariant with regard to the range of spatial changes (extension and compression).

Falconer in his book [19] gives a good comparison: "To define fractals in mathematics is as difficult as to define what the life is in biology. It is only possible to specify some features, which (not necessarily all) these objects may possess. Usually, if they say that a set $\mathfrak{F}$ is a fractal, they mean as follows:

1) set $\mathfrak{F}$ has a fine structure, i.e. arbitrary small-scale components.

2) set $\mathfrak{F}$ is too irregular to be described in terms of traditional geometry both locally and globally.

3) set $\mathfrak{F}$ has some self-similarity which may be approximate or statistical.

4) usually, any-defined "fractal dimension" $\mathfrak{F}$ is greater than its topological dimension.

5) in many interesting cases the set $\mathfrak{F}$ can be defined easily, maybe "recursively".

The forth feature corresponds to the initial definition given by Mandelbrot [17], and in this definition by a fractal dimension the Hausdorff-Besikovitch dimension was meant.

Dimension is the main numerical value of a fractal object [20]. In the simplest way a dimension can be defined as a number of variables (or measurements) which are necessary to specify location of a point in space. Thus, two coordinates are required to describe location of a point on a plane, and, therefore, a plane as any other smooth surface has a dimension equal to 2, i.e. it is two-dimensional. Location of a point on a line can be defined by one coordinate, so a line is one-dimensional, and its dimension is equal to 1. By analogy a point dimension is equal to 0, and the space we live in is three-dimensional. The definition of dimension introduced in such an intuitive way corresponds to a topological dimension in mathematics that is always an integer.

Now, passing to the subject matter of a fractal dimension, it is worth to remind that the physical nature of the notion of a geometrical object dimension, including a fractal one, is determined by a change of the mass of the object (or a number of elements it consists of) $M(r)$ with the growth of its linear sizes r [12, 15–17]. For a small part of a system with dimensions λr ($\lambda < 1$) the fragment mass is:

$$M(\lambda r) = \lambda^{d_f} \cdot M(r). \tag{1.1}$$

The solution of functional equation (1.1) is simple:$M(r) = \text{const} \cdot r^{d_f}$. So, the mass of a long wire changes linearly with λ i.e. $d_f = 1$. For a thin plate we will find that $d_f = 2$ and for a bar $d_f = 3$.

Of course, such a "physical" definition of dimension correlates with an intuitively understandable possibility to divide an object into parts. Indeed, according to this classical approach, an object is n-dimensional, if it can be broken down into parts by hyperplanes, which are $(n-1)$-dimensional objects themselves. In this way we come to a recurring definition of dimension, assuming that volumes are parts of space, surfaces are boarders of volumes, lines

are boarders of surfaces and points are boarders of lines.

Let us consider an object, which can be reproduced by enlarging any of its part, as self-similar or invariant at the similarity transformation, i.e. a fractal.

Returning to functional equation (1.1) , it may be asserted that solution (1.1) with non-integral d_f confirms fractal or self-similar objects:

$$M(r) = \text{const} \cdot r^{d_f}. \tag{1.2}$$

The dimension value d_f of fractal objects appears to be less than the dimension of the comprehensive Euclidean space $d_f < d$ .Thus, the density of fractal structures $\rho(r)^{\dagger}$ decreases according to a power law with the increase of their linear sizes r:

$$\rho(\lambda r) = \frac{M(\lambda r)}{(\lambda r)^d} = \lambda^{d_f - d} \cdot \frac{M(r)}{r^d} = \lambda^{d_f - d} \cdot \rho(r). \tag{1.3}$$

Ratio 1.3 gives an intuitively understandable definition of a fractal object: a fractal is a structure with holes at any scale. The greater linear dimensions of a fractal are the larger holes we can find in it. Therefore, the increasing of fractal linear scales implies reduction of its density.

1.2 Regular fractals

Let us consider fractal properties using some simple examples. We start with the Cantor set. This famous fractal is constructed in the following way: a line segment of a unit length (called a base) is divided in to three equal parts $l = 1/3$, and its middle third is removed. In the next step this procedure is repeated for the remaining two segments, and so on. Fig.1.1 shows the result of several initial iterations.

It is easy to understand that the total length of the removed segments is equal to 1. In fact the total lengths of the segments removed at a subsequent step of iteration form an infinite decreasing geometric sequence:

$$\frac{1}{3}, \quad 2 \cdot \frac{1}{9} = \frac{2}{3} \cdot \frac{1}{3}, \quad 4 \cdot \frac{1}{27} = \frac{2}{3} \cdot \frac{2}{9} = \left(\frac{2}{3}\right)^2 \cdot \frac{1}{3}, \quad \cdots,$$

[†]The volume, surface or linear density is implied depending on the value of an enveloping Euclidean space dimension d.

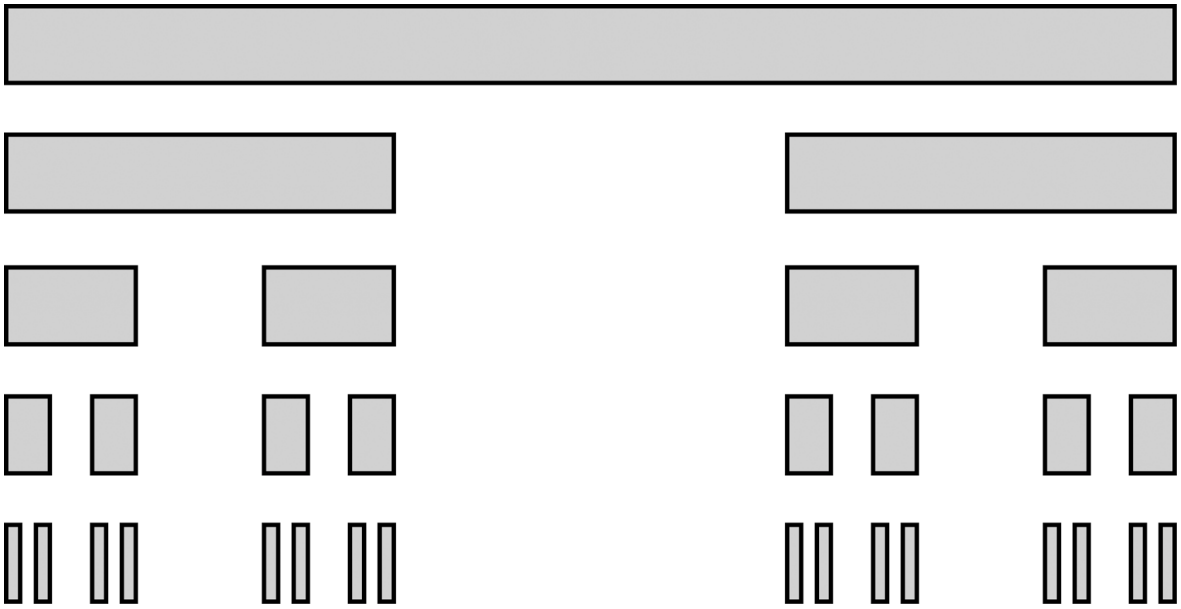

Figure 1.1: Cantor set generation

the sum of which $\frac{1}{3}\cdot\sum_{n=1}^{\infty}\left(\frac{2}{3}\right)^n$ is equal to 1. It means that a fractal set we have made (the Cantor set) has no length.

Let us take the right (or if you would like the left) third of the initial segment subjected to the iterative Cantor set generation. This third is a reduced copy (three times smaller by linear dimensions) of the Cantor set, and at the same time it contains half of its mass (just to remind, the middle third of the segment was cut away during the Cantor set generation). Now all that we have just formulated in words, we will write down by formulas. For this purpose we will use functional equation (1.1) with $\lambda = 1/3$ and $r = L = 1$:

$$M\left(\frac{1}{3}\cdot 1\right) = \frac{1}{2}\cdot M(1) = \left(\frac{1}{3}\right)^{\frac{\ln 2}{\ln 3}}\cdot M(1). \tag{1.4}$$

Comparing (1.4) with (1.1) we find out that the fractal dimension of the Cantor set is equal to $d_f = \frac{\ln 2}{\ln 3} \approx 0.6309$. The dimension is less than one and confirms the fact that the Cantor set has no length.

Constructing the Cantor set, we started from a single segment and replaced it by a "generator" consisting of two segments of a $1/3$ length located in line at an $1/3$ interval between their nearest ends. At each consecutive iteration step all new segments are replaced by a new "generator" that is a copy of a previous one, but three times smaller. It is also possible to turn to magnification by doubling the number of segments and increasing linear sizes of the construction three times. Both procedures may be combined as well.

Let us consider a Cantor set density. Relation (1.1) with $d = 1$ and $d_f = \dfrac{\ln 2}{\ln 3}$ shows that the density $\rho(L)$ of the Cantor set decreases according to a power law as its linear sizes L grow:

$$\rho(L) = L^{\ln 2/\ln 3 - 1} = L^{-0.3691}. \tag{1.5}$$

In 1904 Swedish mathematician Helge von Koch described a so-called triad curve that is widely known as the Koch curve [21]. Construction of the curve starts with a linear segment of unit length, which is divided into three segments of an equal length. The middle segment is replaced by a "fiord" of two segments forming an equilateral triangle with a removed one as its base (Fig. 1.2). A new figure is a generator of a new fractal. During the next steps of the Koch curve construction all line segments are replaced by reduced copies of the fractal generator, i.e. their middle thirds are cut out and replaced by a "fiord". Multiple iterations of this simple procedure result in a very beautiful figure. Any arbitrarily small part of this figure is similar to the whole construction. Using functional equation (1.1), it is easy to calculate a fractal dimension of the Koch curve: $d_f = \dfrac{\ln(4)}{\ln(3)} \approx 1.2619$. The length of the Koch curve is not defined, for it depends on the measurement accuracy and become divergent as the accuracy rises. Indeed, the length of the kinked curve increases at each iteration step 1.2 by $4/3$ and constitutes $(4/3)^n$,where n is the number of a procedure step.

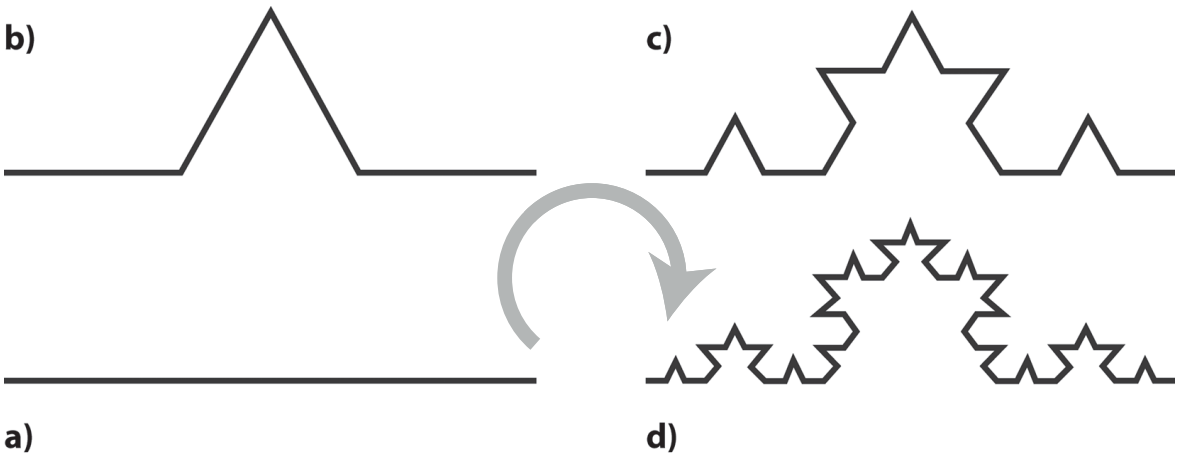

Figure 1.2: The Koch curve iterations

Now let us apply the described Koch procedure at once to three segments which form an equilateral triangle (see Fig. 1.3). The first step of iteration forms the Star of David and then a snowflake which boarder is becoming more indented after each iteration step. This figure with a fractal boarder is called the Koch island (also known as the Koch star and Koch snowflake).

It is obvious, that the perimeter of the Koch island like the length of the Koch curve depends on the measurement accuracy and become divergent as the accuracy rises. At an n-step of iteration the perimeter will be $P_n = 3 \cdot \left(\dfrac{4}{3}\right)^n$.

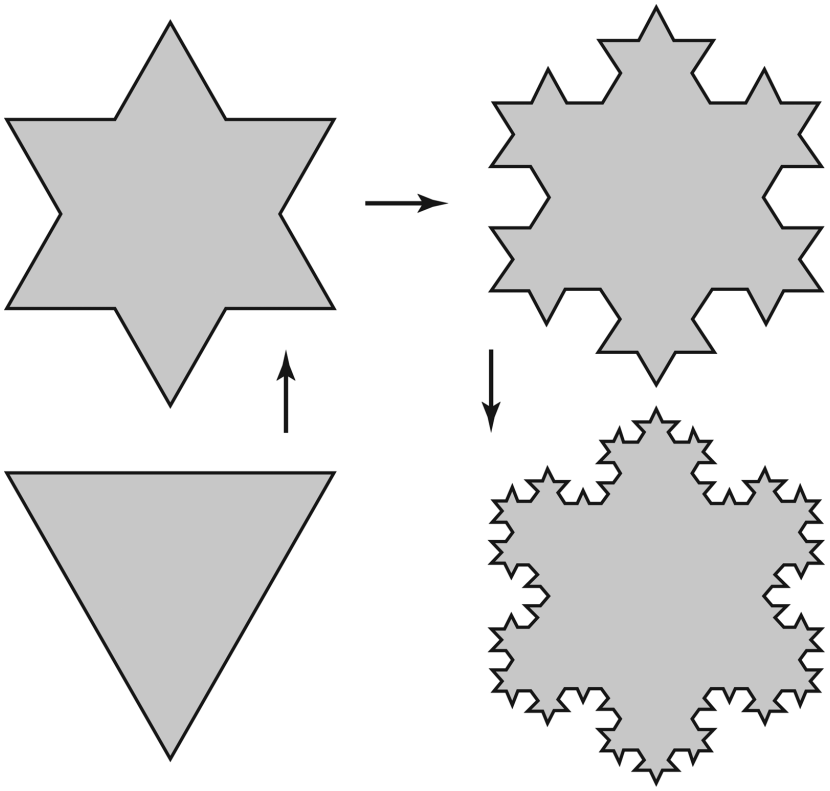

Figure 1.3: The first four iterations of the Koch Island

Let us calculate the Koch Island area. At the first step of the procedure the area of the original equilateral triangle $S_0 = \frac{\sqrt{3}}{4}$ increases at the expense of the cumulative area of the fiords protruding on each of the three sides. It is obvious, that the area of one fiord constitutes $1/9$ of that of the original equilateral triangle, so $S_1 = S_0 + 3 \cdot \frac{1}{9} \cdot S_0$. On each consecutive step of iteration the area of the Koch Island will increase at the expense of the area of new fiords, the number of which on each side of the original triangle will increase as a power of 4 and the area of each new fiord will reduce as a power of $1/9$:

$$S_n = S_0 + 3 \cdot \left(\frac{1}{9} \cdot S_0 + \frac{4}{9^2} \cdot S_0 + \ldots + \frac{4^{n-1}}{9^n} \cdot S_0 \right) = S_0 \left[1 + \frac{3}{4} \sum_{i=1}^{n} \left(\frac{4}{9} \right)^i \right]. \qquad (1.6)$$

In equation (1.6) the right part is the sum of geometric progression with the denominator $\frac{4}{9}$, so finally we have:

$$S_n = S_0 \left\{ 1 + \frac{3}{5} \left[1 - \left(\frac{4}{9} \right)^n \right] \right\}. \qquad (1.7)$$

With infinite iteration, the area of the Koch Island is:

$$S = \frac{8}{5} \cdot S_0 = \frac{2\sqrt{3}}{5}. \tag{1.8}$$

We have obtained an intriguing result – the finite area of the Koch Island is limited by a perimeter of the infinite length.

It is interesting to look at it in another way. The fact is the shape of plane figures can be characterized by an edge index:

$$\alpha_{EI} = \frac{P}{2\sqrt{\pi A}}, \tag{1.9}$$

where P is the total perimeter, including inner boundaries, if available,A is the area of the figure. For a circle, for instance, α_{EI} possesses a possible minimum value equal to one, for a square $\alpha_{EI} \simeq 1.29$. The edge index of the Koch Island is equal to infinity![†]

It is clear, that we cannot find this kind of infinity in the reality of the physical world. Never the less, in Chapter 3 we will see that nature uses such anomalies very often in order to solve specific tasks.

Another classical example is the Sierpiński gasket (also called the Sierpiński triangle or the Sierpiński sieve). Construction of the Sierpiński gasket starts from an equilateral triangle (Fig. 1.4). From its centre an equilateral triangle with a side equal to a half of the length of the original triangle's side and turned upside down is cut out. In the result three equilateral triangles are left with the sides half of the original triangle side length. In the next step, similarly, central triangles are cut out from the remaining triangles to form 9 triangles, which are subjected to the same procedure, and so on. Such iterations construct the Sierpiński gasket. According to functional equation (1.1) its fractal dimension is $d_f = \dfrac{\ln(3)}{\ln(2)} \approx 1.5850$. The self-similarity of the Sierpiński gasket is obvious, since any non-empty triangle is a copy of any other (including gasket itself).

It is easy to prove, that the total area of the triangular holes in the gasket is equal to the area of the original triangle. Indeed, the cumulative areas of the triangles removed at any next step of the iteration procedure constitute an infinite decreasing geometric sequence:

$$\frac{1}{4}, \quad 3 \cdot \frac{1}{16} = \frac{3}{4} \cdot \frac{1}{4}, \quad 9 \cdot \frac{1}{64} = \frac{3}{4} \cdot \frac{3}{16} = \left(\frac{3}{4}\right)^2 \cdot \frac{1}{4}, \quad \cdots,$$

[†]Three-dimensional figures can be characterized by the surface index

$$\alpha_3 = \frac{S}{(6\sqrt{\pi} \cdot V)^{2/3}},$$

where S is the total surface area of a three-dimensional figure including its inner boundaries if they exist, and V is the volume of the figure. For a sphere α_3 is the minimum possible value equal to 1, for a cube $\alpha_3 \simeq 1.24$.

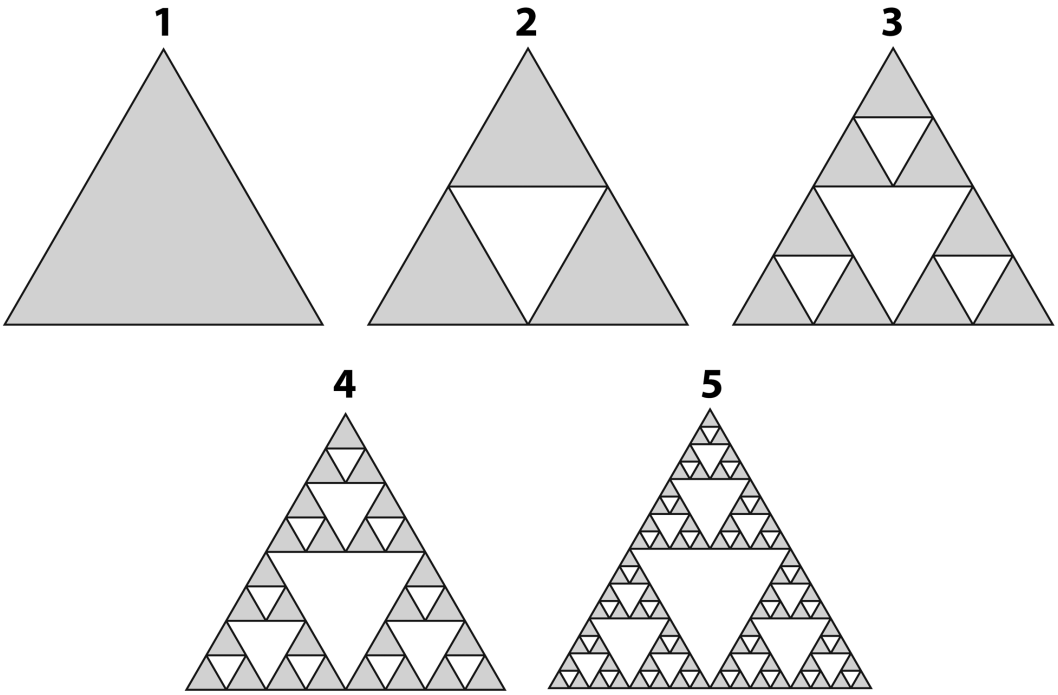

Figure 1.4: The Sierpiński gasket iterations

the sum of which $\frac{1}{4} \cdot \sum_{n=1}^{\infty} \left(\frac{3}{4}\right)^n$ is equal to one. It means that the area of the Sierpiński gasket is equal to 0.

We have to pay tribute to Sierpiński's services. In addition to the gasket he invented also a carpet, which bears his name as well. Figure 1.5 presents an algorithm of construction of a fractal set called the Sierpiński carpet.

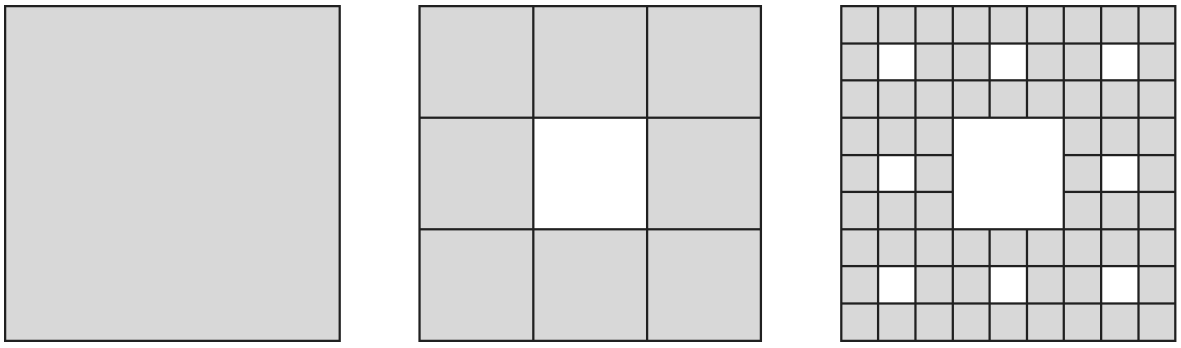

Figure 1.5: Iteration of the Sierpiński carpet

Using functional equation (1.1), it is easy to find that the fractal dimension of the Sierpiński carpet is $d_f = \frac{\ln(8)}{\ln(3)} \approx 1.8928$. We may notice that the procedure of the Sierpiński carpet construction is a plane analogue of the algorithm of the Cantor set generation. A three-

dimensional variant of the Cantor set generation algorithm produces a fractal structure called the Menger sponge with the dimension $d_f = \dfrac{\ln(20)}{\ln(3)} \approx 2.7268$.

1.3 Iterated function systems

The Koch curve and the Sierpiński gasket represent a broad class of so-called "constructive fractals". Construction of these fractals is based on the use of a certain simple procedure-generator applied to the original set-base. A considerable variety of examples of such fractals may be found in literature [21–24].

Another common method of constructing fractals is called a method of Iterated Function Systems (IFS) offered by American researcher Barnsley [25]. IFS is a system of a fixed class of functions overlapping one multidimensional set on another. The simplest IFS consists of affine conversions of a plane:

$$\begin{cases} x_{n+1} &= ax_n + by_n + \eta \\ y_{n+1} &= cx_n + dy_n + \xi \end{cases} \tag{1.10}$$

Let us consider a simple procedure, which Barnsley called a chaos game. Take a randomly selected initial point inside an equilateral triangle. Choose any triangle vertex and join it with the initial point with a line. Set a new point in the middle of the line, which will play now a role of the initial point. Keep repeating this procedure and setting new points. In this case a corresponding IFS is as follows:

$$\begin{cases} x_{n+1} &= \frac{1}{2}(x_n + \eta) \\ y_{n+1} &= \frac{1}{2}(y_n + \xi) \end{cases}, \tag{1.11}$$

where random variables η and ξ with the probability $1/3$ take on values of abscissas and ordinates accordingly of the equilateral triangle vertexes:$(0,0)$; $(1/2, 1/2\sqrt{3})$; $(1,0)$. Surprisingly enough, but the procedure has resulted in nothing but the Sierpiński gasket (Fig. 1.6). In fact, selection of a triangle vertex in this chaos game is equivalent to the selection of one out of three affine conversions applied to the point.

Altering system 1.11 slightly, we can perform the same procedure with a right triangle, when random variables η and ξ with the $1/3$ probability take on values of abscissas and ordinates accordingly of the following vertexes:$(0,0)$; $(0,1)$; $(1,0)$. The result is given in Figure 1.7.

And here is another example of IFS application:

$$\begin{cases} x_{n+1} &= \frac{1}{3}(x_n + 2\eta) \\ y_{n+1} &= \frac{1}{3}(y_n + 2\xi) \end{cases} \tag{1.12}$$

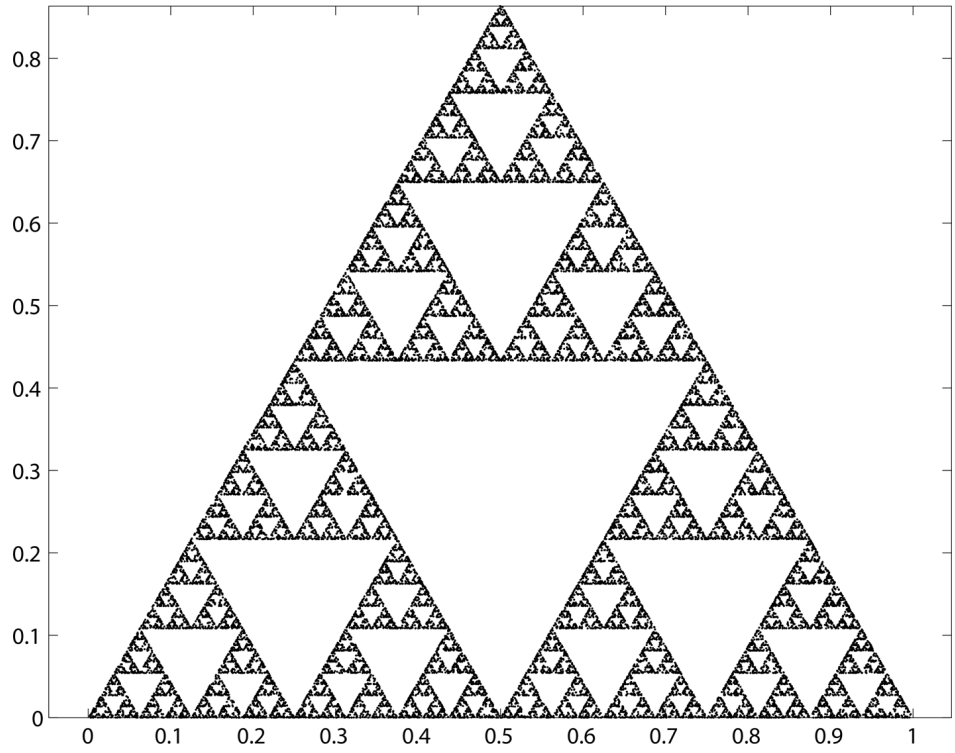

Figure 1.6: Application of the IFS-generator of the Sierpiński gasket to the equilateral triangle

where random variables η and ξ with the $1/4$ probability take on values of abscissas and ordinates accordingly of the unit square vertexes: $(0,0)$; $(0,1)$; $(1,1)$; $(1,0)$. The result of this IFS application is given in Fig. 1.8.

1.4 Stochastic fractals

All the above mentioned fractals may be called regular, for they come out of a repetition of a certain deterministic algorithm. Self-similarity is a strict attribute thereof. However, in nature we usually meet the so called random fractals. Their main difference from the regular fractals is that the self-similarity exhibits only as a result of the appropriate averaging of all statistically independent properties of an object. Herewith, for a specific property the enlarged part of a fractal is not identical to the original fragment, but their statistical parameters are similar [26–29].

A simple example of a stochastic fractal is a trajectory of the Brownian motion, i.e. random walks, when in any step of the model time a particle moves to a distance a in to a randomly chosen neighbouring site of a d-dimensional model lattice. Let us assume that at time $t = 0$ a particle started from the origin of coordinates of a d-dimensional lattice space. Then after a certain number t of steps of the model time the current position of the diffusing particle will

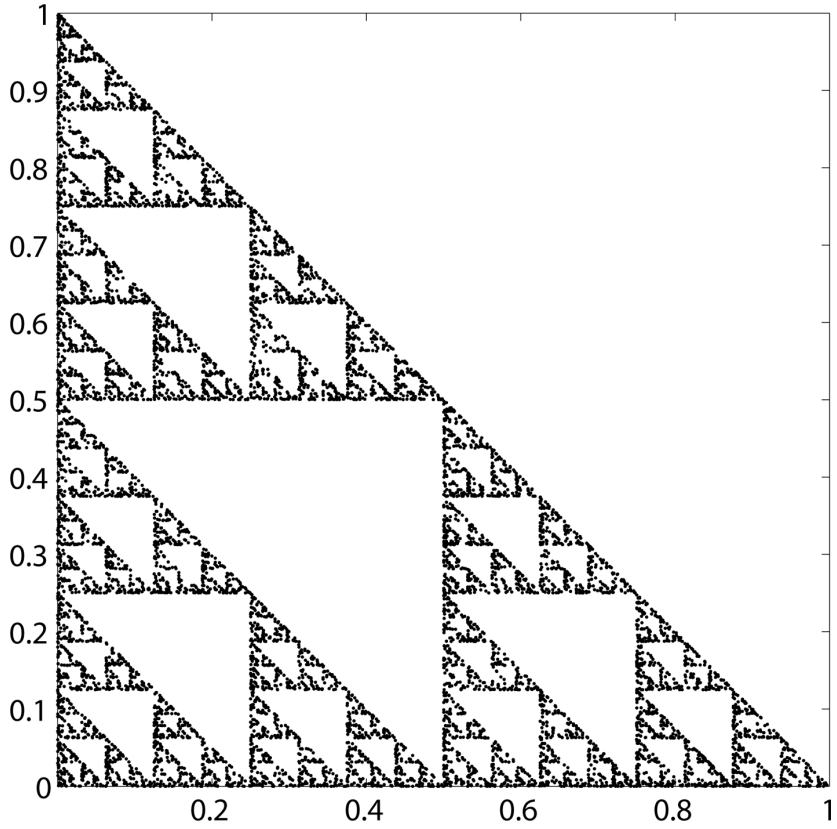

Figure 1.7: Application of the IFS-generator of the Sierpiński gasket to the right triangle

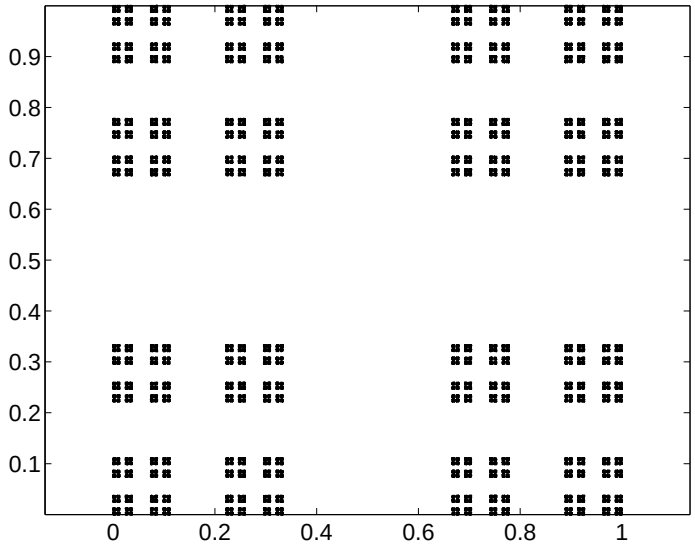

Figure 1.8: Result of the application of the IFS-generator of eq.1.12

be described by the shift-vector:

$$\mathbf{r}(t) = a \sum_{k=1}^{t} \mathbf{e}_k, \tag{1.13}$$

where $\mathbf{e}_k$ is the unit vector to the direction of a jump at the k-step of the model time.

A characteristic distance the particle shifts in the average during the random walking in t steps of the model time is described by a mean-squire shift $\langle r^2(t)\rangle^{1/2}$, where the mean $\langle\ldots\rangle$ is conceived as the average of every possible pattern of random walking on the lattice. Using eq. 1.13 we find:

$$\langle r^2(t)\rangle = a^2 \sum_{k,k'=1}^{t} \langle \mathbf{e}_k \cdot \mathbf{e}'_k \rangle = a^2 t + \sum_{k\neq k'}^{t} \langle \mathbf{e}_k \cdot \mathbf{e}'_k \rangle.$$

So far as the particle jumps are not correlated with each other at different times k and k' we have $\langle \mathbf{e}_k \cdot \mathbf{e}'_k \rangle = \delta_{kk'}$ that finally leads us to the Fick diffusion law:

$$\langle r^2(t)\rangle = a^2 t \tag{1.14}$$

Fig. 1.9 graphically demonstrates several options of random walking in a one-dimensional case as a result of eq. 1.14. Note, that the result of eq. (1.14) does not depend on the lattice dimension d. In a more general case, when there is a probability for a particle to stay put, the mean-squire shift is described by the Einstein equation:

$$\langle r^2(t)\rangle = 2dDt, \tag{1.15}$$

where D is the coefficient of diffusion.

If a wire is laid along a trajectory of random walks, its mass will be proportional to the time of the travel $M \sim t$. Herewith, the characteristic radius of the Euclidean sphere containing the whole trajectory by the time t is described according to relation $r \sim \sqrt{t}$ (1.15). Thereby, $M \sim r^2$ i.e. the fractal dimension of the Brownian motion trajectory equals two and does not depend on the space scale.

It's remarkable that a crossplot of a Brownian particle shift turns out to be invariant with regard to the so-called affine transformation, when the time and distance scales change in different proportions (see section 3.1).A curve of a Brownian particle shift retains its static properties at the affine conversion and, therefore, is called self-affine. This is a highly indented curve, and the nature of its irregularity is scale independent. At the scale increase we observe the same (in terms of statistics) frequency of movement direction changing. Fig. 1.9 shows a typical form of such a crossplot. The diagrams on Fig. 1.9, for example, may correspond to the integral results $F(t)$ of the coin tossing game: two players are tossing a coin and if the coin lands heads up then $F(t+1) = F(t)+1$, but if the coin lands tails up then $F(t+1) = F(t)-1$. It is evident that the mean of the F-function equals zero $\langle F\rangle = 0$, but its mean-squire fluctuations increase as $t^{1/2}$. Moreover, the F-function crosses the zero level (when players owe nothing to each over) more and more infrequently, i.e. the intervals between the neighbour crossings asymptotically increase as $t^{1/2}$. This fact is the basis for the folk saying: "*play but not gain back*"!

Finally, let us refer to the problem of a coastline measurement put forward for the first time by Richardson when analyzing the British coastline [27–29]. The method he used for the length

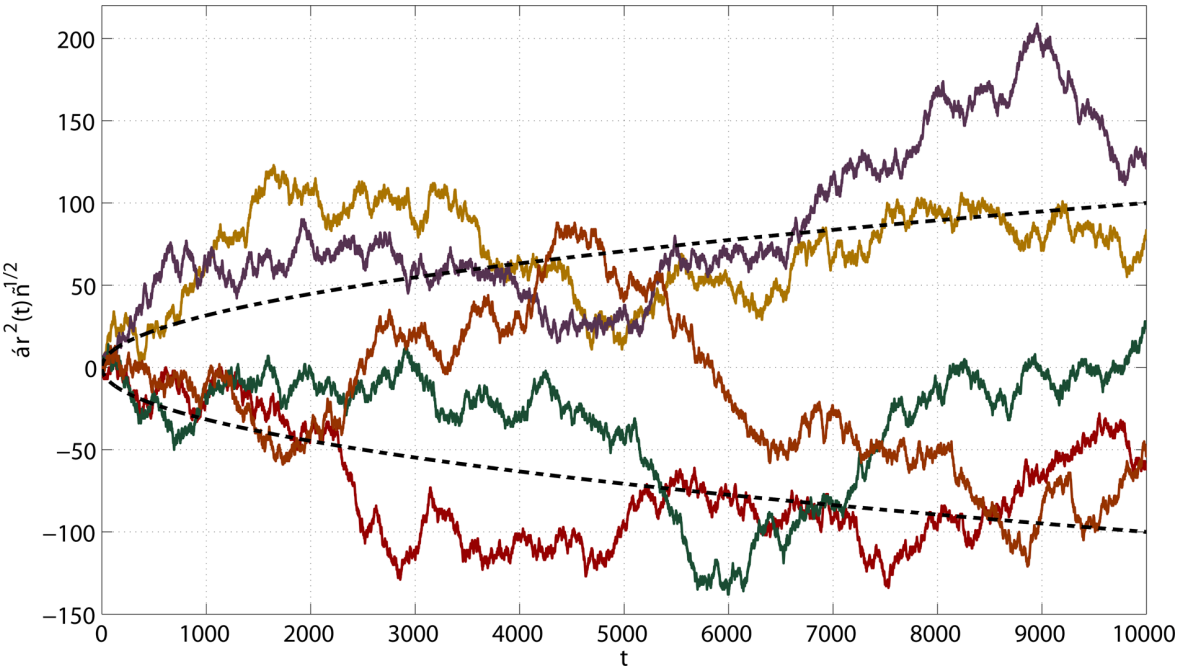

Figure 1.9: One-dimensional random walk $r(t)$. The dotted line shows the mean-square shift $\langle r^2(t)\rangle^{1/2}$ according to the Fick law (1.14) for $a = 1$

measurement can be described in the following way. Set the spread of a pair of compasses to a certain given length ε, which we will call a step length. Then pace with the compasses along the coastline to be measured, starting each new step from the point where the previous one ended. The number of steps multiplied by the selected length ε makes an approximate coastline length $L(\varepsilon)$. It would be logical to expect that at the reduction of the step length ε the coast length approaches quickly a value called a true length. But Richardson came across a totally different effect. At the reduction of the step length ε the coast length $L(\varepsilon)$. tends to increase without limit, becoming practically infinite. Such a behaviour of the coast line is explained by the fact that it is not a smooth curve but a fractal. Fig. 1.10 illustrates the idea of a coastline scale invariance. As the scale increases (i.e. at the reduction of ε) new details inevitably appear, new peninsulas and harbors containing smaller peninsulas and bays in their coast lines, etc.

Comparing the coast line images in different scales it is impossible at a glance to determine what scale corresponds to what image, since they look statistically similar. This means that a coast line is self-similar being a scale-invariant object or, in other words, an object that has no characteristic length. Star clusters, mountainous landscapes, river systems [30], surfaces of clouds [31], mosaic structure of magnetosphere plasma [7, 8] are the examples of stochastic fractal systems we have abundantly gifted by Nature.

Mathematically, the result obtained by Richardson can be described as follows:

$$L(\varepsilon) \sim \varepsilon^{1-D}. \tag{1.16}$$

So, a coast line is infinite and, therefore, has no practical value. What was wrong in the proce-

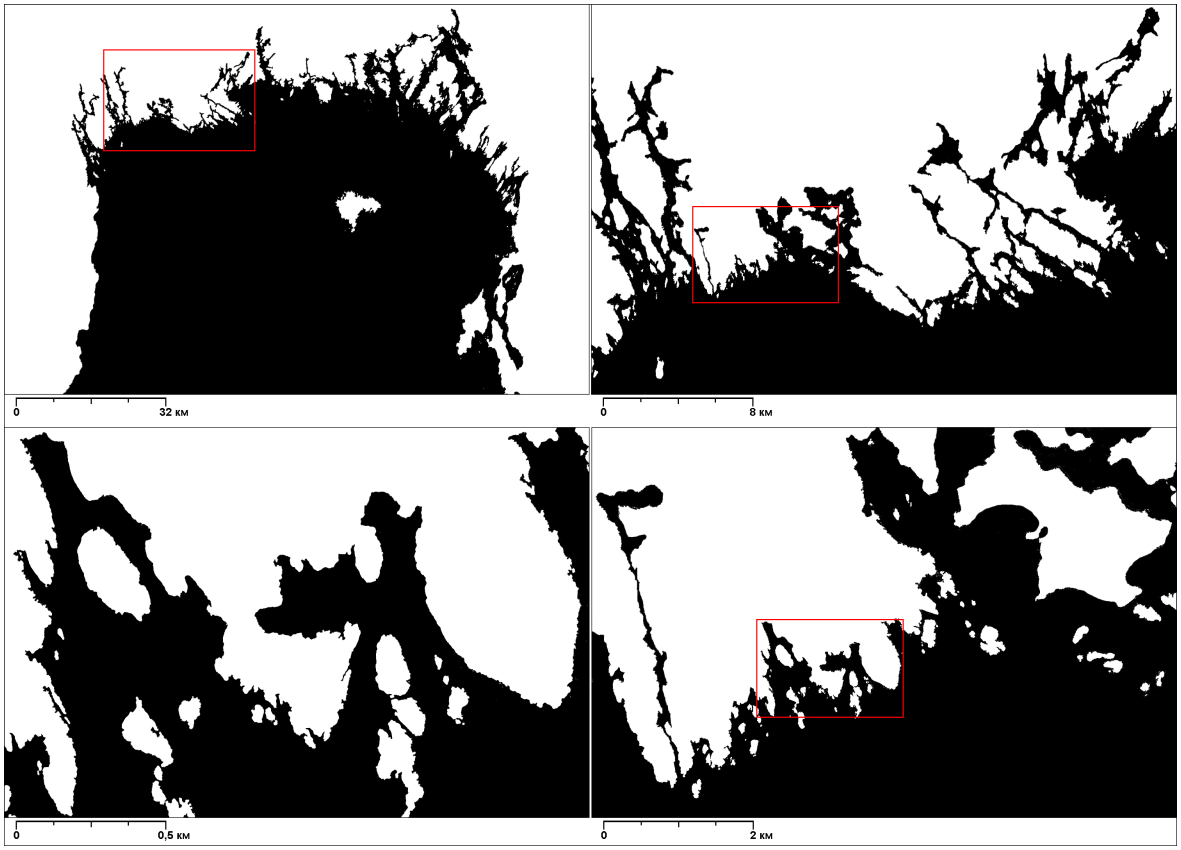

Figure 1.10: The Lake Ladoga coastline scaling. The water surface is in black. The pattern in the top left corner is subjected clockwise to a successive fourfold resolution increase

dure and how to obtain an adequate quantitative characteristic of a coast line? The fact is that the occurrence of the infinity was the result of selecting a wrong concept of measurement. For smooth geometrical sets the measure is defined by their topological dimension. Thus, a line is described by its length, a surface – by its area, a set in a three-dimensional space – by the volume. If a wrong measure is used to characterize a set, the result will have no meaning. For example, if we try to measure a surface length, we shall find that it is infinite, and the area of a line is equal to zero.

1.5 Methods of fractal dimension calculation

A general scheme of a set measure determination is the following. A space where a set is located is divided into boxes of a certain size ε. For example, a plane can be covered by a grid with a box side length ε. Then the number of such boxes $N(\varepsilon)$ containing pixels of the analyzed set is counted. The procedure is repeated for different ε and the measure is calculated as a limit:

$$\Pi = \lim_{\varepsilon \to 0} N(\varepsilon)\varepsilon^D. \tag{1.17}$$

In this expression D corresponds to the object dimension. If D is chosen incorrectly, either 0 or the infinity will be obtained. This is what happens during the coast line length calculation. When we consider it as a smooth line with $D = 1$, the calculated length is $L = \infty$. Increasing the number of dimensions by one and considering it a surface with $D = 2$, we get an area $S = 0$. The only way to get a sensible measure is to consider a coast line as an object with a fractional dimension between 1 and 2. A non-zero limit of measure (1.17) exists only with one certain value of dimension D. Only this feature may be used for the calculation of the fractal object dimension:

$$d_f = -\lim_{\varepsilon \to 0} \frac{\ln N(\varepsilon)}{\ln \varepsilon}. \tag{1.18}$$

Mathematicians call the dimension obtained by covering the set with boxes of fixed form and size the set capacity or Kolmogorov dimension. Mathematically, the conception of the Hausdorff dimension [32] is stricter, and just this dimension was used in the first fractal definition by Mandelbrot.

A key moment of the Hausdorff dimension calculation is that unit areas of arbitrary form and size may be applied to cover the set. Assume that a set $\mathfrak{F}$ is a subset of a n-dimensional space. Let us consider its coverage with the elements of arbitrary form and size. The only restriction is that the diameter of a set enclosed in any element of the coverage does not exceed a given value δ. The diameter of the i-element E_i is defined as the largest distance between two points thereof:

$$\varepsilon_i = \mathrm{diam} E_i = \sup_{x,y \in E_i} \|x - y\|. \tag{1.19}$$

Let us introduce the sum of all the coverage elements, which depends on the d and δ parameters:

$$\Gamma_d(\delta) = \sum \varepsilon_i^d \tag{1.20}$$

and define the smallest sum for all the elements:

$$\gamma_d(\delta) = \inf(\Gamma_d(\delta)). \tag{1.21}$$

If d is large, then:

$$\gamma_d(\delta) \xrightarrow{\delta \to 0} 0. \tag{1.22}$$

If d is small, then:

$$\gamma_d(\delta) \xrightarrow{\delta \to 0} \infty. \tag{1.23}$$

The intermediate critical value d_H is the Hausdorff dimension of the set $\mathfrak{F}$, and is such that at the decrease of δ the value γ_d tends to zero for $d > d_H$ and to the infinity for $d < d_H$.

There are some other definitions of the dimension, e.g. similarity dimension, Minkowski dimension [25, 27]. The reason of such a wide variety of dimensions is that there exist some special sets, for which different dimensions have different values. However, in practice we meet more frequently objects, for which all these dimensions are equal. That is why terminologically they are not differentiated being called a fractal dimension of an object denoted by d_f.

Let us come back again to the coast line example. According to Richardson's calculations, the exponent in equation (1.16) for the west coast of Great Britain is equal to -0.22, and the fractal dimension is $d_f = 1.22$ respectively. This result shows that the coast line is something in between an ordinary smooth curve and a surface. It is too twisting to be considered an ordinary line, but not enough for a surface. In this case the fractal dimension characterises the extent of a coast line convolution. There are curves such as the Peano curve or the Brownian particle trajectory on a plane which have the fractal dimension $d_f = 2$, i.e. they are so flexuous that fill up the plane.

It is the easiest way to calculate dimensions of constructive fractals. Due to their deterministic construction the fractal dimension can be calculated precisely. Let at a certain stage of construction a structural fractal consist of $N(\varepsilon)$ elements of size ε, and at another stage $N(\acute{\varepsilon})$ elements of size $\acute{\varepsilon}$. Then the fractal dimension can be calculated according to the formula:

$$d_f = -\frac{\ln\left(\dfrac{N(\varepsilon)}{N(\acute{\varepsilon})}\right)}{\ln\left(\dfrac{\varepsilon}{\acute{\varepsilon}}\right)}. \tag{1.24}$$

As an example, let us calculate dimensions of the Koch curve and the Sierpiński gasket. At each stage of the Koch curve construction a line segment of a fixed length is replaced by four segments of a three-times-smaller length. Therefore:

$$d_f = -\frac{\ln\left(\dfrac{1}{4}\right)}{\ln\left(\dfrac{\varepsilon}{\varepsilon/3}\right)} = \frac{\ln 4}{\ln 3} = 1.2816. \tag{1.25}$$

The Sierpiński gasket construction implies that each fixed-size triangle is replaced by three triangles half of its size. So:

$$d_f = -\frac{\ln\left(\dfrac{1}{3}\right)}{\ln\left(\dfrac{\varepsilon}{\varepsilon/2}\right)} = \frac{\ln 3}{\ln 2} = 1.5849. \tag{1.26}$$

At each stage of the Menger sponge construction a fixed-size cube is replaced by two tens of cubes of a three-times-smaller size. Therefore, for the Menger sponge we find: $d_f = \dfrac{\ln 20}{\ln 3} = 2.7268$.

It becomes much more complicated when we deal with the random fractals, the dimension of which has to be defined separately for every specific realization. This leads inevitably to an error due to the stochastic nature of such fractals, and more often the statistic properties of such an estimation are unknown [33]. Many methods have been developed for the fractal dimension assessment, though yet there is no clear classification of them. For example, Vstovsky et al. [34] specify direct and indirect geometrical methods, as well as physical ones. However, more commonly, the methods are grouped according to the type of data they are applied to.

The following are the algorithms of dimension calculation methods, which are frequently used for some types of data [35].

I. Box-counting method

This method is one of the simplest. It is most often applied to calculate the dimension of a set on a plane by its image, though it can be easily generalized to a space of any dimension.

1. The image is covered by a grid with a box of side length ε.

2. The number of boxes $N(\varepsilon)$ required to cover the set is counted.

3. Steps 1 and 2 are repeated, increasing the box size ε from minimum to maximum (usually the increasing follows the geometric series such as 2, 4, 8, 16).

4. An $N(\varepsilon)$ diagram is plotted in the log-log coordinates.

5. A slope of the diagram is estimated by a least-squares method, which is equal to the reversed sign fractal dimension.

II. Gliding box method

This method is a modification of the previous one. It is applied when each box of a grid is either occupied or empty (it is easy to modify any image this way).

1. A reference box of size ε is selected.

2. The box is placed in all possible positions on a grid and the number of boxes which contain at least one pixel of the object $N(\varepsilon)$ is counted.

Steps 3-5 are similar to those used in the previous method.

III. Divider method

In fact this is the method that was used by Richardson. It is applied to estimate a line

dimension by its image.

1. The spread ε of a pair of imaginary compasses is selected.

2. The line is measured by the compasses, and the number of the required steps $N(\varepsilon)$ is counted.

Steps 3-5 are similar to those used in the box-counting method.

IV. Perimeter-area ratio method

The method is applied to calculate the fractal dimension of coastlines of the islands in an archipelago on a map.

1. The perimeter P and the area A are defined for each island.

2. A $P(A)$ diagram is plotted in the log-log coordinates.

3. A slope of the diagram is estimated by a least-squares method. The fractal dimension is equal to the doubled slope value.

V. Semivariogram method

The method can be applied when there is a set of points characterized by a certain value. This may be a time series or measurements on a plane.

1. A distance between each pair of points (usually Euclidean) is measured.

2. The difference of the studied value for each pair of points is computed and squared.

3. A diagram of dependence of the squared differences on the distance between the points is plotted in the log-log coordinates.

4. The fractal dimension is calculated as $d_f = n - m/n$, where m is the diagram slope, n is the space dimension.

To conclude the review of the fractal dimension calculation methods, it should be noted that all of them are based on a power law. This kind of dependency is typical to fractals, and it expresses their self-similarity mathematically. Though for real natural fractals this property is valid only within a finite range of scales. Out of this range the self-similarity and the fractal properties disappear. Therefore, for this type of fractals the limit transition which is used in Hausdorff and Kolmogorov definitions of dimension is meaningless. Their fractal dimension is to be determined on the power-behaved sections of the diagram, i.e. in all algorithms given above the diagram slop in the log-log coordinates is to be measured only on a linear section.

1.6 Chemical fractal dimension

Structures of identical fractal dimension may nevertheless differ greatly from one another. There-fore, very often the fractal dimension value can not characterize the fractal structure completely. Let us consider a fractal structure which is the result of iteration procedure showed in Fig. 1.11.

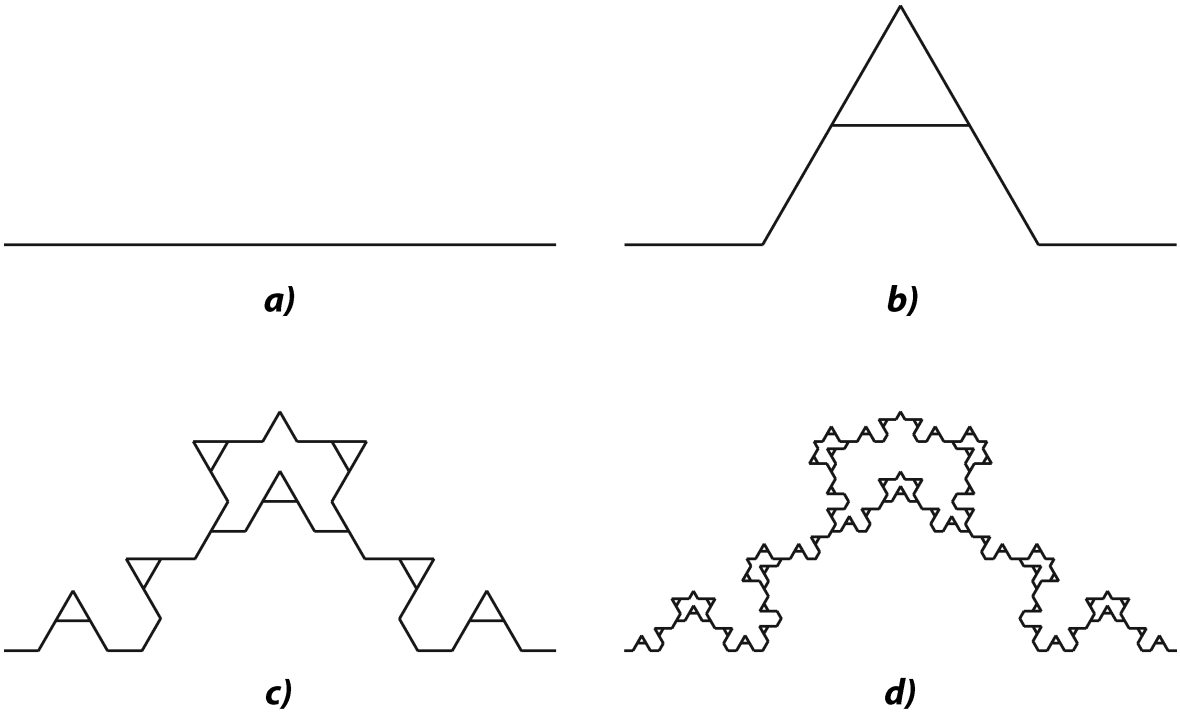

Figure 1.11: Unit length segment (a) is divided into four equal parts, the extreme parts keep their position but the central ones are changed by an A-shaped generator of five segments (b). Then the procedure is repeated for each of 7 segments of $1/4$ length (c), and then for each of 49 segments of $1/16$ length (d)

Calculated by a box dimension method the dimension of the presented structure is equal to $d_f = \dfrac{\ln 7}{\ln 4}$. To obtain new significant information about the fractal nature let us consider the shortest path between the two extreme points of the fractal structure. It is evident that the cluster elements belonging to this path form a self-similar structure with the fractal dimension equal to $d_{\min} = \dfrac{\ln 5}{\ln 4}$. Such a dimension is called the shortest path dimension or minimal fractal dimension. Therefore, the length l of this shortest path which is often referred to as the chemical distance [28, 29] changes with the increase of the Eucledian distance between the selected elements of the cluster according to the following law:

$$l \sim r^{d_{\min}}. \tag{1.27}$$

The inverse relation

$$r \sim l^{1/d_{\min}} \equiv l^{\tilde{\nu}} \tag{1.28}$$

shows how r changes with the increase of l.

The so-called chemical dimension d_l is closely connected with the d_f and $d_{\min}$ dimensions, which describes the change of the number of elements belonging to the cluster M due to the increase of the distance l which does not exceed the chemical distance from a certain fixed element:

$$M(l) \sim l^{d_l}. \tag{1.29}$$

While the fractal dimension d_f characterizes the growth of the cluster's mass due to the increase of its size in the Eucledian space, the chemical dimension d_l describes the growth of the cluster's mass in the space of chemical distances. Combining eqs.(1.2), (1.27) and (1.29) we find the relationship

$$d_l = \frac{d_f}{d_{\min}}. \tag{1.30}$$

For example, the chemical dimension of the Koch curve is equal to one $d_l = 1$ as its minimal and fractal dimensions coincide $d_{\min} = d_f$. On the contrary, for the Sierpiński carpet, its minimal dimension is equal to one $d_{\min} = 1$, and its chemical dimension coincides with the fractal dimension $d_l = d_f$.

The application of the minimal and chemical dimensions in the percolation theory is discussed in section 2.3.

1.7 Multifractals and multifractal formalism

Multifractals are heterogeneous fractal objects which, unlike the regular ones, cannot be described solely by a single exponent, i.e. the fractal dimension d_f. Instead, a whole spectrum of such dimensions is needed, the number of which, generally speaking, is infinite [22, 27]. The reason is that in addition to the geometric characteristics described by the dimension d_f such fractals have an important property related to the distribution of a certain measured value over its geometric basis. Practically everything may stand for such a measured value: population density, substance concentration, intensity of magnetization, energy. What is important that the measured value is distributed over a multifractal irregularly but self-similarly [22, 27–29, 34].

Let us explain what a heterogeneous fractal is on the example of the Sierpiński gasket generated by means of a modified chaos game (see Section 1.3). Let us change its rules in the following way: we give our preference to a certain vertex (for example, vertex A), and we will be choosing it with a 90% probability, while two other vertices will be chosed equally with 5% probability each. This "asymmetric game" results in extremely uneven distribution of the points within the triangle. The major part of the points is located at the vertex A and its preimages, and very few points are at the B and C vertices (and their preimages). Nevertheless, this set of the points is a fractal, since it possesses the property of self-similarity. Though the number of points within the triangle DFC is 20 times smaller than within the big triangle ABC, they are similar as the points concentrate at the analogue vertices D and A. Fig. 1.12 illustrates this procedure.

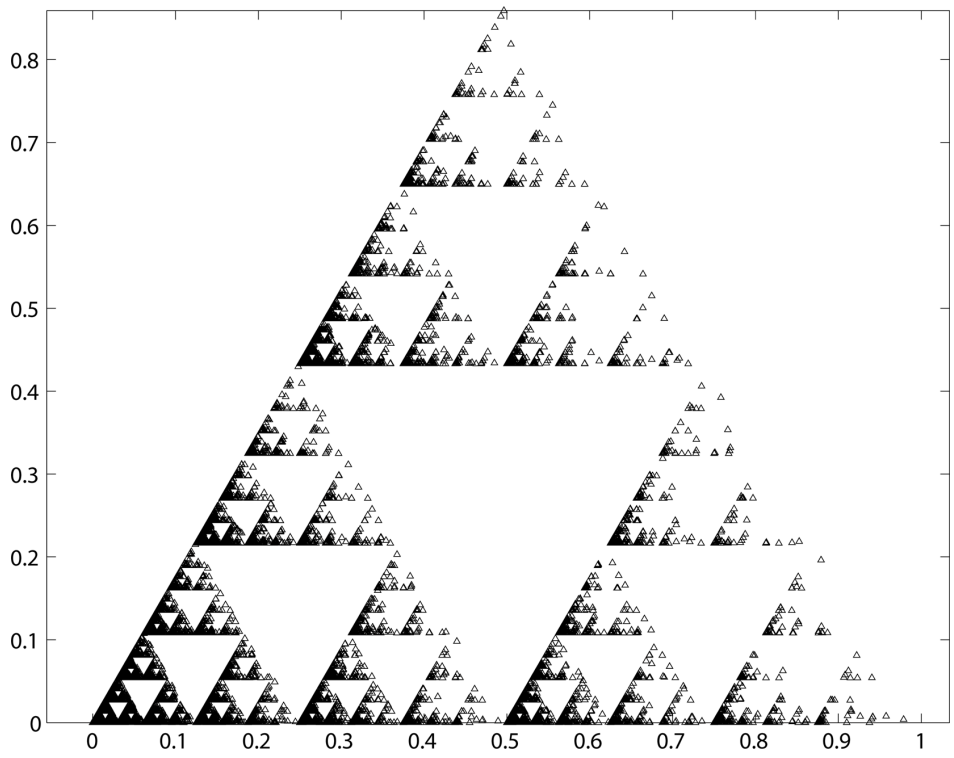

Figure 1.12: The multifractal Sierpiński gasket

Speaking about the heterogeneity of this type of the Sierpiński gasket, we mean the different concentration of points in its various parts. In this case the points' concentration is the measure of their distribution over the geometrical bearer we discussed above. And the geometrical bearer is identical to the ordinary Sierpiński gasket. Indeed, if the number of points tends to infinity, then all possible positions (scaling down triangles) will be occupied and the fractal dimension will not alter being equal to $\ln 3 / \ln 2$.

Thus, the standard fractal approach does not distinguish homogeneous and heterogeneous objects. The heterogeneous fractals have some new features as compared with the homogeneous ones, and the fractal dimension d_f does not describe them totally. It makes necessary to find new quantitative parameters. In order to solve this task the specific mathematic tool has been developed and became widely known as multifractal formalism [36–38].

Mandelbrot introduced the basic concept of the multifractal geometry [15]. We are going to expound the ABC of the multifractal formalism using the binominal multiplicative process as an example [27]. The generator of the multiplicative process is a pair of numbers p and $1-p$, where $0 < p < 1$. The binominal multiplicative process starts on a unit segment, along which a mass or population is distributed with a unit density. The initial segment is divided into halves that redistribute its mass in the following way: the density p is assigned to the left half and $1-p$ to the right one. Then the mass redistributing procedure is applied to each of the halves. This makes four segments of $\varepsilon = 2^{-2} = 1/4$ length with respective densities $\{p^2;\ p(1-p);\ (1-p)p;\ (1-p)^2\}$. At the next step the number of segments is doubled again followed by the corresponding mass redistribution. Fig. 1.13 shows the density distribution on the segments of $\varepsilon = 2^{-12}$ length after the 12th iteration of the multiplicative process with $p = 0.25;\ p = 0.4$ and $p = 0.5$. Fig. 1.14 demonstrates the relation of integral mass as the function of the position on a unit segment after 12 iterations of binominal multiplicative processes with different p values.

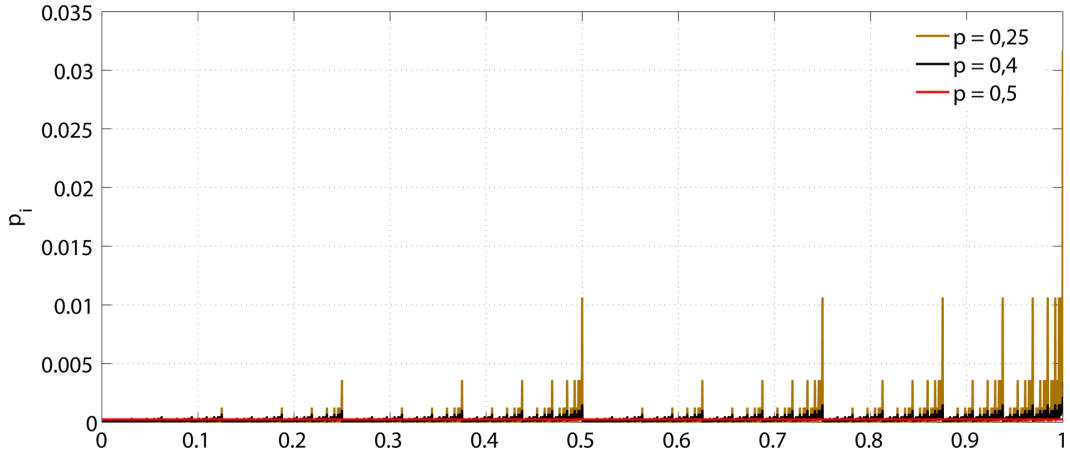

Figure 1.13: Results of 12 iterations of binominal multiplicative process for different p values

In a general case, a fractal object occupying a certain bounded space $\mathfrak{F}$ of size L in the Euclidean space of d-dimension is considered. In our case $d = 1$ and $L = 1$. Let at a certain stage of construction it represent a set of points $G \gg 1$ some way distributed in this bounded space. Let us assume that finally $G \to \infty$. We will decompose the entire space $\mathfrak{F}$ into cubic cells (d-cubes) of ε-side and ε^d-volume, and we will be interested only in the occupied cells containing even just one point.

Let the number of the occupied cells i vary within the range $i = 1, 2, \ldots N(\varepsilon)$, where $N(\varepsilon)$ is the total amount of the occupied cells, which depends on the size of the cell ε. In our example of the multiplicative process $N(\varepsilon) = \varepsilon^{-1}$.

Let $n_i(\varepsilon)$ be the quantity of points in the cell with number i, then the value

$$p_i(\varepsilon) = \lim_{G\to\infty} \frac{n_i(\varepsilon)}{G} \tag{1.31}$$

is the probability that any point randomly chosen from our set is located in the i-cell. In other

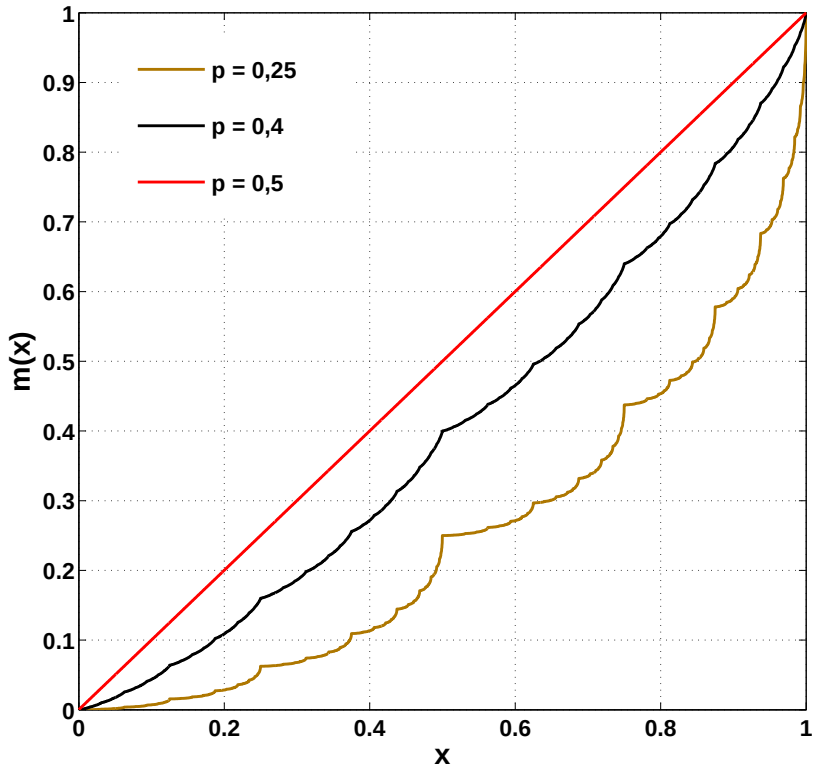

Figure 1.14: Integral mass relation as the function of the position on a unit segment after 12 iterations of the binominal multiplicative process for different p values

words, the probability p_i characterizes the density or occupancy of cells. From the definition of p_i the normalization condition is derived

$$\sum_{i=1}^{N(\varepsilon)} p_i(\varepsilon) = 1. \tag{1.32}$$

Let us introduce now a moment of points distribution in the cells characterized by the exponent q which may be of any value within the interval $-\infty < q < +\infty$:

$$M_q = \sum_{i=1}^{N(\varepsilon)} p_i^q(\varepsilon). \tag{1.33}$$

It is obvious that $M_1 = 1$ and $M_0 = N(\varepsilon)$. Fig. 1.15 demonstrates behaviour of $M_q(\varepsilon)$ moments in the multiplicative process with the change of ε in a log/log scale.

Fig. 1.15 shows that $\ln(M_q)$ changes linearly with the growth of $\ln(\varepsilon^{-1})$ for different p and q values. In other words, the $M_q(\varepsilon)$ moments are power functions of the ε-size cells:

$$M_q = \varepsilon^{-\tau(q)}, \tag{1.34}$$

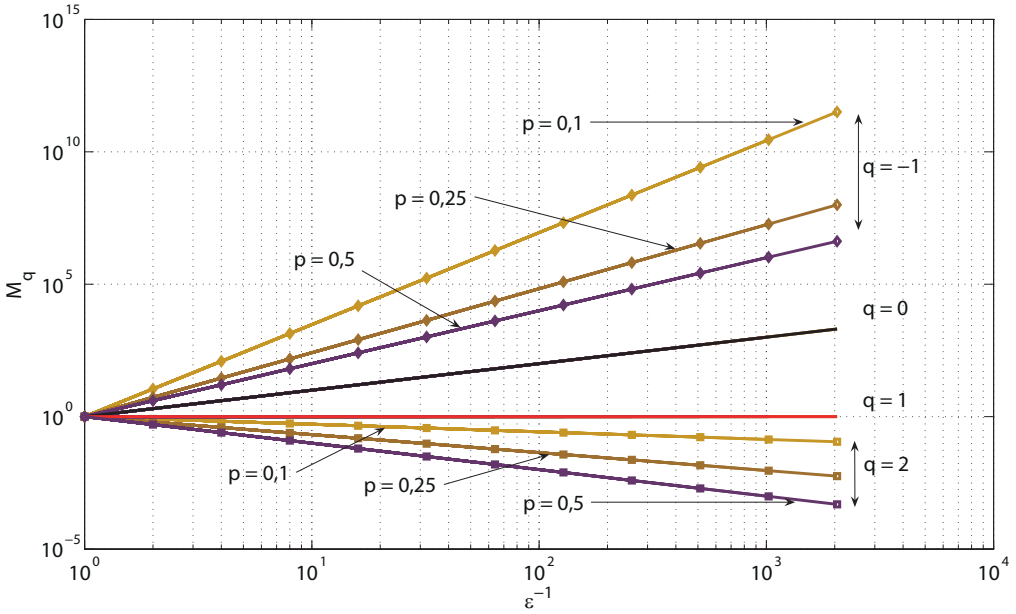

Figure 1.15: Behaviour of $M_q(\varepsilon)$ moments with the change of ε

where the $\tau(q)$ function is

$$\tau(q) = -\lim_{\varepsilon \to 0} \frac{\ln M_q}{\ln \varepsilon}. \tag{1.35}$$

Fig. 1.16 shows the relation $\tau(q)$ for the binominal multiplicative processes for different p values. It is clear that the function $\tau(q)$ is linear for $p = 0.5$, and for $p/(1-p) \neq 1$ it deviates from the linearity as much as $p/(1-p)$ differs from one.

In the multifractal theory a system of generalized dimensions is used to estimate the extent of deviation of the $\tau(q)$ function from the linearity.

The generalized dimension D_q (the generalized dimension of Rényi) of a distribution is the decreasing function q, defined as:

$$D_q = \lim_{\varepsilon \to 0} \left\{ \frac{1}{1-q} \frac{\ln M_q(N)}{\ln \varepsilon} \right\} = \frac{\tau(q)}{1-q}. \tag{1.36}$$

For a standard homogeneous fractal, the function $\tau(q)$ is linear, and all Rényi dimensions are equal $D_q = D_0 = d_f$ and do not depend on q. It has only one dimension, and, therefore, such objects are often called monofractals as opposed to the multifractals, the description of which requires the whole spectrum of the Rényi dimensions. In a general case, a multifractal is characterised by the non-linear function $\tau(q)$ that controls behaviour of the moment M_q at $\varepsilon \to 0$.

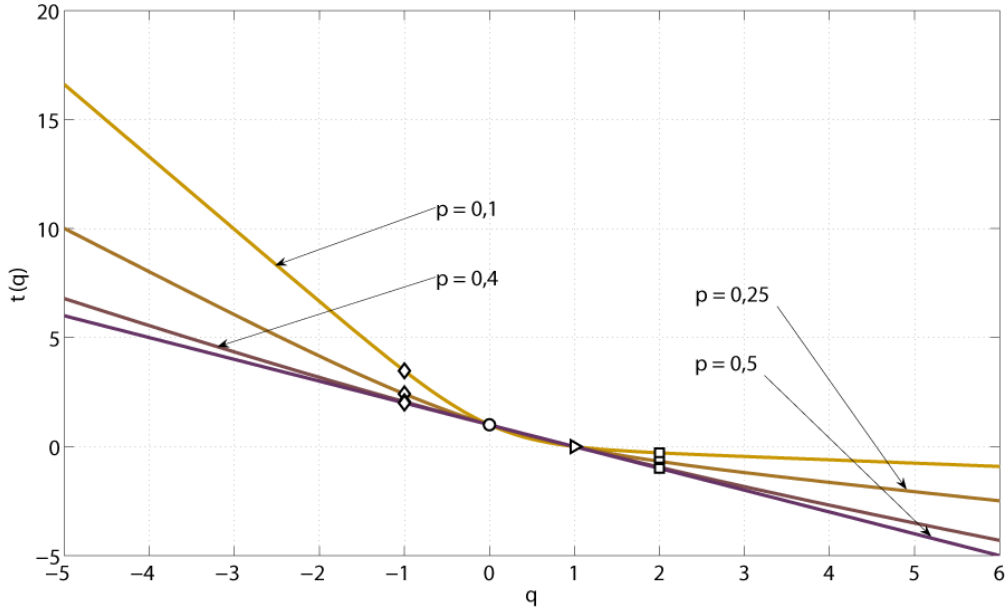

Figure 1.16: Relation $\tau(q)$ for the binominal multiplicative process for different p values

Fig. 1.17 shows the relation $D_q(q)$ for different p values in the binominal multiplicative process.

The generalized Rényi dimensions D_q always decrease monotonically with the growth of q, so

$$D_q \geq D_{\acute{q}} \quad \text{at} \quad q > \acute{q}. \tag{1.37}$$

The given equality is valid for a homogeneous fractal. The dimension D_q reaches its maximum value $D_{max} = D_{-\infty}$ at $q \to -\infty$ and its minimum value $D_{min} = D_{\infty}$ at $q \to \infty$.

Now let us find out the physical meaning of the generalized fractal dimensions D_q for some specific q values. If $q = 0$ then equation (1.33) results in

$$M_0(\varepsilon) = N(\varepsilon). \tag{1.38}$$

At the same time equations (1.34) and (1.36) lead to

$$M_0(\varepsilon) \approx \varepsilon^{-\tau(0)} = \varepsilon^{D_0}. \tag{1.39}$$

Comparing these two equalities we can conclude that D_0 is a simple fractal dimension of a multifractal set. It is a rough characteristic of a structure and does not contain information on its statistical properties.

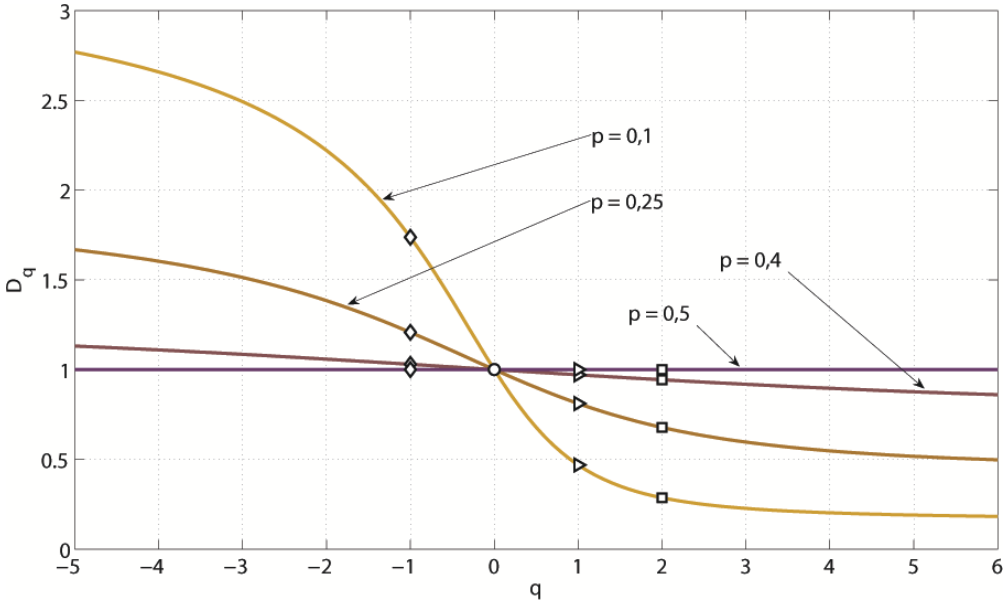

Figure 1.17: Relation $D_q(q)$ for the binominal multiplicative process for different p values

Let us find out now the sense of the D_1 value. If at $q = 1$ according to the probability normalization condition (1.32) the first moment is equal to

$$M_1 = 1, \tag{1.40}$$

then $\tau(1) = 0$. Thus, in equation (1.36) for D_1 there is an uncertainty. Let us describe this uncertainty by means of the limit transition operation. Assuming $q = 1 + \varepsilon$ where $|\varepsilon| \ll 1$ we use the evident expression

$$p_i^q = p_i p_i^{q-1} = p_i \exp[(q-1)\ln p_i].$$

Since the argument of the exponent is small we use a well-known asymptotic form

$$\exp(x) \approx 1 + x,$$

for $|x| \ll 1$, then

$$p_i \exp[(q-1)\ln p_i] \approx p_i[1 + (q-1)\ln p_i],$$

and

$$p_i^q \approx p_i[1+(q-1)\ln p_i].$$

Substituting the last expression into equation (1.36) we get:

$$\lim_{q\to 1} M_q = \sum_{i=1}^{N(\varepsilon)} p_i + (q-1)\sum_{i=1}^{N(\varepsilon)} p_i \ln p_i.$$

According to normalization condition (1.32) the first sum in the last equation is equal to one and

$$\lim_{q\to 1} M_q = 1 + (q-1)\sum_{i=1}^{N(\varepsilon)} p_i \ln p_i.$$

Taking into account that $\ln(1+x) \approx x$ for $|x| \ll 1$ we get:

$$\lim_{q\to 1} \ln M_q = \lim_{q\to 1} \ln\left\{1 + (q-1)\sum_{i=1}^{N(\varepsilon)} p_i \ln p_i\right\} = (q-1)\sum_{i=1}^{N(\varepsilon)} p_i \ln p_i.$$

Thus, finally we have:

$$D_1 = \frac{-\sum_{i=1}^{N(\varepsilon)} p_i \ln p_i}{\ln \varepsilon} = \frac{H}{\ln \varepsilon}, \tag{1.41}$$

where the numerator is an entropy of a fractal set or the Shannon information index with an accuracy of a decimal place:

$$H = -\sum_{i=1}^{N(\varepsilon)} p_i \ln p_i.$$

This definition of the set entropy is totally identical to the one used in thermodynamics, where p_i is understood as a probability to find the system in a quantum state i. Just to remind, in the thermodynamics the entropy is a measure of disorder in the system. A simple example, when molecules of gas placed into a half of a vessel fill its entire volume after the removal of the partition, demonstrates that in this process the disorder and, hence, entropy increases. This increase of disorder relates to the decrease of our knowledge about the state of the system, because before the partition removal we knew more about the position of molecules. Inspired by this idea, Claude Shannon generalized the thermodynamic entropy concept adopting it to

the abstract tasks of information transfer and processing. In these tasks the entropy became the quantitative measure of the information necessary to define a certain state of a system. In other words, the entropy is the measure of our ignorance concerning the system. This holds totally true for the distribution of the multifractal set elements in the ε-cells. Indeed, the D_1 value characterizes information necessary to define if an element of a multifractal set is in one or another ε-cell. That is why the generalized fractal dimension D_1 is often called an information dimension. It shows how the information necessary to locate the elements increases with the decrease of ε.

Let us consider another particular case, when $q = 2$, in order to explain the physical meaning of the generalized fractal dimension D_2. The following expression holds for it:

$$D_2 = \lim_{\varepsilon \to 0} \frac{\ln \sum_{i=1}^{N(\varepsilon)} p_i^2}{\ln \varepsilon}. \tag{1.42}$$

Let us find a pair correlation function

$$C(G) = \frac{2}{G(G-1)} \sum_{n,m} \delta_{i(n)j(m)}, \tag{1.43}$$

where the summation is performed over all pairs (n,m) of G elements; $i(n)$, and $j(m)$ are the numbers of the cubes of ε-scale (in our case the segments of ε-length) containing the chosen points; $\delta_{i(n)j(m)}$ is the Kronecker delta, i.e. $\delta_{i(n)j(m)} = 1$, if $i = j$ and $\delta_{i(n)j(m)} = 0$, if $i(n) \neq j(m)$. The sum in equation (1.43) defines the number of point pairs (m,n) in a ε-cube. Therefore, the sum of eq. (1.43) divided by $G(G-1)/2$, i.e. the total number of pairs, defines the probability that two randomly chosen points belong to the same ε-cube. It is evident that a non-zero contribution to the sum (1.43) can only be made by the pairs of points belonging to the same ε-cube, i.e.:

$$\frac{2}{G(G-1)} \sum_{n,m} \delta_{i(n)j(m)} = \frac{2}{G(G-1)} \sum_{i=1}^{N(\varepsilon)} Gp_i(Gp_i - 1)/2, \tag{1.44}$$

where Gp_i is the number of points in the i-th ε-cube. In the asymptotic form of large G when 1 is negligible as compared to G we get as follows

$$C(G) \simeq \sum_{i=1}^{N(G)} \frac{(Gp_i)^2}{G^2} = \sum_{i=1}^{N(G)} p_i^2. \tag{1.45}$$

And thus,

$$C(G) \simeq G^{-D_2}. \tag{1.46}$$

So, we come to conclusion that the generalized dimension D_2 defines the dependence of the correlation function $C(G)$ on G in the limit $G \to \infty$. That is why in the literature the D_2 value is called a correlation dimension [39].

Strictly speaking, the Rényi generalized dimensions D_q are not the fractal dimensions in the common sense of this term. Therefore, in addition a so called function of multifractal spectrum $f(\alpha)$ (spectrum of multifractal singularities) is often used to characterize a multifractal set. And this function fits better the term fractal dimension.

The function of multifractal spectrum $f(\alpha)$ represents the structure of a multifractal, which totally complies with the concept of the Rényi generalized dimensions D_q and the function $\tau(q)$. A multifractal spectrum can be created with the help of the Legendre transformation of the function $\tau(q)$ by applying new variables α and $f(\alpha)$ instead of q and $\tau(q)$:

$$\begin{cases} \alpha(q) &= \dfrac{d}{dq}\tau(q) \\ f(\alpha(q)) &= q\alpha(q) + \tau(q). \end{cases} \tag{1.47}$$

The variable α (the singularity index) and non-negative function $f(\alpha)$ (the singularity spectrum) give an idea about the multifractal structure of the community, which is totally equivalent to the expression with q and $\tau(q)$. Fig. 1.18 presents the multifractal spectrum of binominal multiplicative processes for different p-values.

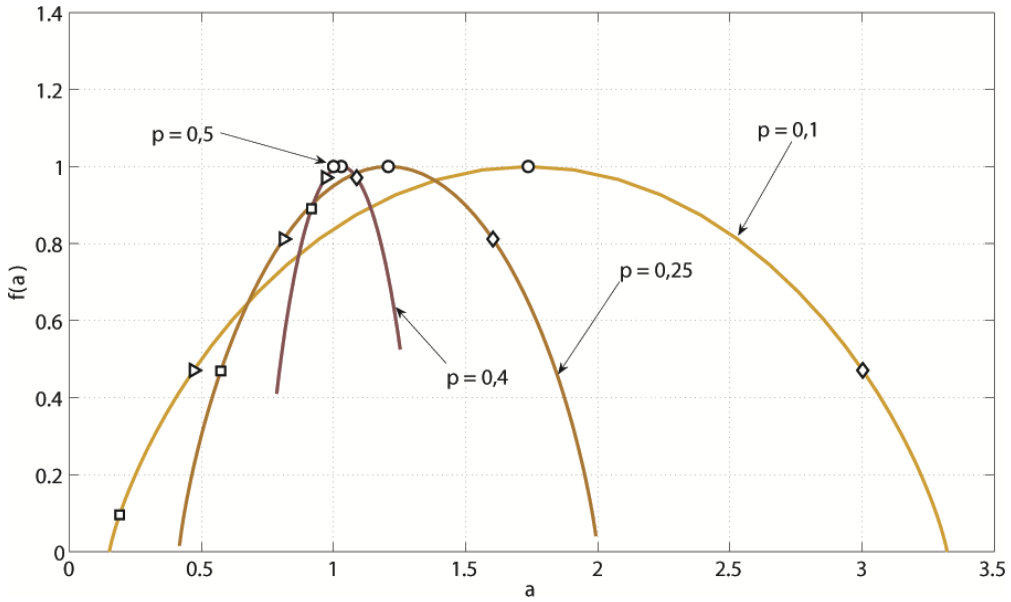

Figure 1.18: Multifractal spectra of the binominal multiplicative process for different p-values

Let us return to the p_i-probabilities which show the relative occupancy of the ε-size cells covering the set. The smaller is the size of the cell, the smaller is the value of its occupancy. For self-similar sets the dependence of p_i on the size of ε-cells has a power law nature:

$$p_i \simeq \varepsilon^{\alpha_i}, \tag{1.48}$$

where α_i is a certain exponent, which is called the singularity index or the Lipschitz-Hölder coefficient. And here we come to an issue of the probability distribution of various α_i-values. Let $n(\alpha)d\alpha$ be a probability that α_i lies in the interval between α and $\alpha + d\alpha$. In other words, $n(\alpha)d\alpha$ is the relative number of i-cells having the same measure p_i with α_i lying in this interval. In the case of a monofractal, when all α_i are the same (and equal to the dimension d_f), this value is proportional to the total number of cells N, which depends on the size of a ε-cell in a power way: $N(\varepsilon) \simeq \varepsilon^{-d_f}$. The exponent in this relation is defined by the fractal dimension of the set d_f.

Fig. 1.19 illustrates the dependence $\alpha(q)$ by the example of the binominal multiplicative process for different p-values. It is interesting to compare the given relationships with a behaviour of the generalized dimensions D_q as functions of the moment q order (see Fig. 1.17).

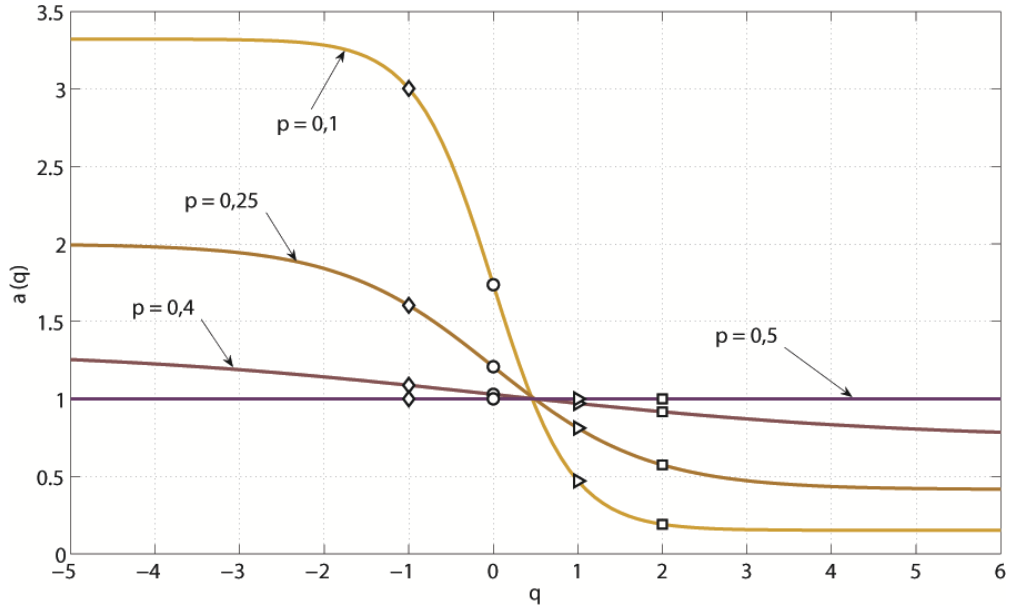

Figure 1.19: Dependence $\alpha(q)$ by the example of the binominal multiplicative process for different p-values

For a multifractal, different α_i-values appear with a probability characterized by different (depending on α) values of the exponent $f(\alpha)$, but not the same d_f-values.

Thus, the physical meaning of the function $f(\alpha)$ is that it is the Hausdorff dimension of a certain homogeneous fractal subset of the initial set $\mathfrak{F}$ characterized by the same probability p_i of cell occupation. Various values of the function $f(\alpha)$ represent a spectrum of fractal dimensions of the homogeneous subsets, which the initial set $\mathfrak{F}$ can be divided into. This

explains the term multifractal. It can be understood as a certain assembly of various homogeneous fractal subsets of the initial set, each having its own value of fractal dimension.

1.8 Fractal geometry and physics

Now we know how to describe a fractal structure and how to define its dimension. But we know nothing about the fractal generation. Why does Nature solve its problems by using the fractal structures so often? Many scientists torment themselves today over the answer to this question. But to the moment, it is early even to speak about the light at the end of the tunnel. We may just offer to enter the tunnel [40].

Behaviour of the dissipative distributed systems is realized in a broad spectrum of dynamic conditions: de-pending on the type of attractor existing in the infinite-dimensional phase space of a system, it may demonstrate both different regular types of movements as well as spatio-temporal chaos. Investigations of chaotic conditions are often reduced to the search for finite-dimensional dynamic analogues of the initial distributed system. The minimum number of independent variables, which uniquely determine a steady motion of a dissipative distributed system is called a minimal underlying dimensionality that can be estimated either by the procedure based on the Tokens theorem [41] or by the more accurate method of P. Grassberger and I. Procaccia [38, 42, 43]. The latter allows to estimate the so-called correlation dimension of a strange attractor [37].

However, the estimation of underlying dimensionality of the system attractor is seriously complicated with the increase of the number of measurements and becomes totally impossible even theoretically in the case of infinite-dimensional attractors and non-stationary processes. The alternative approach to study the non-linear dynamics of the distributed systems may be related to the self-similarity of the system state structure in its configuration space or extended configuration space. Let us consider a simple example. Assume that we have a single-dimensional chain of interacting bi-stable elements. The nature of interaction comes from the rule of the elements transition from one state to the other. The state of an element reverses if a moment before the states of its nearest neighbours (one from the left and one from the right) became opposite, otherwise the state of the element does not change. Initially, all the elements are in the same state, and the system is stable. Let at some moment just one element of the chain be forced into the reverse state. Then a sequence of changes will pass through the chain. Fig. 1.20 shows the system evolution in the extended configuration space, when each horizontal line corresponds to the chain configuration at a certain time. The resulting state structure appears to be a fractal, since the increasing time t leads to the increase of the total switches in the system as t^{d_f}, where the fractal dimension $d_f = ln4/ln3$ corresponds to the dimension of the well-known Sierpiński gasket [28].

Note, that the temporal behaviour of each element in the linear chain appears fractal: the number of switches changes in an asymptotic way as t^{d_f-1}. The behaviour of the system appears to be complex, since there is not a single characteristic spatial or temporal scale (except for the size and time of the element switching) controlling the evolution of the sys-

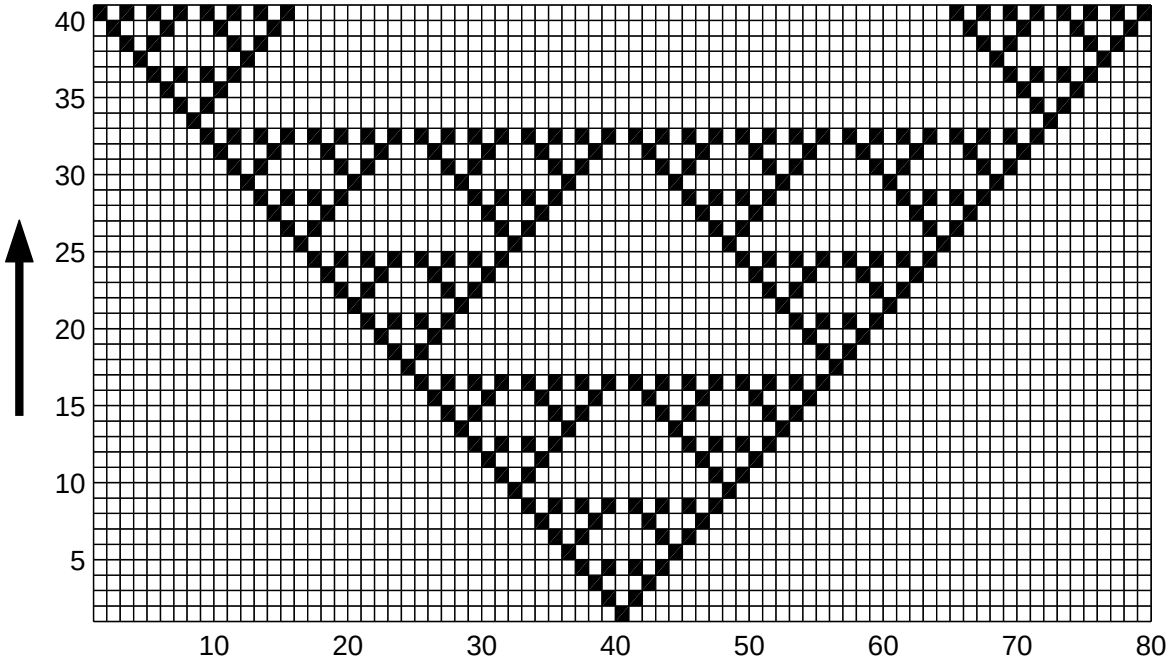

Figure 1.20: Distribution of excitations (black dots) in the linear chain of spins. The system is presented in the extended configuration space, where each moment of time corresponds to a certain line of the structure. The time increases upwards.

tem in time. At the same time the system changing is described by a simple power law. Therefore, the future is clear and predictable in spite of the non-stationarity and the lack of the finite dimensional analogues. Thus, this simple example clearly shows that the self-similarity of a structure in an extended configuration space represents a constructive basis for the assessment of complex dynamics, which goes beyond the frameworks of classical approaches [2, 20, 44–56].

Chapter 2

PERCOLATION THEORY

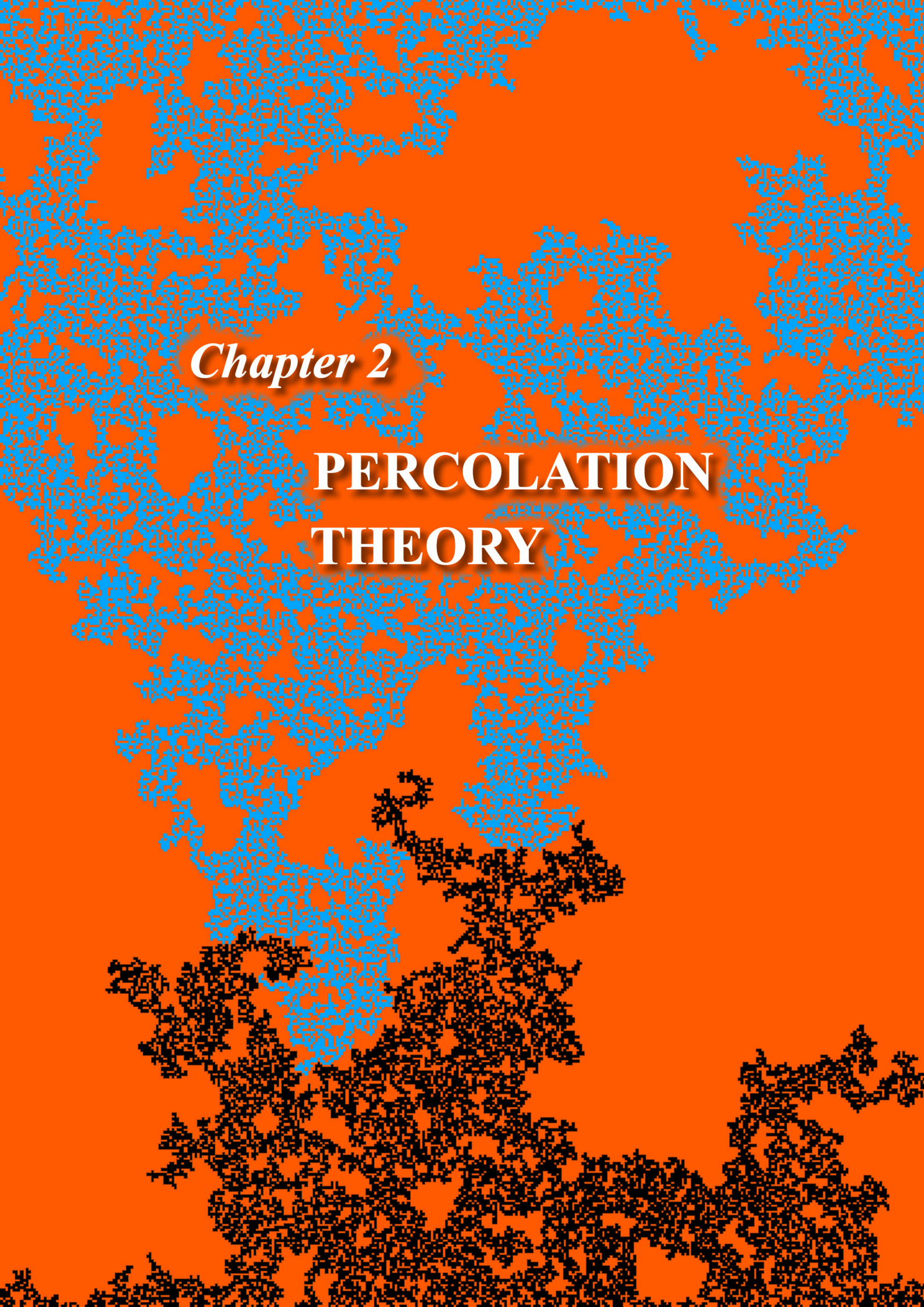

We have already mentioned above that fractal structures encountered in nature, as a rule, turn out to be stochastic, i.e. the self-similarity attributed to fractals manifests in the form of universal probability distributions of system structural elements. The Percolation Theory discussed in this chapter gives an extremely effective and simplest method of fractal generation.

2.1 Percolation on regular lattices

In 1957 mathematicians S.R. Broadbent and J.M. Hammersley published an article [57], in which they shared their idea of a possibility to describe a process of coffee flowing through the grounds in a percolator. Their approach was an alternative to a classical diffusion description of one physical substance, conventionally call liquid, flowing in the other, conventionally called *medium*. In this way a new theory had appeared that later was called a theory of percolation. To be fair, we should mention that originally percolation ideas were first formulated by P.J. Flory [19] as early as 1941 during his study of the processes of polymerization and gelation (see section 2.5).

Percolation represents the basic model of a structurally disordered medium. Simple lattice problems of the percolation theory may be presented in the following way [29, 58–60]. Let us consider a square lattice, where each site is occupied with probability p or is empty with probability $1-p$. The probability p may be interpreted as fracture (concentration) of the randomly occupied sites on the lattice. The empty and occupied sites may stand for very different physical properties. For instance, in section 3.4, when a model of a porous medium is discussed, we will consider the occupied sites as pores, while the empty sites will represent elements of a solid matrix. Or the occupied sites may be considered electrical conductors and the empty sites - insulators. In our example let us do exactly the same and, for illustration, assume that the occupied (black) sites in Fig. 2.1 are electrical conductors, and the empty (yellow) sites represent insulators.

Naturally, we may also assume that electrical current can only flow between nearest-neighbour conductor sites having a common edge. Variants of four nearest neighbours to form a fix cluster of sites on a square lattice are marked in white in Fig. 2.1.

Since the percolation theory deals with probabilistic characteristics, the larger the size of the system the more accurate the results. Fig. 2.1 plays just a demonstrating role showing a small lattice with sizes 11×11 and concentration of the occupied sites, i.e. conductors,$p = 0.3$, while Fig. 2.2 illustrates a 120×120 lattice with concentration of conductor sites $p = 0.1$.

In Fig. 2.2 we can see that at lower concentrations $p \ll 1$ the conductor sites are either isolated from each other or form small clusters of nearest neighbour sites. Two conductor sites belong to the same cluster if and only if they are connected by a path of nearest-neighbour

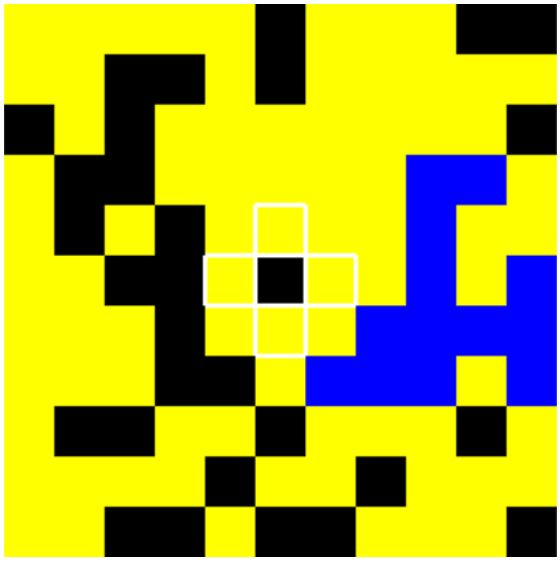

Figure 2.1: Site percolation on the square lattice. The black sites of the square lattice are conductors; yellow sites are insulators; blue sites represent a maximum conductor cluster. The sites marked in white are the nearest neighbours of the central site

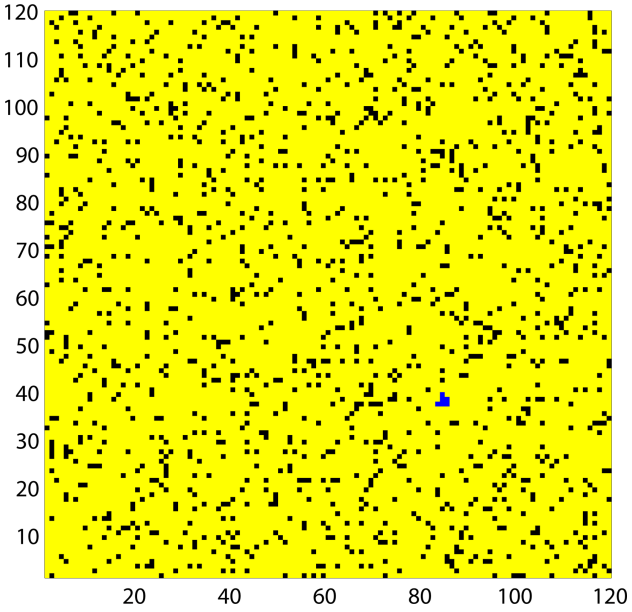

Figure 2.2: Site percolation on the square lattice. The concentration of the conductor sites equals $p = 0.1$. The maximum conductor cluster is represented in blue

conductor sites[†]. The maximum conductor cluster in all the figures of this section is marked in blue.

When the concentration p is increased the average size of the clusters increases. Figures 2.3 and 2.4 demonstrate our 120×120 lattice with the concentration of conductor sites $p = 0.4$ and $p = 0.55$, respectively.

[†]Hereinafter the nearest neighbours are considered sites having a common edge, unless otherwise stipulated

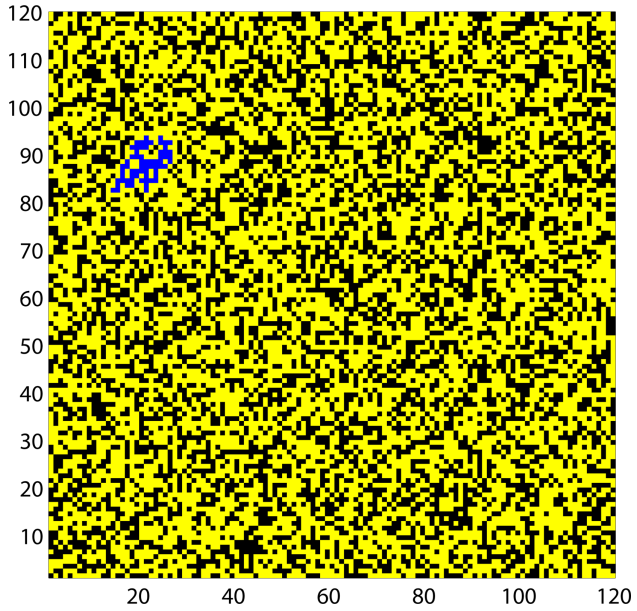

Figure 2.3: Site percolation on the square lattice. The concentration of the conductor sites equals $p = 0.4$. The maximum conductor cluster is represented in blue

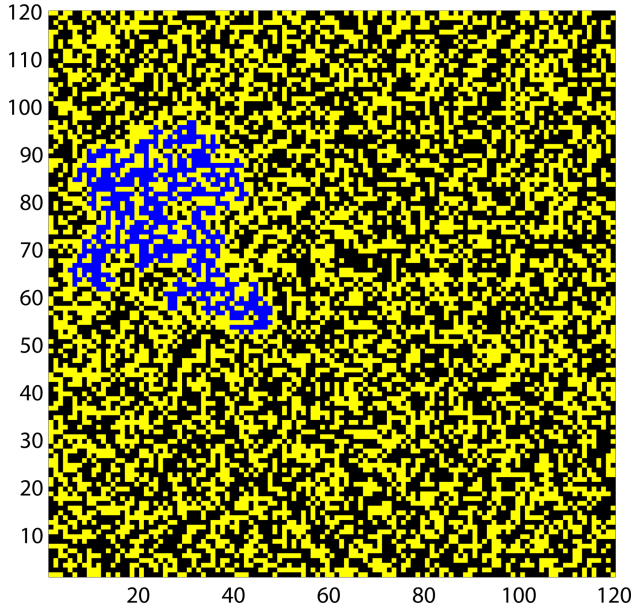

Figure 2.4: Site percolation on the square lattice. The concentration of the conductor sites equals $p = 0.55$. The maximum conductor cluster is represented in blue

At $p \ll 1$ (as well as at $p = 0.3$ and $p = 0.55$) the whole system has dielectric properties, as there are no continuous conductive paths connecting the opposite sides of the lattice. On the contrary, as it is shown in Fig. 2.5, at $p \sim 1$ the most area of the lattice has become conductive, since the blue sites form a giant conductive cluster for electrical current to flow from one side of the system to the other.

There is a critical exponent $p = p_c$ at which transition occurs from a dielectric phase (at

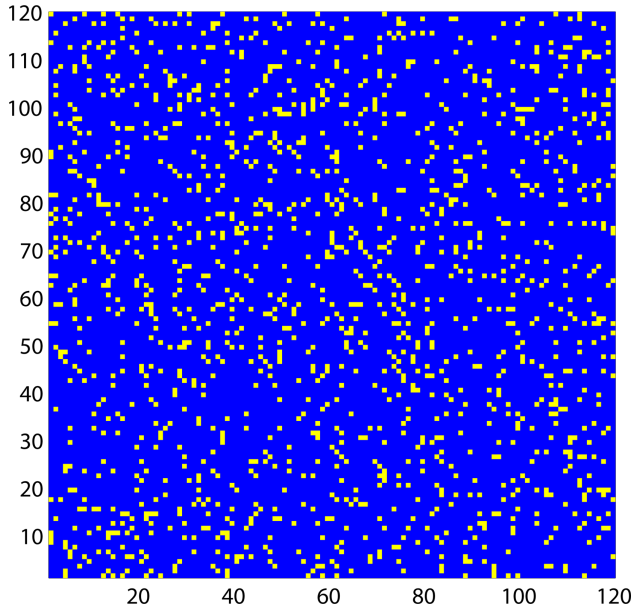

Figure 2.5: Site percolation on the square lattice. The concentration of the conductor sites equals $p = 0.9$. All the occupied sites belong to the same maximum conductive cluster

$p < p_c$) to a conductive phase ($p > p_c$). The critical exponent $p = p_c$ is called the percolation threshold. In this case they say that the percolation takes place through the occupied sites. Looking at our figures, one may say that percolation takes place along the black sites of the lattice (though the percolation cluster itself is coloured in blue to be more vivid).

An attentive reader might have noticed that Fig. 2.2 and 2.5, corresponding to the concentration values $p = 0.1$ and $p = 0.9$, are statistically identical with an accuracy just to the change of the colours. Indeed, due to the random distribution of the empty and occupied sites, our system is invariant with regard to the recolouring, i.e. substitution of the empty sites for occupied sites and vice versa with the simultaneous change of the probability p to the value $1 - p$. In other words, mathematically, there is no difference between the occupied (black) sites and empty (yellow) sites percolation. Anyhow, it should be noted that physical and applied aspects of the percolation depend entirely on what type of sites is chosen: the conductor sites percolation is not identical to the insulator sites percolation.

For the square lattice the percolation threshold is about $p_c \approx 0.59$ (for the cubic lattice the percolation threshold is equal to $p_c \approx 0.33$). The percolation illustrated in Fig. 2.6 is near the threshold.

Contrary to the usual phase transitions occurring at a certain critical temperature, the percolation transition described above is a geometric phase change. The percolation transition is characterized by the geometric properties of the conductive clusters near $p = p_c$. At $p \ll 1$ only small clusters exist. When the concentration of occupied sites p is increased the average size of the clusters increases. At the concentration near critical a large cluster appears which connects opposite edges of the lattice. We call this cluster percolating[†] (blue pixels in

[†]In special literature a percolating cluster sometimes is called a spanning or connecting cluster).

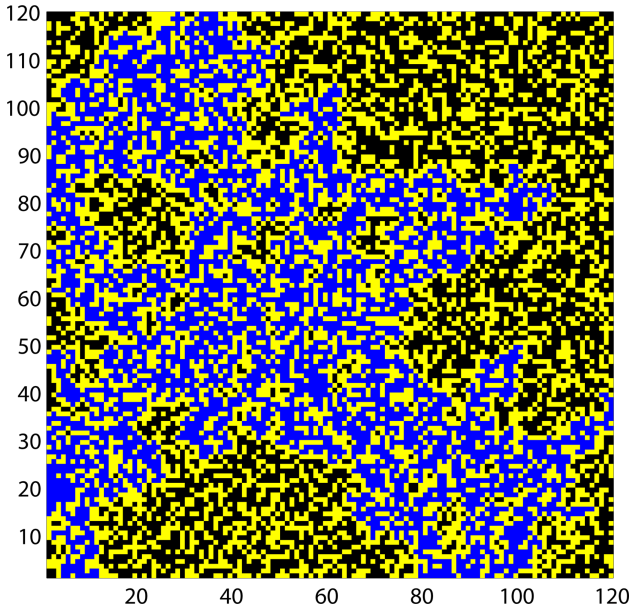

Figure 2.6: Site percolation on the square lattice. The concentration of the conductor sites is near the threshold and equal to $p = 0.59$. The blue colour represents the percolating conductive cluster

Fig. 2.6). In a thermodynamic limit of an infinite lattice the percolating cluster is called the infinite cluster. As it is shown in Fig. 2.7, when the concentration is increased further, the number of sites belonging to the same percolating cluster (the percolating cluster density) increases. A percolating network appears in the system, and its holes decrease in size as p increases. Accordingly, the average size of the finite clusters which do not belong to the percolating cluster decreases, and at $p \sim 1$ all the sites, apparently, belong to the only one cluster.

Mathematically, each cluster is a connected component of the whole set of occupied sites, therefore the percolating cluster may be interpreted as a connected subset of all occupied sites of the lattice, through which we can walk or, as assumed in our example, electrical current can flow from one edge of the lattice to the opposite one. In an infinite system the percolating cluster has become also infinite.

It is natural to characterize the percolating cluster by its strength or weight, which is determined as a fraction of the number of its elements, i.e. the number of sites belonged to it, to the total number of the sites in the lattice. In other words, the strength of the percolating cluster is just a probability that any site randomly chosen in the lattice belongs to the percolating cluster. The strength of an infinite cluster is denoted by P_∞. The P_∞ exponent is also called the percolation probability. We may say that the percolation transition is related to the zero percolation probability in a system. When $p < p_c$ only finite clusters exist, and $P_\infty = 0$. At $p > p_c$, as we will see in section 2.2, P_∞ increases from p according to a power law, what is typical for the ordinary physical phase transitions.

Let us introduce the function n_s of the cluster-size distribution, to be more exact, distribution of clusters by the number s of the elements they consist of:

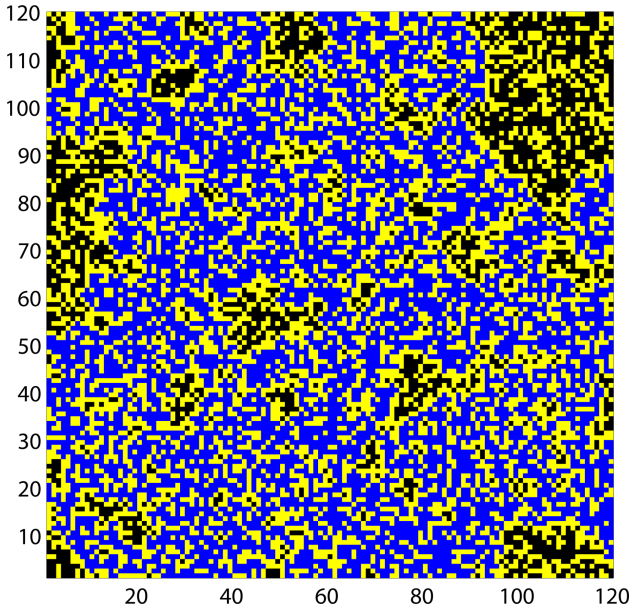

Figure 2.7: Site percolation on the square lattice. The concentration of the conductor sites is above the critical value and equal to $p = 0.62$. The blue colour represents the percolating conductive cluster

$$n_s(p) = \frac{\langle N_s \rangle}{N}, \tag{2.1}$$

where $\langle N_s \rangle$ is the average number of s-size clusters; N is the total number of sites in the lattice. The exponent sn_s defines a specific number (per site) of sites in the s-size clusters. It is obvious, that:

$$\sum_{s=1}^{s=\infty} sn_s(p) = p. \tag{2.2}$$

In other words, the probability that a site belongs to any cluster is equal to the probability that it is just occupied.

Above we have considered the site percolation where the sites of the square lattice were occupied or empty randomly. Choosing the bonds between the lattice sites randomly conductive or non-conductive, we speak about the bond percolation. The bond percolation is illustrated in Fig. 2.8.

Two occupied (conductive) bonds belong to the same cluster if and only if they are connected by a path of occupied (conductive) bonds. The critical concentration of bonds separates a phase of finite clusters from a phase with an infinite cluster on the 2-D lattice. For a simple square lattice the critical bond concentration is equal to exactly the half: $p_c = 1/2$.

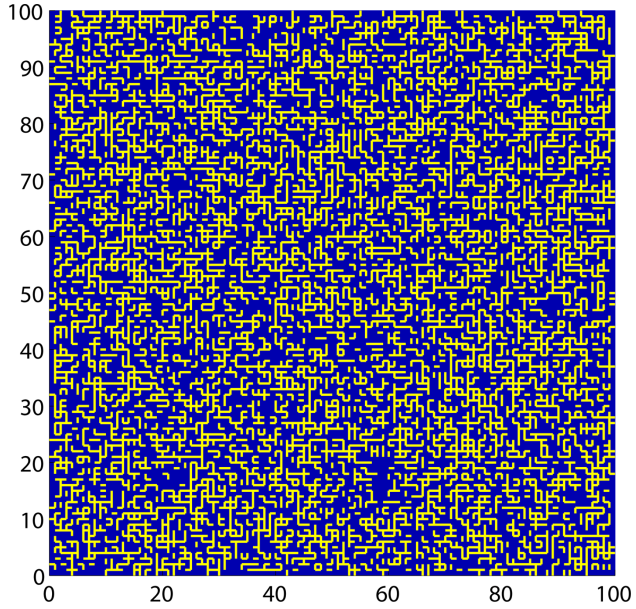

Figure 2.8: Bond percolation on the 100×100 square lattice. The concentration of conductive bonds is below the critical value

2.2 Percolation as a critical phenomenon

The critical phenomenon theory deals with macroscopic statistical systems near the phase transition point. The large-scale instabilities or fluctuations characterize the processes observed in this situation.

As it has been already mentioned, the onset of an infinite cluster of the connected elements in the system may be considered as a geometric phase transition: the critical concentration $p = p_c$ separates the phase of finite clusters $p < p_c$ from the phase $p > p_c$ where an infinite cluster is already exists. We will see that the percolation transformation in many ways is similar to the second-order phase transitions. Following the works [29, 61] let us draw this parallel on the example of the magnetic transformation. So, at low temperatures some materials demonstrate a spontaneous magnetization $\mu > 0$ in the absence of an external magnetic field (ferromagnetic phase). As the temperature rises, the spontaneous magnetization gradually reducing disappears at some critical temperature $\theta = \theta_c$. At the temperatures above the critical value $\mu = 0$ (paramagnetic phase).

Magnetic materials are represented by some elementary magnetic moments (spins). Their interaction maintains an order in which all spins are parallel. On the other hand, thermal fluctuations destroy the order maintaining the state of random spin orientation. At low temperatures the interaction of magnetic moments prevails, and a long-range order exists in the system. The spontaneous magnetization describes this long-range order and is called the parameter of magnetic transition order. With the temperature rise the spontaneous magnetization decreases and near θ_c it tends to zero according to the power law $\mu(\theta) \sim (\theta_c - \theta)^\beta$. Above the critical temperature the heat energy dominates, and only finite clusters of the co-directional spins may exist. Their random orientation ensures the zero spontaneous mag-

netization.

In percolation the concentration p of the occupied sites plays the role of temperature in the thermal phase transitions. As in the thermal phase transitions, long correlation bonds control the percolation transformation, and behaviour of the values near the transition is described by power laws and critical exponents.

The percolation transition is characterized by the geometric properties of the connected sites near $p = p_c$. An important exponent is the probability P_∞ that a site (or a bond) belongs to an infinite cluster. When $p < p_c$ only finite clusters exist, and $P_\infty = 0$. At $p > p_c$, the probability P_∞ acts as the spontaneous magnetization below θ_c increasing with p according to the power law

$$P_\infty \sim (p - p_c)^\beta. \tag{2.3}$$

The same as the spontaneous magnetization, P_∞ describes the order in the percolation system and may be defined as the order parameter. The linear sizes of the finite clusters below and above p_c are characterized by the correlation length. The correlation length ξ is defined as the mean distance between two sites of the same finite cluster. When p approaches p_c, ξ increases as

$$\xi \sim |p - p_c|^{-\nu} \tag{2.4}$$

with the same exponent ν below and above the threshold. The average number of sites (mass) of the finite cluster also diverges

$$S \sim |p - p_c|^{-\gamma}, \tag{2.5}$$

again with the same exponent γ below and above the threshold. To obtain S and ξ, one should calculate mean values of all finite clusters on the lattice. In magnetic systems the spontaneous magnetization μ and sensitivity χ correspond to the exponents P_∞ and S (see Table 2.1).

One more critical exponent characterizes behaviour of the cluster-size distribution function n_s. Dependence of n_s on the critical exponent p is as follows

$$n_s(p) \sim s^{-\kappa} \exp\{-\mathscr{A} s |p - p_c|^\delta\}. \tag{2.6}$$

The exponent δ determines the typical largest size of the finite clusters. Clusters with $s_c \sim |p - p_c|^{-\delta}$ are called critical. Clusters with $s > s_c$ are exponentially unlikely. But

Table 2.1: Critical exponents of the percolation transition

Percolation	$d=2$	$d=3$	$d \geqslant 6$
Order parameter, β	5/36	0.417 ± 0.003	1
Correlation radius, ν	4/3	0.875 ± 0.008	1/2
Mean number of elements in a cluster, γ	43/18	1.795 ± 0.005	1
Magnetism	$d=2$	$d=3$	$d \geqslant 6$
Order parameter, β	1/8	0.32	1/2
Correlation radius, ν	1	0.63	1/2
Sensitivity, γ	7/4	1.24	1

the occurrence of clusters with the number of elements $s \ll s_c$, as illustrated in Fig.(2.6), demonstrates the scaling behaviour

$$n_s(p) \sim s^{-\kappa}. \tag{2.7}$$

Fig. 2.9 illustrates the site percolation on the square lattice in the immediate proximity to the threshold. Clusters of different sizes are depicted with different colouring (the larger the cluster the lighter the tint).

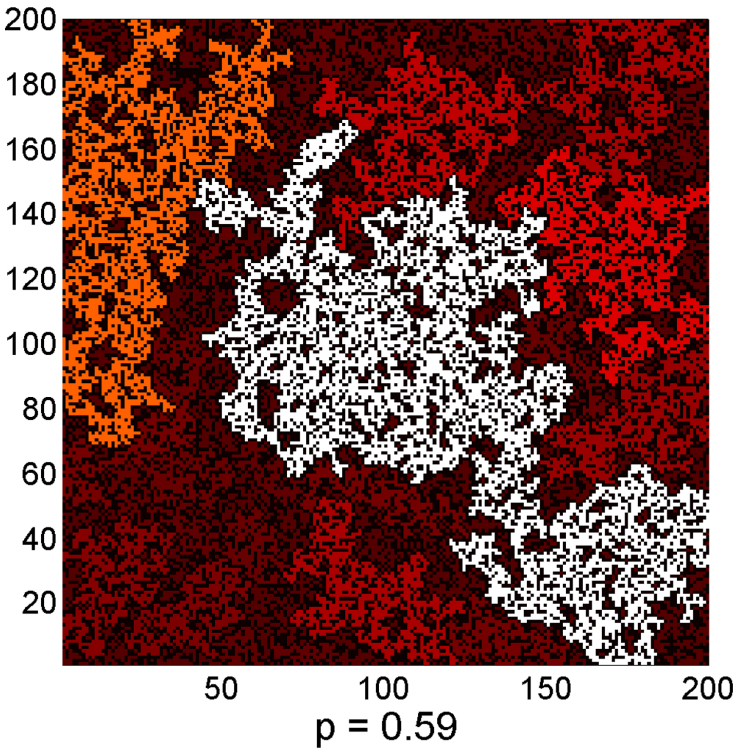

Figure 2.9: Site percolation on the 200×200. square lattice. Different colours correspond to the clusters of different sizes. The maximum cluster is marked in white.

The exponents β, ν and γ describe critical behaviour of the typical values related to the

percolation transition and are called the critical exponents. These exponents are universal and depend neither on the type of the lattice (square, triangular, etc.), no on the type of percolation (site, bond or continuum), but only on the dimensions of the space.

This universality is a typical feature of the second-order phase transitions, where the order parameter always disappears at the critical point. For example, the spontaneous magnetization of all 3-D magnetic materials is described by one and the same exponent β irrespective of the crystal structure and type of interaction between the adjacent spins. Note that all the exponents described above have been determined within the thermodynamic limits of the infinitely large systems. In a finite system P_∞, for example, not necessarily equals zero below the threshold.

2.3 Structure of the percolating cluster

We begin by considering an infinite cluster at the percolation threshold $p = p_c$. A typical example of a 2-D infinite cluster is shown in Fig. 2.10, where one can see that the infinite cluster has holes in all scales, like on the Sierpiński gasket (see Fig. 1.4).

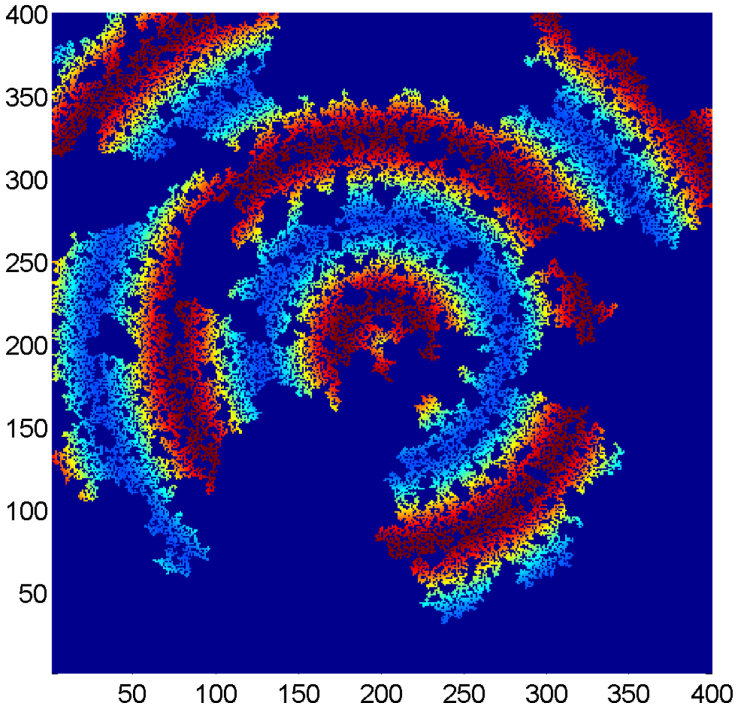

Figure 2.10: Percolation cluster near the threshold. The colour of sites changes as a periodic function of their Euclidean distance from a certain site in the centre of the lattice

The cluster is self-similar in all linear scales which are larger than the lattice spacing and smaller than the size of the system, and thus it may be considered as a fractal. The fractal dimension d_f describes divergence of the cluster mass M (number of its elements) in the Euclidean sphere with the increase of its radius r

$$M(r) \sim r^{d_f}. \tag{2.8}$$

We know that for random fractals $M(r)$ is the result of averaging various numerous configurations of the infinite cluster or, which is the same, numerous spheres with different centres on the same infinite cluster. Above and below the threshold the mean sizes of the finite clusters are described by the correlation length ξ. At the threshold $p = p_c$ ξ diverges, and the holes in the infinite cluster are spotted in all the scales. Above the threshold ξ represents a typical average size of the holes in the infinite cluster. Since ξ is finite above the threshold, the self-similarity of the infinite cluster stretches out only on the scales that are smaller than ξ. We may interpret $\xi(p)$ as a typical scale of the self-similarity within which the infinite cluster possesses fractal properties. On the length scales larger than ξ the infinite cluster structure looses its self-similarity and becomes homogeneous.

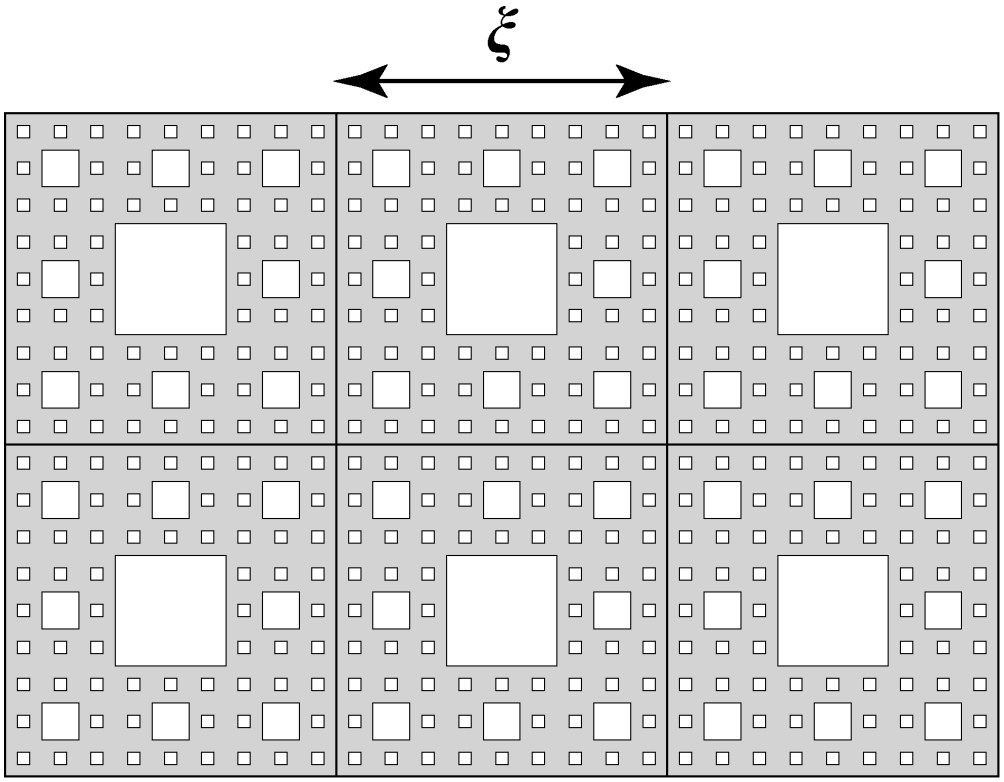

Figure 2.11: Illustration of a crossover phenomenon from the fractal behaviour on small scales to the homogeneous behaviour on large scales of regular parquet made of the ξ-size Sierpiński carpets

Fig.2.11 shows a crossover phenomenon from the fractal behaviour on small length scales to the homogeneous behaviour on large length scales of regular parquet made of the ξ-size Sierpiński carpets. On the length scales $r < \xi$ the illustrated structure is characterized by the fractal behaviour; on the contrary, at $r > \xi$ the structure has become homogeneous, and its density does not change with the length scale.

Thus, we see a fractal cluster on the length scales smaller than ξ. But on the length scales

larger than ξ we find a homogeneous structure which is composed of many cells of size ξ. Mathematically, it can be presented as

$$M(r) \sim \begin{cases} r^{d_f}, & r \ll \xi, \\ r^{d}, & r \gg \xi. \end{cases} \tag{2.9}$$

Fig.2.12 shows a schematic diagram of the crossover phenomenon in a percolation system for the value $r \simeq \xi$.

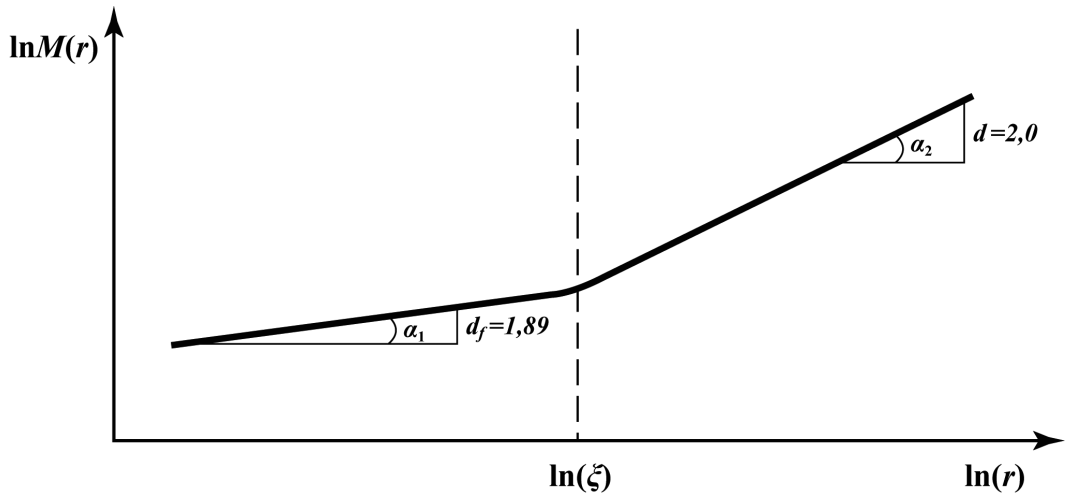

Figure 2.12: Schematic diagram of the crossover phenomenon

Now we will relate the fractal dimension d_f of the percolation cluster to the critical exponents β and ν. The probability that a randomly selected site in a Euclidean sphere of radius r belongs to the infinite cluster is determined by a ratio of the number of sites belonged to the infinite cluster to the total number of sites in the sphere

$$P_\infty \sim \frac{r^{d_f}}{r^d}, r < \xi. \tag{2.10}$$

This ratio is correct for $r = \lambda\xi$, where λ is a certain constant smaller than 1. Substituting $r = \lambda\xi$ in eq. (2.10) we obtain:

$$P_\infty \sim \frac{\xi^{d_f}}{\xi^d}. \tag{2.11}$$

Both sides of this ratio are the power functions of $p - p_c$. Substituting eqs. (2.3) and (2.4) into eq. (2.11) we obtain:

$$d_f = d - \frac{\beta}{\nu}. \tag{2.12}$$

Thus, the fractal dimension of the percolating cluster at the percolation threshold is not a new independent exponent, but is expressed via thermodynamic exponents β and ν. Since β and ν are universal exponents, d_f is also universal, which depends only on the dimension of the space. We can show that below and at the threshold the ratio (2.12) determines also the fractal dimension of the finite clusters with linear dimensions that do not exceed ξ. Below the threshold clusters with dimensions larger than ξ can also be found, though very rarely. Such clusters are called lattice animals, and their fractal dimension is less than d_f.

In section 1.6 we have already mentioned that structures that have the same fractal dimension may, however, differ considerably from each other. Therefore, to get new significant information about the structure of a percolation network, in addition to the fractal dimension of the percolating cluster, it is useful, in analogy with section 1.6, to consider its minimal path and chemical dimension.

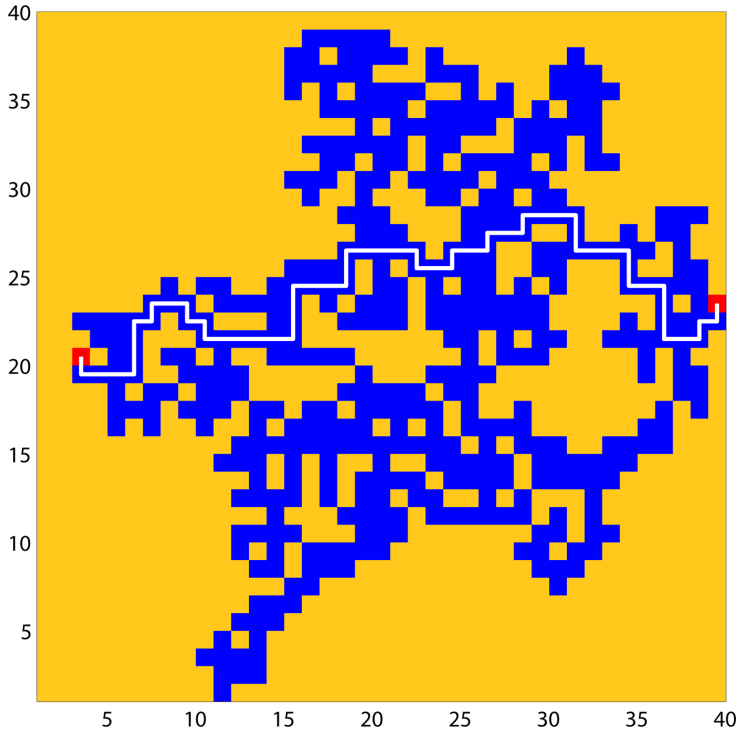

Figure 2.13: Percolating cluster of sites (blue cells) on the 40×40 square lattice. The shortest path connecting the red cells with coordinates $(3,20)$ and $(39,24)$ is marked by a white broken line

We start by finding the shortest path between the two sites of the percolating cluster shown in Fig. 2.13. The selected sites are marked in red.

The cluster elements belonging to this path form a self-similar structure (the white broken line in Fig. 2.13) with the fractal dimension $d_{\min}$, which is called, as we already know, the shortest path or minimal dimension on a percolating cluster. The length l of this shortest path called the chemical distance [28,29] changes with the increase of the Euclidean distance between the selected elements of a cluster according to a law

$$l \sim r^{d_{\min}}. \tag{2.13}$$

The reverse relation

$$r \sim l^{1/d_{\min}} \equiv l^{\tilde{\nu}} \tag{2.14}$$

demonstrates how r changes with the increase of l.

Let us choose any element of a cluster and at a certain moment of time $t = 0$ begin considering it as a source of information or infection (often it turns out to be the same). The distance which the front of the spreading infection can cover in time t is controlled by the minimum dimension of the percolating cluster.

The chemical dimension d_l of the percolating cluster describes the changing of the number of its elements M with the increase of the chemical distance, which is smaller than distance l, from a certain fixed site:

$$M(l) \sim l^{d_l}. \tag{2.15}$$

If the fractal dimension d_f characterizes the increase of the mass of a percolating cluster with the increase of its size in a Euclidean space, then the chemical dimension d_l describes the increase of the cluster mass in a space of the chemical distances. Combining eqs. (2.8), (2.13) and (2.15) we find the relation

$$d_l = \frac{d_f}{d_{\min}}. \tag{2.16}$$

The travelling along the labyrinths of the percolating cluster with a periodic colour change of its sites with the increase of the chemical distance is illustrated in Fig. 2.14.

Values of the minimal dimension and chemical distance are given for reference in Table 2.2.

Table 2.2: Morphological dimensions of a percolating cluster [28, 29]

Dimensions	$d = 2$	$d = 3$	$d \geqslant 6$
Cluster size, $d_f = d - \beta/\nu$	$91/48$	2.54 ± 0.008	4
Minimal dimension, $d_{\min}$	1.13 ± 0.004	1.84 ± 0.02	2
Chemical dimension, d_l	$1,678 \pm 0.005$	1.795 ± 0.005	1
Hull dimension, d_h	$7/4$	2.54 ± 0.008	4

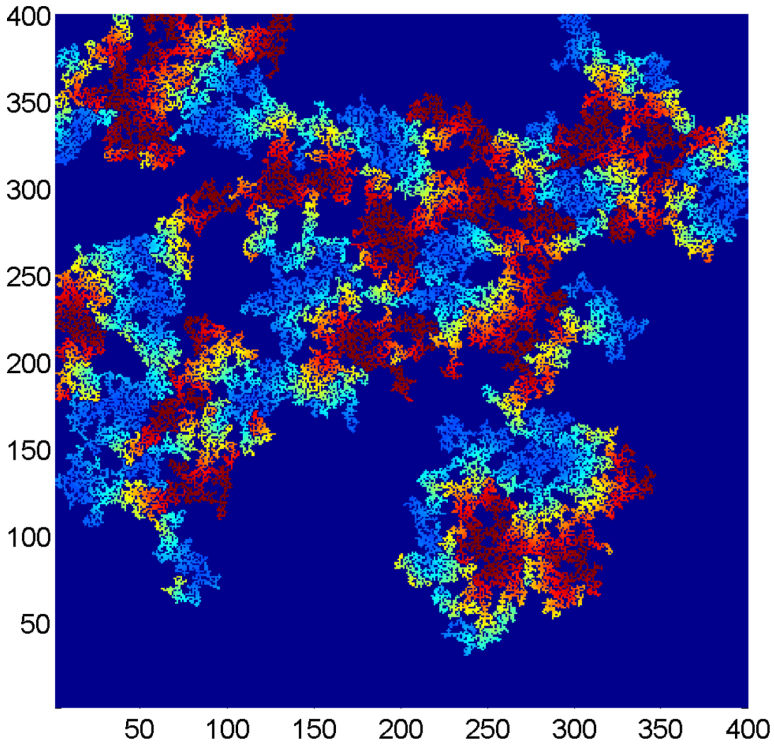

Figure 2.14: Travel along the labyrinths of the percolating cluster with the periodic colour change of the sites with the increase of the chemical distance

To describe the structure of a percolating cluster, several geometric models have been suggested [28, 29, 58]. We will consider a model based on the Mandelbrot-Given fractal [62]. Generations of the Mandelbrot-Given fractal are shown in Fig. 2.15. The process starts with a single segment of length (Fig. 2.15*a*). In the first step we obtain the generator of the Mandelbrot-Given fractal (Fig. 2.15*b*), which is applied in the next generation to all new segments of length $1/3$ (Fig. 2.15*c*). We draw your attention to the fact that on fragments d and e in Fig. 2.15 we have increased the length scale of the construction by 3 times for illustration. The fractal dimension of the Mandelbrot-Given structure is very close to the dimension of a 2-D percolating cluster and equal to $d_f = \ln 8/\ln 3 \approx 1,893$. The dimension of a percolating cluster on a plane, just for reminding, is $d_f = 91/48 \approx 1,896$. The Mandelbrot-Given structure contains loops, branches, and dangling ends of all length scales.

2.4 Exact solution in a one-dimensional case

Like many other problems of the theoretical physics, a percolation problem can be solved exactly in one dimension, and some aspects of this solution are true for higher dimensions as well. Let us study the site percolation on an infinite linear chain, i.e. a one-dimensional lattice with an infinite number of sites of equal spacing arranged in a line (Fig. 2.16).

Each site on the lattice is occupied at random with the probability p or is empty consequently with the probability $1 - p$. A group of the adjacent occupied sites that do not contain empty

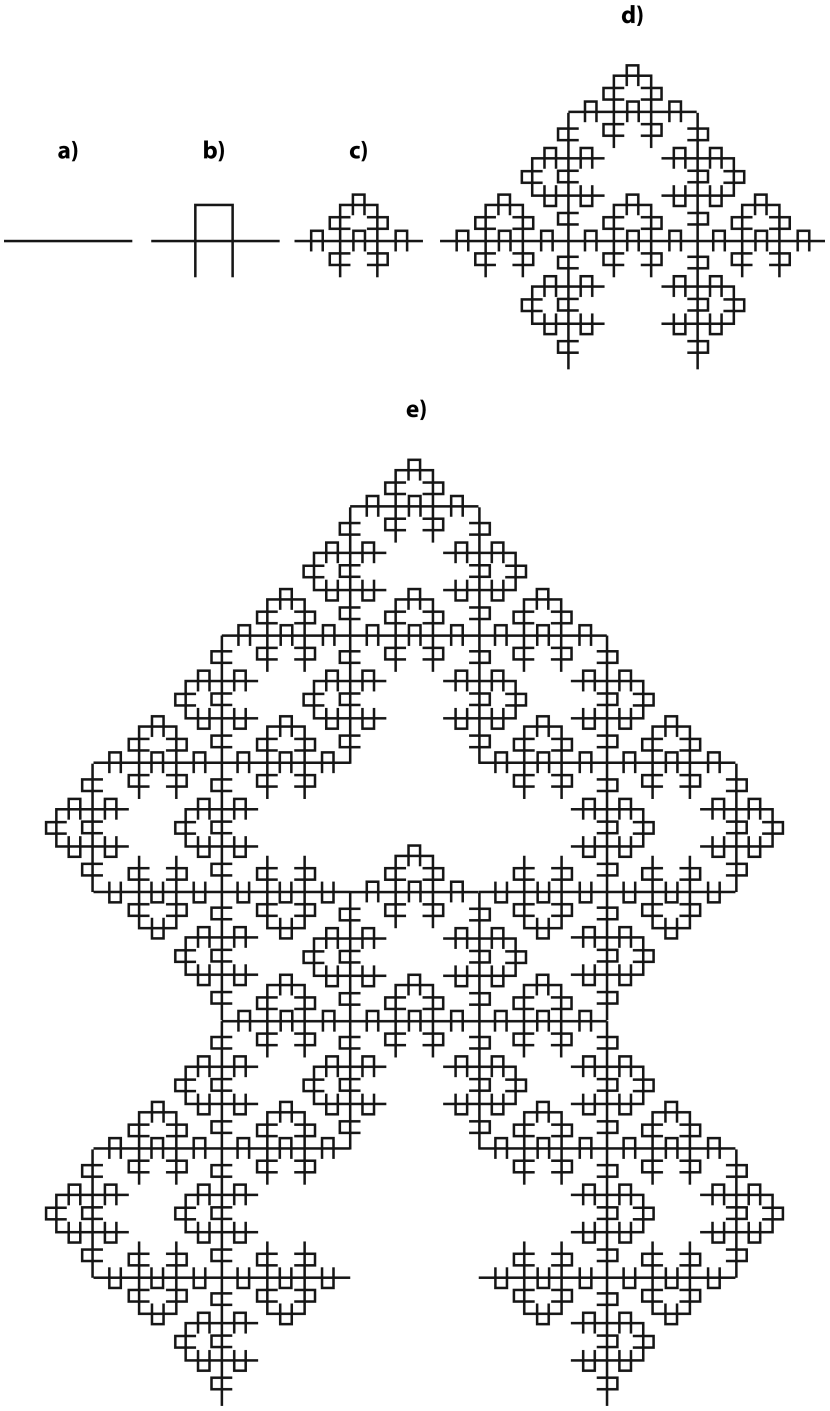

Figure 2.15: Generations of the Mandelbrot-Given fractal

sites in-between forms a cluster. In a 1-*D* case the cluster is a linear chain of the occupied sites with the number of elements from 1 to ∞. Occurrence of an empty site divides the group of the adjacent occupied sites into two different clusters. For a cluster to be separated from other clusters, the sites located on its boundaries on the right and left must be empty. Fig.2.16 shows the isolated occupied sites and clusters of two and six elements. To form, for example, the central cluster of size 6 in Fig. 2.16, there must be a sequence of six occupied sites bounded by two empty neighbours from the right and left.

Figure 2.16: Example of the clusters on the 1-D lattice. The occupied sites are grey, the empty sites are white

Since the occupied sites are distributed randomly, the probability that two randomly selected nearest-neighbour sites are occupied equals p^2, for three sites p^3, for five sites p^5, etc. (the product of probabilities for independent events). Since in the one-dimensional case any cluster has only two ends, the probability to form a cluster containing s elements (s-cluster) is a product of

$$n_s = p^s(1-p)^2. \tag{2.17}$$

The value of eq. (2.17) can be defined as the specific number (number of the clusters divided by the total number of the lattice sites) or density of the s-clusters. For $p < 1$ the specific number of the finite clusters decreases exponentially to zero when s tends to infinity. What is the percolation threshold in a 1-D case? At $p = 1$ each site of the linear chain is occupied, and the whole linear chain forms a single cluster. For any $p < 1$ there is at least one empty site dividing the infinite cluster into fragments and preventing it to percolate. Thus, the percolation threshold, being the critical density p_c and ensuring the onset of the infinite cluster, in the 1-D case is equal to one

$$p_c = 1. \tag{2.18}$$

Since in one dimension $p > p_c$ is not possible, one may investigate only the half of the phase transition below the percolation threshold. The percolation probability in the 1-D lattice of size L may be described as follows:

$$\lim_{L\to\infty} P(p,L) = p^L = \begin{cases} 0, & \text{at } p < 1 \\ 1, & \text{at } p = 1 \end{cases} \tag{2.19}$$

The probability that a site belongs to the s-cluster is $n_s s$. The probability that a site belongs to any cluster coincides with the probability that it just occupied:

$$\sum_{s=1}^{\infty} n_s s = p \quad (p < p_c). \tag{2.20}$$

The latter relation can be checked up analytically with the help of eq. (2.17):

$$\begin{aligned}\sum_{s=1}^{\infty} p^s(1-p)^2 s &= (1-p)^2 \sum_{s=1}^{\infty} p\frac{d(p^s)}{dp} = (1-p)^2 p\frac{d\left(\sum_{s=1}^{\infty} p^s\right)}{dp} = \\ = (1-p)^2 p\frac{d\left(\frac{p}{1-p}\right)}{dp} &= p.\end{aligned} \tag{2.21}$$

Equation (2.20) is valid even for higher dimensions when the sites which belong to the infinite cluster are considered separately and not included into the sum of all clusters of all sizes. In one dimension when $p = p_c = 1$, there is only one cluster covering the lattice in such a way, $s = \infty$ and $n_s = 0$, that makes eq. (2.20) indefinite at $p = 1$ and valid only for $p < 1$.

Let us now choose randomly the occupied sites. How large on average are clusters we can come across? In other words, let us define the characteristic mean cluster size of a finite cluster on the 1-*D* lattice. We know that the probability that an arbitrary site (occupied or empty) belongs to an s-cluster is $n_s s$, and the probability that a site belongs to a finite cluster is $\sum_s n_s s$. Thus,

$$w_s = \frac{n_s s}{\sum_s n_s s} \tag{2.22}$$

is the probability that the cluster, which the occupied site we have randomly chosen belongs to, contains exactly s sites. The mean cluster size[†], which we define by choosing the occupied sites at random, is determined by the equation:

$$S = \sum_{s=1}^{\infty} w_s s = \sum_{s=1}^{\infty} \frac{n_s s^2}{\sum_{s=1}^{\infty} n_s s}. \tag{2.23}$$

Let us now calculate the mean cluster size exactly. The denominator according to eq. (2.20) is p. For the numerator:

$$(1-p)^2 \sum_{s=1}^{\infty} s^2 p^s = (1-p)^2 \left(p\frac{d}{dp}\right)^2 \sum_{s=1}^{\infty} p^s,$$

where the summing of the derivatives of simpler sums is carried out again from $s = 1$ to infinity. Thus,

[†]The term *mean cluster size* is generally accepted for the exponent S, though there are other types of averages being used. For example, $\sum_s n_s s / \sum_s n_s$ is the mean cluster size when each cluster, but not site as in equation (2.23), is chosen with an equal probability.

$$S = \frac{1+p}{1-p} \quad (p < p_c) \quad — \tag{2.24}$$

is the mean cluster size, which diverges with the approach to the percolation threshold. Later we will get the same results for a number of dimensions larger than one. The found singularity is very natural, since above the percolation threshold there is an infinite cluster, and just below the threshold there already exist very large (but finite) clusters. Thus, the size average of these large clusters is also quite large just below the threshold.

Let us define the *correlation function* or *pair connectivity* $g(r)$ as a probability that a certain site at position r from the occupied site belongs to the same cluster. For $r = 0$ the probability $g(0)$ equals one. For $r = 1$ the neighbouring site belongs to the same cluster if and only if the site is occupied, which occurs with the probability p. For the site at position r, this site and all $(r-1)$ intermediate sites located between it and the initial site at the beginning of coordinates $r = 0$ must be occupied without exception, which occurs with the probability p^r. Thus,

$$g(r) = 2p^r \tag{2.25}$$

for all p and r. Factor 2 appears from the fact that r-cluster may occur to the left or right of the initial site. For $p < 1$ the introduced correlation function, which is also called the connectivity function, exponentially decreases to zero when the distance r tends to infinity:

$$g(r) = 2\exp\left(\frac{-r}{\xi}\right),$$

where

$$\xi = -\frac{1}{\ln(p)} = \frac{1}{p_c - p}. \tag{2.26}$$

The latter equality in equation (2.26) is valid only for the p-values near the threshold $p = p_c$, where the expansion $\ln(1-x) = -x$ may be used for small x. We see that the correlation length (or the connectivity length) ξ also diverges near the threshold. Moreover, the correlation length is proportional to the diameter of a typical cluster. In the 1-D case it is quite obvious and valid for larger dimensions. The length of a cluster containing s sites is $(s-1)$, which does not differ much from s, when s is large. Thus, the mean length ξ changes like the mean cluster size S:

$$S \propto \xi \quad (p \to p_c). \tag{2.27}$$

The relation between the sum of the correlation function and mean cluster size turns out to be universal over all distances r:

$$\sum_r g(r) = S. \tag{2.28}$$

The sum in eq. (2.28) includes not only $r = 0, 1, 2, \ldots,$, i.e. the neighbouring sites from the right, but also the sites from the left. Since r cannot be a negative value, one should calculate first the sum of the neighbouring sites on the right and in the centre,$r = 0, 1, 2, \ldots,$ then multiply the result by 2 to take into account the left part of the lattice, and subtract one, being contribution from the centre, from the product to avoid the central site to be calculated twice.

In this exact solution of the 1-D percolation problem we may see that certain exponents diverge at the percolation threshold, and this divergence can be described by simple power laws of type $1/(p_c - p)$, at least asymptotically close to the threshold. This remains true for higher dimensions as well, though the problem there cannot have the exact solution. The exponents S and ξ have analogues in thermal phase transitions. In the experiments with liquids on light dispersion near their critical point, the critical opalescence can be observed, since the compressibility (analogue of S) and correlation length ξ diverge. Further investigation of the 1-D percolation is connected with the calculation of the cluster density in the finite 1-D chains. This permits to illustrate the finite-size universality and scaling.

Another case of the exact solution is the Bethe lattice, which we are going now to discuss.

2.5 Percolation on the Kayley tree

It is remarkable that the percolation on a 1-D chain is a particular case of another, more complicated, but fortunately exactly soluble problem, which in a certain way resembles the infinite-size percolation. This is the Bethe lattice or Kayley tree a fragment of which is shown in Fig. 2.17.

What is in common between the Bethe lattice and the infinite dimension $d = \infty$? Trees have no closed cycles loops, and their volume coincides with their surface. For $d = 2$ the area of a circle of radius r equals πr^2, while the length of its circumference is $2\pi r$. The surface of a 3D sphere of radius r equals $4\pi r^2$, while its volume is proportional to r^3. In a d-size case the sphere's volume is equal to r^d, and its surface is r^{d-1}. Thus,

$$S \propto V^{(1-1/d)} \tag{2.29}$$

in d dimensions. We may see that for $d \to \infty$ the surface becomes proportional to the volume.

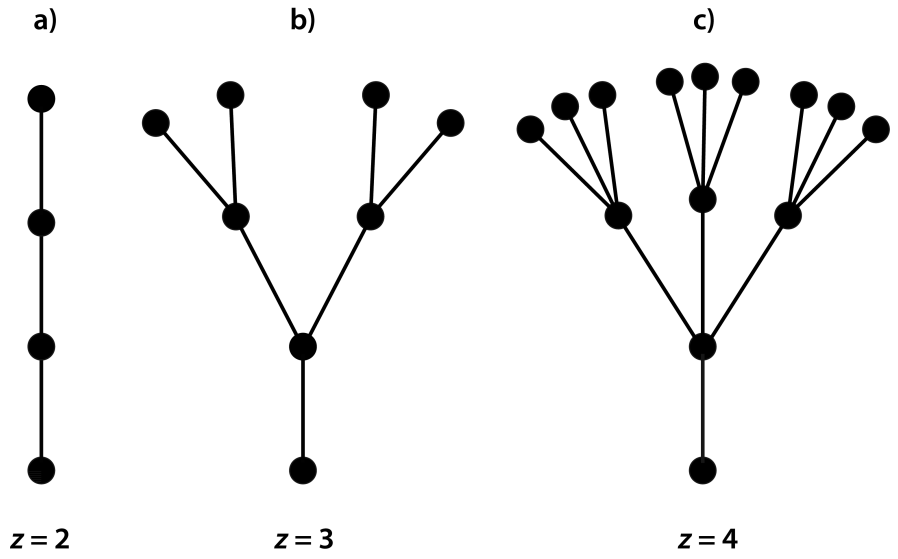

Figure 2.17: Fragments of the Bethe lattice or Kayley tree with the coordination numbers (z): a) $z = 2$, b) $z = 3$, c) $z = 4$

This is a fundamental property of a d-volume, and it lies in the fact that for the very large d the volume of a d-figure concentrates near its surface. For example, the volume of a ball ring between spheres of radius 1 and $1-\varepsilon$ equals $V_d[1-(1-\varepsilon)^d]$, which tends to the ball's volume V_d at the arbitrarily small ε but increasing d. For example, a twenty -dimensional water melon of radius 20 cm with the rind thickness of 1 cm almost to two thirds consists of the rind (65% versus 14% for an ordinary $3D$ water melon):

$$1-\left(1-\frac{1}{20}\right)^{20} \approx 1-e^{-1}.$$

We will obtain the same results in the case of squares, cubes and hypercubes.

Another important aspect is connected with the probability to encounter closed cycles or loops in high dimensions. To calculate this probability we may use clusters containing four sites. For very large d, the number of variants of how a chain of four sites may be arranged in a hyper-cubic lattice is proportional to $(2d-1)^3$ (each of the following three sites can be placed on another axis). However, the number of variants for construction of a closed cycle, when these four sites lie in the same plain arranging a square, is proportional to $d(d-1)$. Therefore, the probability of loop occurrence becomes infinitely small for $d \to \infty$, which is just typical for trees.

So, formation of the Bethe lattice starts from the centre site or the root having z branches (in the example in Fig. 2.17b $z = 3$).Each branch ends in a site, which, in its turn, serves the starting point of z branches. In this arrangement, one of these z branches connects its site with the root, while others $z-1$ lead to new sites. And this branching process repeats again and again. Thus, if we reach a certain site inside the Bethe lattice, we may proceed in other $z-1$ directions in addition to the direction we have been walking along. Only on

the surface of the lattice, where the branching stops, there is only one branch connecting the surface site with the inner part of the lattice. The obtained structure has no closed cycles meaning that between two arbitrary sites there is only one path. In more simple way the Kayley lattice may be described with the help of the chemical distance l, which we have introduced in section 1.6. For example, the chemical distance between the central site and an arbitrary one belonging to an l-shell is exactly l, in this case the tree's l-shell contains exactly $z(z-1)^{l-1}$ sites. Thus, in Fig.2.17 we see that the number of sites of the Bethe lattice increases exponentially with the distance from the centre, while for a d-dimensional lattice the number of sites increases as the distance in power d. In our example with $z=3$ (Fig. 2.17*b*), the root site is encircled by a shell of three sites (the first generation), the second shell containing six sites is followed by the third generation of twenty sites and so on.

We recommend the reader, for practice, to calculate the total number of sites of the Bethe lattice with the coordination number z on the i-generation step using the following equation:

$$N_{\text{total}}(i,z) = 1 + z(1 + (z-1) + \cdots + (z-1)^{i-1}) = 1 + z \cdot \frac{(z-1)^i - 1}{(z-1) - 1}. \tag{2.30}$$

In our example $z=3$, and

$$N_{\text{total}}(i,3) = 3 \cdot 2^i - 2. \tag{2.31}$$

Accordingly, the number of the surface sites of the lattice is calculated as follows

$$N_{\text{surf}}(i,z) = z \cdot (z-1)^{i-1}, \tag{2.32}$$

and

$$N_{\text{surf}}(i,3) = 3 \cdot 2^{i-1}. \tag{2.33}$$

Thus, for $z=3$, the number of surface sites relative to the total number of sites in the lattice is $1/2$, that is the surfaces specific fraction is a constant. Easily we may define that in general the following ratio is typical for the Bethe lattice:

$$\frac{N_{\text{surf}}}{N_{\text{total}}} = \frac{z-2}{z-1}. \tag{2.34}$$

Thus, for arbitrary $z > 1$ the surface's specific fraction of the Kayley tree $N_{\text{surf}}/N_{\text{total}}$ approximates a finite limit, while for $z \to \infty$, $\dfrac{N_{\text{surf}}}{N_{\text{total}}} \to 1$. For common lattices, such a behavior,

as we have seen in equation (2.29), may be observed only at $d = \infty$, that is in the infinitely dimensional cases.

Let us find the percolation threshold on the Bethe lattice. Standing in the centre of the lattice we try to find an infinite path going on the occupied sites. If we make one step outwards, beside the path which we have arrived on, we encounter $(z-1)$ new paths. Each of these $(z-1)$ paths leads to a new neighbour, which may turn out to be occupied with the probability p. Thus, on average, we have $(z-1)p$ occupied neighbours, meaning that there is the same number of possible paths for us to continue walking. If $(z-1)p$ less than one, the mean number of paths leading to infinity decreases $(z-1)p$ times in every generation (with each step). Thus, even if all z neighbours of the occupied site in the centre are also occupied and give us z different paths to continue walking, and even if z is very large, for $p < 1/(z-1)$ the probability of encountering a continuous chain of the occupied neighbours exponentially tends to zero with the increase of the length of the trajectory. Therefore, for the Bethe lattice with the number z of the nearest neighbours, for each site we obtain:

$$p_c = \frac{1}{z-1}. \tag{2.35}$$

The above arguments are valid for the bond percolation on the Bethe lattice as well, when the bonds between the neighbouring sites are open or blocked. Thus, the percolation threshold on the Bethe lattice does not depend on the percolation type, and eq.(2.35) is true both for the site percolation as well as bond percolation.

The equation of the percolation threshold on the Kayley tree may be also obtain by calculating the correlation function $g(l)$, which is defined as a mean number of sites located at the chemical distance l from an arbitrarily chosen occupied site of the same cluster. If two sites at a distance l belong to the same cluster, then all $l-1$ sites between them must be occupied. Since the sites are occupied at random with the probability p, and the number of configurations of the l-clusters containing the selected site as the root site coincides with the number of sites in its l-shell $z(z-1)^{l-1}$, then

$$g(l) = z(z-1)^{l-1}p^l = \frac{z}{z-1}((z-1)p)^l. \tag{2.36}$$

For $z = 2$ (Fig. 2.17*a*), the Kayley tree is a 1-*D* chain, and eq. (2.36) transforms to eq.(2.25). Equation (2.36) yields that for $l \to \infty$ the correlation function $g(l)$ exponentially tends to zero for $p(z-1) < 1$ and diverges for $p(z-1) > 1$. Therefore, an infinite cluster may occur only when $p \geqslant \dfrac{1}{z-1}$ and again we come to the result of eq. (2.35).

From eq. (2.36) one can easily calculate also the correlation length ξ_l in chemical dimensions, i.e. in l-dimensions

$$\xi_l^2 = \frac{\sum_{l=1}^{\infty} l^2 g(l)}{\sum_{l=1}^{\infty} g(l)}. \tag{2.37}$$

Calculating sums in eq. (2.37), one may see that for $p < p_c$

$$\xi_l^2 = p_c \frac{p_c + p}{(p_c - p)^2}. \tag{2.38}$$

So, like in the 1-D case, the critical exponent ν of the correlation radius in the l-dimensions equals 1. Therefore, the average number of elements of a finite cluster on the Kayley tree may be written in the form of the 1-D case

$$S = 1 + \sum_{l=1}^{\infty} g(l). \tag{2.39}$$

Inserting eq. (2.36) into eq. (2.39), we find for $p < p_c$:

$$S = p_c \frac{p_c + p}{p_c - p}. \tag{2.40}$$

This expression generalizes the result (see eq. 2.24) obtained for the 1-D case. Thus, for the Kayley tree, the critical exponent of the mean cluster size $\gamma = 1$.

Even if p is above the percolation threshold $1/(z-1)$, the central site is not always connected to infinity. If, for instance, the central site is occupied and all z of its neighbours are empty, then it does not belong to the infinite network. We define the percolation probability P_∞ as the probability that the central or an arbitrary site belongs to the infinite cluster. Obviously, this probability is zero for p below the percolation threshold, therefore, we calculate it only for $p > 1/(z-1)$. Let us assume that, as in the 1-D case, $n_s(p)$ is the probability that an arbitrary site of the Kayley tree belongs to the s-cluster. There is a simple relation between n_s and P_∞. Each site of the lattice either empty with the 1 p, or occupied and belongs to the infinite cluster with the probability $p(1-P_\infty) = \sum_s s n_s$. This leads to the exact ratio

$$P_\infty = 1 - \frac{1}{p} \sum_{s=1}^{\infty} s n_s. \tag{2.41}$$

We may show that near the percolation threshold the exponent P_∞ increases proportionally to $p - p_c$, and for the Kayley tree the critical exponent of the parameter is in the order of $\beta = 1$ [29, 58].

2.6 Percolation level

Above we have discussed lattice problems of the percolation theory describing the site and bond percolation. The lattice percolation problems are very simple and convenient for both analytical study and computer modelling. However, numerous natural disordered media have no lattice structure and require development of other approaches. In this section we will consider a *model of potentials* or a problem of percolation level.

We will start with a 2-*D* case by defining a chance function $\Psi(X,Y)$ on a coordination plane (X,Y), where X and Y are coordinates. For illustration, we may assume that Ψ denotes a random relief and stands for an altitude above sea level at a point on the earths surface with the given coordinates. We will confine ourselves by the case of a normally distributed random relief. The normal distribution, also known as the Gaussian distribution, plays an important role in many fields of knowledge, especially in the statistical physics. A physical value subjected to the influence of numerous independent factors, which are capable to deviate it positively or negatively with an equal error, regardless of the nature of these random factors, often comply with the normal distribution; therefore, out of all distributions in nature the normal distribution is encountered most often (from this fact one of the names of this probability distribution is derived).

The simplest method of defining the Gaussian chance function $\Psi(X,Y)$ may be described in the following way. Let us consider an area of a plane (X,Y) with a characteristic linear size L. For specificity, let $L = 1$, and our area be a one-unit square. Let us introduce a characteristic scale of the relief details $r_0 \ll L = 1$ and select points randomly distributed over the square with the concentration $n \gtrsim r_0^{-2}$. In every of these points with the coordinates (X_i, Y_i) we will specify the Gaussian distribution of altitudes with the characteristic radius r_0:

$$\Psi_i(X,Y) = h_i \exp\left(- \frac{(X-X_i)^2 + (Y-Y_i)^2}{r_0^2} \right),$$

where the amplitudes h_i have been chosen from the discrete normal distribution with the zero mean and one-unit dispersion. The positive h_i values correspond to the mountains and negative values stand for the depressions. The required function $\Psi(X,Y)$ is defined by the additive composition or simply by the superposition of all the peaks Z_i: $\Psi(X,Y) = \sum_i \Psi_i(X,Y)$. A typical realization of the potential $\Psi(X,Y)$ obtained by means of the above algorithm is shown in Fig. 2.18.

We may introduce a distribution function of the potential Ψ.Let us denote it $f(\Psi)$. According to the definition, the probability that at an arbitrary point of space the function $\Psi(X,Y)$ has a value ranging in a narrow interval from Ψ_1 to $\Psi_1 + d\Psi$ equals $f(\Psi_1)d\Psi$. We may show that the obtained potential $\Psi(X,Y)$ demonstrates the Gaussian distribution in the form:

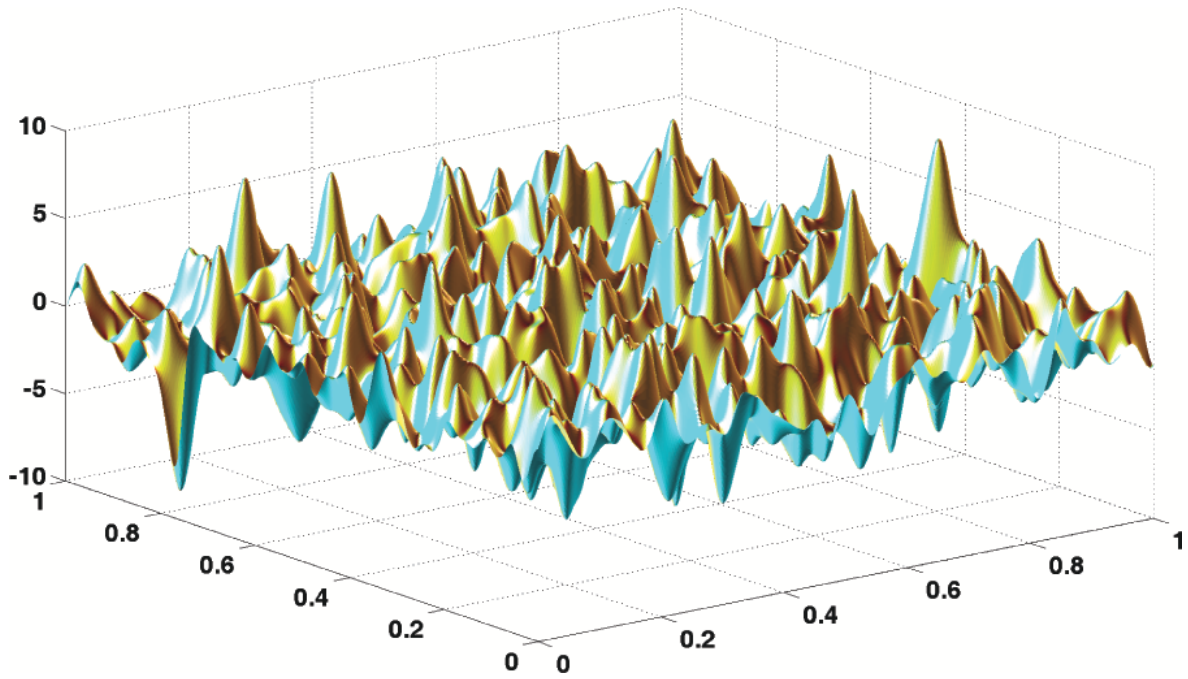

Figure 2.18: Gaussian chance function $\Psi(X,Y)$ on the one-unit square. For construction 5000 Gaussian peaks with the characteristic width $r_0 = 0.02$ have been overlapped

$$f(\Psi) = \frac{1}{\sqrt{2\pi}} \exp\left(-\frac{1}{2}\Psi^2\right). \tag{2.42}$$

being normalized

$$\int_{-\infty}^{\infty} f(\Psi) d\Psi = 1. \tag{2.43}$$

It is obvious that the mean value of $\Psi(X,Y)$ over all points on the plane equals zero.

Let us now construct a reservoir with the bottom relief as illustrated in Fig. 2.18 and the walls formed by vertical planes going through the squares sides. Fig. 2.19 shows the distribution of the same height levels $\Psi(X,Y) = \text{const}$ for our stochastic reservoir. Let us start filling it up with water.

To specify the water level, we have to introduce the exponent χ which changes in the interval from $-\infty$ to ∞. The plane areas in which $\Psi(X,Y) < \chi$ we will colour in blue (filled with water), and the areas where $\Psi(X,Y) > \chi$ will be marked in yellow (protruding above the water level). The fraction of the water surface increases with the water level rise. In Fig. 2.20 the lakes (blue areas) have no connection with each other yet.

Then the water level is raised higher; and in Fig. 2.21 water paths have already occurred that traverse the entire system. We may note, that in Fig. 2.21 there exist simultaneously the land

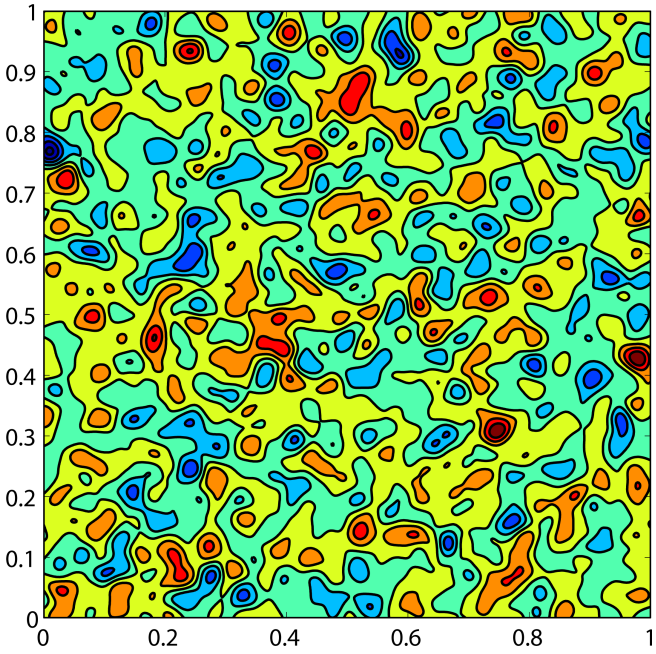

Figure 2.19: Distribution of equipotential levels for a random potential

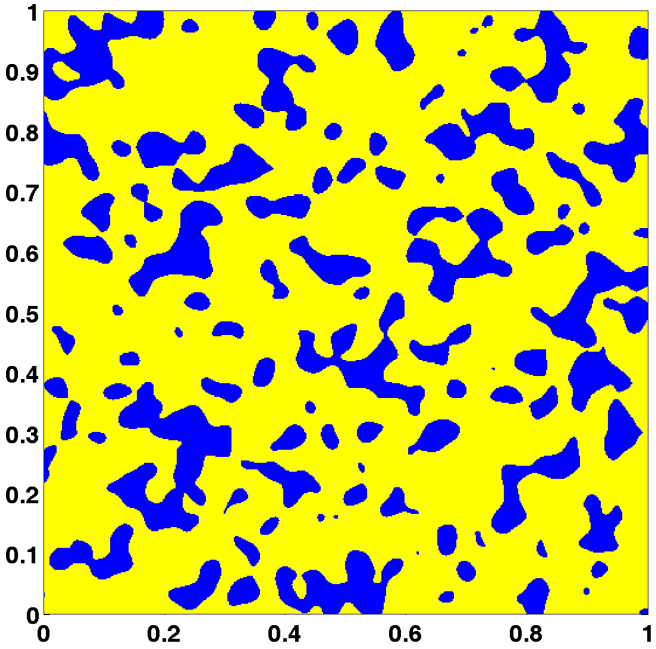

Figure 2.20: Map of the reservoir at the level of filling $h = -1$. The areas filled up with water is coloured in blue

and water paths connecting the opposite sides of the model system.

Finally, the level of filling has reached $h = 1$, and in Fig. 2.22 only discrete mountain peaks rise above the water level.

Thus, in the percolation level problem we are interested in the question: Up to what level

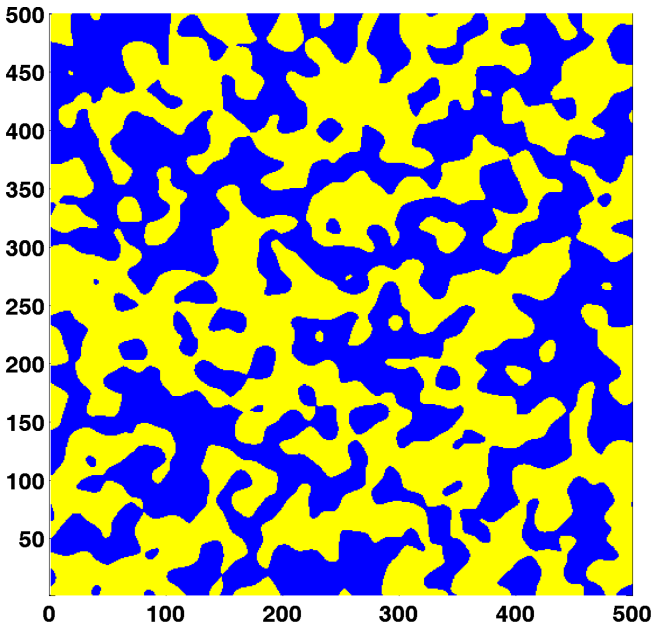

Figure 2.21: Map of the reservoir at the level of filling $h = 0$. The areas filled up with water is coloured in blue

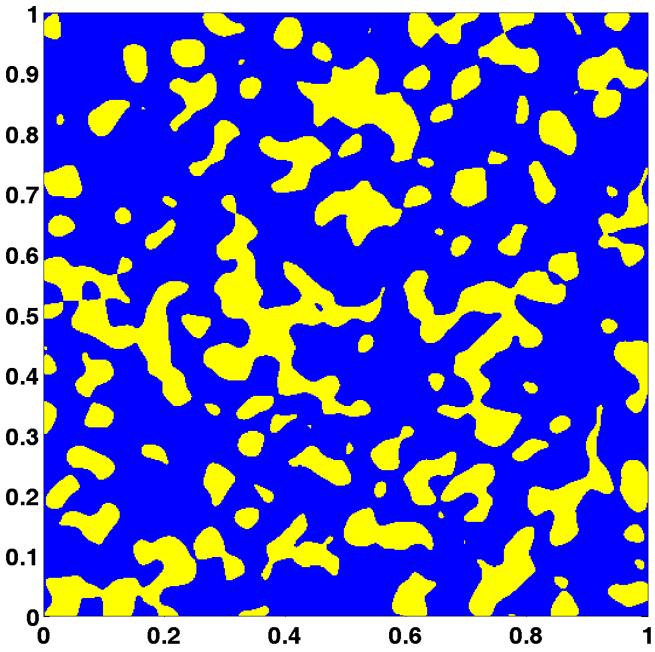

Figure 2.22: Map of the reservoir at the level of filling $h = 1$. The areas filled up with water is coloured in blue

must fall or rise water in our reservoir for a water path connecting its opposite sides to disappear or occur? It is clear that such a path exists until a certain number of passes of an arbitrary relief $\Psi(X,Y)$ come out of the water, after that it disappears. The water level at which a water path occurs (or disappears) is called the percolation level. The problem of its determination represents a 2-D problem of the percolation theory.

Figures 2.20, 2.21 and 2.22 suggest that the percolation level problem may be formulated in other way. Let us assume that the plane is chaotically painted with the yellow and blue colours. The characteristic correlation radius of the spots $r_0$is much smaller than the size of the system $r_0 \ll L$. Let the fraction of the area coloured in blue be p. When the p-values are small, the blue fragments form isolated lakes, while at the p-values close to one, isolated are the yellow islands. At the critical value $p = p_c$ the path crossing the entire system only through the blue (or only yellow) areas disappears or occurs.

Contrary to the lattice problems, the above statement is a typical example of the so called continuum percolation [63]. A 2-*D* problem is exactly solved if the properties of a random function $\Psi(X,Y)$ are, in average, symmetrical relatively to $\Psi = 0$. Such properties, in particular, are attributed to the Gaussians. It is obvious, that beside the percolation level of the blue areas, the percolation level of the yellow areas may be determined as well. From the symmetry of the function $\Psi(X,Y)$ it follows that $\chi_c = -\chi_c^{'}$. Indeed, let us change the function $\Psi(X,Y)$ in every point of the plane (X,Y) by $-\Psi(X,Y)$. By doing this, we get the function $\Psi(X,Y)^{'} = -\Psi(X,Y)$ that, in average, possess the same properties, so that the percolation levels calculated with its help must be the same as those calculated by means of the initial function. From the inequation $\Psi(X,Y) < \chi_c$ it follows that $\Psi(X,Y) > -\chi_c$ meaning that $\Psi(X,Y)^{'} > -\chi_c$. For $\chi = \chi_c$, in case of the function $\Psi(X,Y)$, the blue areas $\Psi(X,Y) < \chi_c$) form an infinite cluster. The same areas become yellow if we consider the function $\Psi(X,Y)^{'}$ and $\chi = -\chi_c$, because in this case $\Psi(X,Y)^{'} > -\chi_c$. Thus, the value $\chi = -\chi_c$ is the percolation level of yellow areas for the function $\Psi(X,Y)^{'}$. But, as we have already mentioned, the percolation levels of the functions $\Psi(X,Y)$ and $\Psi(X,Y)^{'}$ must be the same. Then, the percolation level of the yellow areas $\chi_c^{'} = -\chi_c$ is valid for the function $\Psi(X,Y)$ as well.

If $\chi_c < 0$, with the increase of χ first the percolation through the blue areas occurs (for $\chi = \chi_c < 0$), and then (for $\chi = -\chi_c > 0$) the percolation through the yellow areas disappears. Within the range $\chi_c < \chi < -\chi_c < 0$ the percolation takes place through both the blue and yellow areas. If $\chi_c > 0$, first the percolation through the blue areas disappears, and then the percolation through the blue areas occurs. And within the range $-\chi_c < \chi < \chi_c < 0$ there is no percolation at all. In the case of a 2-*D* problem the percolation through the yellow areas excludes the percolation of the blue areas, and vice versa. Indeed, if one can cross the system on a boat from the east to the west, then the land trip from the north to the south is impossible, and the case when $\chi_c < 0$ is excluded. On the other hand, the non-existence of the blue area percolation means that necessarily there is the yellow area percolation from the north to the south. (One may see it in Figures 2.20, 2.21 and 2.22). Thus, the case when $\chi_c > 0$ is also excluded, leaving the only one possibility $\chi_c = 0$. We have received an important result: in the 2-*D* case the percolation level is equal to zero.

We may speak also about the critical occupation probability or critical fraction of the surface p_c filled up by the blue areas at the moment of the 2-*D* percolation onset. This fraction equals the probability that the continuous arbitrary exponent Ψ lies in the interval $-\infty < \Psi(X,Y) < \chi_c$. By the implications of the distribution function

$$p_c = \int_{-\infty}^{\chi_c} \Psi(X,Y) dX dY. \tag{2.44}$$

With the help of formula (2.44) the surface critical fraction p_c can be calculated. From the conditions of the distribution function normalization (see (2.43)) it follows that at $\chi_c = \infty$ the right hand side of eq. (2.44) is equal to one. From the symmetry of the function $\Psi(X,Y)$ it follows that for $\chi_c = 0$ the surface fraction $p_c = 0.5$.

Similarly, we may formulate a 3-*D* problem filling up the volume with yellow and blue substances (see Fig. 2.23).Then the fraction of the volume filled up with one of the substances is to be changed until it reaches the state of percolation. Now we will define a 3-*D* distribution of the random potential. Let us consider a one-unit cube in the 3-*D* space (X,Y,Z) and, assuming that the characteristic scale of the relief $r_0 \ll L = 1$, choose $N \simeq r_0^{-3}$ points with the coordinates (X_i,Y_i,Z_i) randomly and equally spaced in it. In every of these points we define the Gaussian distribution of the potential peaks with the characteristic radius r_0:

$$\Psi_i(X,Y,Z) = \psi_i \exp\left(- \frac{(X-X_i)^2 + (Y-Y_i)^2 + (Z-Z_i)^2}{r_0^2} \right),$$

where the amplitudes ψ_i have been chosen from the discrete normal distribution with the zero mean and one-unit dispersion. The required function $\Psi(X,Y,Z)$ is defined by the additive composition of all the peaks Ψ_i: $\Psi(X,Y,Z) = \sum_i \Psi_i(X,Y,Z)$. The result of work of this simple algorithm is presented in Fig. 2.23.

The percolation level in a 3-*D* case is denoted by the critical value $\Psi = \Psi_c$ at which the blue areas form paths that run through the entire system. We may also speak about the critical fraction of the space p_c filled up with the blue areas at the moment of the percolation onset. This fraction equals the probability that the continuous arbitrary exponent Ψ lies in the interval $-\infty < \Psi(X,Y,Z) < \Psi_c$. By the implications of the distribution function

$$p_c = \int_{-\infty}^{\Psi_c} \Psi(X,Y,Z) dX dY dZ. \tag{2.45}$$

Formula (2.45) ties up the critical fraction of space p_c with the percolation level.

Calculations made by means of the Monte Carlo method for the Gaussian chance functions reveal that for the 3-*D* case $p_c = 0.16 \pm 0.01$.

2.7 Problem of discs

Now we will consider a slightly different off-lattice percolation problem. Let us assume that equal discs of radius R are randomly (i.e. chaotically and in average evenly) distributed on a plane. In other words, both coordinates of the discs centres are defined by random numbers uniformly distributed in the interval from zero to L, where L is a very large (as compared

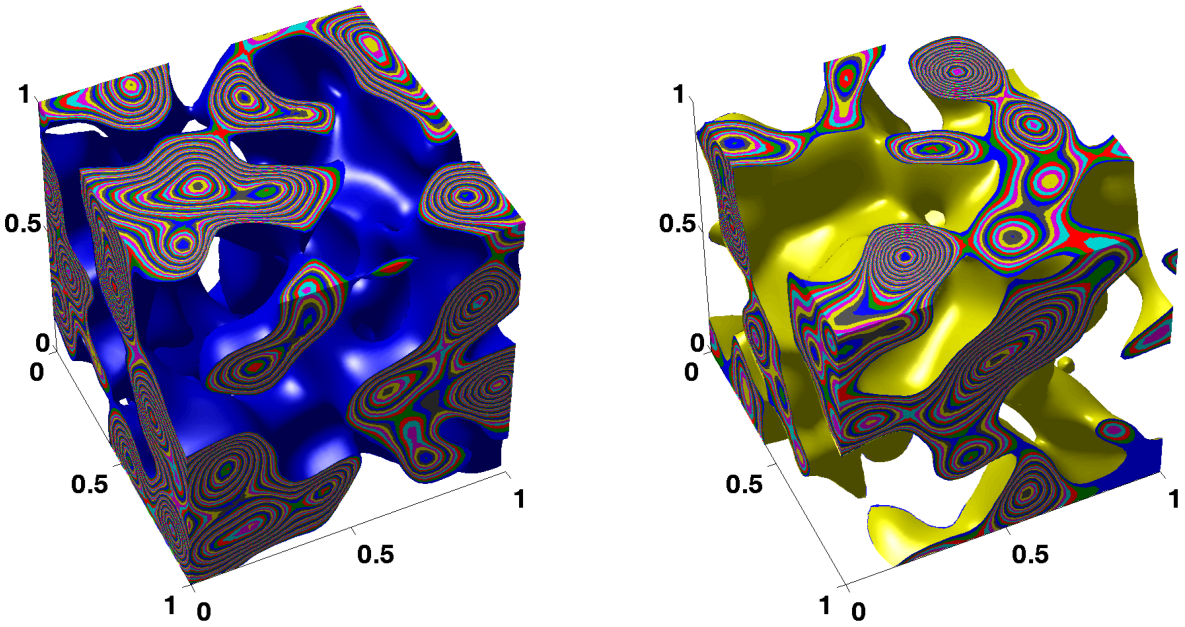

Figure 2.23: Illustration of the 3-*D* Gaussian potential. In the left block the areas of space with the potential below the fixed level $\Psi(X,Y,Z) < 0.001$ are marked in blue. In the right block the areas of space with the potential above the fixed level $\Psi(X,Y,Z) > 0.001$ are marked in yellow

with R) length characterizing the size of the system concerned. An important feature of the problem is that the discs may overlap with one another to any extent. The mean number of the centres of the discs per unit area (discs centres concentration) equals n.

Two discs are considered connected, if they have common points, i.e. overlap. If the disc A is connected to the disc B, and the disc B is connected to the disc C, then A is connected to C. Thus, remote discs may be connected by a chain of overlapping discs (Fig. 2.24). Our task is to find the critical concentration n which leads to the percolation through the connected discs, i.e. to the onset of paths running through the entire system and consisting of the overlapping discs. (In other words, there occurs an infinite cluster of connected discs. In Fig. 2.24 the maximum cluster of the overlapping discs is marked in red).

Generally speaking, only two parameters the concentration n and the radius R have been introduces in to the problem. (Though there is also the size of the system L, it is clear that if the system is large enough, the critical value n depends little on L). Meanwhile, it is easy to see that the absence or presence of the percolation depends just on one parameter, which is the average number of disc centres located within one disc. It is equal to:

$$B = \pi n R^2.$$

One may most easily ascertain that the percolation appears at a certain B-value and does not depend on the values n and R in the following way. Suppose there is a plane with drawn circles. Let us enlarge the picture several times, for example, with the help of a projector.

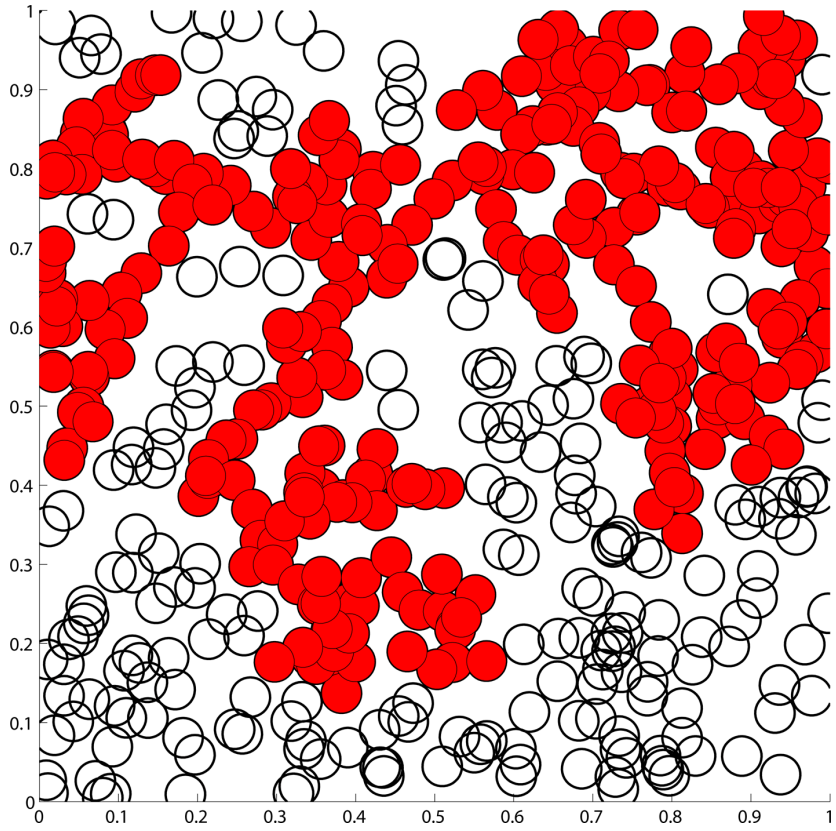

Figure 2.24: Continuum percolation of the randomly distributed discs

Altering n and R, this transformation does not change B, since the average number of the circles centres in a circle does not change with magnification. It is also easy to understand that this transformation has no effect on the percolation. If there was no percolation in the initial image, than it is absent in the magnified one, and vice versa, if the percolation through the overlapped circles existed in the initial image, it would not disappear after magnification.

Thus, the magnification, that changes n and R, but not B, does not control the percolation. Therefore, the presence or absence of the percolation in the system depends only on the B-value. At the large B-values the percolation exists, and at the small values of this parameter there is no percolation.

The problem has thus formulated is called a problem of discs. Its three-dimensional analogue is called a problem of spheres and can be formulated as follows. In a three-dimensional space the coordinates of the centres of R-radius spheres are defined with the help of a random-number generator. Two crossing spheres are considered to be connected. The task is to define the critical concentration of the centres that leads to the sphere percolation[†].

[†]There is an alternative formulation of the problem of spheres (discs): two spheres (discs) are considered to be connected, if the centre of one of them is located within the other. Such spheres (discs) sometimes are called encompassing. The formulation given in the text has become alternative when a sphere's (discs) radius is doubled. In this case, the critical B-value increases as much as 2^d times, where d is the Euclidean dimension of the encompassing space.

It is easy to understand that alike the 2-*D* case the percolation is controlled only by the parameter, which is the average number of sphere centres within one sphere:

$$B = \frac{4\pi}{3} nR^3,$$

where n is the average number of spheres centres per unit volume. The problem of spheres is important for the theory of electrical conductivity of semiconductors at low temperatures. Therefore, many authors have investigated the problem by a number of various methods. According the latest data, the critical value of B_c at which the sphere percolation occurs is equal to 0.34 ± 0.01. The problem of discs has been investigated by physicists less intensively, and the results presented by different authors vary considerably. Publication [60] gives for the 2-*D* case $B_c = 1 \pm 0.1$.

2.8 Gradient percolation

Let us assume that the concentration p of the occupied sites in a square lattice changes linearly from zero to one with the vertical distance (Fig. 2.25). This case is known as the gradient percolation [64, 65].

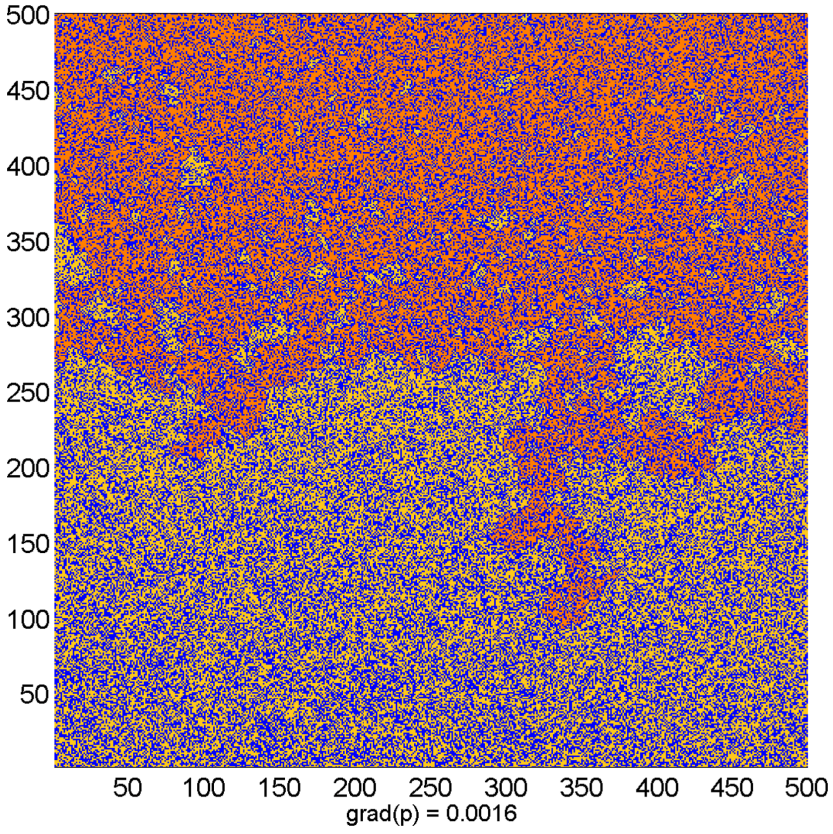

Figure 2.25: Gradient percolation

Employing the commonly used terms, we will call the lattice area occupied by the maximum cluster the "land" (white pixels in Fig. 2.25), and the area of connected empty sites not surrounded by the land the sea". Clusters of the occupied sites that are not connected with the land are called "islands" (grey pixels in Fig. 2.25), the groups of connected empty sites surrounded by the land are called "lakes". The seashore - the line between the sea and the land has a fractal structure and is called "diffusion front". The average position of the front $z = z_c$ corresponds to the percolation threshold: $p(z_c) = p_c$. In a 2-*D* site percolation problem $p_c \approx 0.59 > 1/2$, and we have two diffusion fronts for $p = p_c$ and $p = 1 - p_c$, respectively (see Fig. 2.26).

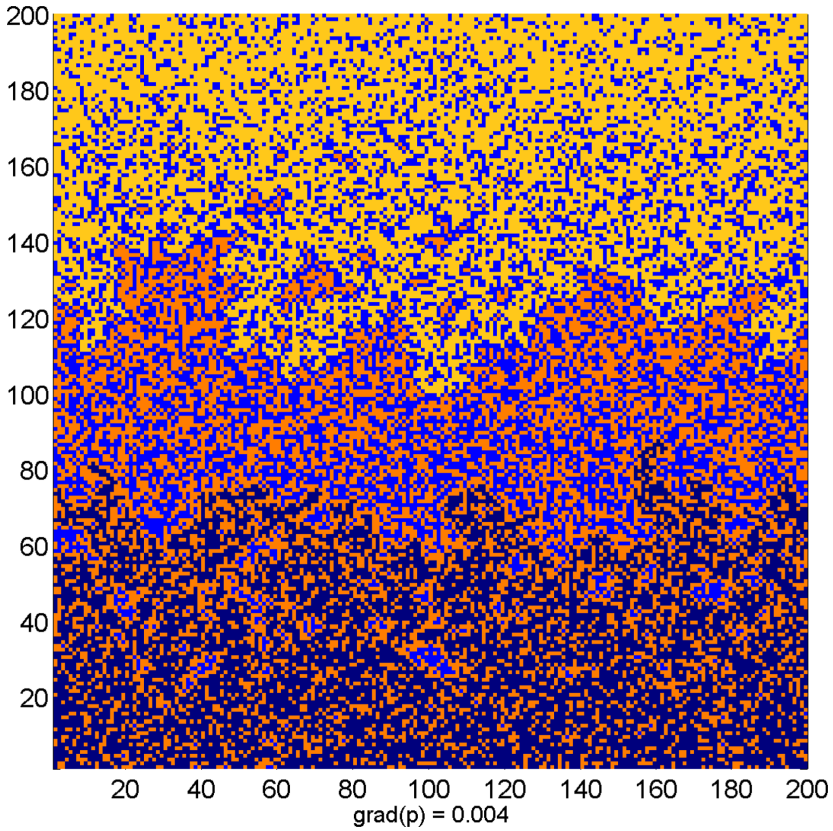

Figure 2.26: Gradient percolation. The yellow pixels denote the maximum cluster of the occupied sites, the dark-blue pixels represent the maximum cluster of the empty sites

The diffusion front is characterized by its average width h_f, which can be related to the concentration gradient near $p = p_c$. In Fig. 2.25 we can see that the lakes and islands are infinitesimally small away from the front; on the other hand, close to the front their sizes are commensurable with the width h_f.The islands correspond to the final clusters of the percolation system, while the lakes - to the isolated holes. With the approach to the front, both, the islands and lakes increase as a correlation length according to eq. (2.4). However, because of the finite gradient $\bigtriangledown p$, their sizes remain finite even at $p = p_c$, and their maximum size does not exceed the front width h_f, which is the only characteristic length scale in the problem. Thus, we may assume that

$$h_f \simeq R_c(z_c \pm h_f). \tag{2.46}$$

This assumption expresses our observation that the clusters near the front have the size comparable with the width of the front. Using eq. (2.46) and expanding $p(z)$ in a Taylor series around $z = z_c$ we obtain

$$h_f \simeq |p(z_c \pm h_f) - p_c|^{-\nu} \simeq \left| h_f \frac{dp}{dz}(z_c) \right|^{-\nu},$$

which gives

$$h_f \simeq \left| \frac{dp}{dz}(z_c) \right|^{-\beta_f}, \tag{2.47}$$

where

$$\beta_f = \frac{\nu}{1+\nu}. \tag{2.48}$$

From expression (2.47) it follows that the diffusion front width h_f increases with the decrease of the critical parameter gradient. Since the percolation is a critical phenomenon, the front structure is also demonstrates universality - the exponent β_f depends only on the dimensions of the lattice and not on the particular lattice structure (square, triangular, etc.).

In a 2-*D* site percolation problem $p_c \approx 0.59 > 1/2$, and we have two diffusion fronts for $p = p_c$ and $p = 1 - p_c$, respectively (see Fig. 2.26).

2.9 Directed percolation

In section 2.1 we have discussed the percolation occurrence at the increase of the structural elements concentration p and have defined the percolation transition as the onset of an infinite cluster of occupied sites. Let us consider now a dynamic percolation model. We advert to a site problem and assume that if at a given moment of time a site is excited, then at the next (discrete) moment of time it returns to its initial quiescent state, but, by doing it, it can excite its nearest neighbours in the lattice with a probability p. As a result a stochastic process occurs resembling the spreading of infection (Fig. 2.27). The colour of infected elements in Fig. 2.27 changes to the cold tones with time unit from the moment of their infection. The yellow pixels on the periphery stand for the newly infected elements. It is clear, that when the probability of excitation transmission is very small, the number of excited elements decreases with time. And vice versa, when the probability of excitation transmission is close to one, the number of excited elements on the lattice infinitely increases with time.

The critical value of the probability p_c of the excitement transmission, at which a finite probability for the epidemic to start from a single infected element, corresponds to the percolation

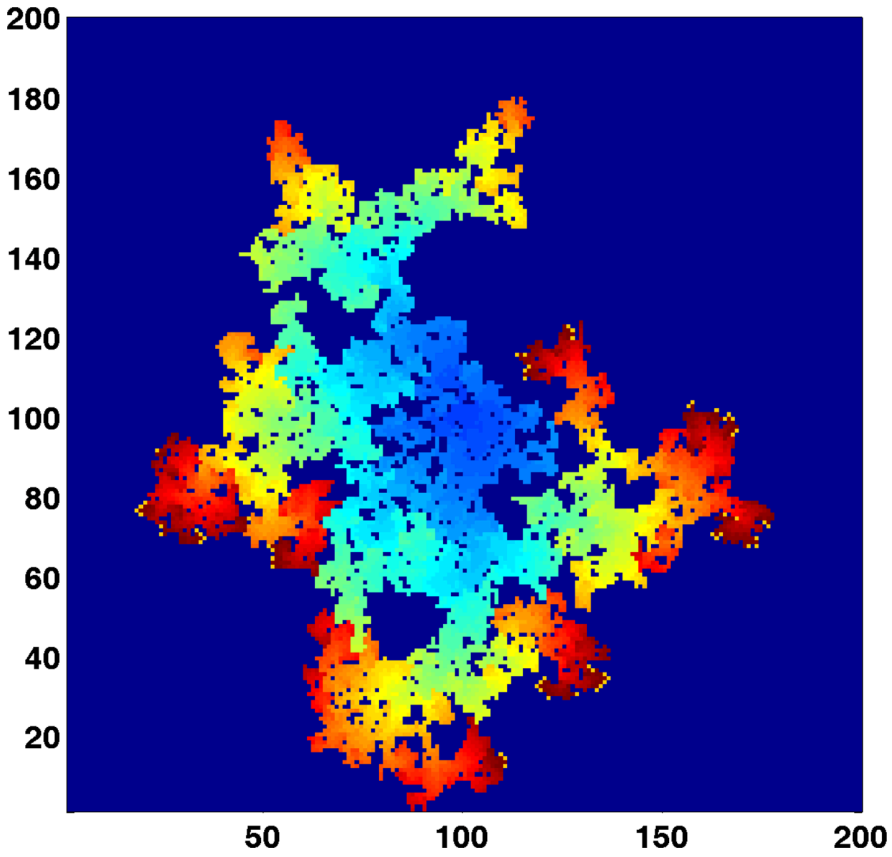

Figure 2.27: Epidemic spreading from a single infected element at the initial moment with the infection transmission probability close to critical. The change of pixel colouring corresponds to the time passed from the moment of the infection contraction. The bright pixels on the periphery belong to the epidemic front

threshold. Note that at any fixed moment of the excitement evolution, elements of the epidemic front are away from its source at the same chemical distance, and the corresponding pixels in Fig. 2.27 are marked in the same colour. Thus, the internal structure of the spreading epidemic pattern for the probability of excitement transmission close to critical is alike the discussed in section 2.3 chemical structure of the percolating cluster near the percolation threshold (Fig. 2.14).

As for other problems of the percolation theory, the value of the directed percolation threshold depends largely on the number of nearest neighbours in a given lattice, i.e. from the coordination number z. The larger the number of the elements contacting the infected element the higher the probability of infection spreading. The coordination number increases with the increase of the lattice scale. For large coordination numbers the percolation threshold can be calculated with the use of a mean field approximation. Let the number of excited elements at a fixed moment of time t be q_t. If the number of the nearest neighbours z of an element is large, we may consider that among its neighbours at time t there were zq_t excited elements. The given element may be infected at the next $(t+1)$ moment of time with the probability

$$1-(1-p)^{zq_t}, \tag{2.49}$$

because we assume independence of the infection transmission via the nearest neighbours. The probability (2.49) defines the fraction of the excited elements at the following $(t+1)$ moment of time, i.e.

$$q_{t+1} = 1-(1-p)^{zq_t}. \tag{2.50}$$

The value q_t above the percolation threshold must tend to the finite limit $\lim_{t\to\infty} q_t = \tilde{q}$, which defines the fraction of the excited elements in the settled mode, while below the percolation threshold $\lim_{t\to\infty} q_t = 0$. Studying point expression (2.50) it is easy to find out that its attractors may be only stationary points, and the lost of steadiness of the stationary point $q = 0$ followed by the appearance of a new steady stationary point $q = \tilde{q}$ takes place when the probability p crosses the value p, which meets the condition

$$1-p_c = \lim_{\tilde{q}\to 0}(1-\tilde{q})^{\frac{1}{z\tilde{q}}} = \exp(-\frac{1}{z}). \tag{2.51}$$

Thus, the percolation threshold is determined by the relationship

$$p_c = 1-\exp(-\frac{1}{z}) = \frac{1}{z}-\frac{1}{2z^2}+\ldots. \tag{2.52}$$

For small coordination numbers the mean field approximation is invalid. In this case fluctuation effects have become significant.

Chapter 3

APPLICATION OF FRACTAL GEOMETRY *and* PERCOLATION THEORY

3.1 Fractal time series

In terms of practical application the fractal time series are an important special case of fractal objects. The examples of these time series are coordinates of a particle in a Brownian motion or time dependence of the integral result of the coin tossing game (see section 1.4). As it was mentioned in section 1.4, such objects are statistically self-affine.

In general, a time curve of any value makes formally possible to calculate its fractal dimension by means of a box-counting method. However, it will depend on relative scale of axes. The self-affine sets are characterized by local and global values of fractal dimension.

The time series self-similarity can be analysed by other methods as well. A R/S method which is also called a standardized range method is used most often [27]. This method was presented by Benoît Mandelbrot who used the results of the research performed by British hydrologist Harold Hurst. It is based on the measurement of the range of a random variable (the maximum and minimum values on the section being studied) and its mean-square deviation.

Suppose we have a sequence of measurements of any value $\xi(t)$. Then the average value in time τ is equal to

$$\langle \xi \rangle_\tau = \frac{1}{\tau} \sum_{t=0}^{\tau} \xi(t),$$

and the *accumulated deviation* from the average is equal to

$$X(t,\tau) = \sum_{k=0}^{t \leqslant \tau} (\xi(k) - \langle \xi \rangle_\tau),$$

Let us call the difference between the maximum and minimum values of the accumulated deviation X a *range*:

$$R(\tau) = \max X(t,\tau) - \min X(t,\tau).$$

Let us compute the standard deviation (as a square root of the dispersion) for the signal $\xi(t)$ being studied:

$$\langle \xi \rangle_\tau = \left(\frac{1}{\tau} \sum_{t=0}^{\tau} (\xi(t) - \langle \xi \rangle_\tau)^2 \right)^{\frac{1}{2}}.$$

Normalization of R to the standard deviation S makes the rescaled range R/S. If the process duration is equal to T then there are $T-\tau+1$ ways to chose the cluster or to make τ- long fragmentation. The procedure described above is to be used for each fragmentation. Then the obtained values need to be averaged over the set of results. We may also consider T value as a cluster size in the random process analysis.

Studying the long-range dynamics of the Nile floods H. Hurst experimentally showed that the observed standardized range R/S can be described by the following empirical relation

$$\frac{R}{S} \sim \tau^{Hu}, \tag{3.1}$$

where Hu - is the Hurst exponent, and $Hu \neq 0,5$.

This is an interesting fact, since in the absence of a long-term statistical relation the R/S ratio demonstrates the asymptotic behaviour $R/S \sim \tau^{1/2}$ if the time series of changes is generated by a random process with independent increments and finite variance.

Later it turned out that many other natural phenomena could be described by this law. It is possible to use the standardized range method or the Hurst method for analysing time series of measurements of such values as temperature, river run-off, amount of precipitation, tree-ring thickness or sea wave height.

The value Hu exceeding 0.5 indicates a time series with a long-term steady tendency (persistence). Positive increments in the past i.e. the increase of the values of the process $\xi(t)$ means that the further increasing on average is anticipated. Therefore, the increasing trend in the past will continue in future in the process with $0,5 < Hu < 1$. And vice-versa, a decreasing trend in the past on the average leads to the same trend in future. The greater is the value Hu the stronger is the tendency.

The value $Hu = 0,5$ indicates that the past and the future increments of the process are not correlated at any time scale, which is true for a random process with independent increments.

The range is antipersistent at $0 < Hu < 0,5$. In this case the increase in the past means the decrease in future and the decreasing trend in the past makes the future increase probable. And the less is the Hu value the higher is the probability. Usually, in such processes the increase is followed by a subsequent de-crease, and then after the decrease again comes an increase. The breaks in the $R/S(\tau)$ relationship correspond to the typical time scales and / or periodic behaviour.

The Hurst exponent concept quite easily defines a generic Brownian motion as a random process in which in eq. (3.1) $0 < Hu < 1$ [Feder, 1991, p.170]. For a regular Brownian motion $Hu = 0.5$. There are other definitions as well: a random process with $Hu = 0.5$ is called brown noise, persistent one is called pink noise, antipersistent black noise.

The one-dimensional realization of the described process (see section D of the Appendix) is

given in Fig. 3.1 for three different values of the Hurst index. It is obvious that the Hurst index decrease leads to the increasing number of sharp swings in the behaviour of the random process.

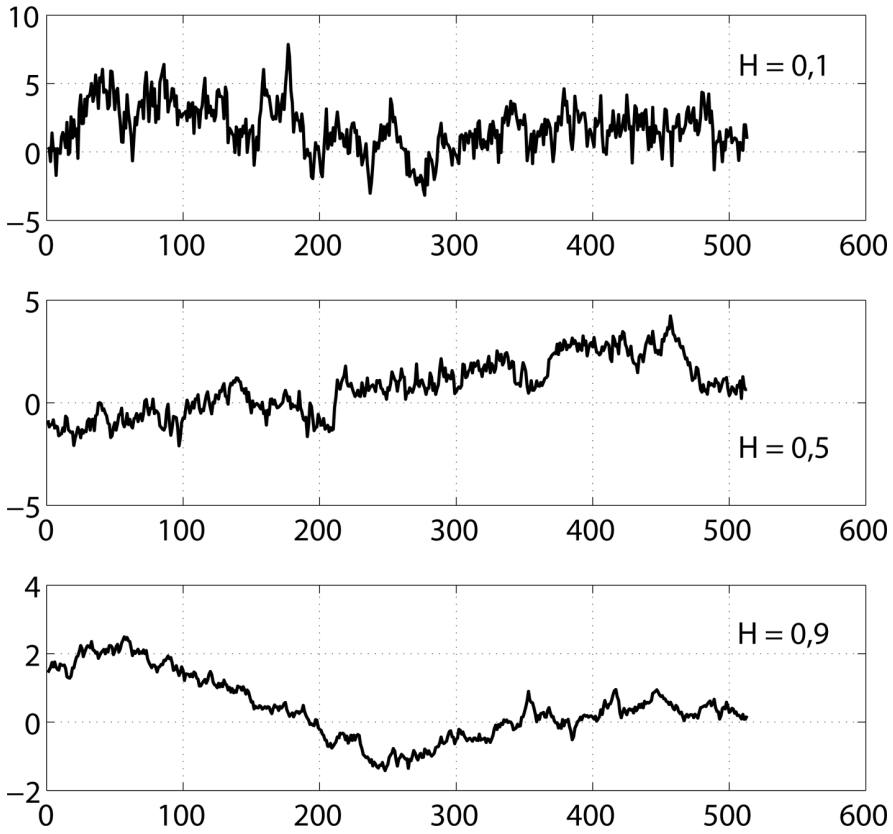

Figure 3.1: Realization of the generic Brownian processes for different values of the Hurst index

The Hurst index relates to the fractal dimension (local dimension) as $D = E - Hu$, where E is the Euclidean dimension of a problem. For the Brownian curve $D = 2 - 0.5 = 1.5$. There are other methods to calculate the Hurts index, which may appear to be more efficient in some cases: with the help of a power spectrum, by return time method. Particularly, for the self-affine time series the power spectrum value β and the Hurst index Hu are related as

$$\beta \approx 2Hu + 1 \quad \text{at} \quad 1 < \beta < 3. \tag{3.2}$$

Table 3.1gives the values of the Hurst index and fractal characteristics for different types of noise.

Note also that the noise integrating also results in a random process (noise) with the power spectrum value greater then the initial noise by 2. For example, the white noise integrating leads to the random process that is of a non-persistent (generic) Brownian motion type.

Table 3.1: Relation between the characteristics of the Generic Brownian motion (GBM)

Power spectrum value, β	Hurst index, Hu	Fractal dimension, D	Description
$\beta = 0$	—	$D = 2$	White noise
$0 < \beta < 1$	—	$D = 2$	Color noise
$\beta = 1$	$Hu = 1$	$D = 2$	$1/f$ - noise
$1 < \beta < 2$	$0 < Hu < 0.5$	$1.5 < D < 2$	Antipersistent GBM
$\beta = 2$	$Hu = 0.5$	$D = 1.5$	Brownian motion
$2 < \beta < 3$	$0.5 < Hu < 1$	$1 < D < 1.5$	Persistent GBM

3.2 Fractal surfaces

An engineering practice often deals with different surfaces or surface properties in a wide spectrum of con-texts. In some cases developing a surface with certain physical or chemical properties is the main objective. But, usually, surfaces appear as an integral result of certain industrial and natural processes. There are three types of surface forming processes:

1. Processes in which the surface growth is caused by substance flows. Examples include crystal growth, deposition of an atom beam or chemical vapours, sedimentation, electroplating, sputtering, growth of biological organisms such as bacterial colonies or tumours.

2. Processes in which materials dissolve or are removed from the surface. Examples are chemical dissolution, corrosion, erosion, deflation, grinding and polishing.

3. Processes that lead to the spontaneous formation of surface and interfaces. Examples include cracking and destruction, burning and flame propagation, turbulence, wetting, absorption, invasion and formation of phase transition boundaries between different aggregate states of a substance.

Similarity and importance of these processes make the development of effective approaches for describing surface structures and their dynamics highly demanded today. Recently, a significant progress in under-standing the surface phenomena has been made due to the use of ideas of the fractal geometry [12] and development of the theory of dynamical scaling [49, 66]. The dynamical scaling has become a standard method for characterizing and quantitative analysis of morphology and development of surfaces and inter-faces. This method is used in both theoretical and experimental (including modelling) researches of surfaces.

Let us consider a fractal surface formation with the help of a 3-*D* Brownian motion model. The generated surface behaves like a mountain landscape which can be modelled by a spatial distribution called a generalized Brownian distribution. Fig. 3.2 shows a typical Brownian surface on a plane model lattice. We use a two-dimensional version of the Voss algorithm to

synthesize a Brownian landscape over the plane square lattice [27, 67].

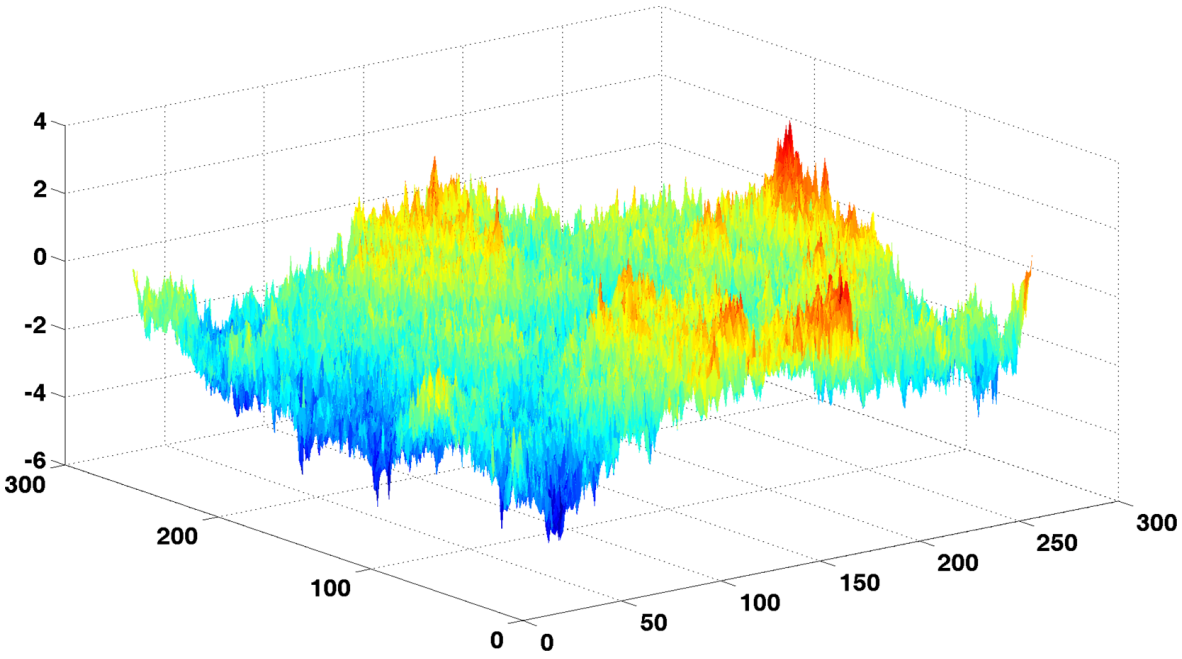

Figure 3.2: Brownian surface generation on the 257×257 square lattice

The coordinates of the model lattice cells are specified by two integers ranging from 1 to $N = 2^n + 1$, where n is a fixed value. In the numerical simulation the linear dimensions of a model squire constituted $N = 129$ at $n = 7$. At the first step let us assign random numbers normalized to 0-mean and 1-dispersion to the cells at the vertexes of the model field with the coordinates $(1,1)$; $(1,N)$; $(N,1)$; (N,N). The h-values in five cells with the coordinates $(1, 2^{n-1}+1)$; $(2^{n-1}+1, 1)$; $(2^{n-1}+1, N)$; $(N, 2^{n-1}+1)$; $(2^{n-1}+1, 2^{n-1}+1)$ containing the midpoints of the sides and the centre of the initial squire are calculated by the proportional parts method. For example, the h-value equal to the arithmetic mean of the h-values at the vertexes: $h(2^{n-1}+1, 2^{n-1}+1) = \frac{1}{2}(h(1,1) + \ldots + h(N,N))$ is assigned to the central cell.

The cells at the vertexes of the model squire and the above-mentioned five cells, containing the midpoints of its sides and the centre, form a lattice of four identical squires of $2^{n-1}+1$ linear size. At the next step all h-values of the nine lattice vertices are incremented by random numbers of zero mean and reduced dispersion $\sigma_2^2 = (1/2)^{2Hu}\sigma_1^2$ selected from the normal distribution, where Hu is any real number from the interval $0 < Hu < 1$. Then the h-values of the cells containing the midpoints of the sides and the centre of each new squire are interpolated again. At the k-step of the procedure the values of $(2k-1)^2$ vertices of the intermediate superlattice are incremented by random numbers of zero mean and dispersion $\sigma_k^2 = (1/2)^{2Hk}\sigma_1^2$ selected from the normal distribution. The procedure ends when all N^2 cells of the initial model lattice are filled with the random numbers. The total number of steps is equal to $2^{n-1}+1$. The surface generated in this way is characterized by a spatial increase of the potential distribution variance. In this case $Hu = 0.5$ conforms to the potential Brownian surface pattern and the Hu values differing from 0.5 correspond to the generalized Brownian surface.

Figures 3.3 and 3.4 show persistent ($Hu = 1$) and antipersistent ($Hu = 0$) potential surfaces respectively.

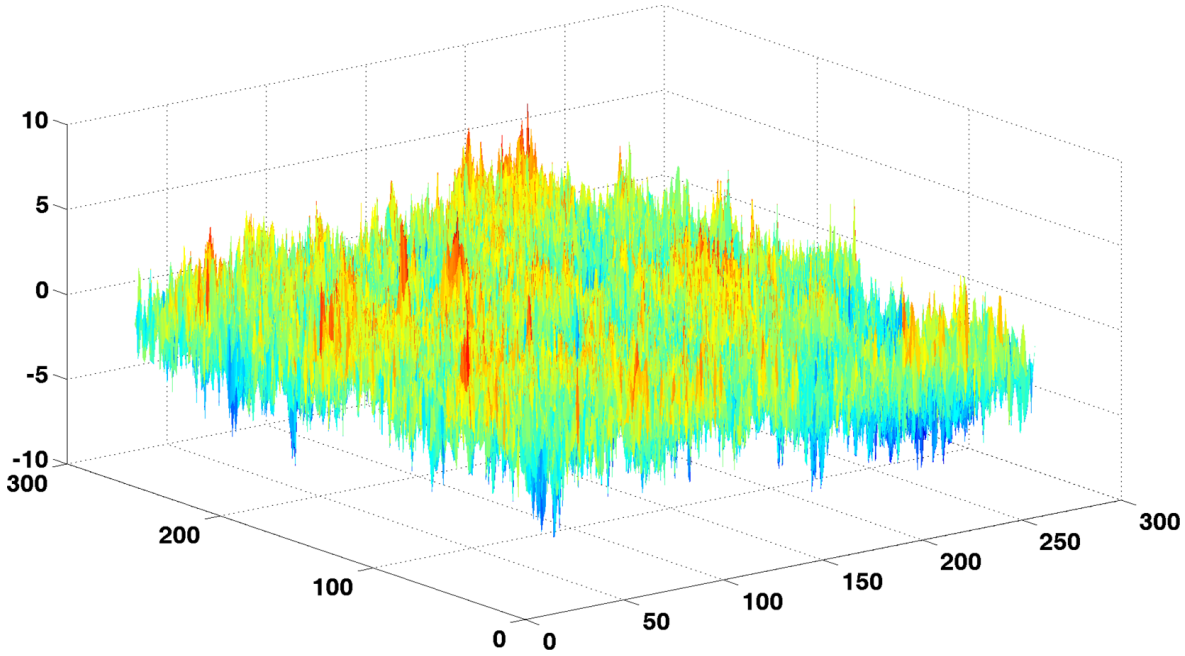

Figure 3.3: Brownian surface generation on the 257×257 square lattice with $Hu = 0.01$

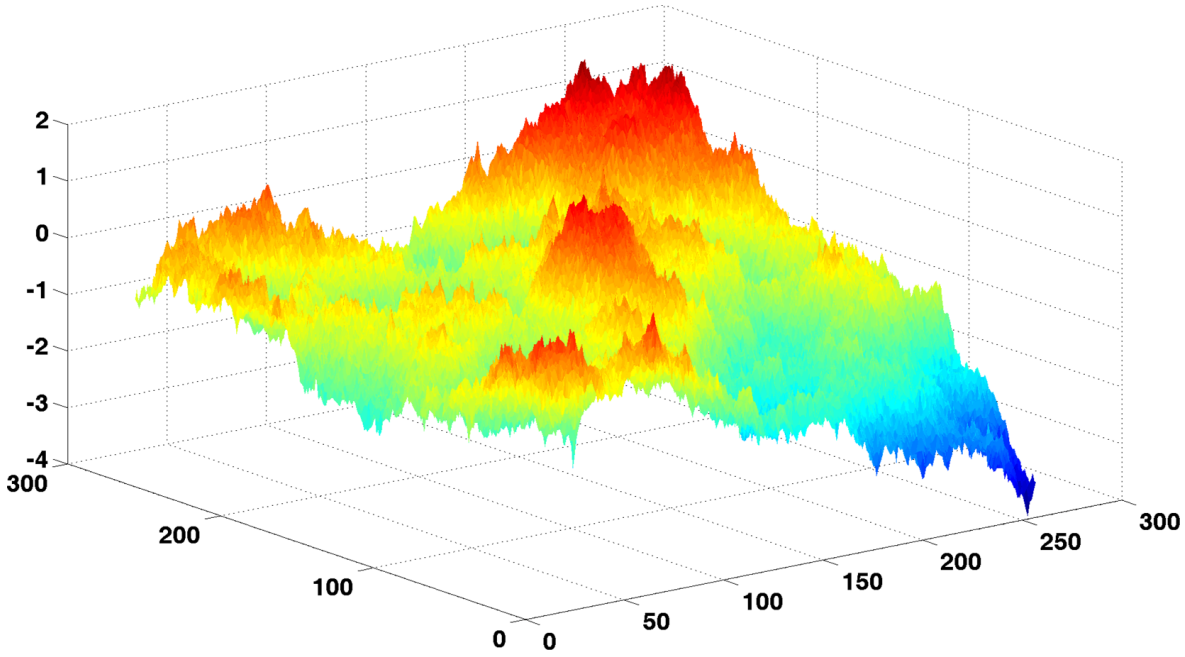

Figure 3.4: Brownian surface generation on the 257×257 square lattice with $Hu = 1$

Section D of the Appendix presents the code of a two-dimensional version of the Voss algorithm which graphical realization is given in Figures 3.2, 3.3 and 3.4.

The equipotential surfaces on the $65 \times 65 \times 65$ cubic lattice for the values $Hu = 0$ $Hu = 1$ $Hu = 0.5$ given in Figures 3.5, 3.6, 3.7 represent a three-dimensional case of the Voss

algorithm. A quasi-electrostatic distribution of the charged aerosol electric potential serves a clear example of the Brownian distribution.

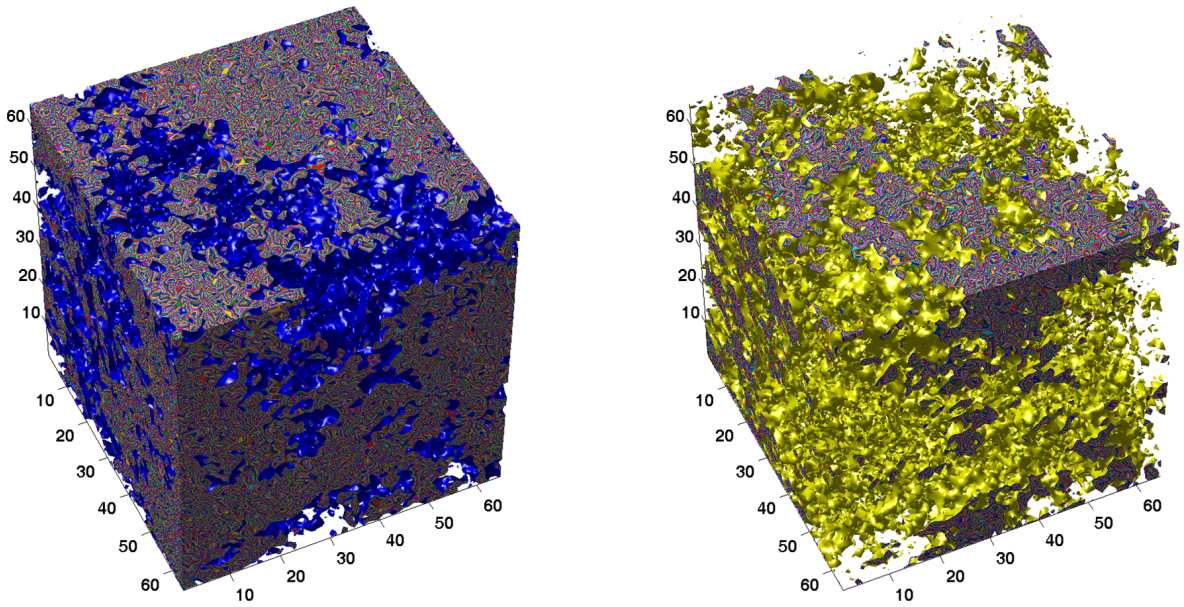

Figure 3.5: Generation of the Brownian relief on the $65 \times 65 \times 65$ cubic lattice with $Hu = 0$

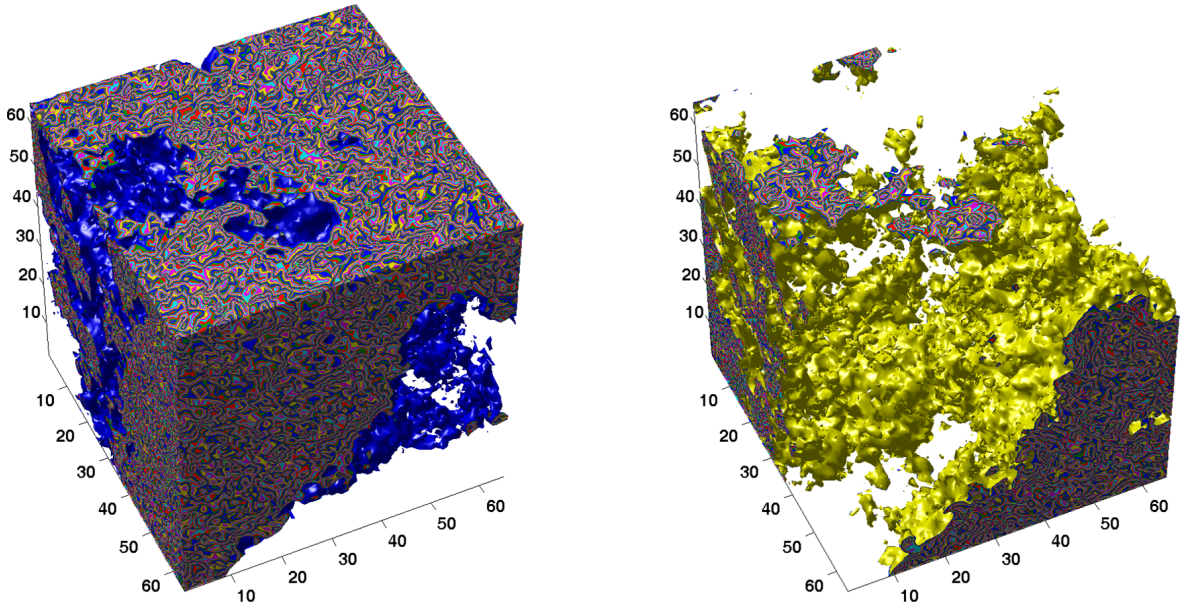

Figure 3.6: Generation of the Brownian relief on the $65 \times 65 \times 65$ cubic lattice with $Hu = 1$

Aerosols are disperse systems composed of fine solid or liquid particles suspended in gaseous medium (usually in the air). These systems are widely spread in nature and engineering. Natural aerosols are the results of natural, first of all, atmospheric processes (thunderstorms, whirlwinds, sand-storms), as well as of volcanic eruptions and large-scale forest fires discharging clouds of smoke and ash. Artificial aerosols are the results of human activities such as an abrasive surface treatment, chamber sputtering or nuclear explosions.

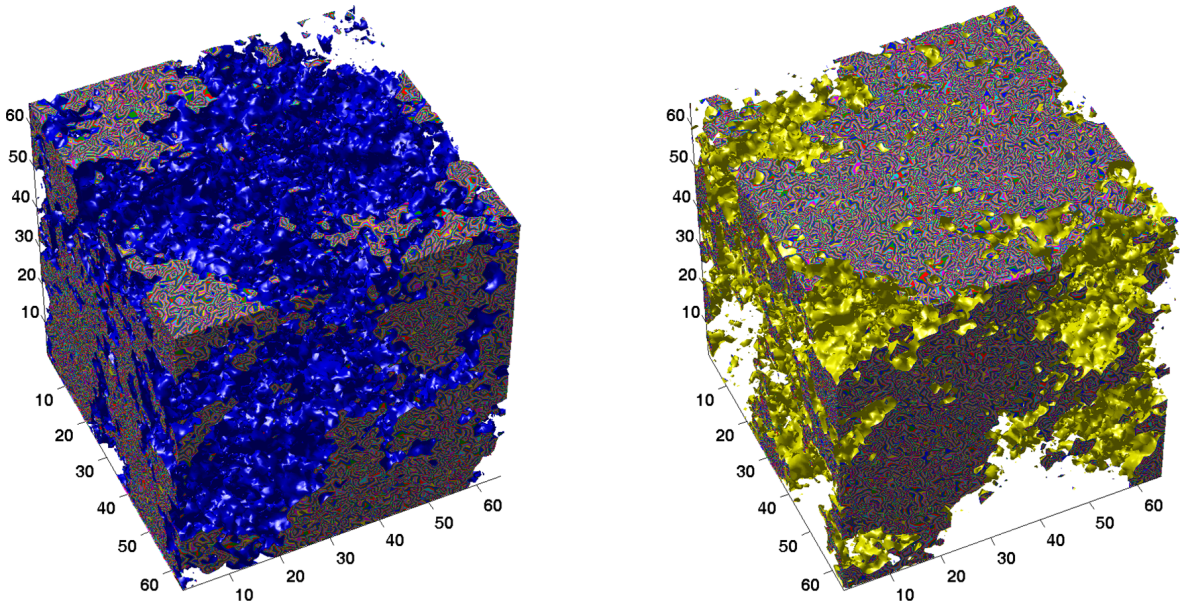

Figure 3.7: Generation of the Brownian relief on the $65 \times 65 \times 65$ cubic lattice with $Hu = 0.5$

Almost all the above mentioned natural and technological processes resulting in the appearance of aerosol systems are accompanied by intensive electrization followed by subsequent initiation of electrical break-down of the atmospheric air [2, 47, 52, 68].

Let us assume that the charge distribution between the particles is normal

$$P(q) = \frac{1}{Q\sqrt{2\pi}} \exp\left[-\frac{1}{2}\left(\frac{q}{Q}\right)^2 \right], \tag{3.3}$$

where Q is a certain characteristic absolute value of the particle charge, which, in its turn, depends on the function of particle size distribution. The following relations are evidently valid for the chosen distribution: $\bar{q} = 0$ and $\bar{q^2} = Q^2$[†].

Let us also assume that the particles are distributed randomly in the volume of a cloud, and the charge volume density $\rho(\mathbf{r})$ represents a spatial white noise satisfying the following relations:

$$\langle \rho(\mathbf{r}) \rangle = 0; \ \langle \rho(\mathbf{r}_1)\rho(\mathbf{r}_2) \rangle = Q^2 n \delta(\mathbf{r}_1 - \mathbf{r}_2), \tag{3.4}$$

where n is the concentration of cloud particles, and $\delta(\mathbf{r})$ is the Dirac delta function (the production $Q^2 n$ characterizes the intensity of the spatial white noise source).

[†]The same result may be found for both homogeneous $P(q) = \dfrac{1}{2\sqrt{3}Q}$ $-\sqrt{3}Q < q < \sqrt{3}Q$ and binary charge distribution $P(q) = \dfrac{1}{2}\delta(q+Q) + \dfrac{1}{2}\delta(q-Q)$.

Let us give a quasi-electrostatic description of the assembly of the cloud internal charges based on the fulfilment of the following conditions:

$$Q\left(\frac{\partial Q}{\partial t}\right)^{-1} \gg \frac{L}{c} \quad \text{and} \quad \frac{n^{-1/3}}{u} \gg \frac{L}{c}, \tag{3.5}$$

where L is the linear dimension of thunder cell, u is the characteristic speed of particles, and c is the speed of light.

The potential of the electrostatic field of a charge system with the spatial density $\rho(\mathbf{r})$ can be defined by the Poisson's equation

$$\Delta\varphi = -4\pi\rho(\mathbf{r}). \tag{3.6}$$

Figures 3.8 and 3.9 show the electric potential distribution in the system of 3,000 point charges. Fig. 3.8 corresponds to positive potential values restricted by the zero equipotential surface, and Fig. 3.9 depicts the field of negative potential limited by the same zero equipotentiality. In Figures 3.8 and 3.9 the colour variations at the sections of the model cube reflect the drop of positive and negative values of the electrical potential respectively. It is obvious that spatial structures given in Figures 3.8 and 3.9 are complimentary.

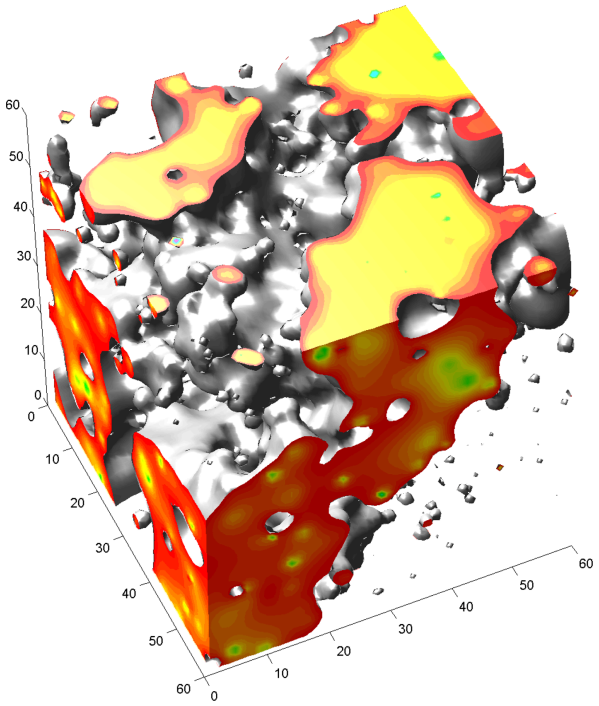

Figure 3.8: Distribution of positive electric potentials in the system of 3,000 point charges

Solution of eq. (3.6) for a random distribution of charge spatial density is as follows:

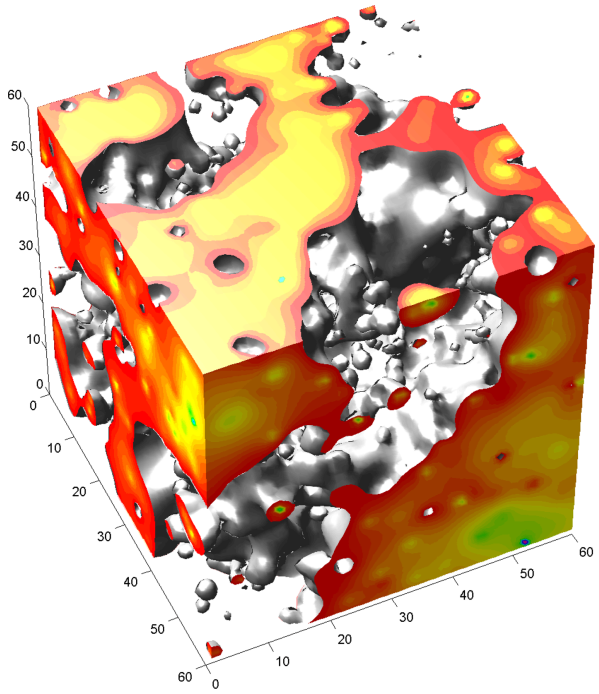

Figure 3.9: Distribution of negative electric potentials in the system of 3,000 point charges

$$\varphi(\mathbf{r}) = \int \mathrm{d}^3\mathbf{r}' \frac{\rho(\mathbf{r}')}{|\mathbf{r}-\mathbf{r}'|}, \tag{3.7}$$

where $G(\mathbf{r},\mathbf{r}') = -\dfrac{1}{|\mathbf{r}-\mathbf{r}'|}$ is the Green function of the Poisson's equation.

The first moment of the potential turns to zero:

$$\langle\varphi(\mathbf{r})\rangle = \int \langle d^3\mathbf{x}\rho(\mathbf{x})\rangle \frac{1}{|\mathbf{r}-\mathbf{x}|} = 0.$$

The second moment:

$$\langle\varphi(\mathbf{r}_1)\varphi(\mathbf{r}_2)\rangle = \int\int \langle d^3\mathbf{x}d^3\mathbf{y}\rho(\mathbf{x})\rho(\mathbf{y})\rangle \frac{1}{|\mathbf{r}_1-\mathbf{x}|}\frac{1}{|\mathbf{r}_2-\mathbf{y}|} =$$
$$= \int\int d^3\mathbf{x}d^3\mathbf{y}q^2 n\cdot\delta(\mathbf{x}-\mathbf{y})\frac{1}{|\mathbf{r}_1-\mathbf{x}|}\frac{1}{|\mathbf{r}_2-\mathbf{y}|} =$$
$$Q^2 n\cdot\int d^3\mathbf{x}\frac{1}{|\mathbf{r}_1-\mathbf{x}|}\frac{1}{|\mathbf{r}_2-\mathbf{x}|}.$$

Then

$$\langle \varphi^2(\mathbf{r}) \rangle = Q^2 n \cdot \int d^3\mathbf{x} \frac{1}{|\mathbf{r}-\mathbf{x}|^2} =$$

$$= Q^2 n \cdot \int_0^r r^2 dr \int_0^\pi \sin\vartheta d\vartheta \int_0^{2\pi} d\phi \frac{1}{r^2} = 4\pi Q^2 n \cdot r.$$

Finally

$$\langle \varphi^2(\mathbf{r}) \rangle^{1/2} = 2Q\sqrt{\pi n r}. \tag{3.8}$$

From eq. (3.8) it follows that a quasi-electrostatic field produced by the charged aerosol is characterized by significant spatial fluctuations having the property of a scale invariance [69]. And the mean-square fluctuations of potential difference between the spatially distributed parts of the system are proportional to the square root of its linear dimensions and may reach significant values even in the absence of the regular field. The fluctuation intensity is proportional to the concentration of aerosol and to the squared characteristic absolute value of the charge of the aerosol particles.

The observed potential reliefs are the self-affine hypersurfaces [27]. The self-affinity of the relief structure implies the existence of $Hu < 11$ value (coinciding in our case with the parameter Hu in the Voss algorithm) at which $\mathbf{r} \to \lambda\mathbf{r}$, $u \to \lambda_H uh$ keeps the relief surface statistically invariant. In contrast to a self-similar case, a self-affine structure is characterized by two different dimensions - global and local. The local fractal dimension is connected with the Euclidean space dimension by simple relation $d_f = d - Hu$. In a two-dimensional case the fractal surface is a fractal curve. For example, if $Hu = 1/2$ we have a diagram of the Brownian particle of the fractal dimension $d_f = 3/2$.

The global dimension characterizes the relief structure in asymptotic of global scales and equals just the dimension of the radius-vector. In our case it is equal to $d-1$. It means that a self-affine fractal looks absolutely smooth at large distances (the relation of the surface width to its linear scale of extension tends to zero with the scale growth).

Mandelbrot was the first to notice that real surfaces are fractal objects [12]. This fact in its turn caused the development of dynamic scaling approximation [49] to describe not only morphology but also dynamics of fractal surfaces. In this case evolution of a growing surface with time starting from a plane state at the moment $t = 0$ in a d-dimensional space is considered. Let us be interested in a part of the surface of L-length in a $d-1$-dimensional sub-space perpendicular to the direction of growing.

The surface can be described by the function $h(\mathbf{r},t)$ defining the height (or depth at $h < 0$) of the surface protruding in the point $\mathbf{r}$ of the initial $d-1$-dimensional hyperplane at the moment t. Let us introduce the basic parameters of the random hyperplane. The average relief height $\langle h \rangle$ at the moment t is defined as

$$\langle h \rangle = \bar{h} = \frac{\sum_{\mathbf{r}} h(\mathbf{r},t)}{L^{d-1}}, \tag{3.9}$$

where the broken brackets $\langle \ldots \rangle$ mean averaging over the space $\mathbf{r}$. The surface points fluctuate relative to this average value, and their mean-square deviation is the quantitative measure of the surface width, which may be identified as the transversal correlation length $\xi_{\perp}$ of the relief

$$\xi_{\perp}(L,t) = \langle (h(\mathbf{r},t) - \langle h(\mathbf{r},t) \rangle)^2 \rangle^{1/2} = (\langle h^2(\mathbf{r},t) \rangle - \langle h(\mathbf{r},t) \rangle^2 \rangle)^{1/2}. \tag{3.10}$$

The dynamic scaling concept is based on the statement that irregularity and coarseness of evolving surface rise according to the power low:

$$\xi_{\perp}(L,t) \sim t^{\nu_{\perp}}, \tag{3.11}$$

where the parameter $\nu_{\perp}$ describes the fluctuation growth of the surface height with time. The linear dimension of the system or the extension length of the given surface L is the maximal spatial scale restricting longitudinal dimensions of the height growing fluctuations in $d-1$-dimensions along the surface. The longitudinal correlation length $\xi_{\parallel}(L,t)$ controls dimensions of the growing fluctuations over the hypersurface (over the sea level). Once the transversal dimension of the fluctuations has reached the linear scales of the system L, further growth of the correlation length $\xi_{\parallel}(L,t)$ becomes impossible, and the surface evolution turns to the stationary mode characterized by the width constant value $\xi_{\perp}(L,t)$. For small time intervals, when $\xi_{\parallel}(L,t) \ll L$, the longitudinal correlation length also changes with time according to the power law:

$$\xi_{\parallel}(L,t) \sim t^{1/z}, \tag{3.12}$$

and as it can be seen by comparing eqs. (3.11) and (3.12) the longitudinal and transversal correlation lengths are interconnected by the following relation:

$$\xi_{\perp}(L,t) \sim \xi_{\parallel}(L,t)^{\nu_{\perp} z}. \tag{3.13}$$

Let us stress again that relations (3.11) and (3.12) are valid only in short-time intervals, which are shorter than the crossover time τ, when the longitudinal correlation length reaches the linear scales of the system $\xi_{\parallel}(L,\tau) = L$. It is worth to note that in practice the state of the most surfaces we have to deal with correspond to the short-time intervals.

A fluctuating surface is a scale-invariant object, and, therefore, the transversal scale corresponding to the saturation of the surface width at long-time intervals $\xi_{\perp}(L, t \to \infty)$ according

to the scaling hypothesis is to be described by a power dependence on L:

$$\xi_{\perp}(L, t \to \infty) \sim L^{\alpha}, \tag{3.14}$$

with the characteristic parameter α. In a steady growth regime the surface is a self-affine fractal, and exactly the α-parameter characterizes quantitatively its morphology. As we will see below, the exponent α is equivalent to the Hurst index Hu introduced by Mandelbrot.

Dependence of the self-affine surface width $\xi_{\perp}(L,t)$ from t and L presented by relations (3.11) and (3.14) respectively can be combined in one expression representing the idea of dynamic scaling [29]:

$$\xi_{\perp}(L,t) = L^{\alpha} f\left(t/L^{\alpha/\nu_{\perp}}\right), \tag{3.15}$$

where the scaling function $f(x) \sim x^{\nu_{\perp}}$ for $x \ll 1$. At long-time intervals the parameter $\xi_{\perp}(L,t)$, having reached a certain constant value, becomes independent of time. Within this range the width $\xi_{\perp}(L,t)$ changes according to relation (3.14), and the scaling function $f(x) = \text{const}$ for $x \gg 1$. Dynamic scaling expression (3.15) reveals that all diagrams of the product $\xi_{\perp}(L,t)L^{-\alpha}$ dependence on $tL^{-\alpha/\nu_{\perp}}$ value for different L-values merge into one curve.

The surface parameters α and $\nu_{\perp}$ can be found with the help of different types of surface correlation functions. For example, let us consider the function $C(r,t)$ describing correlation of surface height deviations from the mean value in different points of the basic hyperplane at different moments of time:

$$C(r,t) = \left\langle \left(\tilde{h}(\mathbf{r}',t') - \tilde{h}(\mathbf{r}+\mathbf{r}',t+t')\right)^2 \right\rangle_{r',t'}, \tag{3.16}$$

where $\tilde{h} = h - \bar{h}$ and $\langle \ldots \rangle_{r',t'}$ means averaging over all r' and t'. The fact that $C(r,t)$ depends just on r is related to the isotropy of the fractal surface along the $d-1$-dimensional space normal to the direction of growing. The following scaling relations are valid for $C(r,t)$): one at a fixed moment of time:

$$C(r,0) \sim r^{2\alpha}, \text{ at } r \ll L, \tag{3.17}$$

the other at a fixed r:

$$C(0,t) \sim t^{2\nu_{\perp}}, \text{ at } t \ll \tau \sim L^{\alpha/\nu_{\perp}}. \tag{3.18}$$

3.3 Rank distributions

The rank in the systematics is a level in a hierarchically organized set of elements. Rank distributions are used for analysing complex multi-componential systems of entirely different nature: social systems (table of ranks), systems of living organisms (species, classes, orders, families), technocenoses (nomenclature of products), etc. The ranks in the systematics are regulated by the natural scale values that divide the system into components characterized by a certain status (income, distribution, price, energy consumption, etc.) [70–77].

Each rank accounts for a certain magnitude of elements or parameters, which permits speaking about the rank as a function of the specific status. In any system there are components comparatively few in number, but of high status, and there are comparatively numerous components of less importance. As the status descends, the number of the corresponding ranks increases. The coenotic paradigm states that this dependence is usually of a hyperbolic nature

$$P_i = \frac{P_1}{i^{\beta}}, \tag{3.19}$$

where i is the rank number, P_1 is the first rank representation.

For the first time, relation (3.19) with $\beta = 1$ was obtained by researchers of linguistic materials, which is now well-known as the Zipf law [78]. The Paretos distribution, commonly used in economic statistics to describe population income, in the rank form has also a hyperbolic view:

$$P_i = (P_1 - b)\left(\frac{a+1}{a+i}\right)^{\beta} + b, \tag{3.20}$$

where a and b are distribution parameters. For $b = 0$ relationship (3.20) is called the Mandelbrot formula [79].

The hyperbolic rank parametrization of complex hierarchic structures in principle is related to their self-similarity. We will try to shed a light on this relationship by means of the tools of multifractal formalism. For illustration, we will use ecological phraseology identifying ranks as species diversity of a certain cenosis [80–85].

To be more specific, let us take a hyperbolic model and consider the absolute populations N_i of the rank representations P_i being related in the following way: $N_i = P_i N$, where N is the total cenosis population. Then we have to rewrite relation (3.19) in the following way:

$$N_i = \left[\frac{N_1}{i^{\beta}}\right], \tag{3.21}$$

where the square brackets denote an integer number (the absolute population can be defined only by integer numbers), and the parameter β changes from infinity at the superdomination to 0 at the complete equality. Examples of the rank distributions are given in Fig. 3.10.

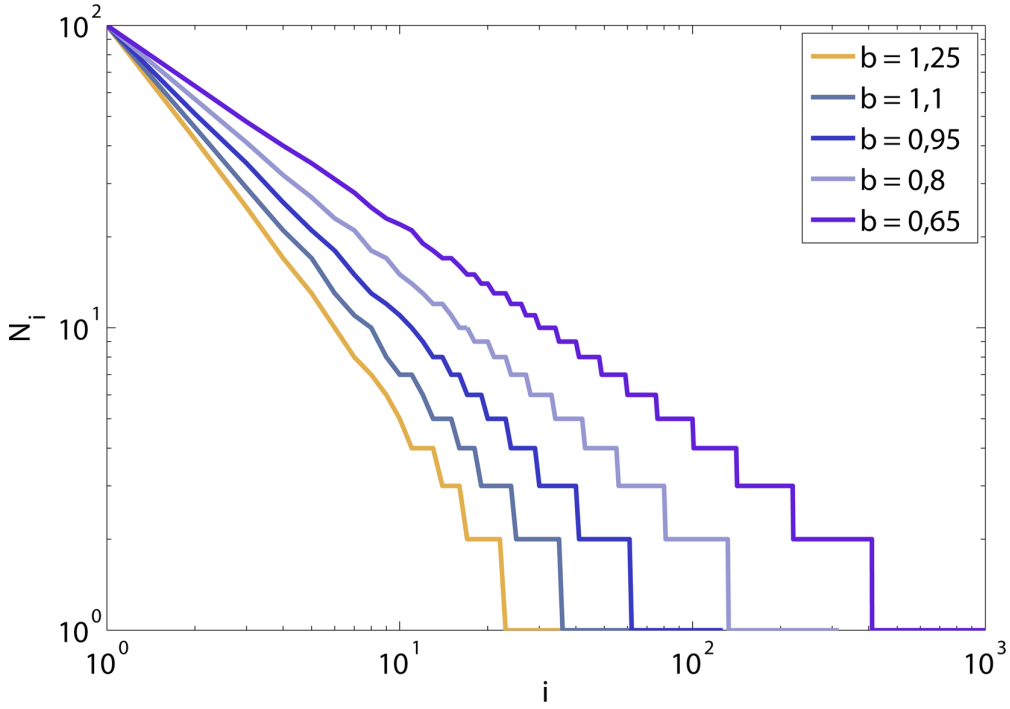

Figure 3.10: Hyperbolic rank distributions in log-log scale at the fixed N_1 and varying β

For the fractal analysis of the species diversity it is principally important to have a possibility to vary the sampling volume of the community under study. Therefore, to carry out the desired comparison of the fractal description of the species diversity with a traditional approach based on the rank distributions, we have to deal with the whole family of distributions with the fixed parameter β and variable N_1. In this case calculation of the total population N of the model community is carried out in accordance with the following formula:

$$N = \sum_{i=1} \left[\frac{N_1}{i^\beta} \right]. \tag{3.22}$$

It is clear that only members with a non-zero integer part will contribute into the sum of eq. (3.22). Exactly the quantity of the non-zero ranks will correspond to the found number of S-species.

Then we need to apply the ideas of section 1.7 and in analogy with eq. (1.33) to consider distribution of individuals by species:

$$M_q(N) = \sum_{i=1}^{S(N)} p_i^q, \tag{3.23}$$

where the continuously changing value $-\infty \leq q \leq \infty$ is called the moment order. We are interested in the asymptotic behaviour of the moments for large populations N:

$$M_q(N) = \sum_{i=1}^{S(N)} p_i^q \propto N^{\tau(q)}. \tag{3.24}$$

In other words, the exponent

$$\tau(q) = \lim_{N\to\infty} \frac{\ln M_q(N)}{\ln N} \tag{3.25}$$

characterizes the rate of change of a corresponding moment at the increase of the sample size N. The behaviour of the moments M_q for various β and q is given in Fig. 3.11. Fig. 3.11 illustrates the effects related to the limitation of the non-zero ranks or, which is the same, the number of the found species. It is obvious, that the apparent saturation in the behaviour of the moments of the individuals distribution by species M_q is determined by an artificial limitation of the species list.

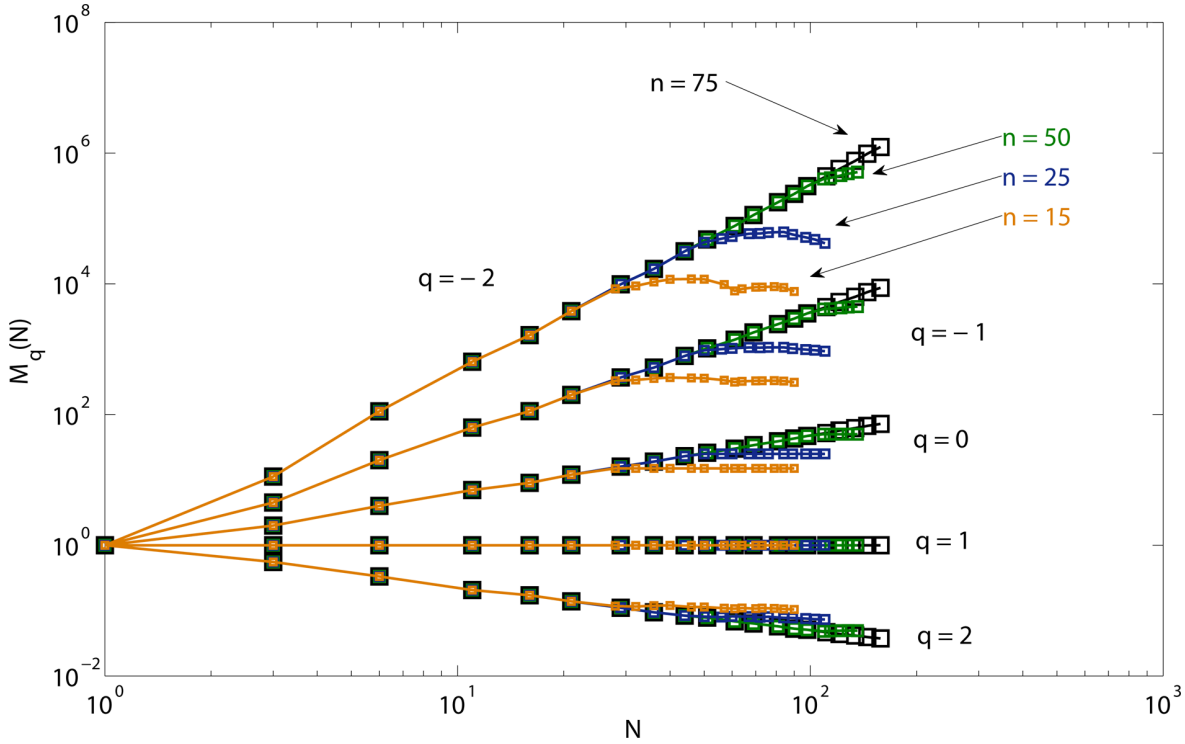

Figure 3.11: Behaviour of the moments of individuals distribution by species M_q for various β and q

A researcher in practice may encounter with another anomaly in the moments behaviour [86] [31]. It is illustrated in Fig. 3.12, where the behaviour of the moments of the individuals distribution by species M_q is plotted for various β. It is clear, that in small samples all or

almost all individuals belong to the same species. The species poorness of the small-size samples is becoming more and more obvious with the increase of β.

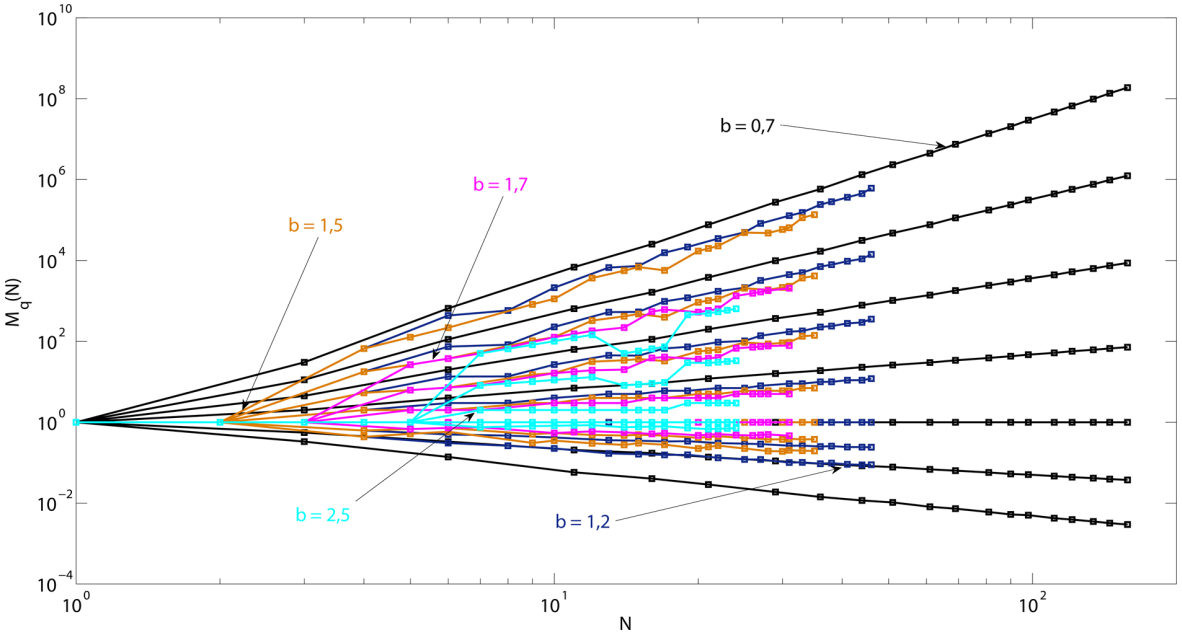

Figure 3.12: Effects connected with the strong domination

Note, that in the case of the evenly represented species, when all p_i are equal to each other $p_i = 1/S$, the asymptotic behaviour of the moments at various q is described by a very simple formula:

$$M_q(N) = S(N)^{1-q}. \tag{3.26}$$

The asymptotic behaviour of the number of S-species is described by the Margalef formula:

$$S = N^{\tau(0)}. \tag{3.27}$$

Using eq. (3.27) for the exponent $\tau(q)$, in the case of the even representation we will obtain

$$\tau(q) = k(1-q). \tag{3.28}$$

The linear character of relation (3.28) is not valid for real communities. The dependence of the exponent $\tau(q)$ on the moment order has become considerably non-linear. To find out the extent of deviation from the function $\tau(q)$ linearity, in the theory of multifractals they use an instrument of generalized dimensions described in section 1.7.

We see that the hyperbolic model fully corresponds to the Margalef hypothesis

$$S = N^k. \tag{3.29}$$

In this case the Margalef index $k = \tau(0)$ tends to one at the decay of the exponent β to zero (museum exposition or the Noah's Ark) and, vice versa, $k = 0$ at $\beta \to \infty$ (individuals).

Using a family of rank distributions with the fix β, one may construct a multifractal description of a model community. The corresponding multifractal spectrums are illustrated in Fig. 3.13.

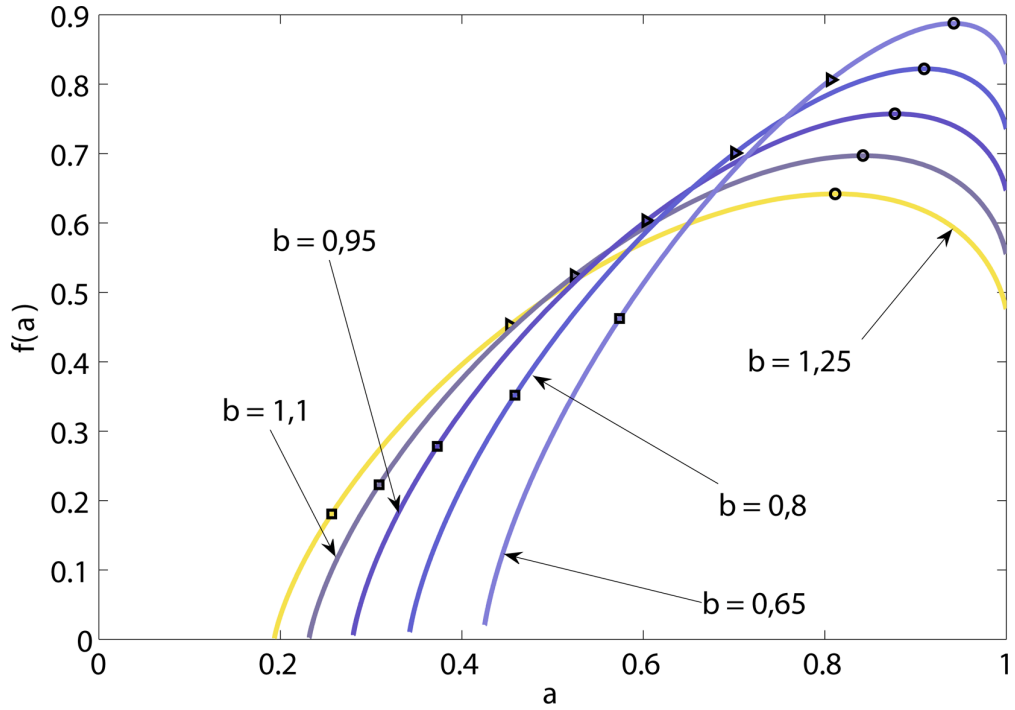

Figure 3.13: Multifractal spectrums of the rank distributions with $\beta = 0.65$

Let us consider now the multi-componential parametrization of the rank distribution by the example of a logarithmically normal distribution of the species number:

$$s(n) = \left[s_0 \exp\left\{ -\frac{(\ln(n) - \ln(n_0))^2}{2\sigma^2} \right\} \right], \tag{3.30}$$

where $s(n)$ is the number of species of population n, s_0 is the maximum value of $s(n)$ at $n = n_0$, σ is the standard deviation, the square parenthesis imply the integer number being used. In this case the integer number of species and community population are defined by the following relations, respectively:

$$S = \sum_{n=1}^{\infty} s(n); \quad N = \sum_{n=1}^{\infty} ns(n). \tag{3.31}$$

In accordance with the central limit theorem the logarithmically normal distribution is observed always when the relative importance of species is controlled by a large number of independent factors. In this case one may simulate the growth of the community population by increasing distribution parameters s_0 and n_0 at the same logarithmically normal species distribution. Fig. 3.14 presents the calculation results of the moments M_q dependence on the population for the logarithmically normal distribution with the distribution parameters s_0 and n_0 being linearly increased from 1 to 10. The zero moment M_0, as it follows from eq. (3.23), corresponds to the number of the S-species. With a deviation not exceeding one-tenth of a percent the obtained dependence of the species number on the population is approximated according to a power law:

$$S = N^{0,62}. \tag{3.32}$$

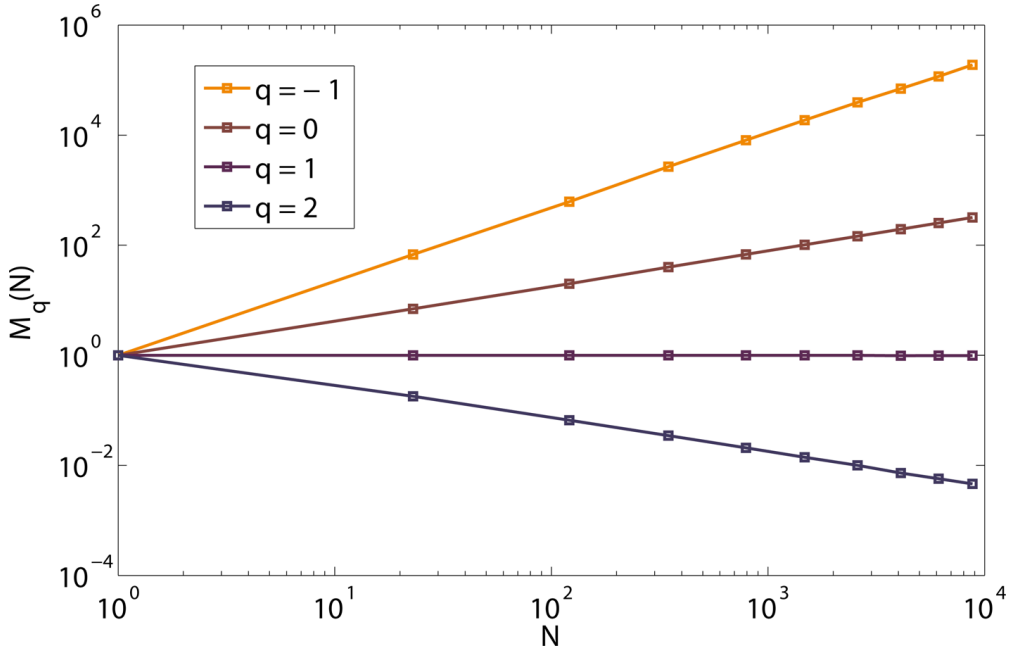

Figure 3.14: Dependence of the moments M_q on the population N in the log-log scale for the logarithmically normal distribution at the linearly increased distribution parameters. The behaviour of the zero moment $q = 0$ corresponds to the dependence of the S-species number on the population N

3.4 Percolation in disperse systems

As it has been mentioned in the previous article, the fact that a percolation transition is a critical phenomenon implies that the physical values connected with it behave according to a power law, i.e. they change as the powers of parameter $|p - p_c|$. This statement remains valid for the dynamic properties of the percolating media as well [59]. The first experimental proof of the power behaviour of the extensive dynamic characteristic of a percolating system

was put forward by Last and Thouless in 1971 [87] during the study of the diluted 2-D system conductivity. The analysis of the obtained experimental data showed that above the threshold $p_c \simeq 0.6$ the conductivity σ in the critical zone behaves as

$$\sigma \sim (p - p_c)^{\mu} \tag{3.33}$$

for the exponent μ more than 1.

Let us discuss the results of experimental verification of the continuum percolation theory for filtration flows in a disperse media with changing porosity [88]. Its main statement that near the percolation threshold the system active porosity and permeability change according to a scaling law was confirmed in a series of experiments [88, 89], where the total porosity of the model medium was changed by a uniaxial compression in a cylinder. Experimentally the dependence of the percolation threshold on the correlation properties of the pore spatial distribution was studied. In the experiments with monodispersed systems the rate of propagation of the front excitation caused by a sharp application of the pressure gradient in the system was measured. At the end of this section prospects of a heterogeneous generalization of a percolation problem in the disperse systems are discussed [90, 91].

In the description of the transmission phenomena in the disperse media the stochastic geometry methods have found their practical application. So, recently models of oil and gas collectors based on the lattice problems of the percolation theory have appeared [27,92]. The models are well-designed to be used for computer simulation and give a good idea about typical filtration modes. However, they cannot lay a claim to the quantitative correspondence to real processes, since they operate with the parameters of phenomenological character not related with physically measurable values. The quantitative comparisons are possible in continuum percolation models, where the total porosity of a system is considered as the critical value, and the active porosity is naturally interpreted as the order parameter of the percolation transition. Thus, the ideology of the continuum percolation theory permits considering a continuous set of media, which differ from each other by the value of the critical parameter, from the common viewpoint. This set of various media is compared to the same generalized system of a non-uniform porosity. The main statement of the theory says that the active porosity and permeability of the generalized system near the percolation threshold change according to a scaling law.

Let us rephrase the lattice problem of the percolation theory described in section 2.1 in the following way. For illustration let us take a 2-D square lattice (see Fig. 2.1) each site of which stands for either a pore with the probability x or an element of the solid matrix with the probability $1 - x$. Assume that the black squares in Fig. 2.1 are pores, and the yellow squares represent the solid matrix. It is obvious, that in such a way the value x corresponds to the total porosity of the system.

Let us further assume that the filtration flow can exist only between the nearest black squares having a common edge. It is obvious, that at small concentrations $x \ll 1$ the pores are either isolated or form small groups clusters of the nearest neighbours. Two black sites

belong to the same cluster when and only when they connected by a chain of the nearest neighbours being pores. The maximum cluster in Fig. 2.1 is shown by blue pixels. At $x \ll 1$ (see Figures 2.2, 2.3) the system is not permeable for the filtration flows, since there are no large clusters connecting the opposite sides of the lattice. Contrary to this, at $x \sim 1$ (see Figures 2.5, 2.7) the overwhelming fraction of the lattice has become permeable for filtration; the blue sites form a cluster connecting the opposite sides of the lattice and ensuring the filtration flow from one side of the system to the other.

As it was previously mentioned, the occurrence of the infinite cluster of connected elements in the system may be considered as a geometric phase transition: the critical concentration $x = x_c$ separates the phase of the finite clusters $x < x_c$ from the phase $x > x_c$, where there already exists the infinite cluster. Note, that all the finite clusters contribute to the total porosity, while the active porosity is presented only by the elements of the infinite cluster as well as an insignificant number of the finite clusters that come out to the surface of the sample. The fraction of the surface finite clusters decreases linearly with the increase of the system size. It is true, the surface pores number increases as an area of this surface, but the total number of pores changes proportionally to the volume of the sample. Thus, below the percolation threshold in the phase of finite clusters $x < x_c$ the active porosity is negligible and has become rather noticeable only above the threshold in the phase $x > x_c$, where the infinite cluster exists.

In the works [88, 89] the results of experimental researches on filtration in a medium with changing porosity are discussed. A schematic diagram of the experimental installation is shown in Fig. 3.15. The porous medium is represented by polyurethane particles of irregular form packed in a cylindrical sleeve between the permeable wall E and the permeable piston F. The polyurethane particles sizes in various experiments were 0.7 and 5 mm with the cylinder diameter 0.2 mm.

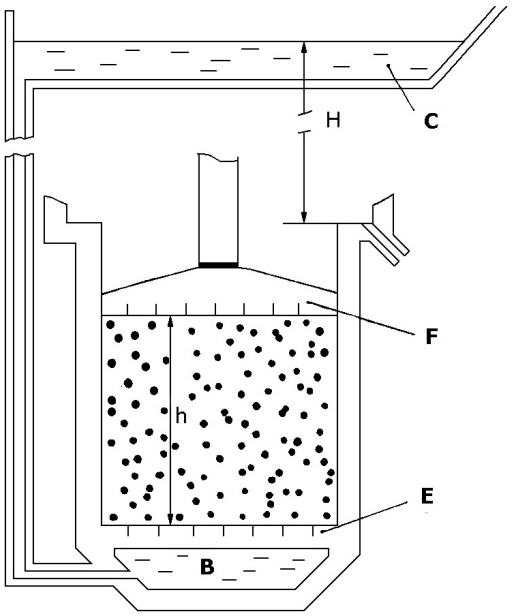

Figure 3.15: Schematic diagram of the experimental installation

The change of the total porosity is achieved by the piston F motion relatively the wall E: $x = 1 - \dfrac{M}{\rho S h}$, where M is the total mass of the polyurethane particles in the sleeve, ρ is the density of polyurethane, h is the distance between F and E, S is the area of the sleeve cross section. The tray B communicates with the pan C positioned at the height H relatively the outflow level such that the filtration in the installation is controlled by the pressure drop which is described by the relation

$$\nabla p - \rho_0 \mathbf{g} = \rho_0 \mathbf{g} \frac{H}{h}, \tag{3.34}$$

where p is the water pressure, ρ_0 is the water density, $\vec{g}$ is the gravitational acceleration. In the one-dimensional geometry of the experiment the filtration rate is determined by the discharge θ: $u = \theta / S$. With each discrete porosity value (discrete value h) the pressure gradient in the system was changing from zero to the value of order 10^5Pa/m. The corresponding experimental dependences of the filtration rate on the pressure differential for various porosity values are given in Fig. 3.16. The experimental values coincide well with the theoretical dependences calculated with the help of a binominal filtration law [93]:

$$-\frac{k}{\mu} \rho_0 \mathbf{g} \frac{H}{h} = \vec{u}(1 + \mathrm{Re}), \tag{3.35}$$

where $\mathrm{Re} = \frac{\rho_0 d_0 u}{\mu}$ is the Reynolds number for the filtration flow, μ is the water viscosity, k is the permeability, d_0 is the length scale characterizing the small-scale structure of the pore space.

In the experiments with the monodisperse ensembles of particles with various characteristic sizes (relative variations of sizes in each ensemble did not exceed 20%) the system became impermeable for the filtration flow at one and the same critical value of the total porosity $x_c = 0.16 \pm 0.1$. In Fig. 3.17 the permeability as the function of the total porosity is presented in the log-log scale.

The permeability values obtained in the experiment approximate well by a power relation

$$k = k_0 (x - x_c)^{1,7 \pm 0,1}, \tag{3.36}$$

where x_c is the porosity critical value, $t = 1.7 \pm 0.1$ is the critical permeability index. The value k_0 is proportional to the square of the particle sizes in an ensemble only within the limits of the experimental accuracy $k_0 = d_0^2$. The value d_0 does not change noticeably with the change of porosity near the threshold. It may be explained by the fact that the inertia effects that cause deviation from the linear Darcys law are determined by the local features of the porous space and depend little on its large-scale geometry. At the same time the change of the total porosity manifests itself, first of all, exactly in the global structure of

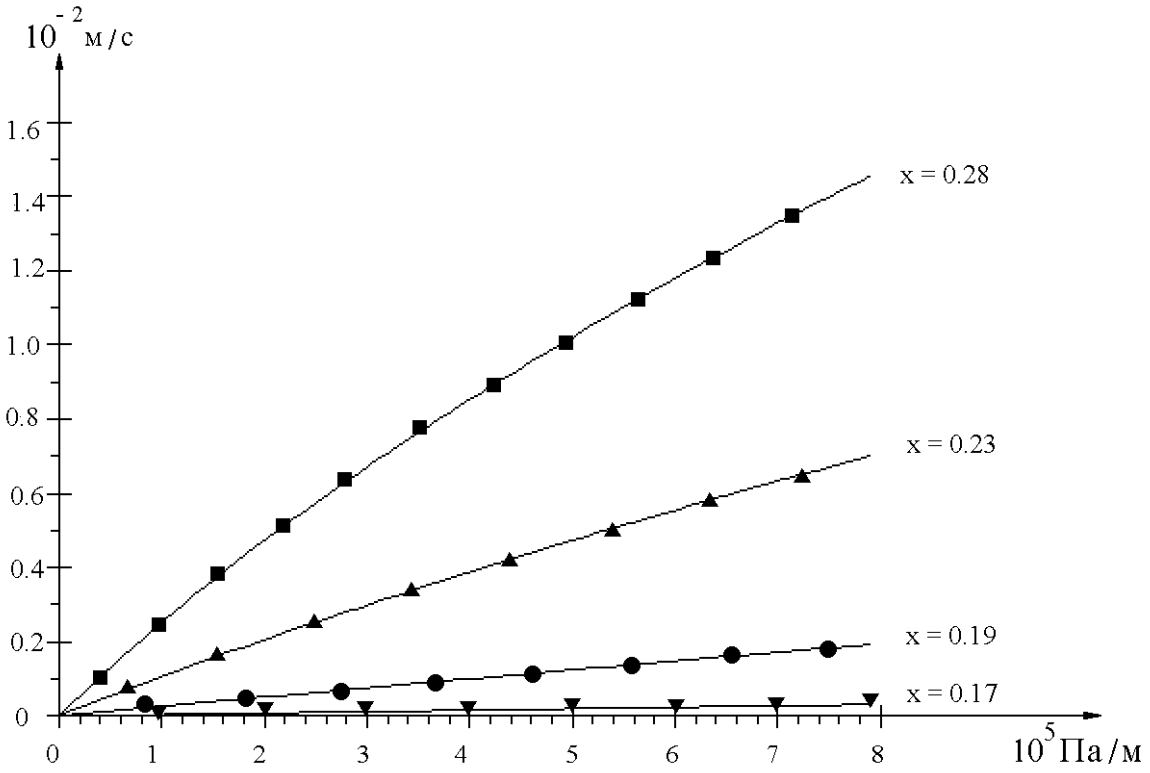

Figure 3.16: Experimental dependences of the filtration rate on pressure differential for various porosity values

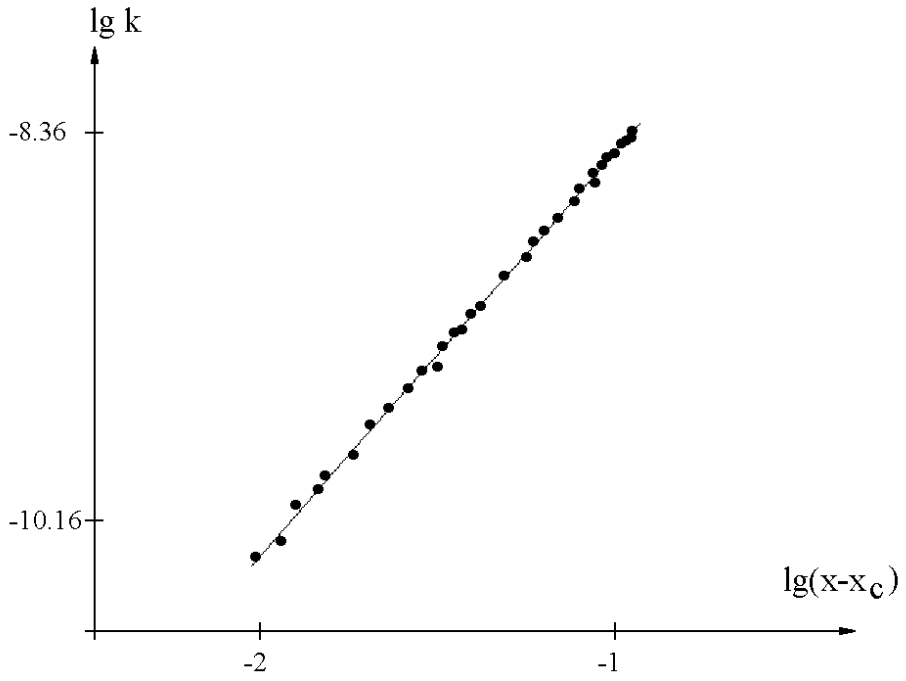

Figure 3.17: Permeability as the function of the total porosity

the porous space, to a lesser degree affecting its local geometric parameters. Therefore, using relation (3.36) and recalling that the active porosity m is the order parameter of the percolation transition, which changes near the threshold according to a scaling law as

$$m \cong (x - x_c)^{\beta}, \tag{3.37}$$

where β is the critical exponent of the order parameter (see section 2.2) we obtain:

$$\mathrm{Re} = \frac{u\rho\, k^{1/2}}{\mu\, m^{t/2\beta}}. \tag{3.38}$$

In the past repeated efforts were undertaken to express the Reinolds number Re (or the characteristic dimension d_0) via the parameters of a disperse system in such a way that the filtration process in the porous media of various structures was described by a common formula [93]. The result (3.38) provides a universal form to write the binomial law of filtration (3.35) for a wide range of disperse media tied up by a common geologic history.

Observed in the experiment the critical value $x_c = 0.16 \pm 0.1$ serves as a standard for 3-D problems of the percolation theory, belonging to the same class of universality like such classical objects as the problem of spheres (see section 2.7) and the 3-D problem of the percolation level (see section 2.6). It is assumed that the percolating elements in these problems are distributed at random. Large correlations in the distribution may change considerably the threshold value. It is quite enough, for instance, to substitute balls for cubes that significant correlations occur in the pore distribution due to the short range ordering in the assembly of spherical particles. In this case the critical value decreases to the value of about 3%, which does not differ much from the value of the theoretical threshold calculated for the case of the regular cubic face-centred packing of balls [91, 94].

Fractal structures, where slowly decreasing correlations in a pore assembly are conditioned by the system self-similarity, may serve another example of a sharp decrease of the threshold as compared with the problem of the randomly homogeneous function of distribution. For instance, in work [89] a case was experimentally studied, when the system was formed by two types of cubes of largely different sizes (0.7 and 5 mm).

The structure of the assembly is controlled by the parameter

$$\wp = \frac{q}{q+Q}, \tag{3.39}$$

where q, Q are the specific volumes of small and large cubes, respectively. In this case

$$q + Q = 1 - x. \tag{3.40}$$

It is obvious, that the values $\wp = 0$, $\wp = 1$ correspond to the monodisperse assemblies. Within the range of the largely different sizes it is easy to obtain analytic expressions for the critical value of the total porosity as the function of the structural parameter $\wp$. Indeed, for the values $q \ll 1$ ($\wp \ll 1$) the largest quantity of the small cubes is located in the pores of the structure formed by the assembly of the large cubes. It is obvious, that in this case the critical value of porosity decays linearly with the increase of q: $x_c(q) = x_c(0) - q$ or using eqs. (3.39), (3.40):

$$x_c(\wp) = \frac{x_c(0) - \wp}{1 - \wp}. \tag{3.41}$$

On the contrary, when $Q \ll 1$ ($\wp < 1$) the change of the total porosity critical value depends on the decrease of the system size by the volume occupied by the large cubes, i.e. $x_c(Q) = (1 - Q)\, x_c(0)$. Again using eqs. (3.39), (3.40) we obtain:

$$x_c(\wp) = \frac{x_c(0) \cdot \wp}{1 + x_c(0)\, \wp - x_c(0)}. \tag{3.42}$$

Asymptotics (3.41), (3.42) are represented in Fig. 3.18 by the solid graphs.

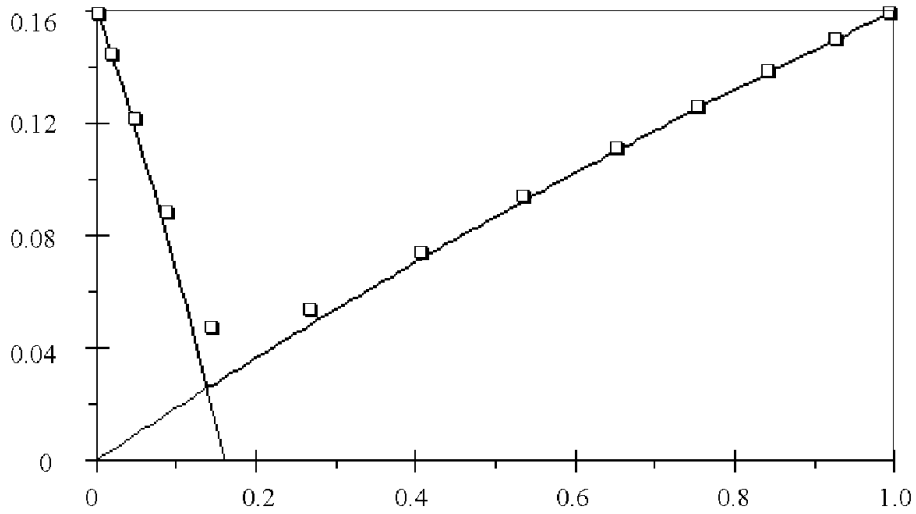

Figure 3.18: Critical value of the total porosity as the function of the structural parameter

We may see that at $\wp_c = \dfrac{x_c(0)}{1 + x_c(0)}$ a peculiar geometric phase transition takes place from regime (3.41) to regime (3.42). The minimal critical value of the total porosity equals $x_c(\wp_c) = x_c^2(0)$. The results of the experiments are depicted in Fig. 3.18 with the square markers.

Let us address now to the results of the experimental determination of the dimensions of the shortest path between the distant points of the percolating cluster $d_{\min}$. The fact is that this

dimension is closely connected with another critical exponent having contensive analogy in the classical thermodynamics. We speak about the exponent of the critical deceleration. It is well known that the critical deceleration is the integral part of any phase transition. Let us discuss the meaning of this phenomenon for the percolation transformation and at the same time identify the relation between the exponent of critical deceleration and value $d_{\min}$.

Assume that there is a certain excitation, which is spreading in the following way. If at the time t the site i is excited, then at the time $t+1$ all nearest sites connected with i get excited, too. A site which got excited at any time in the past remains excited in all the following moments of time. Let us at the time $t=0$ excite the site 0. The front of excitation at the time t is represented by a group of the sites the chemical distance from which to the site 0 equals t.

At $x < x_c$ the excitation in the system does not spread. At any $x > x_c$ the asymptotic behaviour of the front is described within the limits of a certain high rate dependable on x. When x approaches x_c from above, this rate decreases: the critical deceleration takes place. At $x = x_c$ the rate of excitation turns into 0.

Let the concentration of the excited sites be $x > x_c$. The correlation length in such a system equals $\xi = (x-x_c)^{-\nu}$. In the fractal regime the time in which the front of excitement covers distance R is $t \sim R^{d_{\min}}$; particularly, the distance ξ will be covered in time $t_\xi \sim \xi^{d_{\min}} \sim (x-x_c)^{-d_{\min}\nu}$. On large scales the systems behaviour becomes uniform, and $t/t_\xi = R/\xi$. Thus, in time $t \gg t_\xi$ the front of excitement propagates to the distance $R \sim (\xi/t_\xi)t$; the effective rate of its spreading $v \sim \xi/t_\xi \sim (x-x_c)^{(d_{\min}-1)\nu}$. The exponent $\psi = (d_{\min}-1)\nu$ of the effective rate controls the critical deceleration. In the 3-D case $\psi = 0.31 \pm 0.06$.

The rate of the excitement front propagation in the monodispersed assemblies provoked by the appearance of a sharp pressure gradient in the system was measured experimentally. Approaching the transparency threshold the rate was tending to zero as a power of the $x - x_c$ value. The corresponding critical exponent, defining the value of critical deceleration in the system, constituted $\psi = 0.31 \pm 0.02$, which coincided with the results of the computer calculations [61].

In conclusion let us consider a simple heterogeneous generalization of a problem, which concerns a well-known situation when, for example, during the well boring process the petrophysical data deviate from the curve of the normal density, caused the occurrence of the zones of the so-called anomalous pressure, see [95, 96]. The generalization in this case is the dependence of the critical parameter on just one spatial coordinate. Exactly such a situation occurs during the fluid filtration in a porous medium subjected to the lithostatic pressure [88, 97, 98]. Under its own weight the material changes its porosity, which at a certain layer reaches its critical value. Below this layer the system is impermeable for the fluid, and the zones of transparency are separated from each other by the fluctuation front, the structure and width of which can be determined within the approximation of the gradient percolation [64, 99, 100].

The more interesting model for the geophysical application occurs, when the total porosity of

the system is a random function of the spatial coordinates. In this case it is more convenient to consider not the clusters of pores, but the percolation of the zones of transparency. The presence of the mean-value gradients of the total porosity in the system ensures existence of the hierarchy of the fluctuation fronts. It should be noted here that the analogous fluctuation fronts can occur due to the spatial non-uniformity of the total porosity critical value.

Moreover, when the porosity has become a dynamic variable that changes with time due to the geochemical and geophysical processes, effects occur in the system, related to the porosity-permeability non-linearity near the percolation threshold [101, 102]. And the fluctuation front has become an active element of the distributed stochastic generator [98, 103], an example of which will be discussed in section 3.8.

3.5 Fractal networks and labyrinths

Fractal labyrinths are quite common in nature and technology [4, 103]. These are transport and communication networks, filtration channels, systems of collection and distribution of resources and information, river systems, circulatory systems, lightning, etc. We already know that the density of fractal structures decays according to a power law with the increase of their linear dimensions. Thanks to this, transport properties of the fractal networks differ considerably from a regular case. We will see it by considering conductivity, random walking and oscillation excitation in the self-similar structures [50, 51, 103, 104].

Conductivity. We will start with a regular case by considering a metal lattice of L^d dimension under the voltage applied to its opposite sides. Its impedance changes with the change of the linear dimensions L in the following way:

$$\rho \sim \sigma^{-1} \frac{L}{L^{d-1}}, \tag{3.43}$$

where σ is the metal conductivity. Since σ does not depend on L, the lattice impedance changes with the dimension change according to the power law $\rho \sim L^{2-d} \equiv L^{\tilde{\zeta}}$ with exponent $\tilde{\zeta} = 2-d$. Equation (3.43) is true for the regular homogeneous conductors, when the density of the conducting material does not depend on the scaling. For the fractal conductors the density is proportional to L^{d_f-d} and tends to zero as $L \to \infty$. This is explained by the fact that holes of various sizes, even to the size of the system itself, exist in the fractal structures. By increasing L, we, thereby, increase dimensions of the non-conductive holes, which, in their turn, decrease the conductivity. Because of the self-similarity, σ decreases on all scales, following the power dependence:

$$\sigma \sim L^{-\tilde{\mu}}. \tag{3.44}$$

As the result of eqs. (3.44) and (3.43), the impedance behaves as

$$\rho \sim L^{\tilde{\zeta}}, \tag{3.45}$$

where the critical exponent $\tilde{\zeta} = 2 - d + \tilde{\mu}$ is now larger than the analogous exponent $2 - d$ for the homogeneous conductor. In the case of the percolating cluster the exponent $\tilde{\mu}$ introduced in eq. (3.44), is connected with the critical exponent of the correlation radius ν and the exponent μ defined in eq. (3.33) as $\tilde{\mu} = \mu/\nu$.

Let us calculate the exponent $\tilde{\zeta}$ value for the Sierpiński gasket (Fig. 1.5). Let us define the potential difference between the gasket vertex and two vertexes of its bottom edge and compare the impedance of the large L-scale gasket with that of the smaller one of the scale $L/2$. According to the Kirchhoffs current law, the resistance of the large structure $\rho(L)$ measured between two vertexes of the gasket is the sum of the resistance of the small resistor $\rho(L/2)$ and the resistance of a small resistor connected in-parallel with two other small resistors:

$$\rho(L) = \rho(L/2) + \left(\frac{1}{2\rho(L/2)} + \frac{1}{\rho(L/2)} \right)^{-1} = \frac{5}{3}\rho(L/2). \tag{3.46}$$

Using eq. (3.45), we find for the Sierpiński gasket: $\tilde{\zeta} = \ln(5/3)/\ln 2$. In analogy, for the Mandelbrot-Given fractal (Fig. 2.15) we find: $\tilde{\zeta} = \ln(11/4)/\ln 3$.

Diffusion. For diffusion modelling a random walk process is usually used, when at every step of the model time the particle moves randomly to a distance a into a neighbouring site of the d-dimension model lattice. Let us assume that at the moment of time $t = 0$ the particle started from the beginning of coordinates of the d-dimensional lattice space. Then after a certain number of t steps of the model time the current position of the diffusing particle would be described by the vector of displacement:

$$\mathbf{r}(t) = a \sum_{k=1}^{t} \mathbf{e}_k, \tag{3.47}$$

where $\mathbf{e}_k$ denotes the unit vector in the direction of the particles jump at the k-step of the model time.

The characteristic distance the particle covers on average in the process of the random walk in t steps of the model time is described by the mean-square displacement $\langle r^2(t) \rangle^{1/2}$, where mean $\langle \ldots \rangle$ is understood as the average possible configurations of random walk on the lattice. From eq. (3.47) we find

$$\langle r^2(t)\rangle = a^2 \sum_{k,k'=1}^{t} \langle \mathbf{e}_k \cdot \mathbf{e}_{k'}\rangle = a^2 t + \sum_{k\neq k'}^{t} \langle \mathbf{e}_k \cdot \mathbf{e}_{k'}\rangle.$$

Since the particles jumps in different moments of time k and k' are not correlated, we have $\langle \mathbf{e}_k \cdot \mathbf{e}_{k'}\rangle = \delta_{kk'}$ which leads us consequently to the Ficks law of diffusion:

$$\langle r^2(t)\rangle = a^2 t. \tag{3.48}$$

Note that eq. (3.48) does not depend on the lattice d-dimension. In the more general case, when the particle has a probability to stay in place, the mean-square displacement is described by the formula $\langle r^2(t)\rangle = 2dDt$, where D is the coefficient of diffusion.

The mean-square displacement may be obtained through the density of the probability $P(r,t)$, which is a probability to find the diffusing particle within the radius r from the starting point by means of the relation $\langle r^2(t)\rangle = \int dr r^2 P(r,t)$.The probability density of the random walk can be easily found for a 1-D chain of sites, when the particle can jump just in two directions. Jumps to the right or left occur with the probability $p = 1/2$. For the sake of simplicity let us assume that $a = 1$. In the process of random walk during the t steps of the model time the particle will make m jumps to the right and $t - m$ jumps to the left. Thus, its current coordinate will be $x = m - (t - m) = 2m - t$. The probability that this will occur is described by the binominal distribution:

$$P(m,t) = \begin{pmatrix} t \\ m \end{pmatrix} p^m (1-p)^{t-m} = \begin{pmatrix} t \\ m \end{pmatrix} \left(\frac{1}{2}\right)^t. \tag{3.49}$$

For large t, m, and $t - m$ the binominal coefficients can be calculated according to the Stirlings formula: $t! \simeq (2\pi t)^{1/2}(t/e)^t$ and so on. Since the current coordinate of the particle x is much smaller than the total number of its jumps to the right or left, the resulting expression can be resolved as a Taylor series of the powers of the exponent $x/t \ll 1$, and finally we obtain:

$$P(x,t) \simeq \frac{1}{(2\pi t)^{1/2}} e^{-x^2/2t}. \tag{3.50}$$

Relation (3.50) is a Gauss distribution with t-width, which is identical to $\langle x^2(t)\rangle$. Since $P(x,t)$ is a probability, than $\int_{-\infty}^{\infty} dx P(x,t) = 1$, which is true for eq. (3.50). In the more general case of the d-dimensional hyperlattice eq. (3.47) transforms into the following expression:

$$P(r,t) \simeq \frac{1}{\langle r^2(t)\rangle^{d/2}} e^{-(d/2)r^2/\langle r^2(t)\rangle}, \tag{3.51}$$

where $\langle r^2(t)\rangle = 2dDt$, and the probability that the particle will return to the beginning of coordinates in t steps of the model time is proportional to $\langle r^2(t)\rangle^{-d/2}$.

Let us see now what is happening during the random walking in the self-similar labyrinths. It is obvious, that large holes, red bonds and dead ends of a fractal slow down the particles movement in it. And since they exist on every scale, the slowing-down occurs on all scales. The Ficks law (3.48) has lost its validity and is substituted by a more general formula for the mean-square displacement:

$$\langle r^2(t)\rangle = t^{2/d_\omega}, \tag{3.52}$$

where a new critical exponent d_ω (diffusion exponent or fractal dimension of the random walk) is always larger than 2.

The critical index of impedance $\tilde{\zeta}$ and the diffusion exponent d_ω can be tied up by means of the Einsteins equation

$$\sigma = \frac{e^2 n}{k_B T} D, \tag{3.53}$$

which relates the direct current conductivity σ with the diffusion coefficient D. In it e and n denotes the charge and concentration of the moving particles, respectively.

To show the relationship of the exponent d_ω with $\tilde{\zeta}$ and $\tilde{\mu}$, we use the standard scaling argumentation. Since the concentration of the particles n is proportional to the substrate density ($n \sim L^{d_f-d}$), the right-hand part of eq. (3.53) is proportional to $L^{d_f-d}\, t^{2/d_\omega-1}$. The left-hand part of eq. (3.53) is proportional to $L^{-\tilde{\mu}}$. Because the time during which the diffusing particle covers the L-distance changes as L^{d_ω}, we finally find that $L^{-\tilde{\mu}} \sim L^{d_f-d+2-d_\omega}$, and the desired relation will be

$$d_\omega = d_f - d + 2 + \tilde{\mu} = d_f + \tilde{\zeta}. \tag{3.54}$$

Knowing that for the Sierpiński gasket $d_f = \ln 3/\ln 2$ and in the case of the Mandelbrot-Given fractal $d_f = \ln 8/\ln 3$, we find that for these structures $d_\omega = \ln 5/\ln 2$ and $d_\omega = \ln 22/\ln 2$, respectively.

For random fractals it is not so easy to determine d_ω values with the exception of the topologically linear fractals with chemical dimension equal to one ($d_l = 1$), which can be considered

as the non-crossing paths. Along such a path (in chemical or L-space) diffusion is normal, and therefore, $\langle l^2(t)\rangle = t$. Since $l \sim r^{d_f}$, the mean-square displacement in the Euclidean R-space behaves as $\langle r^2(t)\rangle = t^{1/d_f}$, leaving $d_\omega = 2d_f$.

For the case of a percolating fractal cluster, d_ω cannot be calculated precisely, but its lower and upper values are quite close to each other in the spaces with $d \geq 3$. An accurate value can be obtained with the help of the Alexander–Orbach conjecture [104]: $d_\omega \simeq 3d_f/2$.

For fractals the function of distribution $\langle P(r,t)\rangle$, averaged over all starting points of the particle on the fractal, is not Gaussian any more. For random walking one may find [29] that for $r/\langle r^2\rangle^{1/2} \gg 1$, $\langle P(r,t)\rangle$ is described by an extended Gaussian distribution:

$$\langle P(r,t)\rangle / \langle P(0,t)\rangle \sim \exp[-\text{const} \cdot (r/\langle r^2\rangle^{1/2})^u], \tag{3.55}$$

where the exponent u is related to d_ω AS

$$u = \frac{d_\omega}{d_\omega - 1}. \tag{3.56}$$

Relation (3.56) have been verified on a large number of random fractals, including the percolating fractal clusters. For the topological linear fractals it is precise. Since in large time intervals each element of the fractal structure is visited by the randomly walking particle approximately with an equal probability, the probability of return $\langle P(0,t)\rangle$ occurring in eq. (3.55) is inversely proportional to the number of visited sites $S(t)$. For fractals $S(t)$ changes as $\langle r^2(t)\rangle^{d_f/2}$, thus

$$\langle P(0,t)\rangle \sim (1/\langle r^2(t)\rangle)^{d_f/2} \sim t^{-d_f/d_\omega}. \tag{3.57}$$

Oscillation excitation. Let us consider L^d particles located in the sites of a regular d-dimensional lattice and connected with their nearest neighbours by springs. The particles can oscillate relatively to the equilibrium positions that coincide with the sites of the lattice. In compliance with the translation symmetry, the lattices oscillation excitations represent waves characterized by the reverse lattice vector $\mathbf{q}$ and frequency $\omega(\mathbf{q})$. For small values $q = |\mathbf{q}|$ corresponding to the large wave lengths λ, these excitations (phonons) are ordinary sound waves with the disperse relation

$$\omega(\mathbf{q}) = cq, \tag{3.58}$$

where c is the sound speed in the lattice.

From eq. (3.58) we find the density of the phonon states:

$$z(\omega) \sim \omega^{d-1}. \tag{3.59}$$

The value $z(\omega)$ can be related to the Fourier image of the probability of return to the beginning of coordinates $P(0,t)$ in the process of random walking. We will use this analogy to consider $z(\omega)$ for fractals.

Let us discuss now the oscillation excitations of fractal networks and consider $N = L^{d_f}$ particles located in the sites of a fractal structure placed in a d-dimensional supercubic lattice in such a way that the nearest neighbours are connected by springs. If we denote the spring stiffness matrix between the nearest neighbours i and j as $k_{ij}^{\alpha\beta}$, the equation of motion will be written in the following way:

$$\frac{d^2 u_i^\alpha(t)}{dt^2} = \sum_j \sum_\beta k_{ij}^{\alpha\beta} \left[u_j^\beta(t) - u_i^\beta(t) \right], \tag{3.60}$$

where u_i^α is the displacement of the i-particle along the α-coordinate.

For simplicity let us assume that the bond matrix $k_{ij}^{\alpha\beta}$ can be considered as the scalar quantity $k_{ij}^{\alpha\beta} = k_{ij}\delta_{\alpha\beta}$. Then the various components of displacement break down into similar equations for all components $u_i^\alpha \equiv u_i$:

$$\frac{d^2 u_i(t)}{dt^2} = \sum_j k_{ij} \left[u_j(t) - u_i(t) \right]. \tag{3.61}$$

The structure of this equation differs little from the equation of diffusion: it is just sufficient to replace the displacement $u_i(t)$ by the probability of occupation of the lattices i-site $P(i,t)$ and substitute the first time derivative for the second one. The bond matrix $k_{ij} = k_{ji}$ in the diffusion equation relates to the probability of particles jumps between the corresponding sites and has the same symmetry as the spring stiffness matrix. To solve eq. (3.61) let us use a standard method of classical mechanics. Substitution of $u_i(t) = A_i \exp(-i\omega t)$ leads to a homogeneous system of equations for N of unknown A_i, by means of which N of characteristic values $\omega_\alpha^2 \geq 0$, $\alpha = 1.2, \cdots, N$ and corresponding eigenvectors $(A_1^\alpha, \cdots, A_N^\alpha)$ are determined. From where it is convenient to choose an orthonormal basis of the eigenvectors $(a_1^\alpha, \cdots, a_N^\alpha)$.

The general solution of eq. (3.61) has the form $u_i(t) = Re\{\sum_{\alpha=1}^N c_\alpha a_i^\alpha \exp(-i\omega_\alpha t)\}$, are to be found from the initial conditions. If at time $t = 0$ just a j-particle is displaced with regard to its equilibrium position, i.e. $u_i(0) = u_j(0)\delta_{ij}$, then

$$u_{i+j}(t) = u_j(0) Re \left\{ \sum_{\alpha=1}^{N} (a_j^\alpha) a_{i+j}^\alpha \exp(-i\omega_\alpha t) \right\}. \tag{3.62}$$

The corresponding diffusion equation looks analogously

$$P(i+j,t) = Re\left\{\sum_{\alpha=1}^{N}(a_j^\alpha)a_{i+j}^\alpha \exp(-i\varepsilon_\alpha t)\right\}, \tag{3.63}$$

where $\varepsilon_\alpha = \omega_\alpha^2$. According to the initial condition $P(i,0) = \delta_{ij}$, $P(j,t)$ denotes the probability of the particles return to the starting point of the random walking. The mean probability $\langle P(r,t)\rangle$ that the diffusing particle can move away from the starting point to the distance r is determined, firstly, by averaging all the sites $i+j$ that are located at the distance r from the initial site, and secondly, by selecting all the sites of the fractal structure as the starting point j of the random walk and their averaging like:

$$\langle P(r,t)\rangle = \mathrm{Re}\left\{\sum_{\alpha=1}^{N} a(r,\alpha)\exp(-\varepsilon_\alpha t)\right\}, \tag{3.64}$$

where

$$a(r,\alpha) = \frac{1}{N}\sum_{j=1}^{N}\frac{1}{N}\sum_{i=1}^{N(r)}(a_j^\alpha)a_{i+j}^\alpha \tag{3.65}$$

and the internal summation in eq. (3.65) is performed over the entire sites located at a distance from the initial j-site. For $r=0$ we have just $a(0,\alpha) = 1/N$ (due to the orthonormality of the eigenvectors), thus

$$\langle P(0,t)\rangle = \frac{1}{N}\sum_{\alpha=1}^{N}\exp(-\varepsilon_\alpha t). \tag{3.66}$$

Within the limit $N\to\infty$ the sum over α can be replaced by the integral of ε by introducing the density of energy states $n(\varepsilon)$:

$$\langle P(0,t)\rangle = \frac{1}{N}\int_0^\infty d\varepsilon n(\varepsilon)\exp(-\varepsilon t). \tag{3.67}$$

Accordingly, we may find $n(\varepsilon)$ by using an inverse Laplace transform of $\langle P(r,t)\rangle$. It is easy to ascertain that relation $\langle P(0,t)\rangle \sim t^{-d_f/d_\omega}$ (3.57) implies that $n(\varepsilon)\sim\varepsilon^{d_f/d_\omega-1}$. From $n(\varepsilon)$ we find the density of states $z(\omega)$. Since $\varepsilon_\alpha = \omega_\alpha^2$ and, according to the definition, $n(\varepsilon)d\varepsilon = z(\omega)d\omega$, we have

$$z(\omega)\sim\omega^{2d_f/d_\omega-1}. \tag{3.68}$$

The exponent $d_s \equiv 2d_f/d_\omega$ is called fracton or spectral dimension that substitutes dimension d of the Euclidean space in eq. (3.59) for the phonon density of states. For a percolating cluster d_s is close to 4/3 for all dimensions.

Oscillation excitations on fractals are called fractons. Contrary to the ordinary phonons, the fractons are strongly localized in space. From the above consideration it is easy to obtain:

$$\langle P(r,t)\rangle = \int_0^\infty d\omega z(\omega)\langle a(r,\omega)\rangle \exp(-\omega^2 t), \tag{3.69}$$

where $z(\omega)$ is normalized to one. As in the previous paragraph, the brackets $\langle\cdots\rangle$ denote the averaging over all possible configurations. For large r the reverse Laplace transform of $\langle P(r,t)\rangle$ can be fulfilled by a method of steepest descent that permits to identify a dominant exponential term:

$$\langle a(r,\omega)\rangle/\langle a(0,\omega)\rangle \sim \mathrm{Im}\left\{\exp\left(-\mathrm{const}\cdot c(d_\omega)(r/\lambda(\omega))^{d_\phi}\right)\right\}, \tag{3.70}$$

where

$$d_\phi = \frac{ud_\omega}{u+d_\omega}, \tag{3.71}$$

$$c(d_\omega) = \cos(\pi/d_\omega) + i\sin(\pi/d_\omega), \tag{3.72}$$

and

$$\lambda(\omega)^{-1} \sim \omega^{2/d_\omega}. \tag{3.73}$$

Using eq. 3.56 we find that $d_\phi = 1$meaning that the fractons are localized oscillations damping exponentially over the length $\lambda(\omega)$.

3.6 Percolation in active media

Percolation theory opens wide prospects for studying two-phase media. We made it certain when we considered filtration flows in section 3.4 We may give many other examples, when percolation in one of the contrast, in terms of physical properties, components of specially formed systems gives meaningful effects. However, a more interesting physical situation

occurs when development and inter-transformation of the components in a two-phase system are controlled by the dynamics of the system itself. Naturally, such transformations take place only in active media and are accompanied by consumption of free energy and dissipation [105]. The key role in this case is played by the phenomenon of the so-called Self-Organized Criticality, when a system evolves automatically to the state of dynamic equilibrium close to the percolation threshold [5, 10, 101, 106–108].

The simplest base model of active bistable media with recovery (inhibitor) is a system of two equations [26, 43, 109, 110]:

$$\begin{array}{rcl} \frac{\partial u}{\partial t} & = & f(u,v) + D\Delta u \\ \frac{\partial v}{\partial t} & = & -\varepsilon(v - v_0(u)) \end{array} , \tag{3.74}$$

where, depending on the problem, u can be local voltage in the nerve fibre or storm-cloud, temperature during propagation of fire fronts, concentration of chemical reagent and so on. The inhibitor v characterizes the rate of recovery of the active component, and the term $v_0(u)$ defines the system transition into the initial (passive) state as the active substance burns out. In the majority of real system ε is a small parameter. For the bistable media, the corresponding (3.74) point system ($D = 0$) represents a relaxation system with N-characteristic (Fig. 3.19) having three states of equilibrium: two stable (passive u_1 and critical u_c) and one unstable (active u_a). Qualitatively, the action of the inhibitor v results in the shift of the curve $f(u,v)$ along the vertical axis, as it is shown on Fig. 3.19. The corresponding (3.74) point system in this case can be either a triggered generator of isolated pulses (if the minimum of the curve $f(u,v)$ remains in the negative value range) or a self-excited oscillator (if in the process of decay of the inhibitor v the case corresponding to the top curve of Fig. 3.19 is realized).

Taking into account the diffusion summand in the first equation of system (3.74) leads to the generation of single excitation pulses in the waiting mode or continuous series of pulses in the case of self-oscillation. The pulse width and rate are determined by the exponents ε and D ($|f| \sim 1$) [26, 43].

Numerous researches of the base model 3.74) and its generalizations performed mainly for a 2-D case have revealed various types of regular and non-regular dynamics in the form of flat, circular and spiral waves of excitations and their modifications occurring at the presence of dislocations, phase correctors, etc. A question emerges if there are conditions in this combination of interactions for the appearance of fractal structures. In advance we may give a plain answer that such fractal dynamics occur in a certain range of control parameters. In our problem there are three such parameters: these are the exponent ε characterizing per se the rate of free energy feeding to the system, the relation $x_c = u_c/u_a$ determining the relative distance between the stable (critical) and unstable (activation point) states of equilibrium (see Fig. 3.19), and frequency ξ of occurrence of the external (trigger) signal on the system inlet. The exponents ε and ξ are non-dimensional and are compared with the reverse time of the excitation pulse formation. The characteristic spatial dimensions of the system also play

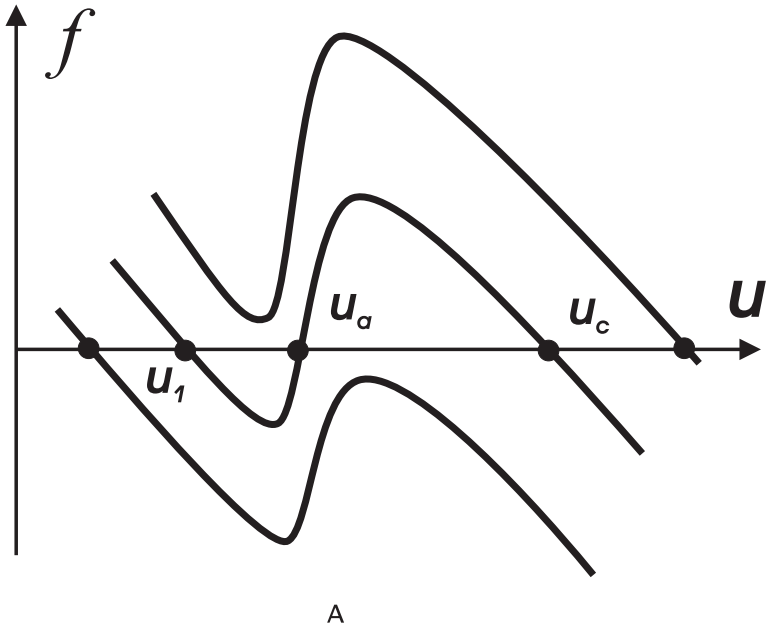

Figure 3.19: Three possible situations for the lumped active element: low curve is the passive state, middle curve is the waiting or bistable mode, top curve is the self-excitation and self-oscillation

an important role. And, at last, we should take into consideration space-time fluctuations at the occupation of the system by the active phase. The role of these fluctuations diminishes according to the law of large numbers as the system is being occupied. However, they may turn out to be principal at $\varepsilon \to 0$. It is extremely difficult to study the role of the above factors within the frameworks of the system (3.74), especially in our 3-D case. Therefore, we will proceed further to more simple description of the dynamics (3.74) by means of cellular automation.

Excitation takes place in the areas with the exceeded threshold of the medium activation. During the slow changes of the above-threshold configurations as compared with relaxation (the time of excitation transfer) the process is controlled by the percolation effects.

We will start by considering a simple but conceptual model, in which the percolating elements are trees growing in the sites of a square lattice. The critical parameter of the geometrical part of the problem most likely can be the density of the sites occupied by trees. First a model of forest fires was presented by Bak, Chen and Tang in 1990 [111] and later in 1992 it was further developed by Schwabl and Drossel [112]. We will discuss exactly this last variant of the model.

So, let us assume that the dynamics of the number of tree is determined by the following simple rules:

1. Trees appear in the sites of the lattice with the probability ε per time unit. We do not take into account the details of trees growing, but offer a binary scheme of the growth: at a certain moment of time the site is considered to be occupied by a tree and before

this it is considered empty.

2. The thunderbolt strikes a site of the lattice with the probability θ per time unit. If the site is occupied by a tree, the tree catches fire. Otherwise, the sites state does not change.

3. If the nearest neighbours of the site occupied by a burning tree are also occupied by trees, then these trees take the fire at the next step of the model time with the probability 1. The nearest neighbours of the site are its four adjacent neighbours.

4. At the following step of the model time the site occupied by the burning tree becomes empty.

Percolation effects in this problem have become significant when the following double limit is observed

$$\varepsilon \to 0, \quad \theta/\varepsilon \to 0. \tag{3.75}$$

In this case the system reaches the stationary level of occupation by tree clusters $p \lesssim p_c$ widely ranging in size. In the absence of lightening the clusters gradually grow and coagulate. Rare thunderbolts burn out only a small part of these clusters, not affecting the distribution of clusters by size attributed to the static percolation. When relation (3.75) is observed, the characteristic time of burning-out of a large cluster cannot compete with the characteristic interval between new trees occurrence.

The top graph in Fig. 3.20 shows evolution of the number of burning trees; the bottom graph depicts dependence of the specific number of growing trees on time. One may see that the specific number of trees fluctuates close to the threshold level $p_c \simeq 0.58$ not exceeding it. This critical level is maintained by the balance between the processes of trees growing and destruction by fires.

Frequency of occurrence of fires seizing a certain number of trees is shown in Fig. 3.21 as function of this number in a log-log scale. A power law character of this dependence is obvious, that points out to the self-similarity of the space-time dynamics of the fires - in a wide range, characteristic sizes of clusters and characteristic frequencies of their occurrence are not available.

Scaling is limited on the one hand by the system dimensions and time of count, on the other hand by the size of the cluster containing just a single tree and the reverse frequency of occurrence of these minimal fires. The characteristic interval between frequent small events constitutes hundreds of steps of the model time.

The dynamics of the studied model is interesting in two aspects. Firstly, it proceeds in the critical mode of strong fluctuations: in advance we cannot say in what cluster, large or small, next thunderbolt will strike. The clusters have a fractal percolating structure, consequently,

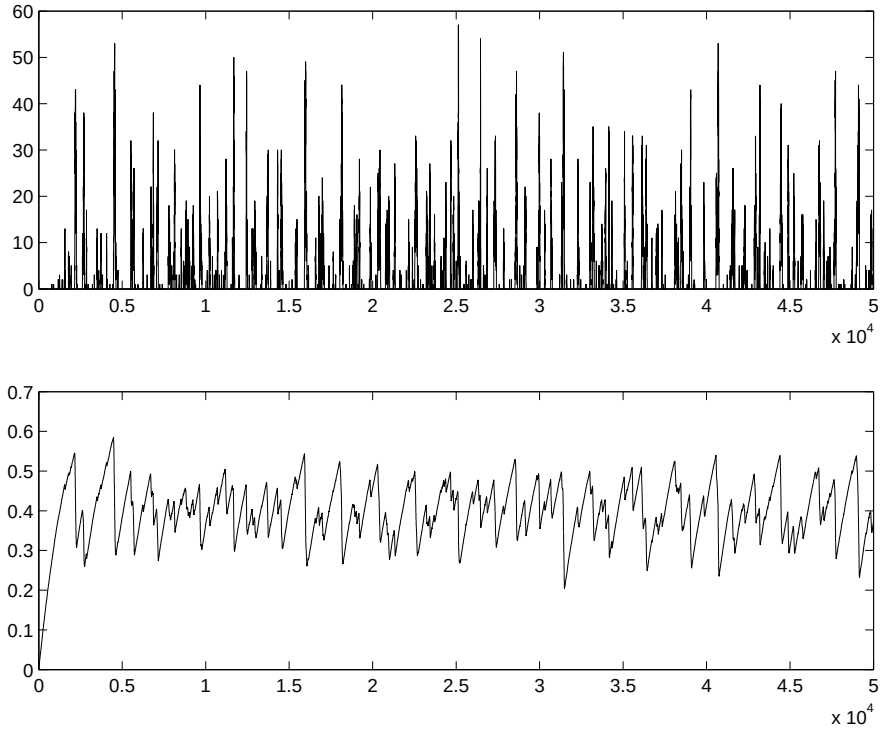

Figure 3.20: Evolution of the number of the burned-out trees

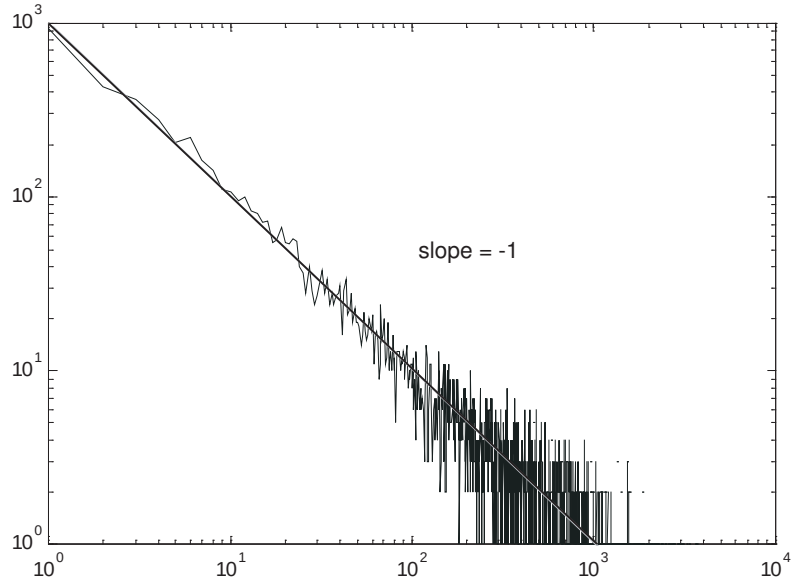

Figure 3.21: Frequency of occurrence of fires as function of their sizes in a log-log scale

the similar structure is observed in the patterns of the fire occurrence. In other words, the dynamics critical character the absence of characteristic space-time scales depends on the fractal nature of real configurations of the system. Secondly, we deal with the self-organized dynamics: when relation (3.75) is observed the system independently passes from the initial state with $p = 0$ to the level of generation of fractal dissipation structures $p \lesssim p_c$. Such

a non-trivial combination of criticality and self-organization is reflected in the name of the actively developing today paradigm of self-organized criticality [5, 10].

Now we will consider a more interesting from the physical point of view analogue of the forest fire model and see that the percolation phase transition can provide a non-trivial fluctuation mechanism of suppression of instabilities growth in active media. Imagine an excited medium formed by a 3-*D* lattice of the cellular automations. Each site of the lattice is given a corresponding time-dependable scalar value u characterizing the value of its electrical potential. Evolution of the potential relief on the lattice is determined by means of a random growth model. Normally distributed random increase of the scalar field value on the lattice sites takes place exactly with each step of the model time. During this, each site performs a Brownian motion in the space of the scalar potential values independently from its neighbours. The potential relief growth is limited by a certain critical value of the voltage u_c between the neighbouring sites; on reaching this value a disruptive discharge takes place that evens the potential between the neighbours. One may suppose that at the next step of the model time this breakthrough can initiate the rapture of the neighbouring bonds (infect the neighbours), provided the potential applied to them exceeds a certain fixed level - the level of activation u_a which is smaller that the critical level.

Let us define general criteria of the critical dynamics occurrence. The numerical experiment, for instance, has revealed the existence of a critical level of population, fluctuations near which possess scaling features. Moreover, the experiment has shown the dependence of this level on the number of the nearest neighbours for the given lattice of automations, i.e. on its coordination number z. The larger the number of elements being in contact with the infected one, the higher the probability of infection spreading, and hence, the lower the critical level of population. The coordination number increases with the increase of the lattice dimensions. Within the limits of high coordination numbers approximation of the mean field can be used for calculating the critical level of population. Let us introduce the function $f(u)$ of the bond distribution by the absolute potential drop. The value $f(u)du$ defines the fraction of bonds with the absolute potential difference in the interval $[u, u+du]$. In any fixed moment of time all the bonds in the system can be divided into three types:

1) active, their specific number $p = \int_{u_a}^{u_c} f(u)du$;

2) passive with the specific number $q = \int_{0}^{u_a} f(u)du$;

and

3) burning, i.e. those that during time τ return from the active state to the passive with the zero voltage.

Evolution of the function of bond distribution by the potential difference at their ends is described by the following equation:

$$\frac{\partial f}{\partial t} = D\frac{\partial^2 f}{\partial u^2} + I - \Omega f, \tag{3.76}$$

where the coefficient D stands for the coefficient of bond diffusion by voltage, and the decrement Ω is defined by the relation:

$$\Omega = \begin{cases} 0 & 0 \le u \le u_a \\ \text{const} & u_a \le u \le u_c. \end{cases} \tag{3.77}$$

The last dissipative term in eq. (3.77) characterizes the mechanism of growth limitation due to microraptures. It is clear that the dissipation in equation (3.76) is formal: all the bonds taken out of the process of growing in the interval from the level of activation and the critical level in the time τ return to the zero voltage point:

$$I = \begin{cases} m\delta(0) & 0 \le u \le u_a \\ 0 & u_a \le u \le u_c, \end{cases} \tag{3.78}$$

where $\delta(u)$ is the Dirac delta function,

$$m = -D\frac{\partial f}{\partial u}\bigg|_{u=u_c} + \Omega p. \tag{3.79}$$

Here the exponent $s = -D\dfrac{\partial f}{\partial u}$ characterizes the density of bond flow in the space of potential difference. The first summand in the right hand part of eq. (3.79) corresponds to the specific number of bonds that have reached the critical value u_c of the potential difference per time unit. The second summand corresponds to the fraction of bonds taken out of the process of growth by the mechanism of activation. The sum of them characterizes the rate of bond occurrence in the point $u = 0$.

In the absence of the last two terms this equation represents the Fokker-Planck equation that describes the diffusion expansion of the distribution function in the space of potential difference in the process of growth.

It is correct to write down the following condition of maintaining the number of bonds in the system:

$$p + q + m\tau = 1. \tag{3.80}$$

In this case the distribution function takes into account just active and passive bonds; thus:

$$\int_0^{u_c} f(u)du = 1 - m\tau. \tag{3.81}$$

Let us introduce new variables and definitions: $T = u_a^2/D$; $\tilde{t} = t/T$; $x = u/u_a$; $x_c = u_c/u_a$,then eq. (3.76) can be rewritten as follows:

$$\frac{\partial f}{\partial \tilde{t}} = D\frac{\partial^2 f}{\partial x^2} + \tilde{I} - \alpha f, \tag{3.82}$$

where

$$\alpha = \begin{cases} 0 & 0 \le x < 1 \\ \Omega T & 1 \le x \le x_c \end{cases}, \quad \tilde{I} = \begin{cases} mT\delta(0)/ & 0 \le x < 1 \\ 0 & 1 \le x \le x_c \end{cases}. \tag{3.83}$$

A stationary solution of equation (3.82) has the following view:

$$f = \begin{cases} C_2 - C_1 x & 0 \le x < 1 \\ (C_2 - C_1)\exp\sqrt{\alpha}(1-x) & 1 \le x \le x_c \end{cases}. \tag{3.84}$$

Using the flow continuity at the point $x = 1$ and the condition of eq. (3.80) we obtain:

$$C_2 = C_1\left(1 + \frac{1}{\sqrt{\alpha}}\right), \quad C_1 = \left(\frac{1 - \exp\sqrt{\alpha}(1-x_c)}{\alpha} + \frac{1}{2} + \frac{1}{\sqrt{\alpha}} + \frac{\tau}{T}\right)^{-1}. \tag{3.85}$$

Compact expressions for p and have the view:

$$p = C_1\left\{1 - \exp\left[\sqrt{\alpha}(1-x_c)\right]\right\}\Big/\alpha, \quad m = C_1/T. \tag{3.86}$$

The characteristic view of the function of bond distribution by potential difference is shown in Fig. 3.22.

Turning back to the discrete model, one may notice that the value of the coefficient of diffusion D is proportional to the dispersion $\tilde{\delta}$ of normally distributed portions of the potential added to the changing relief at every step of the model time: $D = \tilde{\delta}/\tau$. Thus, $T = u_a^2/\tilde{\delta}\tau$. For calculations we have selected the time of relaxation τ equal to the step of the model time: $\tau = 1$.

The coefficient Ω, characterizing dissipation, can be related to the coordination number z of the discrete model. Indeed, integrating u in equation (3.76) within the range from u_a to u_c, we obtain:

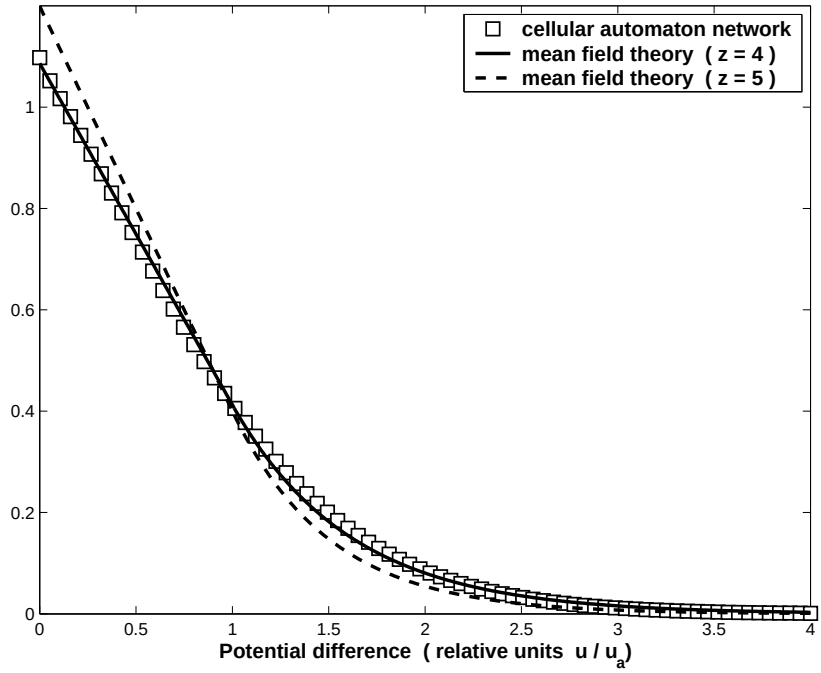

Figure 3.22: Function of bond distribution by potential difference for $x_c = 4$. The solid graph corresponds to the theoretical dependence with $z = 4$. For a simple cubic lattice the number of outgoing bonds $z = 5$. The corresponding curve is shown as a dotted line. The squares represent the numerical experiment.

$$\frac{\partial p}{\partial t} = s(u_c) - s(u_a) - \Omega p. \tag{3.87}$$

Equation (3.87) describes the change of the number of activated bonds. The last member of the equation corresponds to the induced burning-out of the bonds and is equal to the product of multiplying the specific number of bonds m burnt out per time unit by the number of their nearest activated neighbours pz. Thus:

$$\Omega = mz \tag{3.88}$$

or

$$z = \alpha / C_1. \tag{3.89}$$

Dissipation increases with the increase of the number of nearest neighbours, while the exponential term in eq. (3.86) decreases and the value p asymptotically tends to $1/z$. The situation is similar to the percolation spreading of infection on the multidimensional lattices, where the value $1/z$ corresponds to the percolation threshold. In spaces with actual dimensions

wide fluctuations affect the mean field asymptotic form, though solution (3.84) remains true even for small space dimensions. Fig. 3.23 shows the dependence of pz on z.

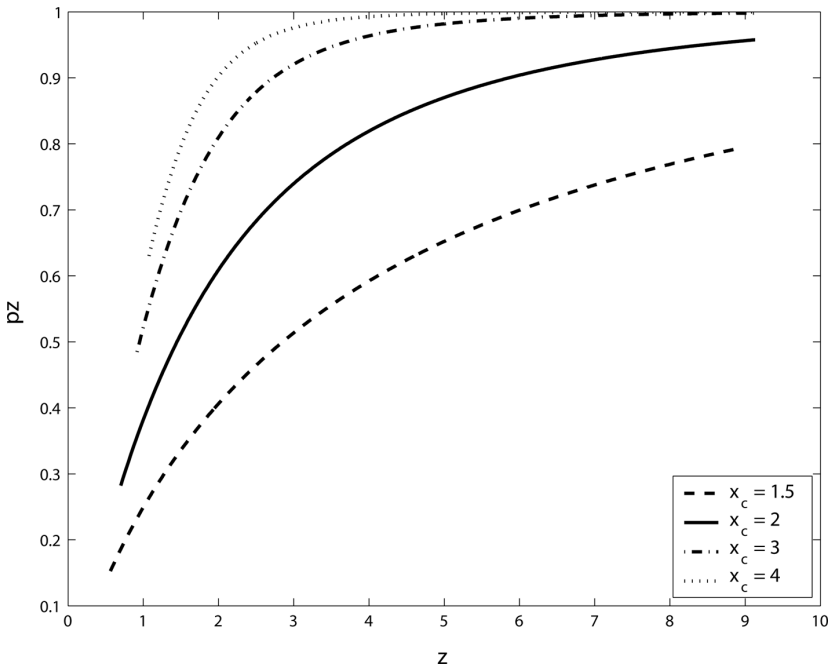

Figure 3.23: Dependence of pz on z at the different ratios of the critical level and level of activation

If in the initial moment of time there is no relief: $f(u,0) = \delta(0)$, then before the appearance of the first pare in the system, bond distribution in the space of potential difference will remain Gaussian:

$$f(u,t) = \sqrt{\frac{2}{\pi\tilde{\delta}t/\tau}}\exp\Big\{-\frac{u^2}{2\tilde{\delta}t/\tau}\Big\}, \quad t < T_c. \tag{3.90}$$

The characteristic time interval T_c before the appearance of the first critical pare depends on the system dimensions and can be calculated by means of the following relation:

$$\int_{u_c}^{\infty} f(u,T_c)du = 1/M, \tag{3.91}$$

where M is the number of bonds in the system (for a simple cubic lattice having N^3 sites, $M = 3(N^3 + 2N - 1)$). Relation (3.91) presupposes the occurrence of at least one critical bond in the limited system. Note that in the thermodynamic limit dealing with an unlimited system the time interval T_c tends to zero: the critical pares appear immediately with the commencement of the growth process. Let us write down an integral in the left-hand part of eq. (3.91) via the probability integral:

$$\int_{u_c}^{\infty} f(u,T_c)du = 1 - \int_{0}^{u_c} f(u,T_c)du = 1 - \mathrm{erf}(y)/2, \tag{3.92}$$

where

$$y = \frac{u_c}{\sqrt{\tilde{\delta}T_c/\tau}}, \tag{3.93}$$

and using a well-known asymptotic form for the probability integral for large arguments

$$1 - \mathrm{erf}(y)/2 \approx \frac{\exp(-y)}{\sqrt{\pi}y}\big(1 - \frac{1}{2y^2}\big), \tag{3.94}$$

we derive an expression for the time T_c assessment:

$$\frac{1}{M} \approx \frac{\exp(-y)}{\sqrt{\pi}y}\big(1 - \frac{1}{2y^2}\big). \tag{3.95}$$

For the cubic lattice having million of sites, $M = 300597$.Choosing parameter $u_c^2/\tilde{\delta} = 2.5 \cdot 10^5$ and using eqs. (3.93) and (3.95) we find $T_c \approx 100\tau$. The influence of the system dimensions on the dynamics nature turns out to be insignificant provided the specific number of activated bonds in the system at the moment of the first rapture does not exceeds the percolation threshold for a site problem on a corresponding lattice:

$$\int_{u_c}^{\infty} f(u,T_c)du = \frac{1}{2}\Big\{\mathrm{erf}(y) - \mathrm{erf}(yu_a/u_c)\Big\} \lesssim p_c, \tag{3.96}$$

From the last expression we obtain a minimum acceptable value of the ratio u_a/u_c. For the above chosen parameters the minimum acceptable value of the ratio $u_a/u_c \simeq 0.25$. If condition (3.96) is not observed, a number of new dynamic regimes occurs in the system: occurrence of periodic and stochastic self-oscillations, spreading of continuous fire fronts under periodic boundary conditions, etc. The mentioned effects depend exclusively on the limited nature of the system and, hence, do not occur in the thermodynamic limit.

3.7 Self-organizing drainage systems

In the previous section we have learnt that the occurrence of fractal structures in the configuration space of active systems requires a sharp contrast regarding a small time of internal

relaxation against the background of a long-continued interval of characteristic changes of an external action. In the model of forest fires, for instance, the time of burning-out of a discrete cluster of trees is considerably smaller than the characteristic period of the tree growing. And the level of occupation of the model lattice by trees constitutes the critical parameter of the percolation transition. In this section we will again analyse the situation when the critical parameter of the percolation transition itself becomes an internal dynamic variable of the system.

Self-organizing drainage systems appear from percolating networks and labyrinths in the presence of an external field, and their structural properties are very much alike the drainage systems of large rivers basins. Therefore, we will start with the description of the stationary structure of the drainage system flows of the river basins which is accepted in hydrology and based on the empirical laws of Hack, Horton and Tokunaga. We should underline from the very beginning that the significant difference between the self-organizing drainage networks and the stationary structure of the river streams is the dynamic nature of the former.

Hydrology laws. The drainage systems are a universal property of the earth landscapes. Small streams merge forming large streams; the large streams join into rivers, and so on. The territory from which a river collects water to discharge it finally into an ocean constitutes a catchment or a river basin. Any basin is characterized by the area (or volume in a more general case) V, the length of the main flow l and the dimensions $L_{\|}$, $L_{\perp}$. There are known several scaling relations empirical laws that relate these exponents to each other. The most commonly used is the Hacks law stating that the main flow length l changes with the increase of the basin area as

$$l \sim V^h, \tag{3.97}$$

where h is usually called the Hacks exponent. In spite of eq. (3.97), there is a whole number of relations connecting the basin area V, the length of its main flow l and its cross-section dimensions $L_{\perp}$ with the characteristic longitudinal dimension of the basin drainage system $L(=L_{\|})$:

$$V \sim L^D, \quad l \sim L^{Dh}, \quad L_{\perp} \sim L^{d_{\perp}}. \tag{3.98}$$

Moreover, it was found out that the histograms of basin areas and main flow lengths for each individual landscape had a power-series distribution.

A quantitative description of the ordered stream system had been introduced by Horton and Strahler even long before the occurrence of the fractal paradigm. Streams depicted on a standard topographic map and having no tributaries upstream are defined as the streams of the first order $(i = 1)$. When two streams of the first order interflow, they form a stream of the second order $(i = 2)$. When two streams of the second order meet, they form a stream of the third order $(i = 3)$, and so on. Moreover, the streams of the first order $(i = 1)$ can flow into the streams of the second $(i = 2)$, third $(i = 3)$ order and any other streams of a higher

order. In a similar manner the streams of the second order $(i = 2)$ can joint the streams of the third order, etc. Summarizing the above mentioned rules, one may state that when an i_1-stream merges with an i_2-stream the resulting stream has the order

$$i = \max(i_1, i_2) + \delta_{i_1,i_2}, \tag{3.99}$$

where δ is the Kroneckers delta. In other words, the order increases only when two equivalent streams merge.

Horton defined the bifurcational coefficient R_b and the coefficient of length ranking R_r as relations:

$$R_b = \frac{N_i}{N_{i+1}}, \quad R_r = \frac{r_{i+1}}{r_i}, \tag{3.100}$$

where N_i is the number of streams of i-order, r_i is the mean length of an i-order stream.

Analysis of real hydrological data has revealed an approximate stability of the coefficients R_b and R_r at the change of the stream order in any drainage system. These empirical facts are called the Hortons laws. Using the iteration definition of the fractal dimension

$$d_f = \frac{\ln(N_i/N_{i+1})}{\ln(r_{i+1}/r_i)} \tag{3.101}$$

and inserting relations (3.100) in it, we obtain an expression for the drainage system fractal dimension

$$d_f = \frac{\ln R_b}{\ln R_r}. \tag{3.102}$$

In other words, the validity of the Horton laws confirms that the drainage networks are fractal trees.

Dynamic generalization of Hacks laws. The suggested dynamic generalization of laws (3.97) and (3.98) is based on the scaling dependency of the lifetime of a drainage system fragment on its characteristic spatial dimensions. Fundamentally, we speak about broadening and transferring the property of self-affinity from the spatial continuum on to the space-time continuum. Relations (3.97) and (3.98) should be supplemented with the scaling dependency of the drainage system lifetime on the longitudinal dimension $L(= L_{\|})$:

$$T_L \sim L^{-d_T}. \tag{3.103}$$

On the analogy of the hydrological parameters we may introduce the coefficient of lifetime ordering according to the formula:

$$R_\tau = \left(\frac{\tau_{i+1}}{\tau_i} \right)^{\delta_\tau}, \tag{3.104}$$

where τ_i is the mean lifetime of the i-stream, and δ_τ is the exponent different from one.

The analysis has shown that at certain δ_τ the coefficient of lifetime ordering demonstrates an approximate stability during the change of the stream ordering.

Previously we already underlined that to construct a consistent algorithm of hierarchical system formation, a vector activation should be taken into consideration. The conductive bonds occurring in the system in this case are characterized additionally by the direction of the current. From the point of view of the graph theory, conductive clusters occurring in our model represent suspended oriented trees, i.e. graphs the edges of which have a certain orientation - the direction from one vertex to another and which are characterized by the value of the current passing along this direction.

Let a pare of figures (a,b) equal accordingly to the number of incoming and outgoing edges be assigned to each vertex. The value $a+b-1$ coincides, apparently, with the ramification index. The entire periphery in this case can be divided into two groups: vertexes of type $(1,0)$ and of type $(0,1)$. The occurrence of a critical pare corresponds to the formation of a pare of two adjacent vertexes, one of which belongs to the type $(1,0)$ and the other to the type $(0,1)$. Then, in the case of the vector activation the state of the active periphery vertex of type $(1,0)$ transfers in to the state of type $(1,n)$, where n is the number of newly activated neighbours of the given vertex. Similarly, the state of the active periphery vertex of type $(0,1)$ transfers in to the state of type $(n,1)$. Thus, the whole array of vertexes of the evolving structure is distributed between the types $(1,n)$ and $(n,1)$ with the positive integers n.

With the vector nature of activation the initial critical pare of vertexes almost always remains in the stem of a forming cluster. A stem is an unbranched central part of a structure representing a chain of vertexes of type $(1,1)$ and their incident edges. The stem ends by a pare of vertexes, one of which is of type $(1,n)$ and the other is of type $(n,1)$. The vertexes of type $(1,n)$ with $n \geq 2$ and the incident edges form the crown of the oriented tree, while the vertexes of type $(n,1)$ and their incident edges form the root.

It is obvious that not all structural elements of the forming conductive cluster are equal in terms of the current passing along them. For instant, the current in the cluster stem exceeds considerably the currents on the periphery, and the closer to the stem, the stronger the current, as well as the longer the lifetime of a structural element. The reverse influence of the currents on the geometry of a forming cluster is also important. It is useful to perform a self-consistent assessment of this influence in terms of the current system hierarchy. The procedure of the hierarchy formation is the following:

1. 1. Consider the crown of an oriented structure (type $(1,n)$). Assign a hierarchy level $h = 1$ to all edges of the crown.

2. 2. Select a vertex on the crowns periphery and move from it towards the stem. Skip all vertexes with $n = 1$. Stop on the vertexes with the ramification index $r \geq 2$.

3. 3. Repeat step 2 for all periphery vertexes on the crown (type $(1,0)$).

4. 4. Cut off the passed edges and define the stops as a new periphery (renormalization). Raise the hierarchy level of the remaining crown edges by one.

5. 5. Repeat steps 2, 3, 4 until you reach the stem.

6. 6. Remember the hierarchy level of the stem $h_t^- = \max(h)$. The sign minus denotes here that the calculations refer to the crown elements.

7. 7. Repeat all the previous steps for the root of the structure and at the last stage remember the hierarchy level of the stem $h_t^+ = \max(h)$ calculated based on the root elements of the structure.

8. 8. Assign the hierarchy level corresponding to the maximum values h_t^- and h_t^+.

9. If $h_t^- > h_t^+$, raise the hierarchy levels of all root elements by $h_t^- - h_t^+$. If the contrary condition is valid, raise the hierarchy levels of all crown elements by $h_t^+ - h_t^-$.

The meaning of the last step of this procedure is that the hierarchical importance of the stem depends entirely on the mass of the maximum construction it supports (root or crown). The recessive part of the structure can be simply absent (discharge to the ground). This step is not valid for $h_t^- = h_t^+$, i.e. in case of hierarchical symmetry of the crown and root. A typical configuration of a conductive tree, the edge thickness of which is proportional to the current passing along them is shown in Fig. 3.24. The modelling was carried out on a cubic lattice $65 \times 65 \times 65$.

The level of bond hierarchy is an additional parameter, which widens the possibilities of the above base model. Let us change, first of all, the rule, according to which the conductive elements of the cluster disappear. If a peripheral vertex does not find activated neighbours and its incident edge has the minimal level of hierarchy $h = 1$, it dies off together with its conducting edge, and the role of periphery is passed over to its nearest predecessor provided the latter is not a branching point. But if the level of hierarchy of its incident edge $h \geq 2$, active properties of the peripheral vertex (i.e. the ability to initiate neighbours) remain.

Due to the above described modernization, at the appearance of asymmetry an interesting effect can be noticed: the elements of the recessive substructure have become long-livers - they cannot disappear while the level of hierarchy corresponding to them exceeds one. Only degradation of the dominant substructure to the level of the recessive substructure can put an end to it.

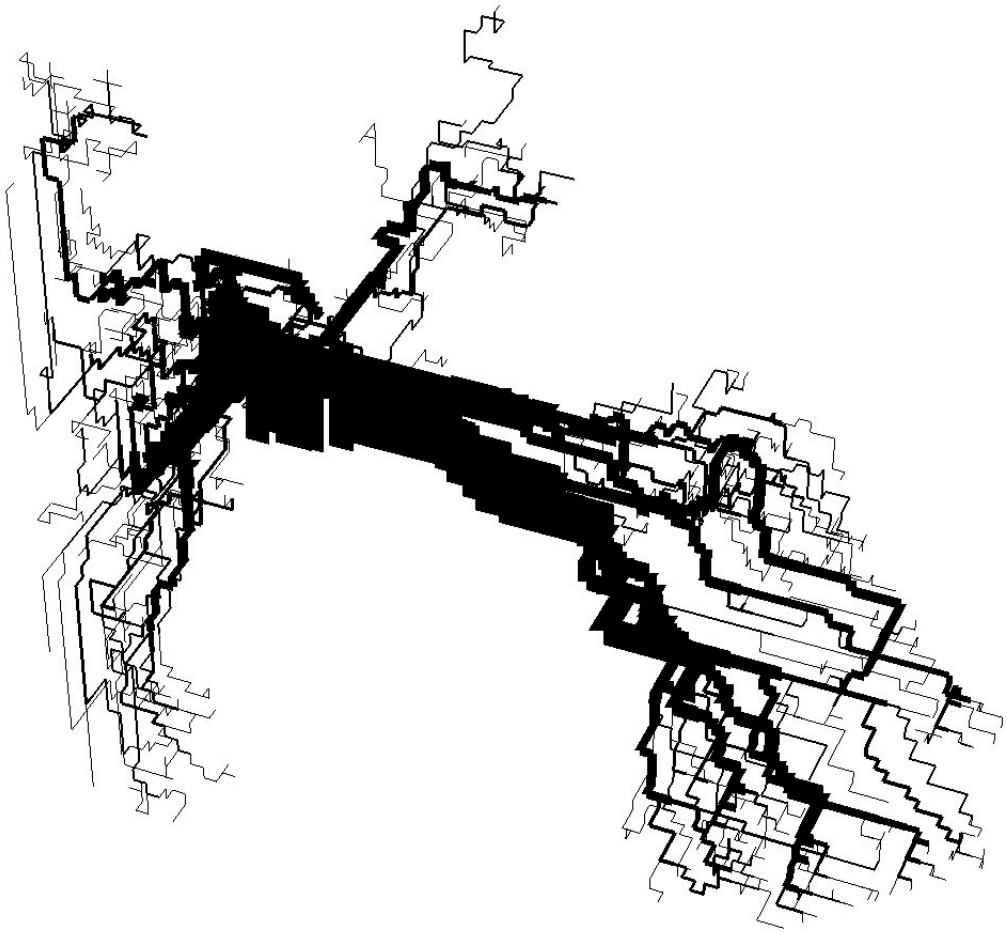

Figure 3.24: Instantaneous 3-*D* configuration of a model tree, the edge thickness of which is proportional to the current passing along them

3.8 Percolation mechanism of gravitational differentiation

In this section for considering the fractal dynamics of a two-component system we will use the example of seismogenesis [97,98,113,114]. In our case lithosphere substrate represented by saturated solution of a light mobile fraction in heavy viscous solvent will be considered as a two-component system. We will see that as the light component reaches the percolation threshold the substrate looses stability in the gravitational field. The discussed mechanism of the lithosphere substrate activity manifests particularly during the shift of the connected field of fractures in the solid lithosphere of the Earth.

Evaluation of the maximum height of mountains on planets, known from the elementary course of geophysics, is based on the statement that the pressure at the foundation should not exceed the shear strength of material σ_0:

$$h_{max} = \frac{3\sigma_0}{\rho g}, \tag{3.105}$$

where ρ is their density, g is the absolute value of the gravitational acceleration. This simple evaluation is well confirmed by the observation data of the planets of the Earth group presented in Table 3.2.

Table 3.2: Maximum height of mountains on the planets of the Earth group

Planets	Parameters		
	g, m/s ^{2}	h_{max}, km	Mountain height, km
Earth	9.78	11	Everest – 9
Venus	8.69	13	Maxwell Mons – 12
Mars	3.72	30	Olympus Mons – 24 Arsia Mons – 27

Obviously, the analogous limitation is true for the maximum size of caverns in the planets lithospheres. The maximum size of a cavern filled-up with liquid or gas is estimated by the value [115]:

$$R_g \approx \frac{\sigma_c}{\Delta\rho g}, \tag{3.106}$$

where σ_c is the minimum value of the rupture and shear strengths of the material, $\Delta\rho$ is the difference between the densities of the material and fluid the cavern is filled with. The density difference of the media controls the hydrostatic pressure distribution along the cavern height. (In particular, a network of connected fractures in a lithosphere can play a role of a cavern). In this case, if a cavern or a network of fractures historically was formed by the fluid it was being filled at that moment, the mean pressure in the cavern should coincide with the pressure in the matrix. The difference of the hydrostatic pressure distribution along the height at a smaller density of the fluid, as compared with that of the hard matrix, leads to the formation of a higher pressure at the upper part of the cavern (or fracture network) and a lower pressure accordingly at the bottom of the cavern comparing with the surrounding pressure. If the cavern is high enough, the pressure difference can exceed either the material ultimate rupture strength at the upper part or shear strength at the bottom. Depending on what part of the cavern the condition of criterion (3.106) is observed, either the fracture opening at the upper part of the cavern takes place, or the material breaking and fracture closing (healing) at the caverns bottom occur. The opening of fractures at the upper part causes gradual fluid flowing into the fractures and the pressure reducing at the bottom that in the end will lead to the fracture closing at the caverns bottom and the fluid pressure increase. If the fracture healing at the bottom of the cavern takes place first, the general pressure of the fluid increases, resulting in the fracture opening at the upper part.

Thus, if the size of the cavern or field of connected fractures in the lithosphere exceeds criterion (3.106), the cavern cannot remain static: it either rise to the near-surface zone of connected pores, or it changes its shape making criterion (3.106) invalid.

Criterion (3.106) can be obtained also based on the energy considerations likewise the clas-

sical Griffiths criterion of formation of a spherical fracture. The idea is based on the energy conservation law. When a load is applied to a sample, elastic potential energy stores in it. Part of this energy is released with the occurrence or growth of a fracture. On the other hand, the formation and growth of a fracture create new free surfaces. Therefore, a fracture grows just when the yield of the elastic potential energy equals or exceeds energy expenditures for creation of new free surfaces. This is the concept of Griffiths energy balance, which can be formally written in compliance with the equilibrium requirements as

$$\frac{dU}{dr} = 0,$$

where free energy $U = \Lambda r^2 - \frac{\sigma_c^2}{\hat{E}} r^3$, Λ is the density of surface energy, $\hat{E}$ is the Youngs modulus. But this criterion is invalid for global scales.

The fact is that under gravitation the occurrence of fractures requires a source of energy which is enough not only to form new surfaces but also and mainly for mass transfer in the field of gravitation. A modified Griffiths criterion (gravitational Griffiths criterion) can be written in the following form:

$$\frac{dU}{dr} = 0, \quad U = \Lambda r^2 - \frac{\sigma_c^2}{\hat{E}} r^3 + \Delta\rho g r^4. \tag{3.107}$$

When the characteristic fracture scale r increases, the last term of equation (3.107) suppresses entirely other parts, and we obtain a corresponding estimation of the critical radius $R_s \simeq \frac{\sigma_c^2}{\hat{E}\Delta\rho g} \simeq \frac{\sigma_c}{\hat{E}} R_g$.

For the lithosphere of our planet $\Delta\rho \sim 2 \cdot 10^3$ kg/m^3, $\sigma_c \sim 10^8$ Pa, and the critical vertical size is estimated $R_g \sim 5$ km. We have obtained an important assessment: in the Earths lithosphere there cannot exist caverns or zones of connected porosity with a characteristic vertical size exceeding 5 km. This estimation has been done for olivine, for sedimentary rocks the σ_c-value is smaller by a factor of ten. That is why the vertical size of the connected porosity zone in the sedimentary rocks does not exceed 500 m. We underline again that this criterion does not depend on the shape of a cavern, just its vertical size matters. So a system of connected pores or fractures permeable to filtration streams of fluid or gas turns out to be unstable in the gravitation field if its vertical sizes exceed the R_g-value [98, 115, 116]. For example, a system of connected fractures that exposes to the day light cannot reach the depth exceeding R_g. And the actual volume of the pore space can constitute an extremely small value as compared with R_g^3.

So, the critical level of porosity leads to the occurrence of transparence zones, i.e. macroscopic zones of geometrically connected pores - clusters of the gas component. The lower part of the transparence zone is characterized by the deficiency of the pore pressure as compared with the lithostatic one. While its upper part includes areas with the superfluous pore

pressure. The pore pressure difference is proportional to the size of the transparence zone and is compensated by the transparency of the solid matrix. At a certain critical size of the gas component clusters the level of pore pressure fluctuation exceeds the rock strength, and the solid matrix fails. Gas rises to the upper layers, where the superfluous pore pressure provokes further destruction of the solid matrix. The process of degassing, in such a way, turns the lithosphere into a distributed seismic generator, which source of energy is a potential energy of undifferentiated lithosphere material in the planet field of gravitation. The discussed percolation mechanism ensures direct transformation of the potential gravitation energy into the energy of destruction.

Based on the conceptions of the percolation theory the described above qualitative considerations can be given quite concrete quantitative features [27, 29, 116, 117]. Let us assume that in a volume of solid substratum there exist randomly distributed zones transparent for filtration flows. We are not interested in the details of rock morphology: the transparency can be caused either by fractures or porosity, or by their combination. The system simulates a small part of the lithosphere with the dimensions exceeding considerably the critical scale, but at the same time much smaller than the planet radius $L \ll R_{\otimes}$), and it can be considered as a flat layer in a homogeneous field of gravitation. Let the characteristic size a of the transparence zones be significantly smaller than the critical scale R_g: $a \ll R_g$. Let us introduce a random function of coordinates $\xi(\mathbf{r})$ being 1 for the transparence zones and 0 otherwise. A corresponding function of distribution is a sum of two delta functions:

$$f(\xi) = q\delta(0) + p\delta(1), \tag{3.108}$$

where p and q are the volumetric fractions of the zones of transparency and opacity, respectively. It is obvious that $p+q=1$. Note that the introduced notion of the medium transparency, by all means, is related to the porosity and fractures, but not directly. For instance, at significant but non-connected porosity the transparency is null. At the same and even less but connected porosity (fractures) the transparency will be non-zero. The global transparency of the system in general is determined by the mean value $\langle \xi(\mathbf{r}) \rangle$, i.e. by a fraction of the space occupied by the transparence zones. For small p-values, discrete transparence zones are either isolated from each other, or form small-size clusters of connected zones. At $p \ll 1$ the global transparency does not exist, for there are no long enough chains of adjacent transparence zones connecting the opposite sides of the system. Vice versa, at $p \sim 1$ the overwhelming fraction of space has become transparent, the transparence zones form a giant cluster ensuring the passage of gas filtration flows from one side of the system to the other. There is a certain critical value $p = p_c$ at which transition of the macrosystem from the opaque (for $p < p_c$) to transparent state (for $p > p_c$) occurs. The critical value $p = p_c$ is called a percolation threshold. In a 3-D case for a wide class of random fields, the autocorrelation function of which decays faster than $1/r^3$, the percolation threshold constitutes $p_c \simeq 0.16$.

Now let us consider mechanical stability of an assembly of transparence zones in the field of gravitation. We will be interested in that part of mechanical stresses in materials that appears in the field of gravitation due to the density difference of gas and solid matrix. If the

vertical dimension of a transparence cluster is H, the gas pressure in its upper part exceeds the mean lithostatic pressure by the value $\Delta P = \Delta\rho gH/2$, while in the lower part the gas pressure yields to the lithostatic pressure by the same value ΔP. Note that for the exposing transparent clusters the deficiency of the pore pressure at their lower part is twice as much of the corresponding pressure difference of the isolated clusters[†].

The disbalance of the pore pressure is being compensated by the rock strength until the value ΔP has reached values comparable with the rock ultimate strength. It happens when the transparence cluster vertical dimensions reach values of R_g order. It means that just transparence clusters with dimensions not exceeding the critical scale R_g can exist stably in the lithosphere of the planet, and, consequently, just an undercritical assembly of transparence zones with the specific volume $p < p_g$, where $p_g = p_c - (R_g/a)^{-1/\nu}$, can be stable in the field of gravitation. If x is the characteristic level of porosity in the transparence zones, the actual volume of voids in a cluster with dimensions close to the critical radius constitutes $xa^3(R_g/a)^{d_f}$.

Note that the instability under consideration is similar to that of the metal-insulator composites with regard to the dielectric breakdown in an external field [118]. When the volume of conducting elements is close to the percolation threshold, the critical field for a composite has become extremely low. This is related to the increase of local fluctuations of the electric field near the clusters of conducting elements, which for the applied static electric field act as equipotential volumes. For the given applied field E_0, the local fluctuations deviate as $\delta E \simeq E_0(p_c - p)^{-s}$, where $s \gtrsim \nu$.

In analogy with electrostatics, one may calculate the scalar potential Ψ for the lithosphere material:

$$\Psi = \frac{1}{3} Sp\hat{\sigma}(\mathbf{r}) + \rho_f(\mathbf{gr}), \tag{3.109}$$

where $\hat{\sigma}(\mathbf{r})$ is the tensor of real stresses in the medium; $Sp\hat{\sigma}(\mathbf{r}) = \sum_i \hat{\sigma}_{ii}$; ρ_f is the gas density; $\mathbf{r}$ is the radius-vector with the starting point on a day surface. (The horizontal pressure difference is accepted to be smaller as compared with $\rho\mathbf{g}$, where ρ is the mean density in the system). The potential Ψ characterizes gas pressure difference in transition from one transparence cluster to another, and each transparence cluster is an equipotential volume for the scalar field Ψ. Fig. 3.25 (left) shows a typical configuration of transparence zones for a 2-D square model near the percolation threshold. Each site of the square lattice can be in a transparent state with the probability p (light sites) and in an opaque state with the probability $1 - p$ (dark sites). The corresponding distribution of the scalar potential Ψ is shown on the right. The change of the site tints from the top to the bottom depicts the growth of the potential Ψ, the mean value of which corresponds to the lithostatic pressure. Within the limits of one discrete cluster (a zone of equipotentiality for Ψ) the colour of sites does not change according to definition (3.109).

[†]This circumstance identifies a horizon at the depth $z \simeq R_g$.

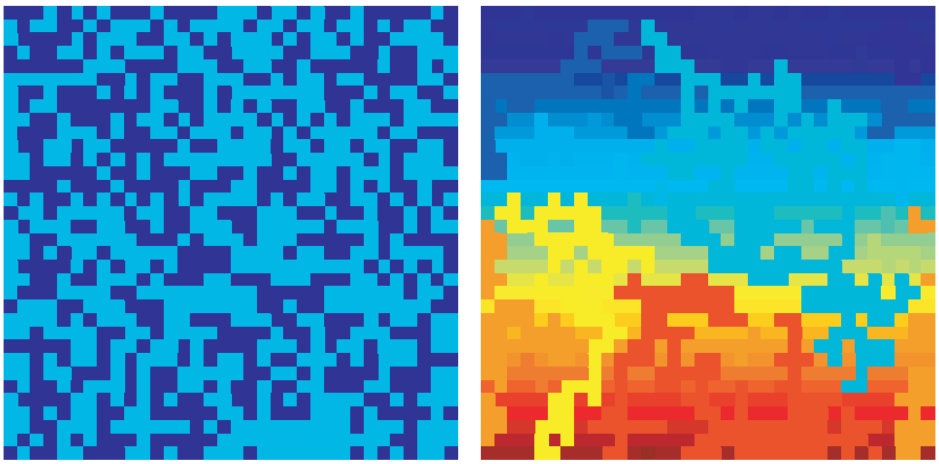

Figure 3.25: Transparence cluster configuration on the 35×35. square lattice. The random distribution of the transparence zones is shown on the left. The fraction of transparent sites is near the percolation threshold for a site problem on the square lattice $p \simeq 0.58$. The corresponding distribution of the scalar potential Ψ is shown on the right.

The characteristic pressure difference between the neighbouring transparence clusters grows along with the correlation radius as it approaches the percolation threshold:

$$\delta\Psi \simeq \Delta\rho g\xi \approx \Delta\rho g a|p-p_c|^{-\nu}. \tag{3.110}$$

For a 2-D square model the value a just coincides with the size of the site and the potential gradient $\bigtriangledown\Psi \simeq \delta\Psi/a$ applied to a non-transparent site separating the neighbouring clusters can be considerably higher the gradient of the lithostatic pressure $\rho\mathbf{g}$.

It is obvious that the weakest point in the system is associated with the maximum cluster which dimensions are close to the critical scale R_g. For a percolation transition the probability of finding an l-size cluster is proportional to $\exp(-l/\xi)$ [27,29,61]. Then the maximum size of the cluster $l_{\max}$, which may be found in the system with the volume L^d, should meet the requirement $L^d\exp(-l/\xi) \approx 1$. Thus, $l_{\max} \approx \xi\ln(L^d) = \xi d\ln(L)$, which at constant $l_{\max} \simeq R_g$ means a logarithmic drop of stability of the porous medium in the gravitation field at the growth of the porous medium characteristic dimensions.

Since lithosphere parameters vary significantly due to the gravitation, it is expedient to consider the following simple generalization of the above percolation system. Let us assume that the transparence parameter p decreases steadily with the depth z from a certain above-critical value on the planet surface to zero at the depths $z_{\max}$ of several hundred kilometres $z_{\max} \simeq \hat{E}/\rho g$, where $\hat{E}$ is, just to remind you, the mean value of the Youngs modulus in the lithosphere). In this case we may speak about the gradient percolation [27, 29]. Fig. 3.26 shows the typical configuration of transparent zones for the gradient percolation on the 2-D square model. The left picture of Fig. 3.26 presents the gradient distribution of the trans-

parence zones on the square lattice depicting the fraction of the transparent sites close to one at the top of the lattice to zero at the bottom. The right picture of Fig. 3.26 shows the corresponding distribution of the pore pressure $\Psi - \rho_f(\mathbf{gr})$.

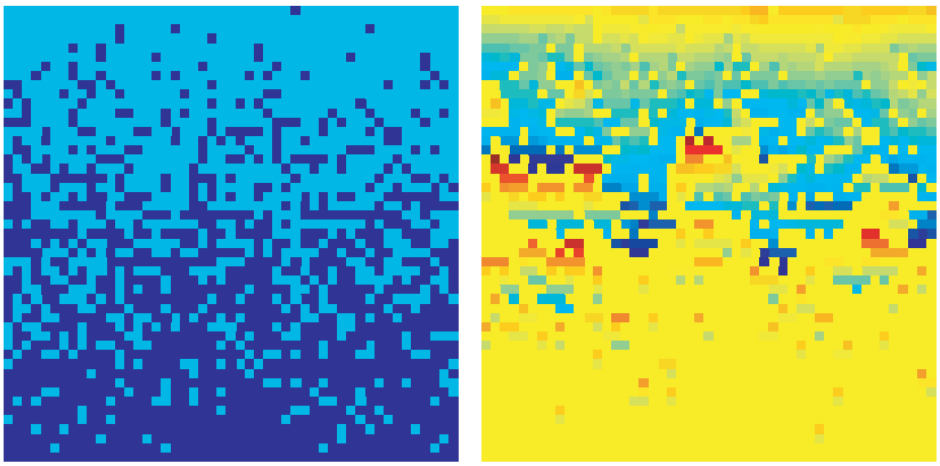

Figure 3.26: Gradient distribution of the transparence zones on the square lattice (*left*). The corresponding distribution of the pore pressure (*right*)

We may see that the maximum fluctuations of the pore pressure correspond to large transparence clusters formed near the middle boundary of the zone of connected porosity (z_c is the depth of the zone of connected porosity).

Let us call the field $z \leqslant z_c$ a zone of connected porosity and the field $z > > z_c$ a zone of unconnected porosity. The boundary between these fields, as shown in Fig. 3.26, has a fractal structure and is called a front of transparency. From the geometric point of view the front of transparency is identical to the diffusion front discussed in the percolation theory in section 2.8, and its mean position $z = z_c$ corresponds to the percolation threshold: $p(z_c) = p_c$. The average width h_f of the front of transparency is connected with the value of the transparence parameter p near z_c by expression (2.47). In Fig. 3.26 we see that the transparence and non-transparence clusters are extremely small away from the front, on the other hand, near the front their sizes are commensurable with the width h_f.The transparence clusters correspond to the finite clusters of the percolation system, while the non-transparent clusters - to the finite impermeable volumes. With the approach to the front both of them grow as the correlation length ξ according to eq. (2.4). However, due to the finite gradient $p(z)$, dimensions of the transparence and non-transparence clusters remain finite even at $z = z_c$. Their maximum size does not exceed the front width h_f, which is the only characteristic scale of the problem. According to the formulated criterion of the transparence cluster stability, the front width of the percolation transition cannot exceed the critical scale R_g. Moreover, transition from the global transparency $p > p_c$ at the surface stratum to the global opacity $p < p_c$ at large depths should exist on the strata with the depth of occurrence that also does not exceed the critical scale R_g.

We have now considered the static system of transparence zones and identified the criterion of its stability. The next principal step to be made is to generalize the developed scheme for

a time-dependent configuration of the transparence zones under conditions of an actual lithosphere, when the rock permeability and gas content therein are dynamic variables [89]. This is the case, for example, of degassing the saturated solid solution, when the transparent zones appear, grow, aggregate, emerge and disappear. Considering the process of transparence zone slow evolution, one may notice that some small-scale events (occurrence or disappearance of discrete transparence zones) cause perceptible changes of the front configuration (acquisition or lost of large clusters by the front). For instance, we may observe the merging of two transparence clusters of an undercritical size into one overcritical cluster with the subsequent destruction of this newly formed overcritical cluster.

The destruction is preceded by the pressure leveling in the merged clusters. Rough estimation of the time of leveling for the filtration rate u can be derived with the help of the Darcy equation:

$$\vec{u} = -\frac{k}{\mu} \bigtriangledown P. \tag{3.111}$$

Assuming that $u\tau \simeq R_g$ we obtain:

$$\tau \simeq \frac{\mu R_g}{\rho g k}. \tag{3.112}$$

For the characteristic values of viscosity and permeability the time of pressure levelling in a critical cluster constitutes $10^5 \div 10^7$ seconds.

Each change of cluster configuration, particularly aggregation of clusters, is accompanied by gas migration from lower layers to upper ones. Thus, we have a nontrivial mechanism of substance differentiation in the field of gravitation. This mechanism, let us call it a percolation mechanism, can serve an alternative to the sedimentation convection under conditions of high viscosity.

To describe the gas migration process within the limits of one transparence cluster, let us write down an equation of compressed gas filtration in the system of connected pores. Let the rate of filtration be defined by Darcys law (3.111). Then the law of gas mass variation in the cluster is as follows:

$$\frac{\partial(x\rho_f)}{\partial t} + div(x\rho_f \vec{u}) = \Upsilon, \tag{3.113}$$

where x is the porosity, ρ_f is the gas density, Υ is the rate of gas mass occurrence in a unit of volume due to the lithosphere degassing and possible mechanic-chemical reactions taking place during rock destruction. Assuming gas and porous medium low-compressible substances and substituting eq. (3.111) into eq. (3.113) we obtain:

$$\frac{\partial P}{\partial t} = \Lambda \Delta P, \tag{3.114}$$

where Δ is the Laplace operator, $\Lambda = \dfrac{k}{x\mu}\left(\dfrac{1}{K_x} + \dfrac{1}{K_\rho}\right)^{-1}$ is the coefficient of piezoconductivity, $\dfrac{d\rho_f}{dP} = \dfrac{\bar{\rho}_f}{K_\rho}$, $\dfrac{dx}{dP} = \dfrac{\bar{x}}{K_x}$ for the characteristic values $\bar{x}$, $\bar{\rho}$. Presenting the pressure in the form $P = -\Psi + \rho_f g z$ we will get the same equation for the potential Ψ:

$$\frac{\partial \Psi}{\partial t} = \Lambda \Delta \Psi. \tag{3.115}$$

Equation (3.115) describes the process of levelling of the potential Ψ in the cluster caused by filtration.

Solution of the diffusion equation for the potential Ψ in individual clusters should be supplemented with a scenario of the change of configuration of connected transparence zones due to the interaction of pore pressure anomalies with the solid matrix strength. During the degassing simulation by means of a network of cellular automations we followed the following game directives. With a certain small probability transparence zones can occur at every step of model time. At first their concentration monotonically increases, transparence clusters appear, their sizes gradually grow. The rate of the transparent sites occurrence characterizes the intensity of the external sources, for example, the rate of the lithosphere degassing. For clusters consisting of two and more sites the levelling of the potential Ψ in accordance with equation (3.115) was performed at every step of the model time. We assumed that the rate of pressure leveling was significantly higher than the rate of degassing. Then we took into account the fact that new transparence zones can occur near the already existing ones due to the superfluous pore pressure in the latter. The probability for an opaque site to become transparent is calculated with the help of the following Weibull distribution [119]:

$$\Omega = \begin{cases} 0, & \Psi_2 \le \Psi_1 \\ 1 - \exp\left\{-\left(\dfrac{\Psi_2 - \Psi_1}{\sigma_1}\right)^m\right\}, & \Psi_2 \ge \Psi_1 \end{cases}, \tag{3.116}$$

where Ψ_1 is the value of potential (3.109) in the given site, Ψ_2 is the value of the potential in its transparent neighbour, m is the Weibull modulus, σ_1 is the material breaking strength. The appearance of new transparence zones is compensated by the disappearance of transparency in the sites under conditions of great pore pressure deficiency in them. The probability of transition into the opaque state is calculated with the help of the formula similar to (3.116):

$$\Omega = \begin{cases} 0, & \Psi_2 \le \Psi_1 \\ 1 - \exp\left\{ - \left(\dfrac{\Psi_2 - \Psi_1}{\sigma_2} \right)^m \right\}, & \Psi_2 \ge \Psi_1 \end{cases}, \tag{3.117}$$

where σ_2 is the shear strength, Ψ_1 is potential value (3.109) in the site under consideration, and Ψ_2 is the arithmetic mean of the scalar potential Ψ of all its nearest neighbours, i.e. $\Psi_2 = 1/4 \sum_i \Psi_i$. Fig. 3.27 shows the modelling of the transparence cluster formation subject to fluid migration according to law (3.115). The configuration of the transparent sites (blue) and opaque sites (yellow) is presented in the left window. The right window depicts the corresponding pore pressure distribution as compared with the lithostatic pressure $\Psi - \rho(\mathbf{gr})$.

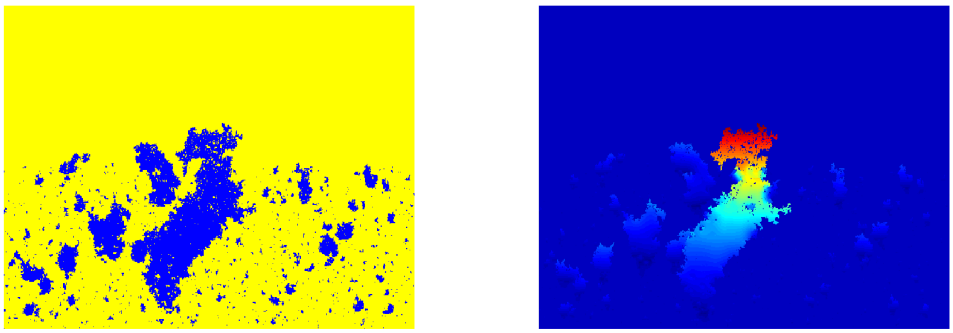

Figure 3.27: Model differentiation of substance in the field of gravitation. The configuration of the transparent and opaque sites is shown in the left window. The corresponding pore pressure distribution is shown in the right window

In the model system the critical radius R_g is expressed by the whole number of sites, at which the difference of the potential Ψ in the vertical direction reaches values that can be compared with σ_1 and σ_2 in formulas (3.116) and (3.117). When a new transparent site appears, its potential is considered to be $\Psi = \rho(\mathbf{gr})$, but when a transparent site becomes opaque, the potentials of its neighbouring transparent sites are increased by the value $\delta\Psi = \rho_0(\mathbf{gr})/n$, where n is the number of the transparent neighbours. Such a model takes into consideration redistribution of fluid at the occurrence or disappearance of transparent sites. If the material rupture strength dominates, large transparence clusters have a tendency to loose their connected components, remaining under the critical size. Otherwise, the transparence clusters tend to grow, which provides for their rising to the daylight or merging with the surface layer of connected transparency. A typical configuration of transparence zones and corresponding anomalies of the pore pressure $\Psi - \rho_f(\mathbf{gr})$ for various values of the Weibull modulus are shown in Fig. 3.28.

Obviously, the most dramatic events must take place on the periphery of the transparence zones (areas of sharp transition from light colour to dark in the bottom windows in Fig. 3.28). Just there one may expect abnormally high rates of rock destruction with a subsequent rush of a mobile light component (fluid) to the upper strata. Fig.3.29 depicts several consecutive moments of the model system evolutional development.

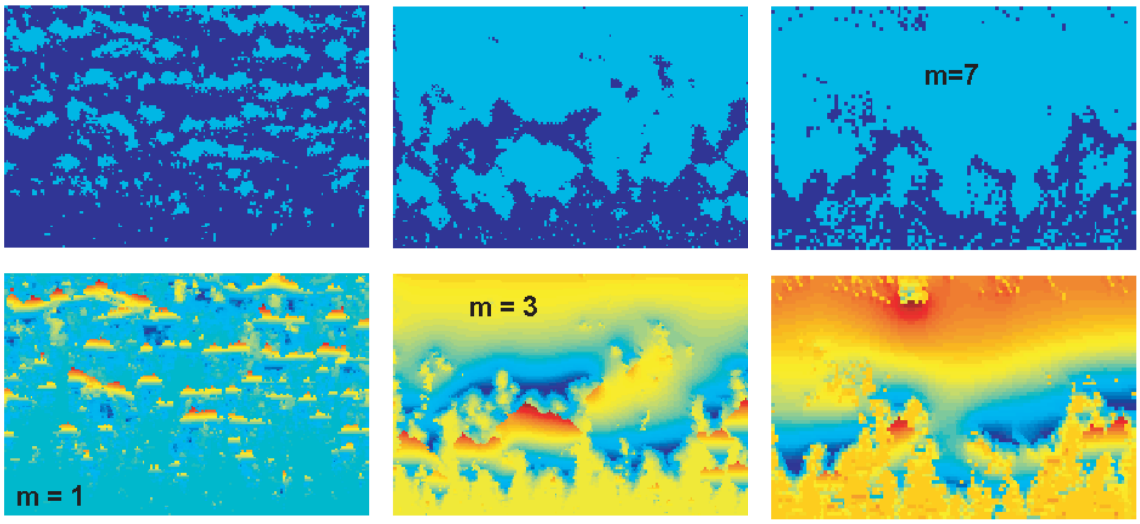

Figure 3.28: Degassing on the square lattice. Transparence zone distribution in a model for Weibull modulus $m = 1$, $m = 3$, $m = 7$ is presented in the top windows from left to right. The corresponding distribution of the pore pressure is shown in the bottom windows

The above model does not fit any longer for the violent or explosive degassing. Hence, its considerable modification is required, i.e. taking into account dependence of the diffusion coefficient in eq. (3.115) on the transparence zone scale and accordingly making the model time step shorter when using eqs. (3.116) and (3.117). Leaving this non-trivial modification for better time, we are, however, prepared to offer a simple phenomenologic model of the explosive degassing.

The phenomenologic approach is based on the idea of dividing the model volume into elementary cells of R_g size. Each of such a cell works as a relaxation generator: gradual accumulation of gas, having reached the percolation transition, causes practically instantaneous relaxation of the stored gravitational energy. This fast stage is accompanied by gas release, which, getting into the upper cells, can in its turn to initiate them. In such a way a chain reaction of the excitation transfer can occur, which like an avalanche will spread in the system.

To demonstrate it, a vessel with a siphon (a Dewar flask) filled in from a reservoir may be used as an elementary relaxation generator, which is shown schematically in Fig. 3.30 as a relaxation generator of saw-tooth oscillations.

A network of such generators can reproduce the dynamics of the degassing process, assuming that a local disbalance (actuation of a discrete siphon) causes an avalanche of events. Each of such an avalanche is accompanied by the fluctuations of the fluid volume stored by the system, see the graph in Fig. 3.31.

The corresponding avalanche sizes, i.e. the number of siphons taking part in the event, are shown in Fig. 3.32. The events statistics reproduces adequately the scaling properties of the

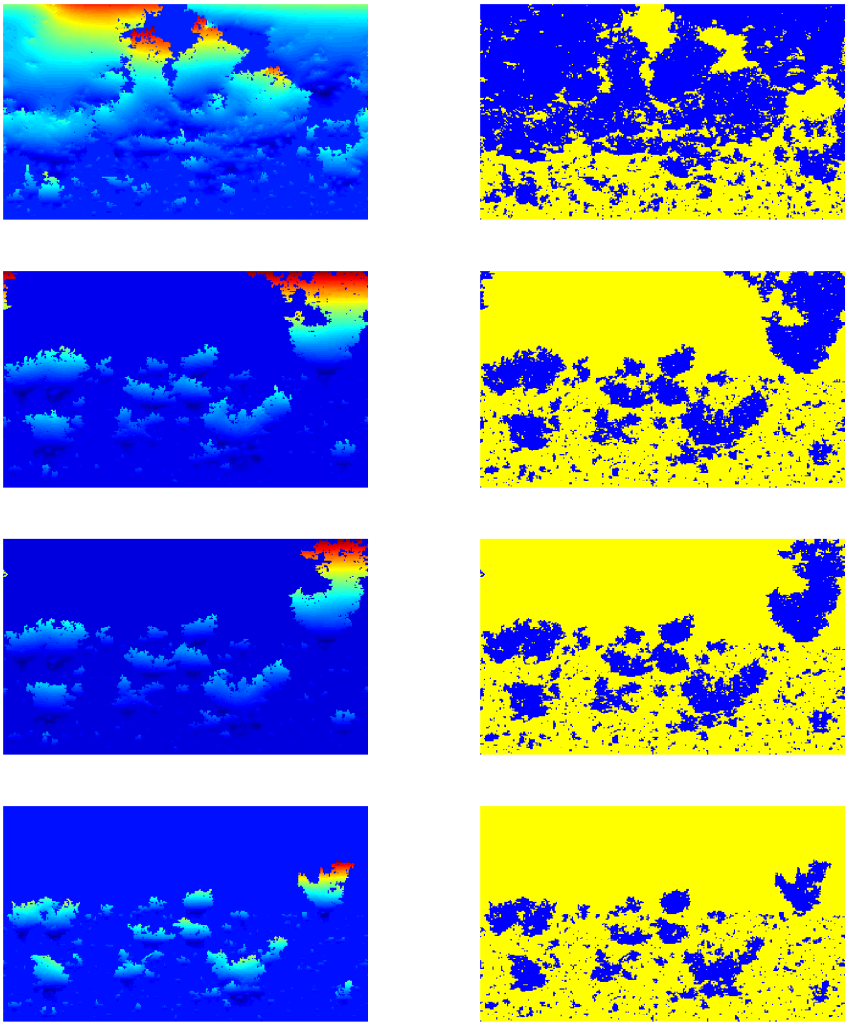

Figure 3.29: Evolution of the model system for Weibull modulus $m = 1$. The evenly spaced time measurements increase upwards

degassing process.

The process of degassing can be considered as a kinetic transition of the type of medium occupation. A traditional approach to the kinetic transition description supposes a space-time location of a non-linear mechanism of population growth suppression (in our case the level of the stored fluid). A situation is less studied, when a non-linear mechanism of the above-threshold limitation is essentially non-local in space and/or time. In this case the dissipation field in the system has an extremely complicated stochastic structure, and the growth limitation includes space-time regions of entirely different configurations and sizes. Nature is organized in such a way that very often these complicated dissipative structures represent physical fractals, i.e. they demonstrate scaling properties in a wide range of spatial and time scales [10, 107]. The space-time scaling is characterized by strong correlations diminishing according to a power law, which is typical for the critical phenomena. Therefore, in terms of quality the dynamics of these systems looks like a self-organized and self-adjusting critical

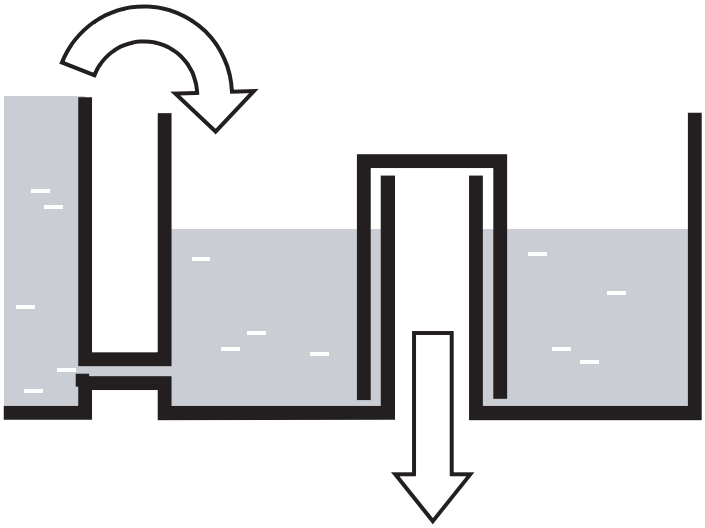

Figure 3.30: Dewar flask

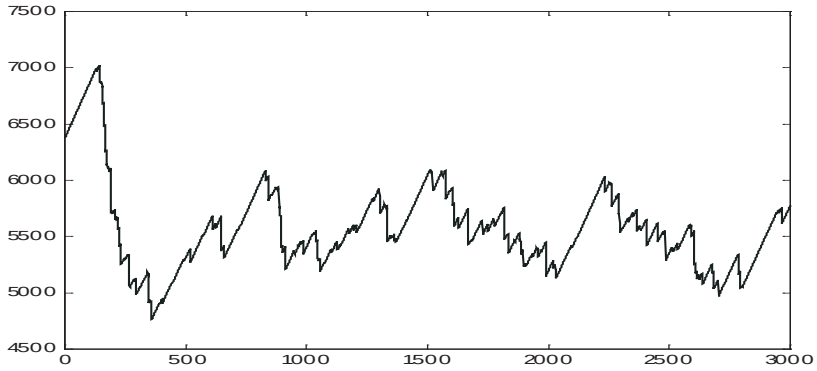

Figure 3.31: Evolution of the fluid stored by the system. Model time steps are plotted on the abscissa axis

mode. The quasistationary conditions of degassing are controlled by equilibrium between the slow process of porosity growth due to diffusion and its quick decrease caused by the vertical migration of microscopic portions of the released gas.

An idea to model the distributed seismicity by means of a network of connected relaxation generators was suggested as early as in 1967. Then it became popular again in the 90s in connection with the discussions of the phenomenon of self-organized criticality. But in the modifications of a well-known stick-slip model the function of an elementary relaxation generator was performed by a load placed on a moving conveyer belt and fixed by a spring. This is also a saw-tooth motion generator, where the elastic energy of a stretched spring is used. According to the traditional understanding of seismogenesis, we may speak about accumulation and release of the elastic energy in the lithosphere elements under deformation.

While in the case of degassing we may speak about the gravitational potential energy released due to the differentiation of substance in the gravitational field of the planet. Indeed, the

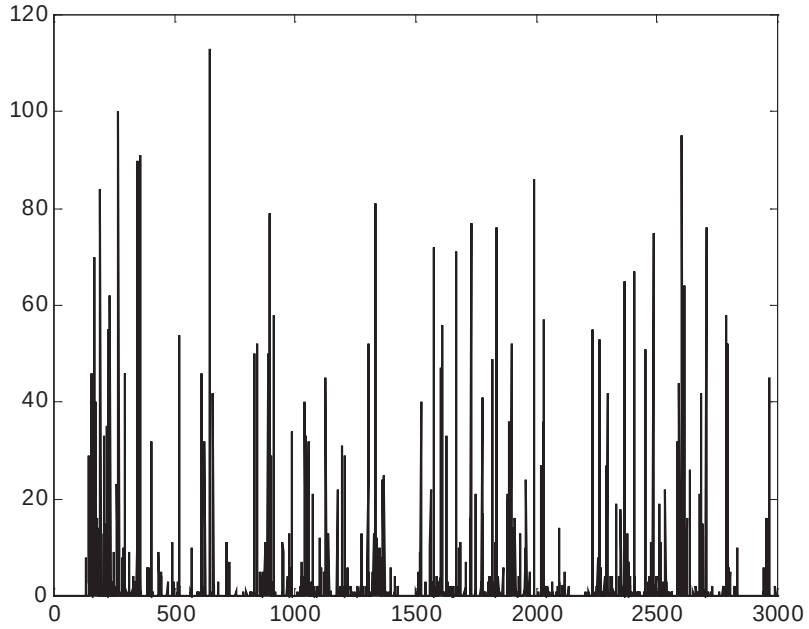

Figure 3.32: Evolution of the number of actuated siphons corresponding to Fig. 3.31

rising of a zone of connected porosity of R-diameter to the height of the same order as its linear dimensions resulting in the change of the total porosity by the value Δq leads to the energy release of the order $\Sigma \simeq \Delta q \Delta \rho g R^4$. For example, if during the degassing of a cube with a 5 m side its porosity has decreased by 10^{-3} and density difference of the solid matrix and fluid constitutes $\Delta\rho = 1.6 \cdot 10^3$ kg/m^3, the released energy will be 10^{16} joules.

The traditional theory of seismic activity connects lithosphere destruction with mechanical action of tectonic forces and identifies deformation of giant objects with the results of miniature laboratory tests, which ignore the gravity entirely. Moreover, the laboratory researches are performed usually on dry, homogeneous and single-phase samples, while the lithosphere substratum basically is a heterogeneous and multi-phase substance. Dry models of an earthquake source present numerous difficulties going beyond the frameworks of the laboratory models. In early 70s it seemed that those difficulties could be overcome by taking into account the influence of water [120, 121]. It was found out that the seismic destruction was usually related to the zones of excessive pore pressure of fluids [121–124]. But the source and the value of the pore pressure remained unknown.

Recently it has become clear that a whole series of seismic process features, presenting a real challenge for the traditional approach, is closely connected with the Earth degassing. For a long time the surface gas release has been considered as one of the most important signs of a coming earthquake [125–128], and just recently it has been suggested that gas plays a fundamental role in formation of the source of an earthquake [115, 129]. Exactly the saturation of rocks with fluids under gravitation provides for the unique features of the lithosphere, which can be simulated entirely in laboratory conditions.

Considering the lithosphere substratum as a double-component two-phase system consisting of an oversaturated solid solution and gas coming out of it, we have found a unique rocks capability of self-destructing in the field of gravitation. The physics of the process is determined by a specific mechanism of substance differentiation in the field of gravitation, governed by the disbalance of the multi-phase medium with regard to the percolation transition. It has been proved that this mechanism provides, in particular, for the rising of the field of connected fractures in the solid lithosphere of the planet. The rate of the rising process depends on the vertical dimensions of the system of connected fractures. Formula (3.106) gives the critical size of a transparence zone at which it becomes unbalanced in the field of gravitation. We constructed a 2-*D* model that described quite satisfactorily the growth and movement of the transparence zones in the field of gravitation. The growth of transparence zones is described by the percolation theory, and in reality it can be caused, for example, by the degassing of the lithosphere substratum or mechanical-chemical reactions. The appearance of new transparence zones is balanced by their continuous disappearance due to the emergence process. The nature of emergence is determined by the interaction of the processes of new fractures opening at the upper part of the transparence zone and their closing (healing) at the bottom part thereof. The system different behaviour depends on a variation of a small number of parameters, the most important of which are shear and rupture strengths. A numerical experiment revealed that near the day surface there was a transparence zone extending to the depth of an order of the critical radius $R_g \sim 5$ km. As this layer being approached, the difference of the pore pressure increases, that can cause catastrophic destructions. We should note that depths of an order of the critical radius and more correspond to the maximum of hypocenters distribution with depth [130].

An important feature of the discussed mechanism is the efficiency of its energy: it transforms the potential gravitational energy directly into the energy of destruction. The energy of an earthquake source is proportional to the fourth power of its linear dimensions and can exceed many times the elastic energy stored in the material, which is proportional to the third power of the linear dimensions of the earthquake source.

Tensile stresses due to the planet rotation as well as the tidal influence of the Moon and Sun by all means cause light component release within the lithosphere. In this sense, the degassing as a seismogeneous process correlates well with such an important aspect of the distributed seismicity as it latitudinal distribution [114].

In analogy with the theory of river basins, we have found out that the basic structural features of a dynamic drainage system are determined by its scale (see section 3.7). A similar approach can be applied as well in the case of the lithosphere degassing process. Let us compare the fluid motion from the depths of the planet with a quasistationary system of channels the effective transport through which corresponds to the required level of degassing of the seismically active region. With such an approach, individual seismic events associate with the fluctuations of a drainage system in various scales. Catastrophic earthquakes correspond to the largest structural fluctuations of the drainage channel system, the stem of which coincides with the fault zone. The catastrophic events of seismogenesis are tied up to a certain fault zone similar to successive thunderbolts are confined in a fixed cloud-earth area.

The fluid leaving a certain lithosphere area leads to the decrease of the porous pressure in it. At the same time in neighbouring zones conditions for the excessive porous pressure can occur. If stresses that appear in this case exceed the strength of a solid matrix, an earthquake occurs. In general the lithosphere cross-section in a seismically active region represents a mosaic picture of pluses and minuses (zones of excessive and low pressure). The dynamics of these zones movement of the minuses downwards, emergence of the pluses and neutralization of the minuses and pluses - determines specific features of the region seismic conditions.

A special role of the stratum occurring at a depth of the order R_g from the day surface should be underlined. The lithosphere material above this layer can remain transparent for fluid for quite a long time: the corresponding overloads on the solid matrix do not exceed its breaking point. The fluid pressure in pores and fractures tends to the value comparable with the fluid pressure on the day surface, i.e. the atmospheric pressure. Thus, almost the entire zone located above the R_g-stratum represents a transparence zone for fluid. The most transparent in this case is the fault zone, where the porous pressure drop reaches the lowest possible strata.

At the same time the pressure in the zones located below R_g reaches values of the order of the lithostatic pressure and higher in a corresponding stratum. Therefore, the maximum pressure difference corresponds to the strata with the depth of occurrence of the order R_g, meaning the maximum loads on the solid matrix. That is why the sources of most destructive earthquakes are located mainly at a depth of the order R_g and near the fault zones.

It is an important fact that the non-linear dynamics of the lithosphere substratum subjected to degassing turns out to be self-consistent, i.e. every movement is an effect of the preceding events and at the same time a reason of the following ones. In view of the approach being developed, such effects as migration of the sources of earthquakes upwards, swarms of earthquakes, impact of nuclear explosions on seismic conditions and so on become clear. The fractal structure of the drainage system is responsible exactly for the self-consistent process of the lithosphere degassing.

A drainage system of a light component formed during percolation represents a fractal structure, and, therefore, it possesses a fundamental property of self-similarity. It means in particular that the relation of the mean number of the $N(R_1)$ events of scale R_1 and the number of $N(R_2)$ events of scale R_2 in the same volume and for the same period of time is determined by the expression:

$$\frac{N(R_1)}{N(R_2)} = \left(\frac{R_1}{R_2}\right)^{-d_f}, \tag{3.118}$$

where d_f is the Hausdorff dimension of the fractal structure.

A fractal dimension depends largely on aggregation conditions. In our case it is a cluster - a cluster association of monodisperse elements and the Hausdorff dimension of the fractal

system is close to two: $d_f \lesssim 2$ [131].

The total energy released in the source of a large event is proportional to the fourth power of its dimensions. Therefore, comparing (3.107) and (3.118) we obtain:

$$N(R) = E^{d_f/4}. \tag{3.119}$$

Quite a different relation is obtained by a seismologist who is capable to observe just E_c – the energy of elastic waves spreading from an earthquake source. With all other equal conditions (epicentral and hypocentral distances) the acoustic energy of the main shock assessed in an observation point is proportional to the volume of the earthquake source. Thus, the observer will find out the relation:

$$N(R) \approx E_c^{d_f/3}. \tag{3.120}$$

Using the magnitude definition [132]:

$$\lg E_c(\mathrm{J}) = 4{,}8 + 1{,}5M \tag{3.121}$$

together with eqs. (3.118) and (3.120) we obtain:

$$\lg \frac{N(R_1)}{N(R_2)} = 0{,}5\, d_f (M_2 - M_1). \tag{3.122}$$

At $d_f = 1{,}8$ the last relationship agrees with the empiric Gutenberg-Richter recurrence law [132]. Law (3.122) is a consequence of a large-scale invariance of the process of light phase clusterization. But the dynamics of the earthquake source destruction caused by the gravitation does not show such an invariance.

Let us underline that numerous experimental data on the signs of the forthcoming events can find their natural explanation within the frameworks of the given conception. For instance, seismic velocity anomalies are caused by the reduction of the substratum compression, geochemical changes by the light component transport, electromagnet changes by the gas ionization, etc. A formal similarity with the dilatancy-diffusion model can be readily observed as well [133]. This is connected with the fact that if a Griffiths radius is considered as an elementary size of the problem instead of the radius of a bubble, then we will obtain a peculiar configuration analogy with the process of microfracture percolation in the continual mechanics.

Since the discussed mechanism of seismic activities is related fundamentally with the processes of planet degassing, it is very important to determine an essential, from the seismoge-

nesis point of view, value of effective rate of degassing per unit of surface area and compare it with the data obtained in the experiment.

Let us determine the rate of degassing of a fixed stratum $z = \mathbf{gR}$ as a number of litres of gas passing through one square meter of the stratum surface during a year:

$$Y(\mathbf{gR}) = \frac{\partial^2(v)}{\partial A\,\partial t}(\mathbf{gR}), \tag{3.123}$$

where v is the fluid volume, A is the stratum area, t is the time. Then the value of potential gravitational energy released due to degassing in a seismic region of the area $A = 10^6$ km^2 for a characteristic period of seismic regime $T \simeq 1000$ years is estimated:

$$\mathscr{E} \simeq AT \int_{-L}^{0} \Delta\rho\, Y(z)\, dz \simeq \Delta\rho\, g\, Y(0)\, LAT, \tag{3.124}$$

where $L \simeq 10^3$ km is the characteristic depth of the active zone. By definition, during the seismic regime period in the region under study one catastrophic earthquake takes place with energy of the order $\mathscr{E} = 10^{20}$ J, which equals 10^5 mt of TNT. Since energy of other seismic events in the region is negligible as compared with the energy of a catastrophic earthquake, we will use exactly the latter in our estimations. Thus, for the minimum required rate of degassing on a day surface we obtain:

$$Y(0) \simeq \frac{\mathscr{E}}{\Delta\rho\, g\, T\, V}, \tag{3.125}$$

where $V = LA$ is the volume of the active zone. Substituting the characteristic values in eq. (3.125), we have:

$$Y(0) \simeq 10^{-5}\,\frac{\mathrm{m}^3}{\mathrm{m}^2 \cdot \mathrm{year}}.$$

The experimentally observed level of degassing [134] is hundreds of times higher the calculated estimation. It means that the discussed mechanism of seismic activity can be maintained by means of geochemical processes with a high degree of safety.

Certainly, this comparison is given for illustrative purposes only. A detail study, in addition to the dependence of all values of eq. (3.124) on the depth of the stratum, will require a whole series of geophysical and geochemical data. In particular, mineral formation and ore-depositing processes are of great interest, which also require availability of a force for the associated mass transfer.

3.9 Vector percolation and neuron networks

Let us consider now a percolation problem in which a system element is represented by a pair of discs. The centres of the discs are connected by a segment of H-length. There are two possible situations. The first one is when the discs are equitable, and the processes of transmission of current, excitation or information can be directed either from one disc to the other and in the opposite direction. In this case the percolation between the pair of discs has a scalar nature, i.e. there is no bypass between the connected components. The second situation appears when the roles of the discs in the pair are differentiated, e.g. one disc is the inlet and the other is the outlet. Formally, it leads to a situation when the discs centres are connected by a vector. In this case the percolation of the pair of discs has a vector character, i.e. in the connected components the outlet of one disc should be linked with the inlet of the other. Both situations are characterized by a new non-dimensional parameter $\Gamma = \dfrac{H}{R}$. It is obvious that at $H = 0$ both the scalar as well as vector problems are reduced to the previously discussed problem of discs.

Let us consider the basic features of a vector generalization of the problem of discs on the example of in-formation dynamics of a neuron network [4]. Each of the network elements (neurons[†]) randomly distributed on a 2-D underlayer receives input pulse signals from a certain environment, and, if the threshold level is exceeded, it generates an output signal. The generated signal propagates to a certain distance entering the field of input effects of other neurons. Each neuron in the network has a number of addressers in which subsets of recipients and transmitters can be singled out. In a general case these subsets do not coincide, though they can cross each other. Here we will limit ourselves with consideration of a culture neuron net-work on a 2-D underlayer assuming that:

1) neuron centres are distributed at random over a flat area;

2) each neuron of the network has an isotropic distribution of neurodendrites covering the circular domain of R. (see Fig. 3.33);

3) there is an isotropic distribution of directions from soma to a single synaptic terminal at the end of the axon, and the distance from the soma to the terminal is of H-length (axon characteristic length).

According to these assumptions the transmitters are distributed isotropely around the chosen neuron, and recipients are distributed isotropely around the presynaptic terminal of its axon. Dimensions of the whole network exceed substantially both the dendritic zone radius and the axon characteristic length. Within the frameworks of the described model it is expedient to investigate the following two cases. The first one is when the probability of the postsynaptic contact with a random neuron is the constant p in the circle of radius R and equal to zero outside it. In other words, the potential of the action reaching the synaptic terminal at the

[†]More information about the structure of neuron is given at http://en.wikipedia.org/wiki/Neuron

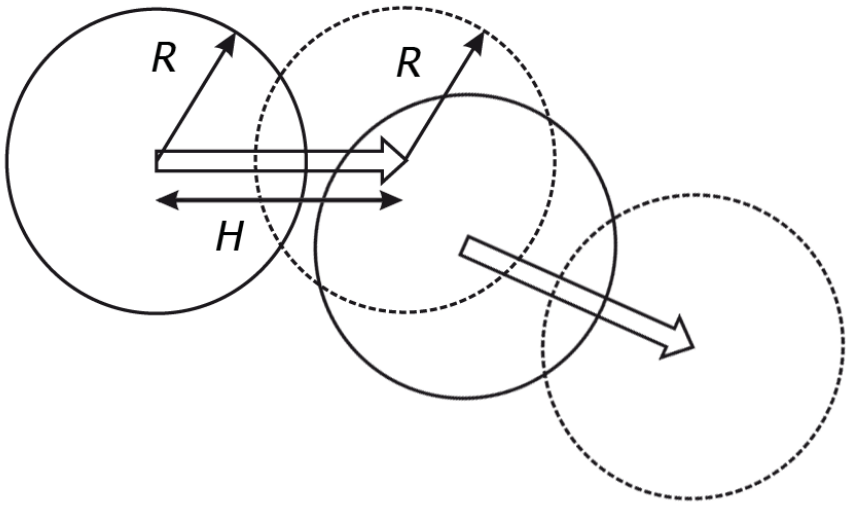

Figure 3.33: Geometric scheme of the model neuron and one of its nearest neighbours

end of the axon with the probability p goes on the excitable membrane of any other recipient-neuron if the distance from the centre of its soma to the given terminal does not exceed R. Thus, in this case each neuron can be represented by a directed pair of discs of R-radius which centres are connected by a H-length vector. And the task is reduced to a problem of percolation in an assembly of directed pairs of discs. The second case corresponds to the more real situation, when the probability of a postsynaptic contact (synaptic efficiency) decreases exponentially with the increase of the distance r from the synaptic terminal at the end of the axon to the soma centre of the recipient $p = p_0 \exp\left(-\frac{r}{R}\right)$. Later it will be demonstrated that this important case is also reduced to the problem of percolation in the assembly of directed pairs of discs.

If $p = 1$, then the assessment of the spike activity in the network is reduced to a problem of vector percolation in the assembly of the directed pairs we introduced (see Figure 3.35). The typology of connections in the network at the fixed parameter Γ equal to the relation of the axon characteristic length to the dendritic zone radius is controlled by the non-dimensional parameter $B = Sn$, where n is the concentration of neurons on the underlayer, and S is the area covered by a pair of connected discs of the R-radius with the H-distance between their centres. This area is calculated in the following way:

$$S = \begin{cases} 2R_c^2(\pi + (H/2R)\sqrt{(1-(H/2R)^2)} - \arccos(H/2R)) & H < 2R \\ 2\pi R^2 & H \geq 2R \end{cases}$$

It is evident that at small values of $B \ll 11$ there are no long bonds in the network of model neurons, and any spontaneous or forced agitation cannot spread in it. And vice versa, if $B \gg 11$ the most part of the network elements belongs to a single bond spreading over

the whole model field. For any fixed Γ-value there is a critical B_c-value at which a chain of connected neurons appears for the first time in the system, which can transfer agitation through the whole model network. And at $H = 0$ the percolation problem under study is reduced to a classical problem of discs (spheres). Fig. 3.34 shows the relation between the threshold value B_c and parameter Γ. It is clear that a significant rise of percolation threshold occurs at small Γ-values.

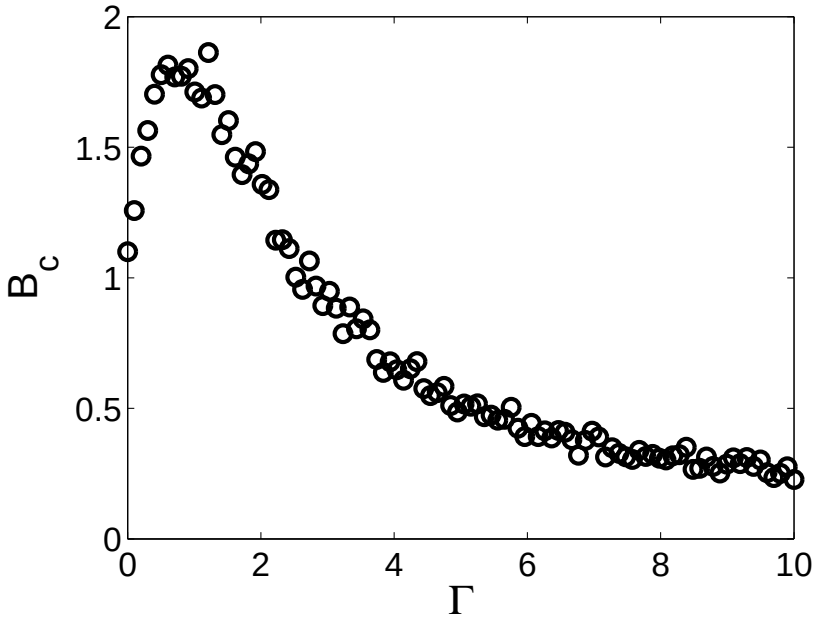

Figure 3.34: Relation between the critical value B_c and parameter Γ

In Fig.3.35 the neurons are presented by segments of H-length and the percolation cluster is marked with red. It is important to underline that the integral synaptic conductivity of a network is defined exactly by a percolation cluster as a maximum bond. If the entering agitation does not affect the elements of the percolation cluster then it cannot run through the entire model field.

The occurrence of percolation transition in an assembly of neurons is a necessary but not sufficient condition for the appearance of a continuous spike activity of a network. The sufficient condition is the generation of large-scale oriented cycles of chains of connected neurons. Note that only ordinary neurons are taken into consideration in the case of the percolation transition as well as formation of cycles. Along with this an array of braking neurons is considered as a separate component the role of which depends greatly on its relative share in the assembly. Above the results of percolation approach with the reliable transition of excitation between the connected neurons were considered. For $p < 1$ the problem is reduced to a complex problem of percolation which complete solution goes beyond the scope of the given consideration.

We confine ourselves here to more realistic and strong condition $p \ll 1$ that ensures transition to a model of dynamic percolation [28]. Indeed, let us assume that if at a given moment a neuron is excited, then at the next (discrete) moment of time it returns to its initial state

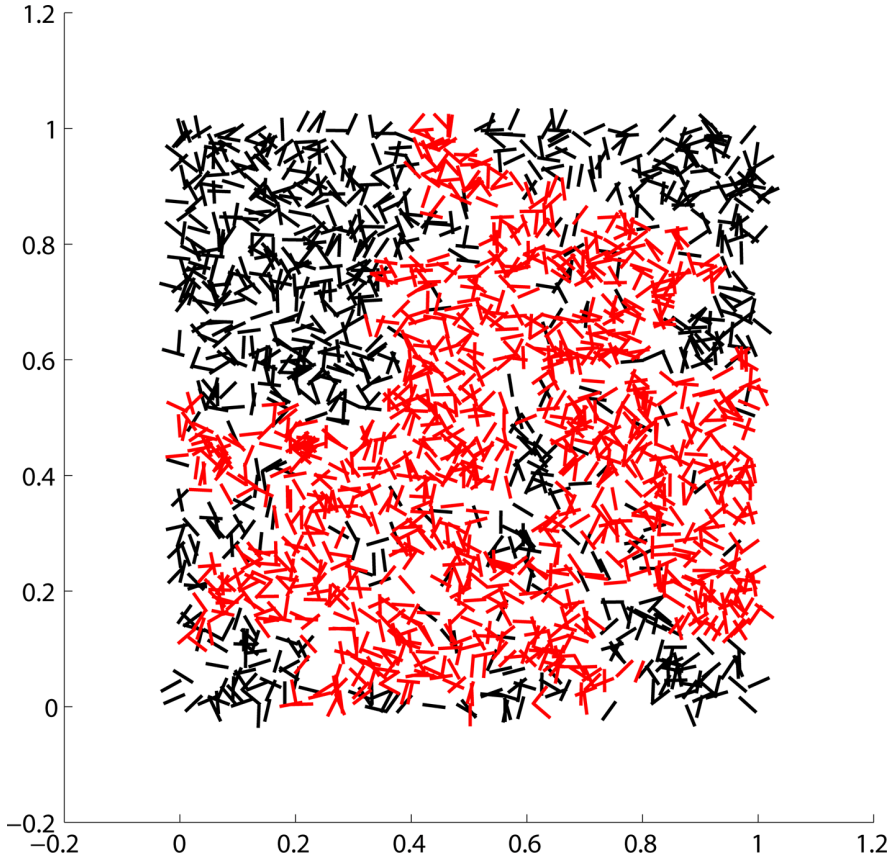

Figure 3.35: The model neuron network at the threshold of vector percolation. The percolation cluster is marked with red

of rest, but at the same time with the probability p being able to excite its recipients. It is clear that if the probability of excitation transmission is very small, the number of excited neurons will be decreasing with time. In the inverse limit, when the probability of excitation transmission is close to one, the number of the excited elements in the network increases with time without limit. The critical value of the excitation transmission probability p_c at which the finite probability of spike activity growth occurs with a single excited neuron at the initial moment corresponds to the percolation threshold. The threshold value of the directed percolation depends greatly on the number of nearest neighbours in the given network, i.e. on its coordination number z. The larger is the number of transmitters z in each element of the network the higher is the probability of the spike activity development. According to the mean field approximation we discussed in section 2.9, the percolation threshold for $z \gg 1$ is defined as follows:

$$p_c = \frac{1}{z}. \tag{3.126}$$

With the decrease of the coordination number the mean field approximation looses its applicability. In this case the fluctuation effects become important.

Now let us say a few words about a situation when the probability of a post-synaptic contact (synaptic efficiency) decreases exponentially with the increase of the distance r from the synaptic terminal at the end of the axon to the soma centre of a recipient $p = p_0 \exp\left(-\frac{r}{R}\right)$. Let us fix the value $r \ll R$ and take into account only bonds with the probability $p > p_0 \exp\left(-\frac{r}{R}\right)$, assuming that no other bonds exist. Then we get the already discussed percolation problem with the radius of dendritic zone equal to r. Gradually increasing r we will reach the percolation threshold $r = r_c$ corresponding to the critical value B_c. Just this threshold value defines the integral synaptic conductivity of the network $p_c = p_0 \exp\left(-\frac{r_c}{R}\right)$, since all other bonds, put out of consideration and shunting the percolation cluster, appear to be exponentially infirm.

3.10 Baton transition of information

The importance of geometric fluctuations related to the directed percolation is clearly revealed in the problems of non-linear dynamics. We are going to consider the fluctuation effects on the example of a distributed system with random multiplication and disintegration.

The concentrated system with a random multiplication and disintegration is described by the stochastic differential equation:

$$\dot{n} = -\alpha n + f(t)n, \tag{3.127}$$

α is the constant decay rate, and $f(t)$ is the rate of multiplication randomly variable with time according to the specified statistical parameters. They usually say [135] that system (3.127) has exceeded its threshold of explosive instability if the average substance density $\langle n(t) \rangle$ in the assembly of realizations increases with time without limit.

Addition of a diffusion member to equation (3.127) generalizes the model for the case of distributed systems in which processes of decay, multiplication and diffusion of a certain substance are possible. It is assumed that the rate of decay is uniform in space and time, and the multiplication occurs only in certain centres of multiplication, which appear randomly in time at random points of the medium but have the same form, intensity and duration of existence. A corresponding mathematical model is described by equation [135]:

$$\dot{n} = -\alpha n + f(\mathbf{r},t)n + D\Delta n, \tag{3.128}$$

where n is the density of substance, and D is the coefficient of its diffusion. Fluctuating field $f(\mathbf{r},t)$ is set by the sum of identical impulses $\vartheta(\mathbf{r},t)$ located at the random points $(\mathbf{r_i},t_i)$:

$$f(\mathbf{r},t) = \sum_i \vartheta(\mathbf{r}-\mathbf{r}_i;t-t_i). \tag{3.129}$$

The average number of impulses in a volume unit per time unit is constant and equal to m. The function $\vartheta(\mathbf{r},t)$ has the following form:

$$\vartheta(\mathbf{r},t) = J\chi(\mathbf{r})\phi(t), \tag{3.130}$$

where J characterizes the intensity of a multiplication centre, $\chi(\mathbf{r}) = 1$ at $r \leqslant r_0$ and $\chi(\mathbf{r}) = 0$ at $r > r_0$; $\phi(t) = 1$ at $0 < t < \tau_0$ and $\phi(t) = 0$ at $t < 0$ and $t > \tau_0$, so r_0 and τ_0 define accordingly the spatial dimension of a discrete centre and its lifetime.

The non-dimensional spatio-temporal concentration of the multiplication centres c is an important parameter of the problem. It can be calculated as follows:

$$c = mr_0^d\tau_0, \tag{3.131}$$

where d is the dimension of the medium.

When the parameter c is small ($c \ll 1$), different multiplication centres act independently from each other, and the threshold of explosive instability is calculated within the framework of a standard analysis based on the mean field approximation [135]. As c grows, the centres of multiplication start overlapping in the spatio-temporal continuum, and their interference becomes considerable: the succeeding centres commence to act on the occupancy background made by the previous centres. The spatio-temporal chains of multiplication centres (clusters of the multiplying substance) appear and evolve at the background of the close-to-zero occupancy.

The spatio-temporal scales of these clusters disperse as the parameter c tends to some critical value corresponding to the threshold of directed percolation. Fig.3.36 shows typical critical dynamics of a one-dimensional model system with the time axis directed upwards.

In the one-dimensional numerical modelling of equation (3.128) the occupancy was continuously maintained on the noise level, as well as a non-linear dissipative member was introduced that limited the occupancy growth above the threshold:

$$\dot{n} = \varepsilon - \alpha n + f(\mathbf{r},t)n + D\Delta n - \beta n^2. \tag{3.132}$$

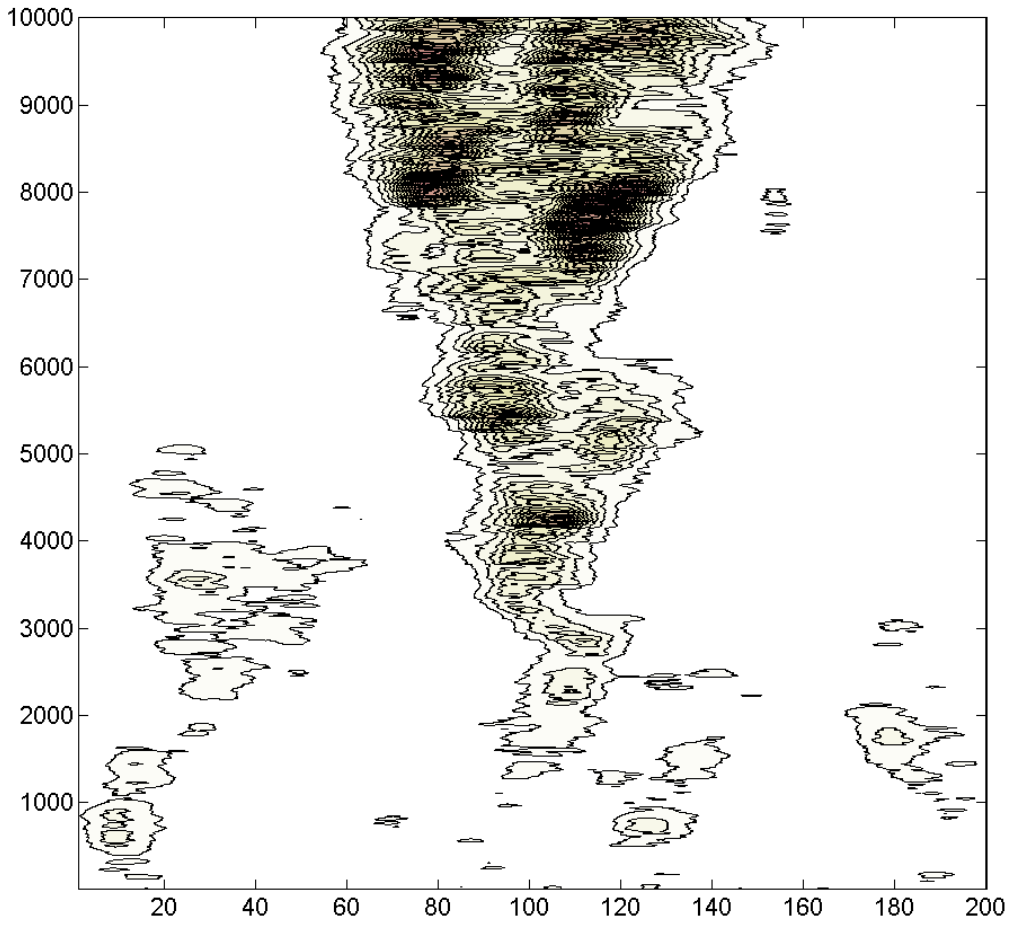

Figure 3.36: One-dimensional dynamics with the time axis directed upwards; the color intensity corresponds to the level of occupancy

Information transmission via a one-dimensional channel can be viewed a close discrete illustration of the constructive role of geometric fluctuations at the directed percolation. Let us consider a one-dimensional chain of cellular automata. Each of them can either block or transfer information. The chain is characterized by the specific number p of the elements transparent for a signal. The automata chain of the length $L = 12$ presented in Fig.3.37 connects the source of information A on the left to its receiver B. The black colour corresponds to the blocking cells, grey to the transparent ones and white to the transparent and information-carrying cells. Let the source A at each moment of discrete time send one bit of information to the system input. This bit can freely pass to the right only to the nearest blocking cell. Thus, it is obvious that the static chain can transfer information to the receiver B only when $p = 1$.

Fig.3.38 reproduces a fragment of the extended configuration space of the given chain of cellular automata.

Figure 3.37: One-dimensional chain of cellular automata. The black colour corresponds to the blocking cells, grey to the transparent ones and white to the transparent and information-carrying cells.

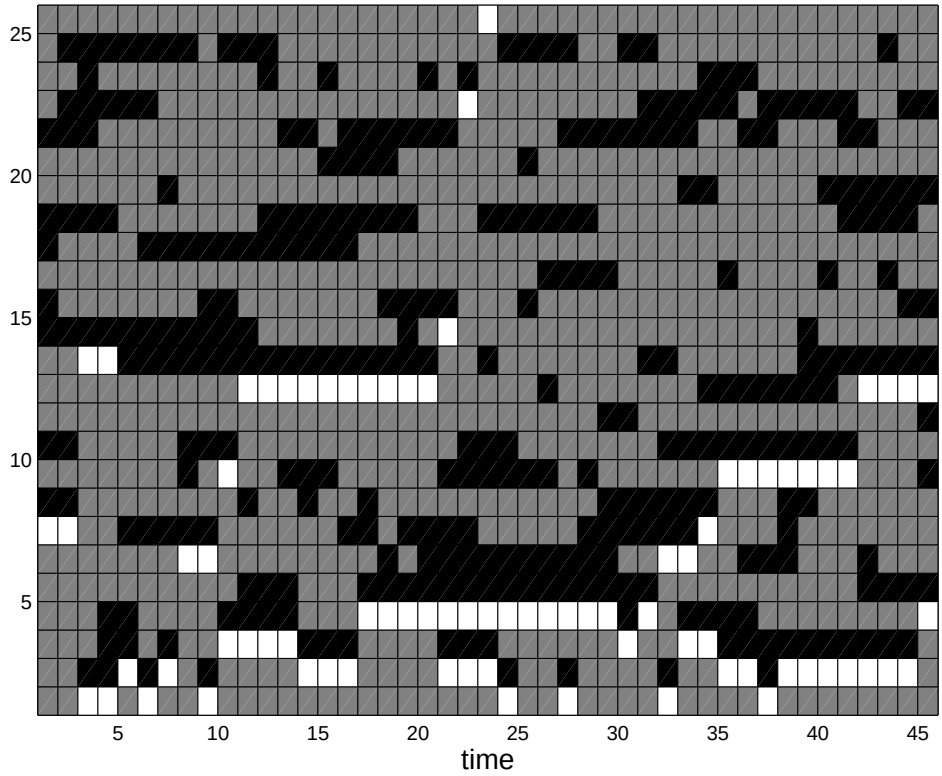

Figure 3.38: Information is transmitted upwards, the time increases rightwards

Figures 3.39 and3.40 show dependence of the volume of transmitted information as the function of the fluctuating channel transparency for three different values of the q-parameter in usual and log-log (right) scales.

Suppose, the network elements can change their state with time in such a way that during one step of discrete time a certain number s of transparent elements becomes oblique and, vice versa, s of the oblique elements becomes transparent (s is a parameter of the system update). Being so, the transparency level p stays constant, and the number of automata renewed in one step is $q = 2s/L$, which is the specific update parameter.

Let us study the possibility of information transmitting through such a fluctuating chain, assuming that in-formation can be stored in the transparent cells, and it disappears only at the change of the cells status. At each step of the model time the information entering the system moves to the right to the nearest blocking cell. It is supposed that the information

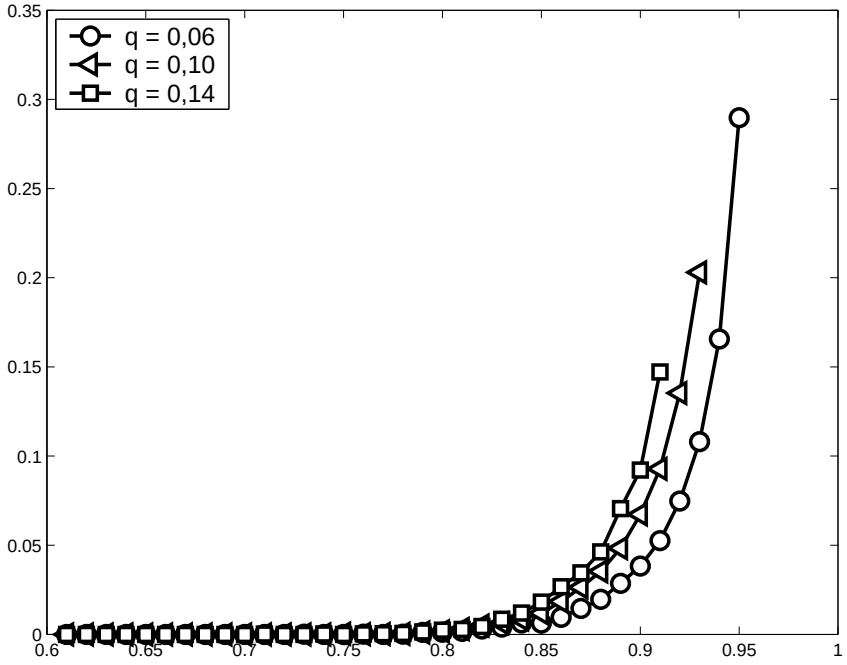

Figure 3.39: Dependence of the channel throughput on the transparency level p

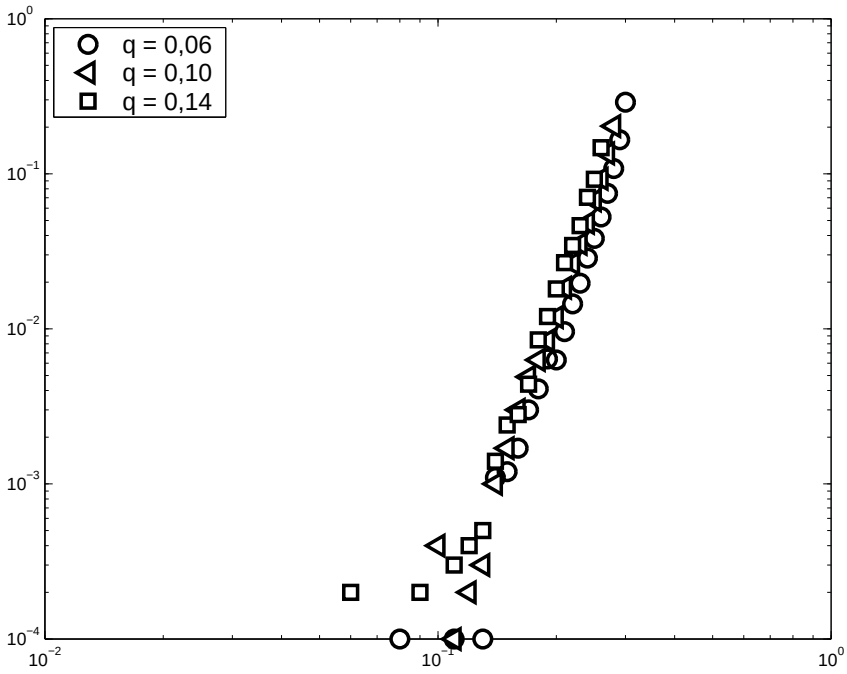

Figure 3.40: The same as in Fig. 3.39 given in a log-log scale at different number of automata renewed in one step

is being transmitted via the transparent cells within a span of time which is smaller than the length of the model time step, and a bit of information always occupies the right-most out of possible positions. At each step of the model time there are three options for the bit of information saved in the transparent cell located in front of a certain blocking cell:

1) 1) it can move forward with the probability $q(1-q)$ equal to the product of the probabilities of two independent events: the first one is when the status of the neighbouring cell on the right changes from oblique to transparent (probability q), and the second one is when the cell containing the bit of information preserves its transparency (probability $1-q$);

2) 2) it can stay at place with the probability $(1-q)^2$, and finally,

3) 3) it can dissipate with the probability q, where $q = 2s/L$ is the probability of the change of the cells status per unit of time.

There are two conditions for the information to be transmitted to the end-user: firstly, the blocking cell pre-venting the information transfer is to become transparent, and, secondly, the transparent element containing information must stay transparent until the moment when the block is removed. It is evident that if the transparency level is low $p \ll 1$ the probability to meet both of these conditions is extremely low, and information will unlikely reach the end-user. On the contrary, if the transparency level is close to one $p \simeq 1$, the information is transmitted to the end-user with a speed close to maximum. There is a certain critical value of transparency $p = p_c$ at which a non-zero probability appears that the information will be transmitted through the system. In this case, the speed of information transmitting tends to zero at the threshold. Fig. 3.38 demonstrates the evolution of the automata chain of length $L = 25$ with time for $q = 0.16$ and the transparency level $p = 0.72$.

Appendix

PROGRAMME CODES

A. The system of iterated functions for the Sierpiński gasket

The following code constructs a system of iterated functions for the Sierpiński gasket in the MATLAB pro-gramme. Fig. 1.6 is the result of this code function. The details of the procedure are discussed in Section 1.3.

```
%==========PROGRAM START============

T = 10^5; %==== dots number ====

A = [0 .5 1; 0 .5*sqrt(3) 0]; %=== position data ===

x = .5; y = 0; a = .5; b = 0;

for t = 1:15000

      ss = 10*rand(1);

      if ss < 8

           s = 1;

      elseif ss < 9

           s = 2;

      else

           s = 3;

      end

      a = .5*(a + A(1,s)); b = .5*(b + A(2,s));

      x = cat(2,x,a); y = cat(2,y,b);

end

plot(x,y,'k.'), axis equal

save('MySG', 'x', 'y')

%=========EOF=========
```

B. One-dimensional chain of the interacting bistable elements

Section 1.8 reviews a one-dimensional chain of interacting bistable elements that illustrates a self-similar structure of the system's states in its extended configuration space. The following MATLAB programme code realizes the stepwise construction of the configuration presented in Fig. 1.20.

```
%==========PROGRAM START============

N=128; A=zeros(N+1,2*N); A(1,N)=1; x=[];

%==========Film===========

aviobj = avifile('MySpin.avi','compression','None','fps',5);

%==================================

for k=2:N

      p=find(A(k-1,:)==1); x(k-1)=length(p);

      for kk=1:length(p)

          A(k,p(kk)-1)=mod(A(k,p(kk)-1)+1,2);

          A(k,p(kk)+1)=mod(A(k,p(kk)+1)+1,2);

      end

      pcolor(mod(A+1,2));

      colormap([1 1 0; 0 0 1]); shading flat;

      pause(0)

      %======film======

      frame = getframe;

      aviobj = addframe(aviobj,frame);

end

figure(1), pcolor(mod(A+1,2));
```

```
colormap([1 1 0; 0 0 1]); shading flat;

figure(2), plot(x,'-ks')

%=========film=========

aviobj = close(aviobj);

%=========EOF=========
```

The programme creates an animation in the file MySpin.avi.

C. Gradient percolation

The following program code describes the fluctuation dynamics of the diffusion transition discussed in Section 2.8.

```
%============PROGRAM START=============

%============MAIN PROGRAM=============

global B N

N=120; a=linspace(N-N/4,N/4,N); a=a/N; a=a';

lev = repmat(a,1,N); A=rand(N); T = 1;

[K,L]=find(A(:,:)>=lev(:,:)); B=zeros(N,N,2);

for t=1:length(K)

     B(K(t),L(t),1)=1;

end

%==========Film==========

aviobj = avifile('MyPercolGrad.avi','compression','None');

%===============

for t = 1:T
```

```
[I,J]=find(B(:,:,1)==1); col=2; s=0; x=[]; t

for k=1:length(I)

    if B(I(k),J(k),2)==0

        s=s+1; y(s)=col; x(s)=artist(I(k),J(k),col);

        col=col+1;

    end

end

kk=find(max(x)-x==0); kk = kk(1);

[P,Q]=find(B(:,:,2)==y(kk));

for h=1:length(P)

    B(P(h),Q(h),1)=1.4;

end

B(N,N,1)=1.6; B(:,:,2) = zeros(N,N,1);

MyMap = [1 1 0; 0 0 0; 0 0 1];

Mytext=['grad(p) = ', num2str(1/(2*N))];

pcolor(B(:,:,1)); shading flat;

colormap(MyMap);

xlabel(Mytext,'FontSize',14);


for k=1:length(I)

    B(I(k),J(k),1)=1;

end

for tt = 1:20

    x1 = ceil((N-1)*rand); x2 = ceil((N-1)*rand);
```

```
          num1 = B(x1,x2,1); B(x1,x2,1) = B(x1,x2+1,1);

         B(x1,x2+1,1) = num1;

      end

      %======================

      %film

      frame = getframe;

      aviobj = addframe(aviobj,frame);

end

aviobj = close(aviobj);

%=========EOF=========

%============SUBPROGRAM=============

function x = artist(i,j,c)

global B N

B(i,j,2) = c; x = 1;

set(0,'RecursionLimit',3000)

if i>1 & B(i-1,j,2)==0 & B(i-1,j,1)==1

      x=x+artist(i-1,j,c); B(i-1,j,2)=c;

end

if j>1 & B(i,j-1,2)==0 & B(i,j-1,1)==1

      x=x+artist(i,j-1,c);B(i,j-1,2)=c;

end

if i<N & B(i+1,j,2)==0 & B(i+1,j,1)==1

      x=x+artist(i+1,j,c); B(i+1,j,2)=c;

end
```

```
if j<N & B(i,j+1,2)==0 & B(i,j+1,1)==1

      x=x+artist(i,j+1,c); B(i,j+1,2)=c;

end
```

D. The generic Brownian landscapes. The Voss algorithm of addition

In a one-dimensional case a generic Brownian landscape is the realization of the generalized Brownian processes for different Hurst exponents. The result of the following programme code of the one-dimensional Voss algorithm of addition is presented in Figure 3.1. The detailed overview of the algorithm is given in Section 3.1.

```
%============PROGRAM START=============

%Generalised Brownian Relief Generator D1

H = [.1 .5 .9]; %Hurst exponents

for kk = 1:3

      R = normrnd(0,1,1,2); k = 9; N = 2^k + 1;

      x = [1 N];

      sigma = 1; h = H(kk);

      for t = 1:k

           n = 2^t + 1; xi = linspace(1,N,n);

           yi = interp1(x,R,xi); sigma = sigma*sqrt(2)^(-h);

           R = yi + normrnd(0,sigma,1,n); x = xi;

      end

      subplot(3,1,kk); plot(R,'k-'), hold on

end

%=========EOF=========
```

The two-dimensional realization of the Voss algorithm is described in Section 3.2 and graphically presented in Figures 3.2, 3.3 and 3.4. The given surfaces are the result of the following MATLAB code:

```
%============PROGRAM START============

%Generalised Brownian Relief Generator 2D

H = .5; %Hurst exponents

for kk = 1:1

    R = normrnd(0,1,2); k = 8; N = 2^k + 1;

    x = [1 N];

    sigma = 1; h = H(kk);

    for t = 1:k

        n = 2^t + 1; [X,Y] = meshgrid(x);

        xi = linspace(1,N,n); [XI,YI] = meshgrid(xi);

        ZI = interp2(X,Y,R,XI,YI);

        sigma = sigma*sqrt(2)^(-h);

        R = ZI + normrnd(0,sigma,n); x = xi;

    end

    %subplot(3,1,kk);

    surf(R), shading flat, colormap jet

    %camlight(-45,45);

    %view(-40,55)

end

%=========EOF=========
```

Figures 3.5, 3.6 and 3.7 illustrate the Voss algorithm operation in a three-dimensional case. The appropriate code is given below. The reader may change the Hurst exponent `'H'` and the section level `'lev'`.

```
%============PROGRAM START=============

%Generalised Brownian Relief Generator 3D

H = 0.75;

R = normrnd(0,1,2,2,2); k = 5; N = 2^k + 1; x = [1 N];

sigma = 1; h = H; lev = .05;

for t = 1:k

     n = 2^t + 1; [X,Y,Z] = meshgrid(x);

     xi = linspace(1,N,n); [XI,YI,ZI] = meshgrid(xi);

     VI = interp3(X,Y,Z,R,XI,YI,ZI);

     sigma = sigma*sqrt(2)^(-h);

     R = VI + normrnd(0,sigma,n,n,n); x = xi;

end

y = x; z = x;

figure(1), subplot(1,2,1), hiso = patch(isosurface(x,y,z,R,lev));

isonormals(x,y,z,R,hiso)

set(hiso,'FaceColor','blue','EdgeColor','none');

%===

hcap = patch(isocaps(x,y,z,R,lev),...

     'FaceColor','interp',...

     'EdgeColor','none');

colormap lines; daspect([1,1,1]);

camproj perspective

view(65,45); camlight(-45,45);

set(gcf,'Renderer','zbuffer'); lighting phong
```

```
set(hcap,'AmbientStrength',.6); axis tight

%============================

subplot(1,2,2), hiso = patch(isosurface(x,y,z,-R,-lev));

isonormals(x,y,z,-R,hiso)

set(hiso,'FaceColor','yellow','EdgeColor','none');

%===

hcap = patch(isocaps(x,y,z,-R,-lev),...

     'FaceColor','interp',...

     'EdgeColor','none');

colormap lines; daspect([1,1,1]);

camproj perspective

view(65,45); camlight(-45,45);

set(gcf,'Renderer','zbuffer'); lighting phong

set(hcap,'AmbientStrength',.6); axis tight

%=========EOF=========
```

E. The forest fire model

In Section3.6 we consider a classical model of forest fires, where trees growing at the square lattice points play the role of percolating elements. In this model the specific number of trees fluctuates at the threshold $p_c \simeq 0.58$ not exceeding it. This critical level is controlled by the balance between the process of tree growing and their destruction by fires. The programme code of the forest fire model is given below. The details of the algorithm are given in Section 3.6.

```
%============PROGRAM START=============

%============MAIN PROGRAM=============
```

```
global B; global N; global count;
hFig1 = figure( 'Name','Forest Fire')
hAxes1=axes( 'Parent',hFig1,'Color',[1 1 1],...
     'Units','pixels','Position',[ 12 52 256 256 ] );
hAxes2=axes( 'Parent',hFig1,'Color',[1 1 1],...
     'Units','pixels','Position',[ 280 52 256 256 ] );
uicontrol(hFig1,'Style','text','Position',[12,16,460,24],...
     'BackgroundColor','white',...
     'HorizontalAlignment','center','String',...
     'specific number of trees ( percentage wise )','FontSize',14);
hText=uicontrol(hFig1,'Style','text','Position',[500,16,36,24],...
     'BackgroundColor','white',...
     'HorizontalAlignment','center','FontSize',14);
N=128; T=10^3; B=zeros(N,N,2); x=zeros(1,T); s=.2;
teta=25;
aviobj = avifile('MyForestFire.avi','compression','None','fps',30);
for t=1:T
     A=rand(N); [q,p]=find(A(:,:)<teta/N^2); count=0;
     for k=1:length(p)
         B(q(k),p(k),1)=1;
     end
     v=rand; psi=.06;
     num=length(find(B(:,:,1)==1));
     if v<psi
```

```
          ii=ceil(N*rand); jj=ceil(N*rand);
          if B(ii,jj,1)==1
              B(ii,jj,2)=1;
          end
      end
      [q1,p1]=find(B(:,:,2)==1-s); counter(s); x(t)=count; t
      B(N,N,1)=1.5; B(:,:,2)=B(:,:,2)-s*B(:,:,2);
      B(N,N,2)=1.5;
      str = int2str(100*num/N^2);
      set(hText,'String',str)
      axes(hAxes2); pcolor(B(:,:,2)); shading flat; axis off
      axes(hAxes1); pcolor(B(:,:,1)); shading flat; axis off
      pause(0)

      frame = getframe(hFig1,[0,0,548,320]);
      aviobj = addframe(aviobj,frame);
end
aviobj = close(aviobj);
figure(1); plot(x)
for kk=1:max(x)
      G2(kk)=length(find(x==kk));
end
figure(2);loglog(G2)
xlabel('lg( cluster size )');
```

```
ylabel('lg( frequency of event )');

%=========EOF=========

%============SUBPROGRAM=============

function counter(s);

global B; global N; global count;

[q1,p1]=find(B(:,:,2)==1-s);

for k1=1:length(p1)

     B(q1(k1),p1(k1),1)=0; count=count+1;

     a=q1(k1)+1; b=p1(k1)+1; c=q1(k1)-1; d=p1(k1)-1;

     if a<=N & B(a,p1(k1),1)==1

          B(a,p1(k1),2)=1;

     end

     if b<=N & B(q1(k1),b,1)==1

          B(q1(k1),b,2)=1;

     end

     if c>=1 & B(c,p1(k1),1)==1

          B(c,p1(k1),2)=1;

     end

     if d>=1 & B(q1(k1),d,1)==1

          B(q1(k1),d,2)=1;

     end


     if a==N+1 & B(1,p1(k1),1)==1

          B(1,p1(k1),2)=1;
```

```
      end

      if b==N+1 & B(q1(k1),1,1)==1

          B(q1(k1),1,2)=1;

      end

      if c==0 & B(N,p1(k1),1)==1

          B(N,p1(k1),2)=1;

      end

      if d==0 & B(q1(k1),N,1)==1

          B(q1(k1),N,2)=1;

      end

end

%=========EOF=========
```

List of Figures

1.1 Cantor set generation 10
1.2 The Koch curve iterations 11
1.3 The first four iterations of the Koch Island 12
1.4 The Sierpiński gasket iterations 14
1.5 Iteration of the Sierpiński carpet 14
1.6 Application of the IFS-generator of the Sierpiński gasket to the equilateral triangle 16
1.7 Application of the IFS-generator of the Sierpiński gasket to the right triangle 16
1.8 Result of the application of the IFS-generator of eq.1.12 17
1.9 One-dimensional random walk $r(t)$. The dotted line shows the mean-square shift $\langle r^2(t)\rangle^{1/2}$ according to the Fick law (1.14) for $a = 1$ 19
1.10 The Lake Ladoga coastline scaling. The water surface is in black. The pattern in the top left corner is subjected clockwise to a successive fourfold resolution increase 20
1.11 Unit length segment (a) is divided into four equal parts, the extreme parts keep their position but the central ones are changed by an A-shaped generator of five segments (b). Then the procedure is repeated for each of 7 segments of $1/4$ length (c), and then for each of 49 segments of $1/16$ length (d) . . . 25
1.12 The multifractal Sierpiński gasket 27
1.13 Results of 12 iterations of binominal multiplicative process for different p values 28
1.14 Integral mass relation as the function of the position on a unit segment after 12 iterations of the binominal multiplicative process for different p values . 29
1.15 Behaviour of $M_q(\varepsilon)$ moments with the change of ε 30
1.16 Relation $\tau(q)$ for the binominal multiplicative process for different p values . 31
1.17 Relation $D_q(q)$ for the binominal multiplicative process for different p values 32
1.18 Multifractal spectra of the binominal multiplicative process for different p-values 35
1.19 Dependence $\alpha(q)$ by the example of the binominal multiplicative process for different p-values 36
1.20 Distribution of excitations (black dots) in the linear chain of spins. The system is presented in the extended configuration space, where each moment of time corresponds to a certain line of the structure. The time increases upwards. 38

2.1 Site percolation on the square lattice. The black sites of the square lattice are conductors; yellow sites are insulators; blue sites represent a maximum conductor cluster. The sites marked in white are the nearest neighbours of the central site 41

2.2 Site percolation on the square lattice. The concentration of the conductor sites equals $p = 0.1$. The maximum conductor cluster is represented in blue . 41
2.3 Site percolation on the square lattice. The concentration of the conductor sites equals $p = 0.4$. The maximum conductor cluster is represented in blue 42
2.4 Site percolation on the square lattice. The concentration of the conductor sites equals $p = 0.55$. The maximum conductor cluster is represented in blue 42
2.5 Site percolation on the square lattice. The concentration of the conductor sites equals $p = 0.9$. All the occupied sites belong to the same maximum conductive cluster 43
2.6 Site percolation on the square lattice. The concentration of the conductor sites is near the threshold and equal to $p = 0.59$. The blue colour represents the percolating conductive cluster 44
2.7 Site percolation on the square lattice. The concentration of the conductor sites is above the critical value and equal to $p = 0.62$. The blue colour represents the percolating conductive cluster 45
2.8 Bond percolation on the 100×100 square lattice. The concentration of conductive bonds is below the critical value 46
2.9 Site percolation on the 200×200. square lattice. Different colours correspond to the clusters of different sizes. The maximum cluster is marked in white. 48
2.10 Percolation cluster near the threshold. The colour of sites changes as a periodic function of their Euclidean distance from a certain site in the centre of the lattice 49
2.11 Illustration of a crossover phenomenon from the fractal behaviour on small scales to the homogeneous behaviour on large scales of regular parquet made of the ξ-size Sierpiński carpets 50
2.12 Schematic diagram of the crossover phenomenon 51
2.13 Percolating cluster of sites (blue cells) on the 40×40 square lattice. The shortest path connecting the red cells with coordinates $(3,20)$ and $(39,24)$ is marked by a white broken line 52
2.14 Travel along the labyrinths of the percolating cluster with the periodic colour change of the sites with the increase of the chemical distance 54
2.15 Generations of the Mandelbrot-Given fractal 55
2.16 Example of the clusters on the 1-D lattice. The occupied sites are grey, the empty sites are white 56
2.17 Fragments of the Bethe lattice or Kayley tree with the coordination numbers (z): a) $z = 2$, b) $z = 3$, c) $z = 4$ 60
2.18 Gaussian chance function $\Psi(X,Y)$ on the one-unit square. For construction 5000 Gaussian peaks with the characteristic width $r_0 = 0.02$ have been overlapped 65
2.19 Distribution of equipotential levels for a random potential 66
2.20 Map of the reservoir at the level of filling $h = -1$. The areas filled up with water is coloured in blue 66
2.21 Map of the reservoir at the level of filling $h = 0$. The areas filled up with water is coloured in blue 67

2.22 Map of the reservoir at the level of filling $h = 1$. The areas filled up with water is coloured in blue 67
2.23 Illustration of the 3-D Gaussian potential. In the left block the areas of space with the potential below the fixed level $\Psi(X,Y,Z) < 0.001$ are marked in blue. In the right block the areas of space with the potential above the fixed level $\Psi(X,Y,Z) > 0.001$ are marked in yellow 70
2.24 Continuum percolation of the randomly distributed discs 71
2.25 Gradient percolation 73
2.26 Gradient percolation. The yellow pixels denote the maximum cluster of the occupied sites, the dark-blue pixels represent the maximum cluster of the empty sites 74
2.27 Epidemic spreading from a single infected element at the initial moment with the infection transmission probability close to critical. The change of pixel colouring corresponds to the time passed from the moment of the infection contraction. The bright pixels on the periphery belong to the epidemic front 75

3.1 Realization of the generic Brownian processes for different values of the Hurst index 80
3.2 Brownian surface generation on the 257×257 square lattice 82
3.3 Brownian surface generation on the 257×257 square lattice with $Hu = 0.01$ 83
3.4 Brownian surface generation on the 257×257 square lattice with $Hu = 1$. 83
3.5 Generation of the Brownian relief on the $65 \times 65 \times 65$ cubic lattice with $Hu = 0$ 84
3.6 Generation of the Brownian relief on the $65 \times 65 \times 65$ cubic lattice with $Hu = 1$ 84
3.7 Generation of the Brownian relief on the $65 \times 65 \times 65$ cubic lattice with $Hu = 0.5$ 85
3.8 Distribution of positive electric potentials in the system of 3,000 point charges 86
3.9 Distribution of negative electric potentials in the system of 3,000 point charges 87
3.10 Hyperbolic rank distributions in log-log scale at the fixed N_1 and varying β 92
3.11 Behaviour of the moments of "individuals" distribution by "species" M_q for various β and q 94
3.12 Effects connected with the strong domination 94
3.13 Multifractal spectrums of the rank distributions with $\beta = 0.65$ 95
3.14 Dependence of the moments M_q on the population N in the log-log scale for the logarithmically normal distribution at the linearly increased distribution parameters. The behaviour of the zero moment $q = 0$ corresponds to the dependence of the S-species number on the population N 96
3.15 Schematic diagram of the experimental installation 99
3.16 Experimental dependences of the filtration rate on pressure differential for various porosity values 100
3.17 Permeability as the function of the total porosity 100
3.18 Critical value of the total porosity as the function of the structural parameter 103
3.19 Three possible situations for the lumped active element: low curve is the passive state, middle curve is the waiting or bistable mode, top curve is the self-excitation and self-oscillation 113
3.20 Evolution of the number of the burned-out trees 115
3.21 Frequency of occurrence of fires as function of their sizes in a log-log scale 115

3.22 Function of bond distribution by potential difference for $x_c = 4$. The solid graph corresponds to the theoretical dependence with $z = 4$. For a simple cubic lattice the number of outgoing bonds $z = 5$. The corresponding curve is shown as a dotted line. The squares represent the numerical experiment. . 119
3.23 Dependence of pz on z at the different ratios of the critical level and level of activation 120
3.24 Instantaneous 3-*D* configuration of a model tree, the edge thickness of which is proportional to the current passing along them 126
3.25 Transparence cluster configuration on the 35×35. square lattice. The random distribution of the transparence zones is shown on the left. The fraction of transparent sites is near the percolation threshold for a site problem on the square lattice $p \simeq 0.58$. The corresponding distribution of the scalar potential Ψ is shown on the right. 131
3.26 Gradient distribution of the transparence zones on the square lattice (*left*). The corresponding distribution of the pore pressure (*right*) 132
3.27 Model differentiation of substance in the field of gravitation. The configuration of the transparent and opaque sites is shown in the left window. The corresponding pore pressure distribution is shown in the right window . . . 135
3.28 Degassing on the square lattice. Transparence zone distribution in a model for Weibull modulus $m = 1$, $m = 3$, $m = 7$ is presented in the top windows from left to right. The corresponding distribution of the pore pressure is shown in the bottom windows 136
3.29 Evolution of the model system for Weibull modulus $m = 1$. The evenly spaced time measurements increase upwards 137
3.30 Dewar flask 138
3.31 Evolution of the fluid stored by the system. Model time steps are plotted on the abscissa axis 138
3.32 Evolution of the number of actuated siphons corresponding to Fig. 3.31 . . 139
3.33 Geometric scheme of the model neuron and one of its nearest neighbours . . 145
3.34 Relation between the critical value B_c and parameter Γ 146
3.35 The model neuron network at the threshold of vector percolation. The percolation cluster is marked with red 147
3.36 One-dimensional dynamics with the time axis directed upwards; the color intensity corresponds to the level of occupancy 150
3.37 One-dimensional chain of cellular automata. The black colour corresponds to the blocking cells, grey – to the transparent ones and white – to the transparent and information-carrying cells. 151
3.38 Information is transmitted upwards, the time increases rightwards 151
3.39 Dependence of the channel throughput on the transparency level p 152
3.40 The same as in Fig. 3.39 given in a log-log scale at different number of automata renewed in one step 152

References

[1] Schroeder, M. Fractals, chaos, power laws / M. Schroeder; in Russian transl. Scientific Publishing house Regulyarnaya i khaoticheskaya dinamika, 2001. P. 528.

[2] Fractals in Physics; in Russian transl.; Eds L. Pietronero, E. Tozatti M. : Mir, 1988. 671 pp., illustrated.

[3] Mandelbrot, B. B. The Fractal Geometry of Nature/ B. B. Mandelbrot. – N. Y.: Freeman, 1982. – 468 p.

[4] Iudin, D.I. Perkolyatsionnye effekty v bioekologicheskikh sistemakh / D.I. Iudin, D.B. Gelashvili // Nelineinye volny 2010; Eds A.V. Gaponov-Grekhov, V.I. Nekorkin. N.Novgorod: IPF RAN, - 2011. P. 412-434.

[5] Jensen H.J. Self-Organized Criticality / H.J. Jensen // Cambridge university press, 1998. – p. 153.

[6] Zelyony, L.M. Fraktalnaya topologia i strannaya kinetika: ot teorii perkolyatsii k problemam kosmicheskoy elektrodinamiki / L.M. Zelyony, A.V. Milovanov // J. UFN (Uspekhi fizicheskikh nauk). 2004. V. 174. No.8.

[7] Ashour-Abdalla, M. The mosaic structure of plasma bulk flows in the Earth's magnetotail / M. Ashour-Abdalla, L.M. Zelenyi, V. Peroomian [et al.] // J. Geophys. Res. 1995. V. 100. P. 19191–19210. DOI: 10.1029/95JA00902.

[8] Zelenyi, L.M. Matresha-model of multilayered current sheet / L.M. Zelenyi [et al.] // Geophys. Res. Lett. 2006. V. 33. P. 5105.

[9] Goltz, C. Fractal and Chaotic Properties of Earthquakes. / C. Goltz. – Berlin: Springer-Verlag, 1997. – 77 p.

[10] Bak, P. How Nature Works (The Science of Self-organized Criticality) / P. Bak // Oxford Univ. Press, 1997.

[11] Broadbent, S.R. Percolation processes. I. Crystals and mazes, Proc. Camb. / S.R. Broadbent, J.M. Hammersley // Phil. Soc. – 1957. – Vol. 53. – P. 629–641.

[12] Mandelbrot, B. Fractal geometry of nature / B. Mandelbrot; in Russian transl. M.: Institute of computer researches, 2002. 656 pp.

[13] Bunde, A. Fractals and Disordered Systems / A. Bunde, S. Halvin. – Berlin: Springer-Verlag, 1995. – 408 p.

[14] Bunde, A. Fractals and Disordered Systems / A. Bunde, S. Halvin. – Berlin: Springer-Verlag, 1995. – 408 p.

[15] Mandelbrot, B. B. Possible refinement of the lognormal hypothesis concerning the distribution of energy dissipation in intermittent turbulence / B. B. Mandelbrot // Statistical models and turbulence. Lecture notes in physics 12. Eds. M. Rosenblatt and C. Van Atta. New York. – 1972. – P. 333-351.

[16] Mandelbrot, B. B. Fractals: Forme, Chance and Dimension / B. B. Mandelbrot. - San-Francisco: Freeman, 1977. – 365 p.

[17] Mandelbrot, B. B. The Fractal Geometry of Nature/ B. B. Mandelbrot. – N. Y.: Freeman, 1982. – 468 p.

[18] Mandelbrot, B. B. Fractals / B. B. Mandelbrot //Encyclopedia of Physical Science and Technology. – N. Y.: Academic Press. – 1987. – V. 5. – P. 579-593.

[19] Flory P.J. Principles of Polymer Chemistry // P.J. Flory – Cornel University, New York 1971.

[20] Zeldovich, Ya.B. Fraktaly, podobie, promezhutochnaya asimptotika / Ya.B. Zeldovich, D.D. Sokolov // J. UFN (Uspekhi fizicheskikh nauk). 1985. V. 146. No.3. P. 493-506.

[21] Peitgen, H.-O. The beauty of fractals / H.-O. Peitgen, P.H. Richter; in Russian transl.; Ed A.N. Sharkovsky. M. : Mir, 1993. P. 176.

[22] Bozhokin, S.V. Fraktaly i multifraktaly / S.V. Bozhokin, D.A. Parshin. Izhevsk, 2001. 128 pp.

[23] Zhikov, V.V. Fraktaly / V.V. Zhikov // Sorosovsky obrazovatelny zhurnal. 1996. No.12. P. 109-117.

[24] Morozov A.D. Vvedenie v teoriyu fraktalov / A.D. Morozov. M. Izhevsk: IKI, 2002. P. 160.

[25] Falconer, K. J. The Geometry of Fractal Sets / K. J. Falconer. – Cambridge: Cambridge Univ. Press, – 1985.

[26] Loskutov, A.Yu. Vvedenie v sinergetiku / A.Yu. Loskutov, A.S. Mikhailov. M.: Nauka, 1990. 272 pp.

[27] Feder, J. Fractals / J. Feder ; in Russian transl. M. : Mir, 1991. 254 pp., illustrated.

[28] Bunde, A. Fractals in Science / A. Bunde, S. Halvin. – Berlin: Springer-Verlag, 1995. – 298 p.

[29] Bunde, A. Fractals and Disordered Systems / A. Bunde, S. Halvin. – Berlin: Springer-Verlag, 1995. – 408 p.

[30] Turcotte D.L. Fractals and chaos in geology and geophysics / D.L. Turcotte // Cambridge university press, 1997. – p. 398.

[31] Lovejoy, S. Generalized scale invariance in the atmosphere and fractal models of rain / S. Lovejoy, D. Schertzer // Water Resour. Res., V. 21. – 1985. – P. 1233–1250

[32] Hausdorff, F. Teoria mnozhestv / F. Hausdorff; in Russian transl. M. L.: ONTI, 1937. P. 304.

[33] Loehle, C. Statistical properties of ecological and geologic fractals / C. Loehle, B.-L. Li // Ecological Modelling. – 1996. – V. 85. – P. 271-284.

[34] Vstovsky, G.V. Vvedenie v multifraktalnuyu parametrizatsiyu structur materialov / G.V. Vstovsky, A.G. Kolmakov, I.Zh. Bunin. M. Izhevsks, 2001. 116 pp.

[35] Halley J. M., Hartley S., Kallimanis A. S., Kunin W. E., Lennon J. J. , Sgardelis S. P. Uses and abuses of fractal methodology in ecology // Ecology Letters. 2004. – V. 7. – P. 254–271.

[36] Harte, J. Self-Similarity and the relationship between Abundance and Range Size / J. Harte, T. Blackburn, A. Ostling // American Naturalist. – 2001. – V. 157. – P. 374-386.

[37] Kuznetsov, S.P. Dinamichesky khaos (lectures) / S.P. Kuznetsov. M.: Fizmatlit, 2001. 296 pp.

[38] Pesin, Ya.B. Teoria razmernosti i dinamicheskie sistemy: sovremenny vzglyad i prilozhenia / Ya.B. Pesin. M.-Izhevsk: IKI, 2002. P. 404.

[39] Goltz, C. Fractal and Chaotic Properties of Earthquakes. / C. Goltz. – Berlin: Springer-Verlag, 1997. – 77 p.

[40] Schuster, G. Determinirovanny khaos / G. Schuster; in Russian transl.; Eds A.V. Gaponov-Grekhov and M.I. Rabinovich. M. : Mir, 1988. P. 240.

[41] Tokens, F. Detecting Strange Attractors in Turbulence / F. Tokens // Dynamical Systems and Turbulence. – Lecture Notes in Mathematics. – Berlin: Springer-Verlag. - 198l. – V. 898. – P. 366-381.

[42] Grassberger, P. Measuring the Strangeness of Strange Attractors / P. Grassberger, I. Procaccia // Physica D. – 1983. – V. 9, No 1–2. – P. 189–208.

[43] Trubetskov, D.I. Sled vdokhnoveniy i trudov upornykh / D.I. Trubetskov. Saratov: Publ. House College, 2001. P. 13.

[44] Abdullaev, S.S. Klassicheskaya nelineinaya dinamika i khaos luchei v zadachakh rasprostranenia voln v neodnorodnykh sredakh / S.S. Abdullaev, G.M. Zaslavsky // J. UFN (Uspekhi fizicheskikh nauk). 1991. V. 161. No.8. P. 1-43.

[45] Batunin, A.V. Fraktalny analiz i universalnost Feingenbauma v fizike adronov / A.V. Batunin // J. UFN (Uspekhi fizicheskikh nauk). 1995. V. 165. No.6. P. 645-660.

[46] Bershadsky, A.G. Krupnomasshtabnye fraktalnye struktury v laboratornoi turbulentnosti, okeane i astrofizike // UFN (Uspekhi fizicheskikh nauk). 1990. V. 160. No.12. P. 189-194.

[47] Wiesmann, H.J. Properties of Laplacian fractals for dielectric breakdown in 2 and 3 dimensions / H.J. Wiesmann, L. Pietronero / Fractals in Physics. Eds L. Pietronero and E. Tozatti. M.: Mir, 1988.

[48] Gardner, M. Ot mozaik Penrouza k nadyozhnym shifram / M. Gardner ; in Russian transl. M. : Mir, 1993. P. 416.

[49] Gennes, P. de. Idei skeilinga v fizike polimerov / P. de Gennes. In Russian transl. ; Editor I.M. Livshitz. M.: Mir, 1982. 368 pp.

[50] Zosimov, V.V. Fraktaly i skeiling v akustike / V.V. Zosimov, L.M. Lyamshev // Akust. zhurn. 1994. V. 40. No.5. P. 709-737.

[51] Zosimov, V.V. Fraktaly v volnovykh protsessakh / V.V. Zosimov, L.M. Lyamshev // J. UFN (Uspekhi fizicheskikh nauk). 1995. V. 165. No.4. P. 361-402.

[52] Iudin, D.I. Nelineinaya dinamika grozovogo oblaka / D.I. Iudin, V.Yu. Trakhtengertz // Izv. Vuzov. Radiofizika. 2001. 44(5-6). P.419-438.

[53] Smirnov, B.M. Fraktalnye klastery / B.M. Smirnov // UFN. 1986. V. 149. No.2. P. 177-219.

[54] Smirnov, B.M. Fraktalny klubok novoe sostoyanie veschestva / B.M. Smirnov // UFN. 1991. V. 161. No.8. P. 141-153.

[55] Smirnov, B.M. Fizika fraktalnykh klasterov / B.M. Smirnov. M. : Nauka, 1991. P. 134.

[56] Anderson, A. N. Soil aggregates as mass fractals / A. N. Anderson, A. B. McBratney // Australian Journal of Soil Research. – 1995. – V. 33. – P. 757-772.

[57] Broadbent, S.R. Percolation processes. I. Crystals and mazes, Proc. Camb. / S.R. Broadbent, J.M. Hammersley // Phil. Soc. – 1957. – Vol. 53. – P. 629–641.

[58] Tarasevich, Yu.Yu. Perkolyatsia: Teoria, prilozhenia, algoritmy: Teaching aid. 2-nd edit. / Yu.Yu. Tarasevich. M. : Book house Librokom, 2012. 112 pp.

[59] Sahimi, M. Aplications of Percolation Theory / M. Sahimi – London: Taylor & Francis, 1992 – 347 p.

[60] Efros, A.L. Fizika i geometria besporyadka / A.L. Efros. M. : Nauka, 1982.

[61] Sokolov, I.M. Razmernosti i drugie geometricheskie pokazateli v teorii protekania / I.M. Sokolov // UFN. 1986. V. 150. No.2. P. 221-255.

[62] Mandelbrot, B. B. Physical Properties of a New Fractal Model of Percolation Cluster / B. B. Mandelbrot, J.A. Given // Phys. Rev. Lett. - 1984. – P. 1853–1856.

[63] Balberg, I. Recent developments in continuum percolation / I. Balberg // Philosophical Magazine B 56(6). – 1987. – P.991 - 1003.

[64] Gouyet, J.-F. Dynamics of diffusion and invasion fronts: on the disconnection-reconnection exponents of percolation clusters / J.-F. Gouyet // In Rabin and Bruinsma pages 163–166.

[65] Sapoval, B. The fractal nature of a diffusion front and relation to percolation / B. Sapoval, M. Rosso, J.F. Gouyet // J. Physique Lett. (Paris), – 1985. L 149.

[66] Stanley, H. Phase Transitions and Critical Phenomena / H. Stanley; in Russian transl. // M.: Mir, 1973. C. 419.

[67] Voss R.F., Random fractals: Characterization and measurement. – In: Scaling Phenomena in Disordered Systems (eds. R. Pynn & A. Skjeltorp), Plenum Press, New York, pp. 1 – 11, 1985.

[68] Hayakawa, M., D. I. Iudin, and V. Y. Trakhtengerts, Modeling of thundercloud VHF/UHF radiation on the lightning preliminary breakdown stage, J. Atmos. Solar-terr. Phys., vol. 70, 1660-1668, doi:10.1016/j. jastp.2008.06.011, 2008.

[69] Iudin, D.I. Fraktalnaya dinamika zaryada v grozovom oblake / D.I. Iudin, V.Yu. Trakhtengertz // Izvestia AN. Fizika atmosfery i okeana. 2000. V. 36. No.5. P. 650-662.

[70] Azovsky, A.I. Analiz prostranstvennoi organizatsii soobschestv i fraktalnaya struktura litoralnogo bentosa / A.I. Azovsky, M.V. Chertoprud // Reports of AoS. 1997. V. 356. No.5. P. 713-715.

[71] Azovsky, A.I. Masshtabno-orientirovanny podkhod k analizu prostranstvennoi struktury soobschestv / A.I. Azovsky, M.V. Chertoprud // J. of Gen. Biol. 1998. V. 59. P. 117-136.

[72] Bigon, M. Ecologia: Osobi, populyatsii, soobschestva: in 2 volumes (in Russian translation). V. 2. / M. Bigon, J. Harper, K.M. Townsand. M.: Mir, 1989. 447 pp.

[73] Gelashvili, D.B. Stepennoy zakon i printsip samopodobia v opisanii vidovoy struktury soobschestv / D.B. Gelashvili, D.I. Iudin, G.S. Rozenberg, V.N. Yakimov, V.G. Shurganov // Privolzhsky Scientific Journal. 2004. No.3. P. 227-245.

[74] Levich, A.P. Struktura ekologicheskikh soobschestv / A.P. Levich. M.: MGU, 1980. 181 pp.

[75] Likhachyova, N.E. O kolichestvennoy obrabotke prob fitoplanktona. Rangovye raspredelenia chislennosti fitoplanktona proliva Vilkitskogo / N.E. Likhachyova, A.P. Levich, T.I. Koltsova // J. Biologicheskie nauki. 1979. No.9. P. 102-106.

[76] Azovsky, A. I. Size-dependent species-area relationships in benthos: is the world more diverse for microbes? / A. I. Azovsky // Ecography. – 2002. – V. 25. – P. 273-282.

[77] Fractal properties of spatial distribution of intertidal benthic communities / A. I. Azovsky, M. V. Chertoprood, N. V. Kucheruk et al. // Marine Biology. – 2000. – V. 136. – P. 581-590.

[78] Pozdnyakov, A.A. Znachenie pravila Willisa dlya taxonomii / A.A. Pozdnyakov // J. of Gen. Biology. 2005. V. 66. No.4. P. 326-335.

[79] Rozenberg, G.S. Ekologia. Elementy teoreticheskikh konstruktsiy sovremennoy ecologii / G.S. Rozenberg, D.P.Mozgovoy, D.B. Gelashvili. Samara: Samara Scientific Centre of RAS, 1999. P. 396.

[80] Margalef, R. Oblik biosfer / R. Margalef. M. : Nauka, 1992. 254 pp.

[81] Maguarran, E. Ecological diversity and its measurement / E. Maguarran; in Russian transl. M. : Mir, 1992. P. 181.

[82] Odum, E. Fundamentals of ecology / In Russian transl. E. Odum. - M. : Mir, 1975. P. 740.

[83] Arrhenius, O. On the relation between species and area: a reply / O. Arrhenius // Ecology. - 1923. – V. 4. – P. 68-73.

[84] Arrhenius, O. Species and area / O. Arrhenius // Journal of Ecology. – 1921. – V. 9. – P. 95-99.

[85] Arrhenius, O. Statistical investigations in the constitution of plant associations / O. Arrhenius // Ecology. – 1923. – V. 4. – P. 68-73.

[86] Iudin, D.I. Multifraktalny analiz struktury bioticheskikh soobschestv / D.I. Iudin, D.B. Gelashvili, G.S. Rozenberg // Reports of AS. 2003. V. 389. No.2. C. 279-282.

[87] Last B. J. and Thouless D. J. Non. Phys. Rev. Lett. 27:1719, 1971.

[88] Koposov, E.V. Universalnaya forma nelineinogo zakona filtratsii v dispersnykh gruntakh / E.V. Koposov, D.I. Iudin, A.A. Panyutin // Privolzhsky Scientific Journal 2007. No.4. P. 108-114.

[89] Iudin, D.I. Filtratsionnoe techenie v srede s peremennoy poristostjyu / D.I. Iudin, D.A. Kasianov, G.M. Shalashov // Reports of AS. 1999. V. 2. P. 257-259.

[90] Armstrong, A. C. On the fractal dimensions of some transient soil properties / A. C. Armstrong // Journal of Soil Science. – 1986. – V. 37. – P. 641-652.

[91] Schwartz L.M. Calculation of eletrical transport in continuum system by diffusin simulation / L.M. Schwartz, J.R. Banavar // Phys. A. – 1989. V.157. N9. – P.230.

[92] Bakurov V.G., Gusev V.I., Izmailov A.F., Kessel L.R. // J. Phys. 1990. V.A23. P.250–257.

[93] Barentblatt G.I., Entov V.M., Ryzhik V.M. Dvizhenie zhidkostei i gazov v prirodnykh plastakh. M.: J. Nedra, 1984. 211 pp.

[94] Roberts, J.N. Crain consolidation and electrical conductivity in porous media / J.N. Roberts, L.M. Schwartz // Phys. Rev. B. 1985.

[95] Dobrynin, V.M. Metody prognozirovania anomalnykh vysokikh plastovykh davleny / V.M. Dobrynin, V.A. Serebryakov // M.: Nedra, 1978. 232 pp.

[96] Iton, B. Ispolzovanie poluchaemykh v protsesse burenia petrofizicheskikh dannykh dlya otsenki perspektiv / B. Iton // J. Neftegazovye tekhnologii. 1993. No.3. P. 15-25.

[97] Koposov, E.V. Perkolyatsionny mekhanism gravitatsionnoy neustoychivosti dispersnykh system / E.V. Koposov, D.I. Iudin // Privolzhsky Scientific Journal 2008. No.1. P. 102-109.

[98] Smirnov, N.N. Perkolyatsionny mekhanism gravitatsionnoy differentsiatsii kak model seismicheskoy aktivnosti / N.N. Smirnov, D.I. Iudin // Vest. Mosk.Un-ta. 2003. V. 2. P. 31-39.

[99] Gouet, J.F. Invasion noise during drainage in porous media / J.F. Gouet // Physica A. – 1990. – V.168. – P.581.

[100] Gouet, J.F. Structura of noise generated on diffusion fronts / J.F. Gouet, B. Sapoval, Y. Boughaleb, M. Rosso // Physica A. – 1990. – V.157. – P.620.

[101] Iudin, D.I. Dinamicheskaya perkolyatsia v aktivnykh sredakh / D.I. Iudin, V.Yu. Trakhtengertz // Nelineinye volny 2004; Eds A.V. Gaponov-Grekhov, V.I. Nekorkin. N.Novgorod: IPF RAN, - 2005. P. 217-242.

[102] Iudin D.I., A.N. Grigoriev, Cellular automaton model of lithosphere degassing, Elsevier NI & MIPR A 502. – 2003. – P. 736–738.

[103] Iudin, D.I. Fraktalnye labirinty: srukturnaya dinamika / D.I. Iudin, V.Yu. Trakhtengertz // Nelineinye volny 2006; Eds A.V. Gaponov-Grekhov, V.I. Nekorkin. N.Novgorod: IPF RAN, - 2007. P. 360-377.

[104] Alexander, S. and Orbach, R. // J. Phys. Lett. 1982. 43:L625

[105] Atkins, P. The second law / P. Atkins; in Russian transl. M. : Mir, 1987.

[106] Trakhtengertz, V.Yu. O fraktalnoy dinamike aktivnykh sred / V.Yu. Trakhtengertz, D.I. Iudin, A.N. Grigoriev // V.Yu. Trakhtengertz, D.I. Iudin // Nelineinye volny 2006; Eds A.V. Gaponov-Grekhov, V.I. Nekorkin. N.Novgorod: IPF RAN, - 2007. P. 287-302.

[107] Bak, P. Self-Organized Criticality: An Explanation of 1/f Noise / P. Bak, C. Tang, K. Wiesenfeld // Phys. Rev. Letters. – 1987. – Vol. 59. – P.381.

[108] Bak, P. Self-organized criticality / P. Bak, C. Tang, K. Wiesenfield // Phys. Rev. A. - 1988. – V. 38. – P. 364-374.

[109] Vasiliev, V.A. Avtovolnovye protsessy / V.A. Vasiliev, Yu.M. Romanovsky, V.G. Yakhno. M.: Nauka. Gl. red. fiz-mat. lit. (Sovrem. Probl. Fiziki), 1987. 240 pp.

[110] Medvinsky, A.B. Formirovanie prostranstvenno-vremennykh struktur, fraktaly i khaos v kontseptualnykh ekologicheskikh modelyakh na primere dinamiki vzaimodeistvia populyatsiy plankton i ryby / A.B. Medvinsky, S.V. Petrovsky, I.A. Tikhonova, D.A. Tikhonov // UFN. 2002. V. 172. No.1. P. 31-66.

[111] Bak, P. A forest-fire model and some thoughts on turbulence / P. Bak, K. Chen // Physics Letters. – 1990. – A 147(5,6). – P.297–300.

[112] Mozner, W.K. Computer simulations of the forest-fire model / W.K. Mozner, B. Drossel, F. Schwabl // Physica A. – 1992. – Vol. 190. – P. 205–217.

[113] Koposov, E.V. Multifraktalny analiz prostranstvennogo raspredelenia karstovykh yavleniy / E.V. Koposov, D.I. Iudin // Privolzhsky Scientific Journal 2009. No.1. P. 140-147.

[114] Levin, B.V. Yadro Zemli direzhyor seismicheskoy aktivnosti? / B.V. Levin // J. Zemlya i vselennaya, No.3. P. 12-19. 2002.

[115] Iudin D. I. and D. A. Kas'yanov. Percolation Model of Seismic Activity. In: Atmospheric and Ionospheric Electromagnetic Phenomena Associated with Earthquakes, edited by M. Hayakawa pp.911-917. Terra Scientific Publishing Company, Tokyo, 1999.

[116] Iudin D. I., N. V. Korovkin, O.A. Molchanov, V.V. Surkov, and M. Hayakawa, Model of earthquake triggering due to gas-fluid "bubble" upward migration I. Physical Rationale, In: Seismo Electromagnetics. Lithosphere-Atmosphere-Ionosphere Coupling Ed. by M. Hayakawa and O. A. Molchanov, pp.177-185. TERRAPUB, Tokyo, 2002.

[117] Stauffer, D. Introduction to Percolation Theory / D. Stauffer. – L.: Taylor & Francis, 1985. – 382 p.

[118] Bowman, B. Dielectric breakdown in metal-insulator composite / Bowman, B., Stroud // Phys. Rev. B, vol. 40, – 1989. – 4641.

[119] Weibull W., J. Appl. Mech., 18, 293, 1951

[120] Scholz, C. H., L.R. Sykes and J. P. Aggarwal, EQ prediction: a physical basic, Science, 1981, 803–809, 1973.

[121] Streit, J.E. Low frictional strength of upper crustal faults: a model / J.E. Streit // J. Geophys. Res. – 1997. – 102, 24, 619–24, 626.

[122] Sibson, R.H., 1990, Rupture nucleation on unfavorably oriented faults, Bull. Seismol. Soc. Am., 80, 1580–1604.

[123] Hickman, S., R. H. Sibson, and R. Bruhn, 1995, Introduction to special section: mechanical involvement of fluids in faulting, J. Geophys. Res., 100, 12, 831–12,840.

[124] Yamashita, T., Mechanical effect of fluid migration on the complexity of seismicity, J. Geophys. Res., 102, 17, 797–17, 806, 1997.

[125] Ozima M., Podosek F. A. Noble gas geochemistry. Cambridge etc., Cambridge Univ. Press, 1983.

[126] Wakita H., Fujii N., Matsuno S., Nagao K., Takaoka N., "Helium spots" caused by a diapiric magma from the upper mantle. – Science, 200, 1978, 430–2.

[127] King, C-Y, Gas geochemistry applied to earthquake prediction: An overview, J. Geophys. Res., 91, 12,269–12,281, 1986

[128] Igarashi, G., S. Saeki, N. Takahata, K. Sumikawa, S. Tasaka, Y. Sakaki, M. Takahashi, Y. Sano, Ground water radon anomaly before the Kobe earthquake in Japan, Science, 269, 60–61, 1995.

[129] Gold T., Vogel J. E. Hydraulic-elastomeric mount displacement decoupler / T. Gold, J.E. Vogel // The Journal of the Acoustical Society of America, Volume 83, Issue 2, February, – 1988. – p. 844.

[130] Scholz, C. H., The mechanics of earthquakes and faulting. Cambridge Univ. Press, – 1997.

[131] Witten T. A., Sander L. M. // Phys. Rev. Lett. 1981. V. 47. P. 1400.

[132] Kasahara, K. Earthquake mechanics / In Russian transl. K. Kasahara // - M.: Mir, 1985.

[133] Rice, J. The Mechanics of Earthquake Rupture / J. Rice; in Russian transl. // - M.: Mir, 1983.

[134] Ponomaryov, A.S. Teplogazodinamicheskaya model korovykh zemletryaseniy / A.S. Ponomaryov // J. Fizika Zemli. 1990. No.10. P. 100.

[135] Mikhailov, A.S. Kriticheskie yavlenia v sredakh s razmnozheniem, raspadom i diffusiey / A.S. Mikhailov, I.V. Uporov // UFN. 1984. V.144(1). P. 79.

Index

dead end, 113

affine conversion, 19
Alexander-Orbach conjecture, 114
antipersistence, 85

bifurcational coefficient, 130
bond hierarchy, 132
box dimension method, 28
Brownian landscape, 88
Brownian motion, 20
  generic, 85
  model, 88
Brownian surface, 88

Cantor set, 13, 14
chaos game, 19
chemical dimension, 29, 30, 57
chemical distance, 29, 30, 57, 58
coefficient of length ranking, 130
coefficient of lifetime ordering, 131
coenotic paradigm, 97
continuum percolation, 73, 104
correlation length, 54
critical deceleration, 109
critical level, 121
  porosity, 136
critical temperature, 51
crossover phenomenon, 54

Dewar flask, 144
dimension, 12
  constructive fractal, 26
  correlation, 39
  Euclidean, 86
  fracton, 117
  generalized, 34
  global, 94
  Hausdorff, 25, 40, 149
  Hausdorff-Besikovitch, 11
  information, 38
  local, 86
  Minkowski dimension, 25
  Rényi, 34
  spectral, 117
drainage networks, 130
drainage systems, 129
dynamical scaling, 88

edge index, 16
Einstein's equation, 114
entropy of a fractal set, 37
equality, 98

Fick's law, 114
filtration law, 106
fractal, 11
  time series, 84
  boarder, 15
  constructive, 18
  dimension, 12, 29, 30, 41, 56, 58, 130
    of the Koch curve, 15
    of the Sierpiński carpet, 18
    of the Sierpiński gasket, 17
  dynamics, 120, 133
  labyrinth, 111
  networks, 116
  paradigm, 129
  random, 20
  structure, 28, 41, 120, 122
  topological linear, 115
  trees, 130

Griffith's criterion
  classical, 135
  gravitational, 135

Hack's exponent, 129
Horton's laws, 130
Hurst exponent, 85

hyperbolic model, 98
hyperbolic rank parametrization, 98
hyperlattice, 113

Koch
  curve, 14
  island, 15
  snowflake, 15
  star, 15

lattice
  supercubic, 116
Legendre transformation, 39
level of hierarchy, 132
Lipschitz-Hölder coefficient, 40
logarithmically normal distribution, 102

Mandelbrot formula, 98
Mandelbrot-Given fractal, 58
Margalef
  formula, 101
  hypothesis, 101
  index, 101
minimum fractal dimension, 57
multiplicative process, 31

noise
  black, 86
  brown, 85
  pink, 85
  white, 87

oscillation excitation, 115

percolating
  cluster, 48
  network, 48
percolation
  cluster, 47
  threshold, 47, 78, 119
  transition, 48
persistence, 85
phonon, 115
potential surface, 89

random hyperplane, 95
random walking, 115
range of a random variable, 84
rank, 97
  distribution, 97
  representations, 98
relaxation generator, 143

self-affine hypersurface, 94
self-organized criticality, 119
Shannon information index, 37
Sierpiński
  carpet, 17
  gasket, 17, 41
  sieve, 17
  triangle, 17
singularity index, 39
species diversity, 98
spectrum
  multifractal, 39
  of multifractal singularities, 39
  of the Rényi dimensions, 35
  singularity, 39
standard deviation, 85
standardized range, 85
Stirling's formula, 113

Tokens theorem, 41
translation symmetry, 115
transversal correlation length, 95

Voss algorithm, 88

Zipf law, 97

Iudin Dmitry Igorevich,

leading specialist of the Institute of Applied Physics of RAS, leading scientist of the Radiophysical Research Institute, professor of the NNGASU UNESCO Chair, professor of the Chair of ecology of the Lobachevsky Nizhny Novgorod State University, PhD in physics and mathematics, PhD in biology.

Koposov Evgeny Vasilievich,

rector of the Nizhny Novgorod State University of Architecture and Civil Engineering, holder of the NNGASU UNESCO Chair, PhD in engineering, professor, Corresponding member of RAACS, honorary worker of the higher professional education of RF, honorary builder of RF, winner of the prize of the Government of the Russian Federation in education, honorary senator of the University of Applied Sciences of Cologne (Germany).

This book is an introduction to the world of scaling. Following the principle "from simple to complex" the authors start with the fundamentals of the fractal geometry. In Chapter 1 definitions of basic concepts and simple examples of regular as well as stochastic fractals are given. Then in Chapter 2 the reader gets acquainted with fractal structures occurring at geometric phase transitions. Application of the fractal geometry and percolation theory in the description of complex systems forms the content of Chapter 3. In addition, the interested reader may find examples of programme codes of fractal and percolation models realized in the MATLAB system on the cellular automation networks.

ECOLOGICALLY SAFE DEVELOPMENT OF THE LARGE REGION – THE VOLGA BASIN

UNESCO

NNGASU

65, Ilyinskaya, Nizhny Novgorod Russia 603950
phone: 007 (831) 437-38-64
fax: 007 (831) 437-36-69

e-mail: unesco@nngasu.ru